Investigation of plasma interactions with microdroplets

Nourhan Hendawy

BSc, MSc.

Faculty of Computing, Engineering and the Built Environment

Thesis submitted for the Degree of

Doctor of Philosophy

August 2022

Content

List of Tables

List of Figures

Acknowledgements

No words can express my gratitude to my supervisor, Prof. Paul Maguire. He has been always supportive and knowledgeable. The PhD journey is generally intensive time with a lot of work in a short time, however this journey surprisingly became tougher due to Covid19 and lockdown. He was also patient and informative so we achieved a significant progress, despite the disruption, as a result of his advice and flexible plans to suit the changes with the unexpected situations. I would also like to thank my second supervisor Prof. Davide Mariotti for his continuous advice and his patience in communicating with companies to solve many devices technical issues.

Big thanks also to all our group members for being such a friendly and collaborative team. They were able to demonstrate skilled teamwork and provide support whenever needed. A special thanks to Dr. Harold McQuaid and Dr. Ruairi McGlynn for sharing their experience and helping in tackling many technical issues. Further, I would like to acknowledge the Vice Chancellor Research Scholarship (VCRS) for funding my PhD and NIBEC academic and technical team for their support especially Brian and Damian.

During this journey, my family and all my friends, especially Shrouk, Fayza, Rania and Debbie, have the most significant impact on me. I had to be away from my home and my country for long times due to work however, they proved that we can challenge distances and barriers by sharing their love and continuous support.

Nourhan Hendawy

Publications and presentations

A. Submitted or in preparation to submit in international journals:

1. N. Hendawy, H. McQuaid, D. Rutherford, D. Diver, D. Mariotti1 and P. Maguire on “The creation of highly charged micron-sized water droplets”, in preparation.

B. Published journal articles:

1. N. Hendawy, H. McQuaid, D. Mariotti, and P. Maguire, “Continuous gas temperature measurement of cold plasma jets containing microdroplets, using a focussed spot IR sensor,” Plasma Sources Sci. Technol., vol. 29, no. 8, 2020.

2. Presentations at conferences and workshops:

1. The 73rd Annual Gaseous Electronics Virtual Conference (GEC), presentation on “Continuous gas temperature measurement of cold plasma jets containing microdroplets, using a focussed spot IR sensor”, October 2020, online.
2. Five-minutes presentation on my Ph.D. project at the 10th X NExT Ph.D. Workshop, March 2021, online.
3. 239th The Electrochemical Society Conference (ECS), presentation on “Plasma Charging of Micron-size Droplets”, May 2021, recording.
4. The 18th Technological Plasma Workshop (LPW) (a poster) on “Charged Water Droplets Characterization”, Liverpool, December 2021, online.
5. 2nd Newton Advanced Fellowship (NAF) Workshop, with Zhejiang University (China) on “Temperature measurements by probe and infrared emission”, December 2021, online.
6. Three-minutes pitch presentation for scientific audiences on my Ph.D. project in PlasTHER CA20114 Training School, February 2022, Portugal as well as attending a training on plasma physics principals and medicine applications, in person.

7. 241st ECS meeting, poster on “Measurements of the Average Droplet Charge Using a Low-Density Stream of Microdroplets in Atmospheric Pressure Plasma Jet”, Canada, May 2022, online.

3. Awards

1. The three minute thesis (3MT) competition runner up Ulster university.
2. The status of Associate fellow at the higher education academy (AFHEA).
3. Awarded a prize from “the Royal Holloway Physics Department” for my performance and management skills as a Chairperson at “ The 10Th NExT Workshop”.

Abstract

Controlling gas temperature via continuous monitoring is essential in various plasma applications especially for biomedical treatments and nanomaterial synthesis but traditional techniques have limitations due to low accuracy, high cost or experimental complexity. Continuous high-accuracy gas temperature measurements of low-temperature atmospheric pressure plasma jets were demonstrated using a small focal spot infrared sensor directed at the outer quartz wall of the plasma. Measured gas temperatures varied from 25 ^{o}C – 50 ^{o}C, increasing with absorbed power and decreased gas flow. The introduction into the plasma of a stream (~10^{5} s^{-1}) of microdroplets, in the size range 12 μm – 15 μm, led to a reduction in gas temperature of up to 10 ^{o}C, for the same absorbed power. This is an important parameter in determining droplet evaporation and its impact on plasma chemistry.

Droplets charging has influenced a wide range of applications due to the importance of electrons in reactive species generation and participation in wide range of reactions. The first measurements of particle charge acquired by microparticles in a fully collisional atmospheric pressure low temperature plasma operated in helium is reported here. Using a constant stream of liquid microdroplets and a plate electrode, the maximum average charge per droplet was 2.5 x 10^{6} electrons (400 fC) for a plasma absorbed power 5 W at a distance of 3 mm from the downstream plasma electrode. This represents a 2 – 3 orders of magnitude increase in charge levels compared to other approaches. In addition, double ring electrode collector has been used to estimate the charge value using a simulation model with MATLAB. The estimated charge was 5.0 x 10^{3} which agrees with the range values obtained from the plate electrodes at the equivalent power and distance.

System development of a custom designed chamber (PAD) attached to XPS analysis unit has been achieved. A frozen water sample was obtained and transferred to the preplock chamber which is ready to be transferred to the XPS for analysis. Freezing and analysis the water sample after treatment would help in studying the plasma-liquid interactions which are challenging to study with traditional techniques due to the very short-lifetime of the reactive species. This would provide promising results serving many applications such as plasma medicine.

ABBREVIATIONS

APPs	Atmospheric pressure plasmas
T_e	Electron temperature
T_i	Ions temperature
T_g	Gas temperature
CAP	Cold atmospheric plasma
RF	Radio frequency
KT	Kinetic temperature
EEDF	The electron energy distribution function
NTP	Non thermal plasma
RONS	Reactive oxygen and nitrogen species
PAL	Plasma activated liquid
NP	Nanoparticle
PLIs	Plasma-liquid interactions
XPS	X-ray photoelectron spectroscopy
LN	Liquid nitrogen
TC	Thermocouple
KE	Kinetic energy
IR	Infrared sensor
SLM	Standard liter per minute
FoV	Field of view

ABR	Allen, Boyd, & Reynolds theory
OML	Orbit Motion Limited
PH	Patacchini - Hutchinson model
ES	Electrospray

NOMENCLATURE

Q_R	Rayleigh limit of charge
γ	Surface tension
ε_0	Permittivity
q	The charge
q'	The image charge
R_C	The collector radius
R_{Ag}	Plasma afterglow resistance
R_{Eff}	Plasma effluent resistance
R_{osc}	The oscilloscope input resistance
Z	The particle distance from the ring
x	The radial distance from axis of ring
D	The ring diameter
W	The ring width

Note on access to content

“I hereby declare that the with the effect from the date on which the thesis is deposited in the Library of the University of Ulster, I permit.

1. the Librarian of the University to allow the thesis to be copied in the whole or in part without reference to me on the understanding that such authority applies to the provision of single copies made for study purposes or for the inclusion within the stock of another library.

2. the thesis to be made available through the Ulster Institutional Respiratory and/or EThOS under the terms of the Ulster eThesis Deposit Agreement which I have signed.

IT IS A CONDITION OF USE OF THIS THESIS THAT ANYONE WHO CONSULTS IT MUST RECOGNISE THAT THE COPYRIGHT RESTS WITH THE AUTHOR AND THAT NO QUOTATION FROM THE THESIS AND NO INFORMATION DERIVED FROM IT MAY BE PUBLISHED UNLESS THE SOURCE IS PROPERLY ACKNOLOWLEDHED.”

1 Introduction

Plasma is a reactive medium which can be generated in labs by applying an electric field to a gas resulting in the generation of ions, electrons, and neutral species. Collisions between neutral species produces more reactive species through energy and charge transfer. Atmospheric pressure plasmas (APPs) can be divided into thermal and non-thermal plasmas depending on the temperature of both electrons (T_e) and ions (T_i) relative to the gas temperature (T_g). The non-thermal plasma system (NTP), also known as cold atmospheric plasma (CAP) where $T_e >> T_g$, is very reactive due to the high concentration of active species, radicals, and excited atoms. NTP has many advantages over thermal plasma ($T_e = T_g$) and other traditional technologies because high energy electrons can initiate high energy reactions without the need for high gas temperatures. Plasma chemistry is strongly influenced by the plasma properties in all APPs applications. The main factors are gas temperature (T_g), electron temperature (T_e) and electron density (n_e). Controlling these factors can be achieved by controlling plasma parameters such as gas type, gas flow, and power source. When applying plasma to a liquid, many reactive oxygen and nitrogen species (RONS) are produced which have oxidative characteristics that are important for many applications.

The possibility of generating non-thermal atmospheric pressure plasmas has led to industrial, agricultural, and environmental applications. For instance, the use of plasmas has led to improving materials properties and synthesis of new nanomaterials in industrial applications as well as enhancing the growth rate of plants and soil reclamation in agriculture sector. Plasmas have also been used in wastewater treatment and air purification in environmental applications. In addition, CAP has enormous number of biological and medical applications e.g. dermatology, wound healing, enhancement of blood coagulation or sterilisation of surfaces [1], cell proliferation, inactivation of cells and microorganisms, and cancer treatment through plasma-induced apoptosis. Traditional therapies for cancer, which depend on surgical extirpation, radiation, or chemotherapy, have many limitations when put in use with cancers due to their significant side effects. Cold atmospheric plasmas may offer greater efficacy, fewer side-effects, and wide-ranging scope, provides a broader range of possibilities for plasma aided medical treatments.

Most atmospheric pressure plasma applications have benefited from plasma-liquid interaction e.g. nanomaterial, biomedical, dermatological, agricultural, and environmental applications [2–5]. Plasma-liquid interaction increases the plasma reactivity therefore, it has most major influence in plasma medicine applications such as skin treatment, biomaterial, cancer treatment and therapeutic applications. For instance, wound healing by plasma would considerably benefit from studying the interface between plasma and liquids as wounds usually have a percentage of water content. The interaction between plasma and liquids involves many complex chemical and physical processes that prompt producing many reactive species and a high flux of radicals e.g., RONS. However, most of these radicals have a noticeably short timescales and propagate in a nanoscale distance. In addition, plasma-liquid system is very dynamic and has a high interface gradient such as temperature, electric field, chemical and mass flux. Therefore, this system requires in depth studies to understand this interaction and improve these applications as well as a special controls on all parameters in particular gas temperature as all medical and biomedical applications are heat sensitive [6].

One of the first commercial APP systems kINPen, such as the one manufactured by “Neoplas med” company for cold plasma therapy, has been widely used as a plasma jet for medical purposes such as skin treatment and wound healing due to the high concentration of reactive species generated [7–9]. It consists of rod electrode inside a capillary tube and connected to a power supply where the target should be exposed to the plasma jet at a millimetre distance (preferably below 8 mm) [10]. SteriPlas and PlasmaDerm are other examples of CAP medical devices used in clinical applications such as skin treatment but they target wider area of the skin than kINPen [11]. Although all these devices have proven successful in many clinical trials, they are only suitable for surface treatment applications and cannot be used for plasma treatment inside the body. In addition, they have limitations due to being in direct contact with patient skin which makes it susceptible to current, electric field and variation of gas temperature. Controlling all parameters is challenging due to the complexity and the non-linearity of plasma devices and would require knowledge about their rate of change, change effect on plasma chemistry and the target and continuous sensitive monitoring and controlling tools. To reduce the complexity of controlling all plasma parameter and to avoid any potential consequent risk, there is a

need to avoid the direct contact between plasma and the target by utilising and investigating remote plasmas. So, plasma reactive species can be delivered to the target while being located further away.

Plasma activated liquid (PAL) is a potential solution by treating the liquid with plasma, storing treated liquid until being used then delivering this liquid which contains reactive species to the target area. This approach has proven its effectiveness in many applications, in addition PAL can be injected into the body. However, PAL effectiveness depends mainly on the shelf lifetime of reactive radicals [12]. There are many studies on the viability of using plasma treatment inside the body including the option of using plasma during surgery and endoscopy which uses flexible long tube where the plasma is generated at the end of the tube [13–16]. In these techniques, reactive species can approach the target area very quickly, however there is a potential serious risk due to using high voltages inside the body and the possibility of elevated temperature arcs as well as tubes erosion risk.

Plasma activated liquid could be delivered very quickly within the lifetime of most of reactive radicals to the target area in the form of microdroplets. Where there are many RONS generated when using water as plasma treated liquid (PAW) some with long lifetime such as nitrates (NO_3^-) that may last for years, nitrites (NO_2^-) that may last for days, hydrogen peroxide (H_2O_2) with half-lifetime of $\sim 10^4$ s and ozone (O_3) with the half-lifetime of a few minutes. Nevertheless, the most effective radicals have very short lifetime e.g. hydroxyl radicals (•OH) with lifetime below milliseconds, nitric oxide (NO•) lasts only for few seconds where superoxide (O_2^-) lasts for 1.5 s and both peroxynitrate ($OONO_2^-$) and peroxynitrites ($ONOO^-$) have half-lifetimes of less than l s [12]. Therefore, plasma needs to be remarkably close or in contact with the target to guarantee the fast delivery of effective radical species. Microdroplets travel through the plasma in the gas flow, without the need for storage. That is because microdroplets act as microreactors that have a faster reaction rates and the potential for keeping the reactive species for longer time than the bulk liquid [17]. Whereas PAL depend on storing the treated liquid until it be used which may lead to the loss of many reactive species. Sremacki et al. [18] used RF argon plasma jet to study the effect of injecting aerosol on the liquid chemistry and performed chemical analysis of RONS in liquid where both short and long-lived reactive species were detected for their

importance in most of the biomedical applications. In addition, Kruszelnicki et al. [19] investigated the activation of water microdroplets by plasma compared to liquid and provided 0 and 2D modelling water of microdroplets activated by plasma. They found that liquid activation is limited by the RONS transport rate to the liquid surface while the injection of microdroplets was found to increase the transport rate from gas to liquid due to the larger surface to volume ratio. However, more studies are required to check the reactive species presence in microdroplets with respect to the delivery time. The use of XPS-PAD system, would enable the study of the reactive species in microdroplets by the rapid freezing of the droplets to slow down the reactions for analysis as presented in chapter 3.

There are applications examples in the literature of spraying aerosol through plasmas, where the aerosol is a form of liquid droplets suspended in a gas, such as disinfection and chemical analysis applications in thermal plasmas as well as nanomaterials synthesis and nanomedicine applications in non-thermal plasmas [20–23]. The addition of particles or water molecules to noble gases is more likely to increase the gas temperature and lead to consequent evaporation of small and large droplets depending on the temperature. Hence, if the droplets are exposed to the plasma for a long period or the gas temperature is too high, there is a high probability that all droplets evaporate before they reach the target area and PAL loses its effectiveness [22]. Droplets evaporation can be avoided by reducing the plasma exposure time, however there would be a challenge to produce the sufficient reactive species required for any application As long as gas temperature is a strong reason behind evaporation, there is a necessity for continuous measurements of gas temperature to keep it under control which is very difficult using traditional measuring techniques. For example, OES is a non-contact and continuous technique but involves complex analysis to fit experimental spectra to theoretical spectra of chosen molecular species to estimate the gas temperature. Other, more precise optical techniques (Raman, Schlieren) require large and complex instruments that cannot be left in place for continuous measurement in the field. Thermocouples and fiber optics are common and simple measuring techniques where the former is a metal wire inserted inside the plasma and the latter consisted of an optical fiber probe which is connected to a source of light and spectrometer. The measurements using these techniques in microplasmas are inhibited with geometric restrictions, flow disruption, contamination and electrical

coupling concerns [24–26]. A full list of the most common measuring techniques along with a review of their limitations will be discussed in detail in chapter 4. In APPs, the increase in gas temperature may result from collisionality of electrons and particles and has a significant impact on most of the chemical and composition reactions. In addition to heat sensitive materials that requires reliable continuous gas temperature monitoring. Gas temperature of APPs has not been well-characterised on a continuous in-situ basis especially with the inclusion of water droplets or molecular gases therefore a continuous and reliable measurements of the plasma gas temperature with and without water droplets will be provided in this thesis.

Measuring the reactive species in liquids is complicated, particularly with the most reactive radicals as they interact very quickly with the medium and with each other. Although the radicals in droplets would have higher concentration than in liquids because larger surface area of the droplet is exposed to the plasma, measuring the radicals inside droplets is more challenging due to the small size of droplets. The use of cold and short high-density plasma such as RF plasmas is a prospective solution for the above challenges. That is because when the droplets travel in a cold medium and for a shorter distance through the plasma, the evaporation is significantly reduced. Whereas the use of high-density plasma increases the production rate of reactive species in a relatively shorter time. In comparison to other contact plasma techniques such as other kHz plasmas, the kINPen is driven at low MHz frequencies but maintains the same mode of operation as kHz jets, i.e. the plasma plume is long and may reach a length of 10 cm which mean that over a long flight time, droplets are much more susceptible to evaporation before they reach the target, therefore losing most of the reactive species [9,27]. Limiting the droplets flow rate may also reduce the evaporation and using bigger diameter droplets would require longer time to evaporate. Measurements of droplets size with respect to droplets velocity were previously carried out in NIBEC using an RF plasma and a similar experimental set up to our current one. A reduction in droplet diameter was noticed when the plasma was on compared to the plasma off, but it was shown possible for the majority (>95%) to pass through the plasma and arrive downstream, without fully evaporating. Estimates of the water released into plasma per droplet was performed using both droplet rate and evaporation rate. Droplet evaporation was shown to be greater in a plasma than in a gas. However the larger water droplets (> 4 microns diameter)

survived travel through plasma without total evaporation [28]. Furthermore, synthesis of small diameter gold nanoparticles was accomplished using the same experimental system and fast transport of nanoparticle was proven which is essential for many applications by reducing the possibility of evaporation and increasing the number of reactive species within a short time. In addition, chemical reactions were responsible for the production of ultra-low energy electrons through electron reduction processes (< 0.1 eV) which has high importance in many applications especially cancer treatment [29].

Studying the plasma liquid reactions and the creation of short lifetime radicals is vital for understanding the plasma chemistry and for many applications including plasma medicine and nanomaterials. Mass spectroscopy (MS) is one of the most common technique for measuring the chemical reactions occurring in liquid due to plasma as well as optical emission spectroscopy (OES) by knowing the reactive species production rates [30,31]. However, these techniques are not suitable for detecting short lifetime radicals such as OH. X-ray photoelectron spectroscopy (XPS) is an effective technique which can provide high resolution for surface analysis around 20-100 Å in the top layer of a surface and consequently provides information about chemical bonds and samples molecular composition. XPS requires high vacuum so it is suitable for solid materials only as liquid samples will evaporate under high vacuum. In addition, the transfer time of samples from the plasma treatment into the XPS chamber would take longer time than the lifetime of most radicals of interest specifically short lifetime ones. Freezing the droplets as soon as they pass through the plasma is a potential solution to slow down the chemical reactions and allow the transfer to XPS for analysis without losing short lifetime radicals. However, freezing and transferring the samples quickly to XPS is incredibly challenging due to the environmental factors and the high vacuum of the XPS that makes most samples are susceptible to evaporation before arriving to XPS analysis unit. In NIBEC, they have initiated the development of a unique XPS system with an integrated plasma chamber (PAD) which may allow direct transfer of plasma treated samples into the XPS in a highly controlled environment. The integrated atmospheric plasma load-lock chamber (PAD) is an additional sample preparation stage and is a custom design chamber attached to XPS. This PAD chamber will allow for specialised sample preparation via atmospheric pressure plasma (APP) exposure, either directly or through plasma-liquid

interactions. However, in order to study the effect of plasma on liquids by XPS, the liquid needs to be frozen rapidly. However freezing bulk liquid, even a small volume, is not possible within the lifetime of short-lived radicals. However, since a microdroplet has a volume of picolitre magnitude it may be possible for these to be frozen fast enough. One objective of this thesis is to pass microdroplets through plasma and allow them to freeze on contact with sample collector or even in flight to collector. Once enough are collected, they can be transferred while frozen to the XPS chamber at high vacuum through an intermediate load-lock stage. This would allow for the first-time surface analysis of plasma treated liquids with the chemical and depth resolution (0.1 nm – 10 nm) of XPS. However, there is a major challenge in freezing and transfer since the PAD chamber when filled with gas, along with transfer arms etc have a large thermal mass possibly making it difficult to maintain the frozen state during transfer.

XPS analysis of surface chemistry may provide details on the transfer of radicals created in the gas phase across the interface as well as details on the liquid reactions occurring in the very first monolayers if these radicals transfer to the liquid. Additionally, electrons and ions existing in plasma have a significant importance and influence most of the major reactions. When high energy electrons (> 1 eV) reach the liquid, they quickly become in equilibrium with the liquid, named as "solvated electrons $e^-_{(aq)}$)", and they initiate and participate in chemical reactions such as the following reactions where equation 2 is in the presence of solvated O_2 and H_2 [30]:

$$2\ e^-_{(aq)} + 2H_2O \rightarrow H_{2(g)} + 2OH^- \qquad (1)$$

$$3\ e^-_{(aq)} + O_2 + H_2 + H^+ \rightarrow H + 2OH^- \qquad (2)$$

Electrons are very reactive and are involved in most of the chemical reactions, but they are difficult to measure due to their noticeably short lifetime in addition to the arrival of OH radicals from plasma which adds more complexity to the reactions. Therefore, the only way to understand and study the short lifetime radicals and this complex chemistry is by chemical simulation with the knowledge of some measured inputs such as radicals' density in plasma, and the reaction rates. Nevertheless, that is not applicable for electrons because of the high collisionality of the system that result

in unknown number of collisions between electrons and droplets and subsequent unidentified collision rate. When electrons and ions hit the droplet, it can become charged depending on the net flux (electrons – ions) [32]. It is expected that an uncharged droplet or particle entering the plasma would be hit with more electrons than positive ions because they are much faster but soon would acquire a negative charge which would repel / slow down further electrons reaching surface until flux of electrons and ions are equal. This means the droplet is expected to carry a negative charge after plasma exposure. However, this has never been measured at atmospheric pressure. If the charge on the droplet can be determined, it may be possible from theories to calculate the electron flux to droplet which can provide vital information for plasma-liquid simulation of electron-based reactions. One objective of this thesis is therefore to estimate the amount of charge on plasma exposed microdroplets from current-voltage measurements. However, particle charging has been studied only in low pressure plasma, but these theories may not be applicable for high pressure plasma because this high collisional system results in some electron energy loss as well as changing in their directions. The electrons concentration is variable with liquid depth and time because electrons are very reactive, and they diffuse in the liquid until they react if they did not react on the liquid surface where the free electrons before interaction may lead to electrical conductivity in the liquid [33]. Simulation is suitable for this case as it breaks droplets into small volume cells and then calculate for each in turn. Electrons arrival rate / collision rate will be required to calculate the solvated electrons density in liquid surface via known rate equations and the concentrations of other species, but this value is unknown and there are no available theories to calculate this rate. However, this rate could be estimated by measuring the charge on the droplet which is one of our objectives and consequently checking if the existing equations that are used for low pressure are valid or useful at high pressure plasmas.

1.1 Research hypothesis

Plasmas have provided promising results in a wide range of applications and offer the potential of use in medical treatments such as wound healing and cancer treatment. However, plasmas in direct contact with tissue may cause problems due to UV exposure, elevated gas temperatures, currents and electric fields that may lead to tissue and cell damage. The inclusion of microdroplets may offer a solution to avoid many of these side effects as passing microdroplets through the plasma creates highly reactive species inside the droplets which are then carried by the droplets to the point of use. If the droplet flight time can be kept short enough, these highly reactive species could be delivered without losing their chemical efficacy while keeping the plasma itself remote from tissue. This would therefore help in eliminating or reducing the side effects of direct contact plasmas. Measurements of radicals and reactive species inside the droplets is necessary to demonstrate the plasma-droplet principle and then to improve plasma-droplets applications. However these measurements are challenging due to the very short lifetime of most of the important radicals. A new technique is proposed where rapid freezing of plasma-treated liquid samples and plasma-treated liquid droplets may offer an effective method to study the plasma – induced chemical reactions at the droplet surface using XPS. One possible disadvantage of droplets is that the addition of droplets to a gas plasma may cause an increase in the gas temperature and may also lead to droplet evaporation before they reach their target. Therefore, a method of continuous gas temperature measurement is needed to be developed to help control plasma and allow the safe inclusion of liquid droplets.

1.2 Research objectives

Plasma interaction with microdroplets induces more chemical reactions and creates highly reactive species in a higher concentration than plasma only. This interaction would support a wide range of applications such as nanomaterial and plasma medicine by offering high efficiency and minimal side effects and would require in-depth study of the plasma-droplets induced chemical reactions. Therefore, measuring the concentration of radicals inside the droplet is our main objective by

freezing the activated liquid sample quickly to slow down the chemical reactions and allowing fast transfer to XPS for surface analysis. Alternatively, measuring charge on the droplets would help in determining the concentration of radicals inside the droplets and understanding the plasma-droplets chemical interactions. Charge measurements can provide estimates of the electron and ion fluxes to the droplet surface. These fluxes are essential parameters required for plasma - liquid chemical simulation. However charge measurements of microdroplets have not previously been made and flux values are unknown. A potential restriction of using plasma-droplets is the possible increase in the gas temperature with introduction of droplets into the plasma which would affect all heat sensitive applications and may lead to droplet evaporation. Hence, controlling the plasma gas temperature by providing in-line continuous measuring technique is another objective of our research where the research objectives are summarised as follows:

- Measurement of the gas temperature of high pressure plasma with and without droplets using a small focal spot IR sensor. In addition to providing a comparison with traditional techniques measurements for validation.
- Developing the PAD system by connecting coils, thermocouples, water and delivery system etc. As well as testing the cooling rate and the pumps pressure performance to allow the measurement of plasma – induced chemical reactions at the droplet surface using XPS.
- Analysis of droplet charge measurements using two techniques i.e. plate collector and double ring electrodes. In addition to providing a comparison between the results obtained from them.

1.3 Thesis structure

Chapter 2 is a literature review that provides an introduction about plasma generation and main collisions focusing on atmospheric pressure plasmas. Plasma-liquid interactions is reviewed in detail and the microdroplets injection in plasma.

Chapter 3 The Escalab XPS system with load-lock chamber, integrated atmospheric plasma chamber (PAD) and sample transfer system is the first such XPS system worldwide, custom built to NIBEC specifications. The Escalab XPS chamber and the load-lock chamber were built to standard manufacturer specifications, but the PAD and sample transfer were entirely new developments. The original objective of chemical measurement of plasma treated droplets by XPS could not be completed within the remaining time available due to errors in the manufacturing. Instead, the research priority became the design/test of various approaches to enable freezing of liquid at atmospheric pressure within the confines of the PAD chamber and compatible with safe frozen sample transfer to the XPS chamber which is demonstrated in this chapter.

Chapter 4 investigates the continuous in-situ measurement of gas temperature in a plasma with and without droplets. A brief review provides details on the main lab techniques for measuring plasma gas temperature and then considers possible minimally invasive or low cost in-situ sensors. Experimental measurements of plasma gas temperature without and with droplets using a small focal spot IR sensor are then presented along with the validation of our measurements. Presenting the main challenge of locating the small focal spot of 0.6 mm on the capillary tube wall and between the 2 mm electrodes. CAD 2D software was used in making drawings for the experimental setup as well as the IR sensor field of view which was useful in determining the centre line of the tube and determining the precise location of the IR focal spot between the two electrodes.

Chapter 5 Plasma-droplets interaction result in same reactive species as plasma-bulk liquid e.g., •OH, •O, e^-, O_3 and H_2O_2 whereas the major difference is the surface to volume ratio of droplets which is much higher than bulk-liquid interaction. In addition, the plasma-liquid interaction takes place on the surface of the liquid, where the rest of the liquid dilutes the chemical reactions products and reduce the chemistry progression. In particular, the number of electrons, as the most reactive species, reaching the bulk liquid is much lower than their number in plasma so droplets, since these are within the plasma, would be surrounded by electrons which would maintain their high concentration. Estimation of neutral atom/molecule/radical flux is an essential parameter required for liquid simulation. The neutral species flux can be

estimated from gas kinetic theory by knowing radical densities and gas temperatures. However, the ion or electron fluxes are unknown so alternatively, the flux estimation may be obtainable by measuring charge on the droplets then using existing theories. However, measurement of charge on microparticles in an atmospheric pressure plasma has never been achieved before. In this chapter the average charge per droplet will be estimated from voltage measurements as a stream of charged droplets impacts on a collector plate downstream from plasma. For charge measurements, estimation of the droplet velocity relative to the gas speed will also be needed and the number of electrons which can hit the droplet will be investigated in this chapter.

Chapter 6 In this chapter, attempts at measuring droplet charge in flight i.e., without impacting at a collector will be described. This will involve simulations using of model from literature related to induced charge due to charged particle flowing through a ring as well as simulations based on droplet number density, size, and the predicted size – charge relationship for plasma charging obtained from existing models.

1.4 References

[1] J. Gruenwald, J. Reynvaan, T. Eisenberg, P. Geistlinger, Characterisation of a simple non-thermal atmospheric pressure plasma source for biomedical research applications, Contrib. to Plasma Phys. 55 (2015) 337–346. https://doi.org/10.1002/ctpp.201400059.

[2] A. Gulec, F. Bozduman, A.M. Hala, Atmospheric Pressure 2.45-GHz Microwave Helium Plasma, IEEE Trans. Plasma Sci. 43 (2015) 786–790. https://doi.org/10.1109/TPS.2015.2403280.

[3] D. Mariotti, Y. Shimizu, T. Sasaki, N. Koshizaki, Gas temperature and electron temperature measurements by emission spectroscopy for an atmospheric microplasma, J. Appl. Phys. 101 (2007) 1–8. https://doi.org/10.1063/1.2409318.

[4] M. Tuszewski, Ion and gas temperatures of 0.46 MHz inductive plasma discharges, J. Appl. Phys. 100 (2006) 0–5. https://doi.org/10.1063/1.2337167.

[5] K.K. Jayapalan, O.H. Chin, Measurement of neutral gas temperature in a 13.56 MHz inductively coupled plasma, AIP Conf. Proc. 1657 (2015). https://doi.org/10.1063/1.4915242.

[6] Y. Sui, C.A. Zorman, R.M. Sankaran, Plasmas for additive manufacturing, Plasma Process. Polym. 17 (2020) 1–25. https://doi.org/10.1002/ppap.202000009.

[7] G. Isbary, T. Shimizu, Y.F. Li, W. Stolz, H.M. Thomas, G.E. Morfill, J.L. Zimmermann, Cold atmospheric plasma devices for medical issues, Http://Dx.Doi.Org/10.1586/Erd.13.4. 10 (2014) 367–377. https://doi.org/10.1586/ERD.13.4.

[8] Industry - neoplas GmbH, (n.d.). https://www.neoplas.eu/en/industry.html (accessed October 22, 2022).

[9] S. Reuter, T. Von Woedtke, K.D. Weltmann, The kINPen - A review on physics and chemistry of the atmospheric pressure plasma jet and its applications, J. Phys. D. Appl. Phys. 51 (2018). https://doi.org/10.1088/1361-6463/aab3ad.

[10] K. Fricke, I. Koban, H. Tresp, L. Jablonowski, K. Schröder, A. Kramer, K.D.

Weltmann, T. von Woedtke, T. Kocher, Atmospheric pressure plasma: A high-performance tool for the efficient removal of biofilms, PLoS One. 7 (2012). https://doi.org/10.1371/journal.pone.0042539.

[11] K.D. Weltmann, T. Von Woedtke, Plasma medicine - Current state of research and medical application, Plasma Phys. Control. Fusion. 59 (2017). https://doi.org/10.1088/0741-3335/59/1/014031.

[12] Kostya (ken) Ostrikov, R. Zhou, R. Zhou, P. Wang, Y. Xian, A. Mai-Prochnow, X. Lu, P.J. Cullen, K. (Ken) Ostrikov, K. Bazaka, Plasma-activated water: Generation, origin of reactive species and biological applications, J. Phys. D. Appl. Phys. 53 (2020). https://doi.org/10.1088/1361-6463/ab81cf.

[13] J.Y. Kim, S.O. Kim, Y. Wei, J. Li, A flexible cold microplasma jet using biocompatible dielectric tubes for cancer therapy, Appl. Phys. Lett. 96 (2010) 1–4. https://doi.org/10.1063/1.3431392.

[14] J. Geng, S. Yin, S. Huang, Q. Tang, H. Luo, F. Chen, Flexible cold plasma jet with controllable length and temperature for hydrophilic modification, Phys. Plasmas. 25 (2018) 083508. https://doi.org/10.1063/1.5040331.

[15] E. Robert, M. Vandamme, L. Brullé, S. Lerondel, A. Le Pape, V. Sarron, D. Riès, T. Darny, S. Dozias, G. Collet, C. Kieda, J.M. Pouvesle, Perspectives of endoscopic plasma applications, Clin. Plasma Med. 1 (2013) 8–16. https://doi.org/10.1016/J.CPME.2013.10.002.

[16] T. Wang, M.S. Hu, B. Yang, X.L. Wang, X. Chen, J.Q. Liu, Long, biocompatible and highly flexible cold atmospheric microplasma jet device for precise endoscopic therapies, Proc. IEEE Int. Conf. Micro Electro Mech. Syst. 2018-January (2018) 365–368. https://doi.org/10.1109/MEMSYS.2018.8346563.

[17] Z. Wei, Y. Li, R.G. Cooks, X. Yan, Accelerated reaction kinetics in microdroplets: Overview and recent developments, Annu. Rev. Phys. Chem. 71 (2020) 31–51. https://doi.org/10.1146/annurev-physchem-121319-110654.

[18] I. Sremački, G. Bruno, H. Jablonowski, C. Leys, A. Nikiforov, K. Wende, Influence of aerosol injection on the liquid chemistry induced by an RF argon plasma jet, Plasma Sources Sci. Technol. 30 (2021).

https://doi.org/10.1088/1361-6595/abe176.

[19] J. Kruszelnicki, A.M. Lietz, M.J. Kushner, Atmospheric pressure plasma activation of water droplets, J. Phys. D. Appl. Phys. 52 (2019). https://doi.org/10.1088/1361-6463/ab25dc.

[20] A. Niveditha, R. Pandiselvam, V.A. Prasath, S.K. Singh, K. Gul, A. Kothakota, Application of cold plasma and ozone technology for decontamination of Escherichia coli in foods- a review, Food Control. 130 (2021) 108338. https://doi.org/10.1016/J.FOODCONT.2021.108338.

[21] N.S.L. Chew, K.S. Wong, W.S. Chang, C.W. Ooi, L.Y. Yeo, M.K. Tan, Nanoscale plasma-activated aerosol generation for in situ surface pathogen disinfection, Microsystems Nanoeng. 2022 81. 8 (2022) 1–13. https://doi.org/10.1038/s41378-022-00373-3.

[22] A. Stancampiano, T. Gallingani, M. Gherardi, Z. Machala, P. Maguire, V. Colombo, J.M. Pouvesle, E. Robert, Plasma and aerosols: Challenges, opportunities and perspectives, Appl. Sci. 9 (2019). https://doi.org/10.3390/app9183861.

[23] P. Ranieri, G. McGovern, H. Tse, A. Fulmer, M. Kovalenko, G. Nirenberg, V. Miller, A. Rabinovich, A. Fridman, G. Fridman, Microsecond-pulsed dielectric barrier discharge plasma-treated mist for inactivation of Escherichia coli in vitro, IEEE Trans. Plasma Sci. 47 (2019) 395–402. https://doi.org/10.1109/TPS.2018.2878971.

[24] K. Knoerzer, A.B. Murphy, M. Fresewinkel, P. Sanguansri, J. Coventry, Evaluation of methods for determining food surface temperature in the presence of low-pressure cool plasma, Innov. Food Sci. Emerg. Technol. 15 (2012) 23–30. https://doi.org/10.1016/j.ifset.2012.02.008.

[25] W. Fu, C. Zhang, C. Nie, X. Li, Y. Yan, A high efficiency low-temperature microwave-driven atmospheric pressure plasma jet, Appl. Phys. Lett. 114 (2019). https://doi.org/10.1063/1.5108538.

[26] C. Engelhard, A. Scheffer, T. Maue, G.M. Hieftje, W. Buscher, Application of infrared thermography for online monitoring of wall temperatures in inductively coupled plasma torches with conventional and low-flow gas

consumption, Spectrochim. Acta - Part B At. Spectrosc. 62 (2007) 1161–1168. https://doi.org/10.1016/j.sab.2007.07.010.

[27] S. Bekeschus, A. Schmidt, K.D. Weltmann, T. von Woedtke, The plasma jet kINPen – A powerful tool for wound healing, Clin. Plasma Med. 4 (2016) 19–28. https://doi.org/10.1016/J.CPME.2016.01.001.

[28] P.D. Maguire, C.M.O. Mahony, C.P. Kelsey, A.J. Bingham, E.P. Montgomery, E.D. Bennet, H.E. Potts, D.C.E. Rutherford, D.A. McDowell, D.A. Diver, D. Mariotti, Controlled microdroplet transport in an atmospheric pressure microplasma, Appl. Phys. Lett. 106 (2015). https://doi.org/10.1063/1.4922034.

[29] P. Maguire, D. Rutherford, M. Macias-Montero, C. Mahony, C. Kelsey, M. Tweedie, F. Pérez-Martin, H. McQuaid, D. Diver, D. Mariotti, Continuous In-Flight Synthesis for On-Demand Delivery of Ligand-Free Colloidal Gold Nanoparticles, Nano Lett. 17 (2017) 1336–1343. https://doi.org/10.1021/acs.nanolett.6b03440.

[30] P.J. Bruggeman, M.J. Kushner, B.R. Locke, J.G.E. Gardeniers, W.G. Graham, D.B. Graves, R.C.H.M. Hofman-Caris, D. Maric, J.P. Reid, E. Ceriani, D. Fernandez Rivas, J.E. Foster, S.C. Garrick, Y. Gorbanev, S. Hamaguchi, F. Iza, H. Jablonowski, E. Klimova, J. Kolb, F. Krcma, P. Lukes, Z. MacHala, I. Marinov, D. Mariotti, S. Mededovic Thagard, D. Minakata, E.C. Neyts, J. Pawlat, Z.L. Petrovic, R. Pflieger, S. Reuter, D.C. Schram, S. Schröter, M. Shiraiwa, B. Tarabová, P.A. Tsai, J.R.R. Verlet, T. Von Woedtke, K.R. Wilson, K. Yasui, G. Zvereva, Plasma-liquid interactions: A review and roadmap, Plasma Sources Sci. Technol. 25 (2016). https://doi.org/10.1088/0963-0252/25/5/053002.

[31] G. Rovelli, M.I. Jacobs, M.D. Willis, R.J. Rapf, A.M. Prophet, K.R. Wilson, A critical analysis of electrospray techniques for the determination of accelerated rates and mechanisms of chemical reactions in droplets, Chem. Sci. 11 (2020) 13026–13043. https://doi.org/10.1039/d0sc04611f.

[32] M. Yamashita, J.B. Fenn, Electrospray ion source. Another variation on the free-jet theme, J. Phys. Chem. 88 (1984) 4451–4459. https://doi.org/10.1021/J150664A002/ASSET/J150664A002.FP.PNG_V03.

[33] D.X. Liu, Z.C. Liu, C. Chen, A.J. Yang, D. Li, M.Z. Rong, H.L. Chen, M.G. Kong, Aqueous reactive species induced by a surface air discharge: Heterogeneous mass transfer and liquid chemistry pathways, Sci. Reports 2016 61. 6 (2016) 1–11. https://doi.org/10.1038/srep23737.

2 Literature Review

2.1 Plasma generation

When a gas is subjected to a high electric field, breakdown occur creating ions and electrons from neutral atoms or molecules. After the first generation of electrons and ions, acceleration of the charges by the electric field leads to multiplication by the production of more ions and electrons so that merely each electron result in a pair of ion-electron production [1]. The phenomena when an electron hits the electrode resulting in generating another electron is known as secondary electron emission (SEE) whereas the phenomena of an ion hitting the electrodes is identified as secondary ion emission [2]. Consequently, the gas becomes conducting instead of insulating and a plasma is generated. Streamers and sparks represent another category of atmospheric plasma discharges. When avalanches of electrons are generated from Townsend discharge, they make a space charge around the electrode where these electrons ionize the surrounding air producing more electrons, increasing the electric field and covering a wider region that lead to the formation of streamer discharge. Streamers create the initial ionized path for spark discharges therefore, streamers are commonly known as sparks precursors. Sparks discharges have a higher gas temperature and degree of ionization than streamers whereas the physical mechanism of these discharges depend mainly on the gas composition, pressure and temperature [3,4]. Plasma consists of enormous number of electrically charged species where the number of positive and negative charges are roughly equal. After the plasma generation, the electric field inside the plasma reduces to almost zero except at the boundaries which is named as plasma sheath. Electrons are then generated in the sheath which moves to the plasma due to the electric field resulting in gas ionisation. Electrons are the most reactive radical that contribute to gas ionisation, therefore high electron losses may cause the plasma to quench. Electrons losses in plasma can be due to many reactions such as formation of reactive oxygen and nitrogen species (RONS), absorption of electrons by molecules (electron attachment) and collisions with gas atoms and molecules [5]. In addition, electrons, and ions diffusion from inside to outside the plasma due to their low concentration outside the plasma compared to inside, results in some electrons loss. The electrons diffuse much faster than ions because they are lighter so more would be lost. However, loss of electrons means the

remaining plasma becomes positive which slows down the electron loss. The plasma becomes sufficiently positive, i.e., plasma potential, so that both ions and electrons diffuse at same rate, and this is known as ambipolar diffusion [6]. The plasma potential depends mainly on electron temperature. Controlling the input power can be used to compensate for this electron loss by providing high voltage sufficient to cause breakdown to the gas. In addition, secondary electrons emission result in more electrons being released into the plasma with high energy which helps in maintaining the plasma.

2.2 Noble gas plasmas and collisions

Noble gases such as argon and helium are electropositive and are responsible for maintaining the stability of the plasma by providing electrons and forming positive ions [7]. In electropositive plasmas, atomic collisions in the gas phase are between gas atoms, ions, and electrons. Collision between particles may lead to changes in particle momentum, energies, ionization of neutral particles and neutralization of ionized particles. Also, collision between electrons and atoms result in alteration in the electron momentum through elastic scattering process in addition to ionization and excitation as inelastic processes. The main processes when ions collide with atoms are resonant charge transfer and elastic scattering that result in changes in their energies and momentum [8]. In electronegative plasma, electrons, negative and positive ions are the main composition of the plasma with negative ions being dominant and formed through many process such as electron dissociation and attachment [9]. In contrast to electropositive plasmas, the introduction of electronegative gases such H_2O or O_2 into a plasma may cause disruption to the plasma because they tend to reduce the electron density due to electron attachment leading to negative ions [7].

2.3 Excitation and ionisation processes in a plasma

Table 1: Electrons reactions in the gas phase [1,10]

Reactions		Description
$e^- + A \rightarrow A + e^-$	(1)	elastic scattering
$e^- + A \rightarrow A^* + e^-$	(2)	excitation
$e^- + A^* \rightarrow e^- + A + h\nu$	(3)	de-excitation
$e^- + A^* \rightarrow A^+ + e^- + e^-$	(4)	two-step ionization
$e^- + AB \rightarrow A + B + e^-$	(5)	fragmentation
$e^- + AB \rightarrow A + B^+ + 2e^-$	(6)	dissociative ionization
$e^- + AB \rightarrow A + B^-$	(7)	dissociative attachment
$e^- + A^+ + B \rightarrow A + B$	(8)	volume recombination

Table 2: Neutrals and ions reactions in the gas phase [1]

Reactions		Description
$A^+ + B \rightarrow B^+ + A$ 'resonant' for B = A	(9)	charge exchange
$A^+ + B \rightarrow B + A^+$	(10)	elastic scattering
$A^+ + B \rightarrow A^+ + B^* + e^-$	(11)	excitation
$A^+ + B \rightarrow A^+ + B^+ + e^-$	(12)	ionization
$A^+ + BC \rightarrow A^+ + B + C$	(13)	fragmentation/dissociation
$e^- + A^+ + B \rightarrow A + B$	(14)	volume recombination
$A^\pm + B \rightarrow AB^\pm$	(15)	oligomerisation
$A + B \rightarrow AB$	(16)	oligomerisation

In the gas phase, there are many phenomena occur such as particles ionisation, splitting and cluste ring of molecular gases that is followed by plasmas formation. These phenomena involving electrons, ions and neutrals are shown in Table 1, and Table 2 [1]. The following are additional reactions result from applying energy source

to the plasma with a demonstration of the processes and the resultant electrons and ions productions [1]:

I. Self-ionisation if the gas is hot in high pressure plasmas as 1eV is corresponding to 11000 K of kinetic temperature

$$A + B^{(\pm)} \rightarrow A^{+} + B^{(\pm)} + e^{-} \qquad (17)$$

II. Resonant process that involves atomic transitions between two energy levels and photons absorption if the atoms have the equivalent energy.

$$A + h\nu \rightarrow A^{+} + e^{-} \qquad (18)$$

$$A^{*} + h\nu \rightarrow A^{+} + e^{-} \qquad (19)$$

III. Species ionisation via long-lived excited states if A species has ionisation energy less than excitation energy of B, known as Penning ionisation

$$A + B^{*} \rightarrow A^{+} + B + e^{-} \qquad (20)$$

IV. Impacts between atoms and electrons with high energy leading to ionisation

$$e^{-}_{fast} + A \rightarrow A^{+} + e^{-}_{slow} + e^{-}_{slow} \qquad (21)$$

Another way of forming negative ions is through electron attachment that is associated with collisions between electrons with neutral atoms/ molecules. This process requires a specific energy for electrons to be able to get attached to the molecules/ atoms. The following equations are representing the attachment process [1]

$$A + e^{-} \rightarrow A^{-} + h\nu \qquad (22)$$

$$AB^{*} + e^{-} \rightarrow A^{-} + B \qquad (23)$$

In the other hand, negative ions destruction through collisions between them and electrons/ photons, or atoms as represented in the following equation

$$O^{-} + h\nu \rightarrow O + e^{-} \qquad (24)$$

The reverse process for ions and electrons recombination requires three elements to maintain momentum and energy conservation

$$e^- + e^- + A^+ \rightarrow A + e^-_{faster} \qquad (25)$$

or the recombination is processed in two stages where the first one is the attachment then ions re-joining again [1]

$$e^- + AB \rightarrow AB^- \qquad (26)$$

$$AB^- + C^+ \rightarrow AB + C \qquad (27)$$

2.4 Plasma species temperatures

The gas temperature is the measurement of average kinetic energy (KE) of the gas atoms. The KE rises in gases due to the fast movement of particles which causes an increase in the system pressure compared to cold gases and leads to attributed increase in the gas temperature [11]. KE is defined in terms of gas molecule average velocity (v) and mass (m) i.e., ½ $m\bar{v}^2$ and the average KE of a gas can be given by its temperature and Boltzmann constant (K):

$$\boldsymbol{KE_{avg} = \frac{1}{2}mv^2 = \frac{3}{2}KT} \qquad \textit{Equation 1}$$

The root mean square value of the molecular speed can be driven from Equation 1 as [12]:

$$\boldsymbol{v_{rms} = \sqrt{\frac{3KT}{m}}} \qquad \textit{Equation 2}$$

In an ideal gas, the dependence of average speed of atoms on the temperature as shown from Equation 2 can be described by the Maxwell speed distribution which is an example of the Maxwell – Boltzmann distribution function. The Maxwell–Boltzmann distribution is a probability functions that provides energy distribution between identical particles and can be used to describe the speed of particles in ideal gases. Equation 3 represents Maxwell Boltzmann function where f(E) is the particle's probability to have energy E, A is a normalised constant and k is Boltzmann constant:

$$\boldsymbol{f(E) = \frac{1}{Ae^{\frac{E}{KT}}}} \qquad \textit{Equation 3}$$

In real gases, although there are many interactions between particles, at normal temperature they follow a Maxwell distribution. Therefore, Maxwell distribution is the closest approximation to describe ideal plasmas where low density gases are ionised. This assumption is justified by Dreicer [13] based on equipartition theorem which links the system temperature and its average energy and the comparison between the equipartition rate of random speeds and Joule heating. However, a small discrepancy between the assumption and the generated distribution from hydrodynamic equations they used was expected because electron-electron encounters occur less frequently than necessary to make the distribution completely Maxwellian. Mladenovic et al. [14] developed a model to study the electron energy distribution function (EEDF) as well as other factors in atmospheric pressure helium plasma where they used initial assumption that neutrals and ions follow Maxwellian distribution. However, the model results revealed that the distribution is not fully Maxwellian because of the high energy threshold of the system. Also Boisvert et al. [15] used a collisional radiative model in a helium discharge APP to describe the EEDF and optical emission spectroscopy for fitting the data. The results they obtained assuming Maxwellian distribution fitted only fitted the lower energy part of the EEDF where the overall shape of the EEDF is similar to EEDF of low pressure RF plasma from the literature. The authors concluded that the EEDF profile and the deviation from the Maxwellian distribution depends on the electrons energy in the system and provided generalized EEDF. The gas speed is described by the average energy and is associated with the gas kinetic temperature (kT) where the gas pressure P is measuring the kinetic energy for a specific number of atoms per unit volume, n_g [1]:

$$P = n_g kT \qquad \textit{Equation 4}$$

There are different temperatures in non-thermal equilibrium (NTE) plasma attributed to the various species in the system (e.g., ion, electron, and neutrals) due to their different kinetic energies. The electron temperature (T_e) indicates the kinetic energy (KE) for electrons whereas gas temperature represents the KE of the neutral species. In NTE plasmas T_e is higher than neutral particles temperature (represents gas temperature T_g) i.e. $T_e >> T_g$ [16]. The gas temperature depends mainly on collisions between electrons or ions and the gas molecules. Although electrons have higher

energy than ions, they do not cause much gas heating due to their very lightweight. However, if there are enough electron impacts, electrons do cause an increase in gas temperature then resulting in sudden changes in the nature of the plasma [17]. There are many factors that influences the plasma chemistry including electron density, electron temperature, neutral species densities, electron energy distribution, type of gas used, and gas temperature whereas atomic states as well as vibrational states were found to have insignificant effect on the plasma chemistry. Although the reactions rate constants are one of the vital factors affecting the species density, they are not well-known and depend mainly on limited experimental measurements. In the case of using helium and oxygen gases, the collision rate between electrons and helium is a prominent factor as long as there is low density of oxygen. However, this may result in diversion of high amounts of power into gas heating which in turns influences the electron density in an indirect way [18,19]. The helium - electron chemistry can be described mainly by the following reactions scheme:

$$e + He \rightarrow He^{+} + 2e \qquad (28)$$

$$e + He \rightarrow He^{*} + e \qquad (29)$$

From the viewpoint of plasma chemistry, the electron energy distributions is the vital factor which impact the determination of the technological application of each type of plasma therefore, it is crucial to study their effect on the chemical kinetics [20–22]. There is a need to keep the gas temperature under control and to provide continuous measurements as there are many techniques that have been developed for APPs applications that requires controlled gas temperature such as biomedical and nanomaterial applications. Where there are some trials have been performed to keep the gas temperature under control such as utilising noble gases rather than molecular gases, because noble gases have elevated thermal conductivity and less voltage required to initiate the plasma, varying gas flow, reducing plasma dimensions such as microplasmas, and the operating power. Helium is the most common used gas in noble gases because of its high thermal conductivity (higher than air by~ 6 times and argon by ~8 times) [4].

2.5 Collisionality in plasmas

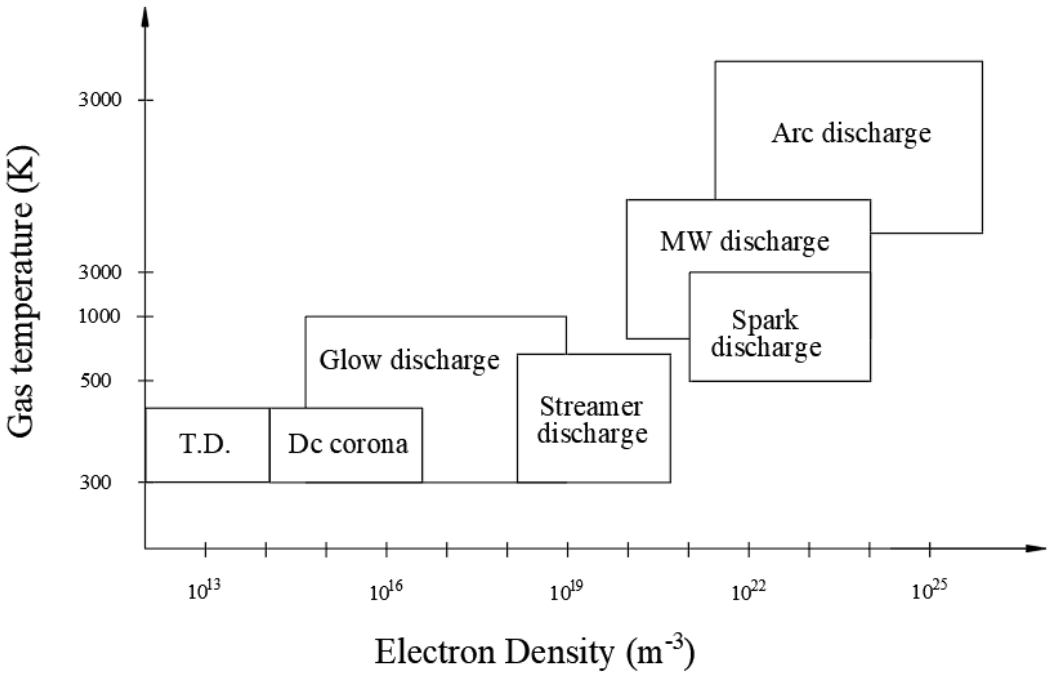

Figure 2-1: Gas temperature vs. electron density for APP plasma classification, TD refers to Townsend discharge [4].

Plasmas are often classified as either low-pressure or atmospheric pressure (APP). The APP is a collisional system because the mean free paths between electrons and heavy particles are noticeably short. When kinetic equilibrium prevails ($T_e \approx T_h$), it leads to thermodynamic equilibrium, as well as chemical equilibrium (that depends on particles concentrations in plasmas). In contrast, the mean free paths between electrons and heavy particles in low pressure plasma (LPP) are much longer leading to less collisions between particles. In this case, the electron temperature is much higher than the heavy particle temperature ($T_e >> T_h$) and the gas density is very low despite high ionisation. Atmospheric pressure plasmas are divided into thermal and non-thermal plasmas. In thermal plasma, $T_e = T_h$ and the gas temperature can reach values above 10,000 K. In non-thermal plasma, the electron temperature, T_e, is remarkably high compared to heavy particles' temperature that remain at ambient temperature. The density of the charged species is noticeably low compared to thermal plasma and the system has lower degree of ionisation that is the reason the gas is at

almost room temperature [23,24]. Bruggeman et al. provided plasma categorisation with respect to gas temperature and electron density in APP plasma as indicated in Figure 2-1 [4]. Where other labels for thermal and non-thermal plasmas are Local Thermal Equilibrium (LTE) and non-Local Thermal Equilibrium, respectively. Plasmas/ gas temperature is described by heavy particles temperature due to the significant difference between electrons and heavy particles masses. The following table summarises the principal properties of LTE and non-LTE plasmas [25].

Table 3: Summary of LTE/ Non- LTE plasmas properties [25]

	LTE plasmas	**Non-LTE plasmas**
Temperature	$T_e=T_h$	$T_e>>T_h$
Electron density	$10^{21} – 10^{26}$ m^{-3} (High)	$<10^{19}$ m^{-3} (lower)
Heavy particles and electrons Collisions	• Inelastic collisions: responsible for reactive species generation • Elastic collisions: results in heavy particles heating and consequently increasing in the electrons energy consumption.	• Inelastic collisions: results in changes in the plasma chemistry. • Elastic collisions: little heat to heavy particles consequently, electrons maintain high energy level.
Examples	Arc plasma $T_e = T_h$ ~10,000 K	Glow discharges T_e~10,000– 100,000 K T_h~300– 1000 K

2.6 Dusty plasma

The interaction between plasmas and particulates is known as dusty plasmas where the ionization frequency increases by increasing the dust particles concentration that is required to keep the discharge current stable. Ions and electrons are mainly responsible for the charge on dust particles in plasma in addition to ion sputtering, secondary electron emission (SEM) and photoelectron emission [26,27]. Studying and controlling particles in low pressure plasma led to different applications such as astronomy applications, powder modification and growth studies [27], synthesis of nano silicon in plasma that is used for manufacturing nano-devices and on the study of the nano-scale surfaces physics on micro-meter scale [28] as well as producing particles with the appropriate surface properties needed for a specific application [29]. At low pressures, semi-analytical approximations are available to calculate charge although some assumptions regarding sticking coefficients and surface recombination can be questioned [30,31]. However injecting micron-sized particles into a plasma and measuring their charge is experimentally challenging. Estimates from ensemble levitation experiments at low pressures suggest charge levels from 4000 [32] to 8000 electrons [33] for a 10 μm particle which indicated increase with increasing the experimental conditions such as input power and gas flow rate. Yet, most of the studies were for low-pressure plasma and none of them investigated the experimental validation for APP conditions and microscale particles.

Complex charging models for atmospheric pressure plasmas were originally developed in the 1960's and have yet to be validated experimentally [34,35]. With simplifying assumptions these models can provide estimates of acquired charge but these assumptions are valid only for very small nano-sized particles (< 50 nm) [36]. In this size range, charge bombardment leads to high surface temperatures [37] and such particles in liquid form would evaporate almost instantaneously. For research study and applications e.g. remote delivery or chemical synthesis, a suitable droplet lifetime is necessary which can only be obtained with larger droplets (> 5 μm) while retaining the surface to volume advantages of droplets imposes an upper limit to the diameter (< 0.1 mm, approximately) [38]. These charging models are not suitable for our plasma system due to the big difference in the particles size range which defer from nano to micro scale as well as the difficulty in using nanodroplets in many

applications that requires in-flight of microdroplets because they tend to evaporate very quickly, therefore another model will be selected for our work to validate the experimental measurements.

Particles charging in non-equilibrium collisional plasmas can be considered in gas-phase corona discharge where corona charging is normally operated in the unipolar ion region, for maximum charging, and ion charging dominates whereas in a glow discharge plasma, ion and electron densities are, on average, approximately equal. Nevertheless, on entering the plasma, particles or droplets quickly acquire a net negative charge, Q, due to the much higher mobility of electrons compared to ions. The magnitude of the acquired charge depends on plasma conditions e.g., electron density, n_e, electron temperature, T_e, and ion temperature, T_i, as well as particle size. However, the relationship between plasma or particle parameters and Q is not well defined in a collisional plasma at high pressure. Under certain restricted conditions applicable to nano-sized objects, analytical approximations are available [36,37]. However for large particles (> 1 μm), different numerical solutions are required depending on T_e/T_i and on the various system scale lengths, namely particle radius, Debye length, ion and electron mean free paths [39].

2.7 Atmospheric pressure plasmas

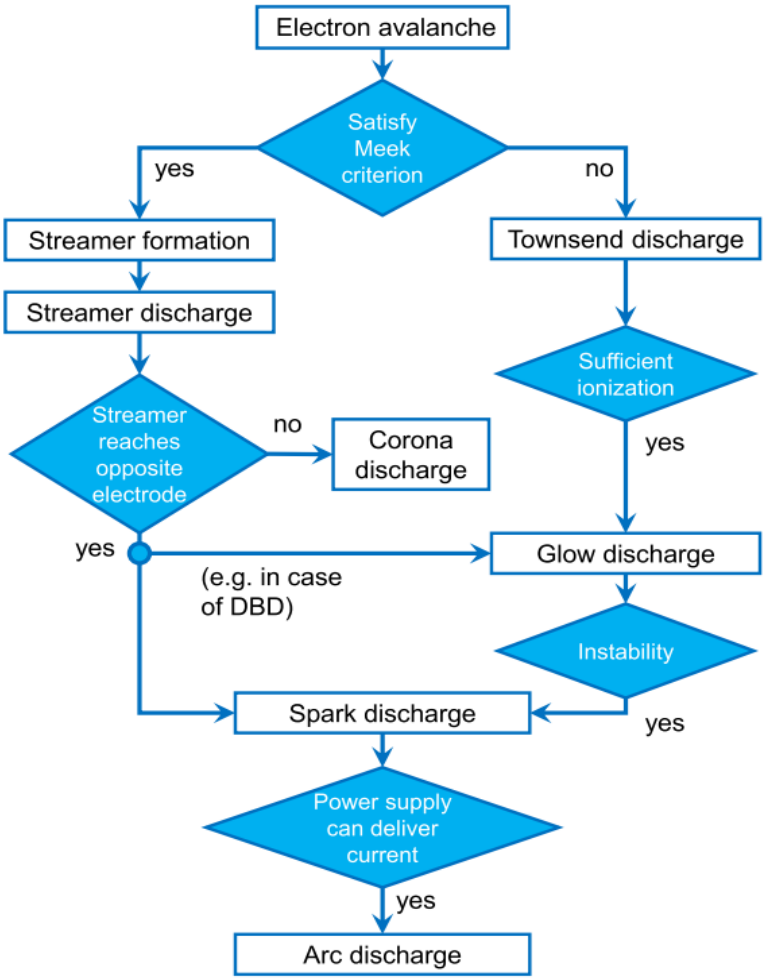

Figure 2-2: APPs different transitions starting by electron avalanche followed by Meek criterion check to identify the type of plasma between Townsend, Glow, Streamer, Corona, Spark and Arc discharges [4].

In APPs, the preliminary transition is the breakdown forming a streamer from an avalanche of electrons in nanosecond time scale. Instability of plasma results in other transitions and Figure 2-2 shows the major transitions in APPs. Meek criterion states the conditions required for initiating a streamer where the field of positive ions near the anode is equal to number of times (constant number) the impressed field [40]. There are two possibilities for APPs, the first is to form a streamer if the avalanche of electrons comply with Meek criterion where the number density of charges is being checked with the required value to form a streamer. The second possibility when the

ignition conditions did not match Meek criterion then diffuse discharges such as Townsend and glow discharges are formed. Instabilities in either glow or streamer discharges can lead to spark discharges which can become an arc if power supply allows. These instabilities are due to the differences in ionisation and recombination rates of electrons [4].

In APPs, electron density n_e is linearly proportional to ionisation process and quadratically proportional to electron recombination process. Ionisation rate depends on T_e, therefore sudden changes in T_e may induce further instabilities. In addition, alterations in T_g and T_e causes instability in recombination and production rates of electrons, hence the plasma is more unstable in APP than in LPP. Fluctuations in the electron density increases the plasma instability. Consequently, a rise in n_e may lead to a rise in T_g and a reduction in the gas density. Electron temperature significantly affects the electron loss process and forming another reason for plasma instability e.g., attachment instability. In electronegative plasma, the detachment and ionisation may have a balance with the attachment. Also, attachment rate depends on electron temperature so if the T_e decreases, the ionisation, and attachment rates decrease. However, it does not affect the detachment rate. So if there is a balance in the attachment and detachment processes (not ionisation), an increase in n_e may result from the fixed detachment rate [4].

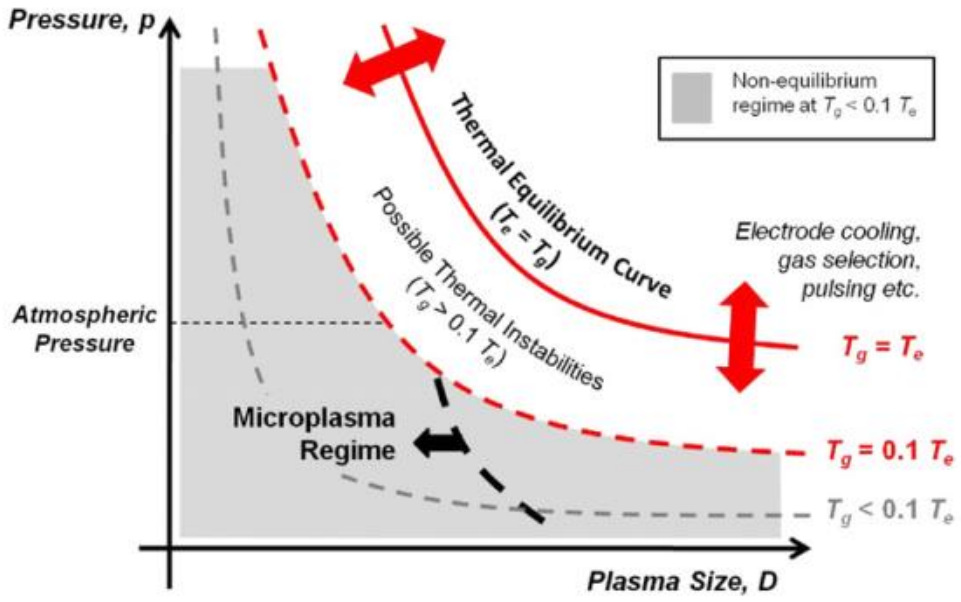

Figure 2-3: Transitions of plasmas between equilibrium and non-equilibrium depending on the plasma size [41].

Microplasmas is the plasma operated with a size range between mm to µm. This small dimension gives microplasmas different physical and chemical characteristics than normal scale plasmas due to the higher ratio between the surface to the volume. Atmospheric pressure plasma with a frequency in the range of dc to GHz is the most common microplasmas operating system because it allows higher rate of electron generation with less losses on the walls whereas increasing the wall area with respect to the plasma volume may lead to increase in the electrons losses [42]. The energy flow is the main parameter used in controlling LTE plasma ($T_e = T_g$) and non-LTE plasma ($T_e > T_g$) and it is affected by changing the volume of the plasma. Reducing the volume leads in a rise in T_e and n_e. Figure 2-3 depicts the transition of plasma between LTE and non-LTE as a variable of plasma size. Knowing that changing the plasma parameters and configurations result in shifting the curves. For example, alterations in the gas composition and flow rate affects the energy flow plot and consequently the plasma transition. Figure 2-3 reveals that reducing the size of the plasma is essential in maintaining NTE plasma. In addition, at constant pressure, the gas temperature increases by increasing the plasma volume along with potential decrease in the electron temperature. Therefore, the energy flow is an effective tool to control both T_e and T_g [41].

Non-thermal atmospheric pressure microplasma jets (APPJs) have been used in a wide range of modern industrial fields including nanomaterials synthesis [41], [43] and new life-science applications by using micro devices for chemical analysis and synthesis, Light, (V) UV sources, and photonic devices [44]. APPJs are able to create reactive and charged species, metastable atoms and UV photons, due to electron temperatures of a few electron volt (eV) [45]. Furthermore, APPJs does not cause thermal damage on the biology as it can be operated close to room temperature therefore, APPJ is considered a promising technique can be applied to the biology of plasma for biomedical applications such as inactivation of bacteria and wound treatment [46]. In addition, Jae et al, changed the design of microplasma system so it can be used effectively in treating interior tumour cells [47]. In the last decade, adding microdroplets to plasma or plasma in contact with liquid promoted more evolving applications such as environmental applications, plasma medicine among others due to the production of strong oxidizing species [48,49].

2.8 Plasma – liquid interactions

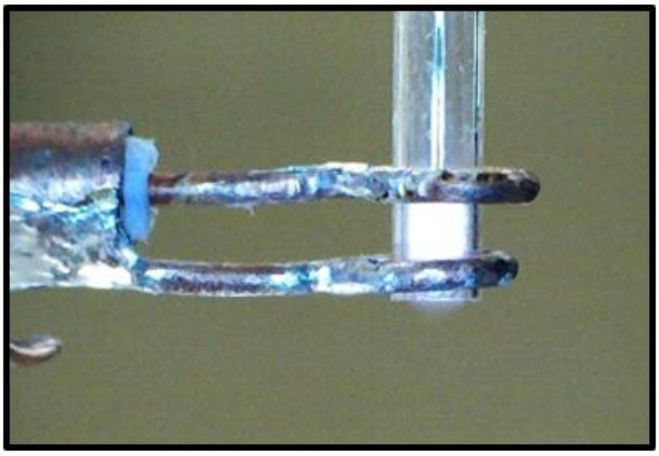

Figure 2-4: Photo of our capacitively coupled plasma which forms of double ring electrodes of copper where one of them is connected to RF power and the other one is grounded. This plasma when applied to a liquid can be identified as non-coupled as the plume is short and does not reach the liquid surface.

There are many factors influence the plasma-liquid interactions such as the nature of the interface and the stability of the system. The system is then highly affected by chemical reactions that cause changes in the internal heat and the transport properties. Chemical reactions are highly impacted by electrons and ions as they commence many reactions and affect the stability of gas-liquid interface through surface charging, currents and electric fields [50]. Applying plasma to water entails energy exchange with the medium. The residence time of plasma generated species in liquid is noticeably short due to the existence of many processes such as collisions, ionisation, stimulation, and common exchange of energy levels between particles. Plasma diffusion dynamics varies between sub-nanoseconds and microseconds range. Many processes take place in this time range that makes this phenomena complex e.g., temperature change, the changes of the charge on the liquid surface, and phase changes with respect to density and pressure. Furthermore, the frequency and the density of electric field has a high influence on the electric characteristics of the liquid [51]. The physical functions of plasma-water interaction can be described as following:

First, the temperature of water experiences a sharp increase when introducing plasma ($dT/dt \approx 10^9$ K s^{-1}) [24]. Second, a pressure as high as 10^5-10^7 MPa is generated

due to plasma having less freedom of movement in water and the limited space. Water medium is incompressible therefore this high pressure would transfer into impact wave in water. Finally, the high voltage used in generating plasma result in electric field in water that increase the power and effectiveness of water [22, 36, 37]. Shirai et al. studied the influence of the liquid temperature on the characteristics of glow discharge plasma due to plasma-liquid interaction and noticed increase in the water temperature where an image taken by a high-speed video showed boiling liquid surface. In addition, this study demonstrated the high influence of the liquid temperature on the water vapor at the liquid surface [54,55]. All these characteristics needs further investigations to facilitate the use of plasma liquids in different applications. Short lived chemistry in an average time scale of seconds has been already identified whereas the plasma chemistry occurs in microseconds timescale that makes it harder to trace.

The plasma has mainly two categories as inductively coupled plasma and capacitively coupled plasma. In the former, the plasma is generated by passing time-varying electric current through a coil resulting in creation of time-varying magnetic field. Whereas the capacitively coupled plasma is generated using two electrodes separated by a small distance and connecting one of the to RF power supply and the other electrode to the ground such as our plasma system as in Figure 2-4 [56]. With respect to plasma-liquid interaction, there are two main configurations to classify the plasma either to be in contact or non-contact plasma depending on whether there is a contact between the liquid surface and the plasma or not [57]. Also, plasma-liquid interaction can be classified as coupled or non-coupled where the plasma is coupled if the liquid is part of the electric circuit of the plasma - liquid system. A RF-driven plasma jet may be non-contact plasma, Figure 2-4, as the plasma is limited mainly between the two electrodes and extends only a few millimetres at most and cannot reach the liquid for distances greater than this. In this case only radicals and other chemical species can reach the liquid surface. In contrast, most of the kHz plasma jet is a contact plasma because the plasma is more likely to propagate beyond the electrodes and contact the liquid surface leading to generating more powerful reactive species. However, this system requires more control on the gas temperature, electric field, and current than the non-coupled plasma systems [58].

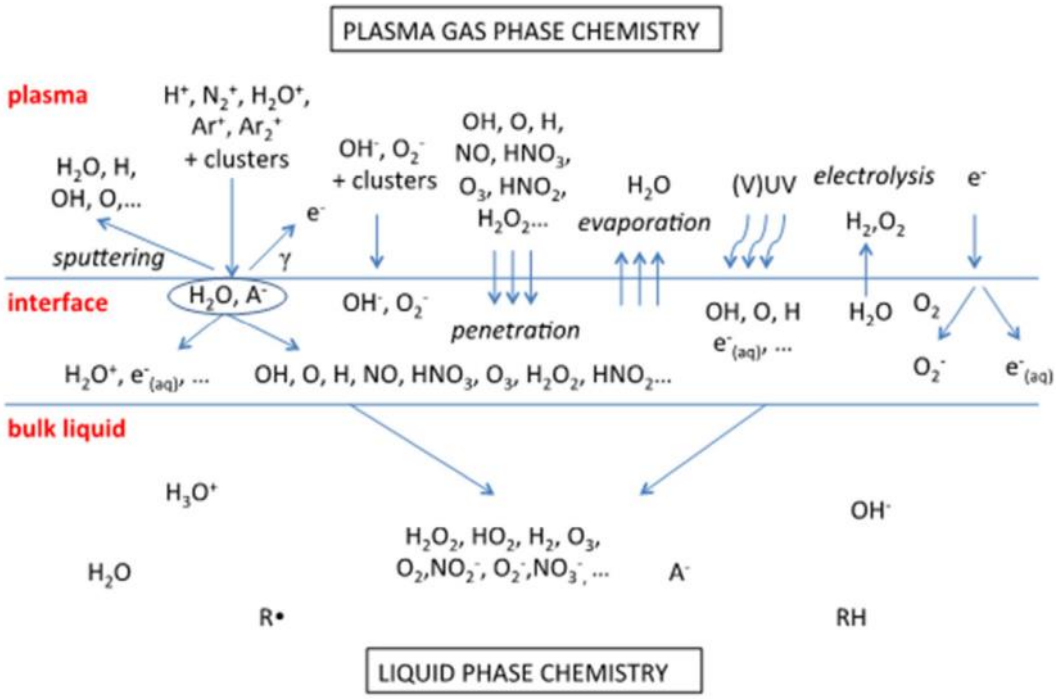

Figure 2-5: plasma-liquid phases and by-products divided into gas phase, liquid interface phase, and bulk liquid phase [50]

Plasma-water interaction comprises of three phases that entails many complicated reactions: gas phase, liquid interface phase, and bulk liquid phase, Figure 2-5. The liquid interface is the medium in which heat, species and masses pass through and that has many reactions by short-life time reactive species. While the bulk liquid comprises of more radicals depending on their lifetime and penetration ability. These two factors as well as the gas used to generate the plasma, are required to study the reactions between the plasma and liquid [50]. In plasma-gas phase many reactive species are generated such as reactive oxygen and nitrogen species (RONS) respectively and many radicals and neutrals. Plasma diagnostics were measured by many convoluted techniques such as Fourier transform IR (FTIR), Raman, laser induced fluorescence (LIF), and optical emission spectroscopy (OES). Bruggeman et al [44] and Dilecce [59] described these techniques in details and demonstrated their limitions of usage. In addition, simulation of the plasma's products and reactions is necessary and varies by changing the gas used for generating the plasma. Schröter et al [60] and Liu et al [61] presented a simulation plasma jet discharge generated by helium gas with H_2O.

In direct-contact plasma with liquid, a high voltage is needed to induce a strong electric field to produce reactive species e.g., corona discharge. The applied voltage and the selected liquid properties are main factors to control the generation of these reactive species. The reaction rate of the species in the liquid is much faster than that in the gas phase because the aqueous-phase reactions consumes species and compounds much faster than gas-phase [62]. Moreover, most of the radicals generated in liquid is short-lived one such as •OH and •O therefore, controlling and measuring these species in the liquid is challenging. The interaction between gas discharge and liquid surface produce strong oxidative species such as •OH, •O, and their by-products (O_3, H_2O_2) that dissolve into the water initiating oxidation processes as by the following reactions [63,64]:

$$O^2 + \bullet O^+ \rightarrow O_3 \quad (30)$$

$$O_3 + hv + H_2O \rightarrow H_2O_2 + O_2 \quad (31)$$

$$H_2O_2 + hv \rightarrow 2OH \quad (32)$$

$$2O_3 + H_2O_2 \rightarrow 2OH + 3O_2 \quad (33)$$

X-ray photoelectron spectroscopy (XPS) has been used comprehensively to characterise the surface chemistry of materials used in bioengineering and is increasingly finding a role in biology as it can be used to identify and image the chemical functional groups present on the surface of virtually any material. Freeze hydration XPS, involves the rapid freezing of a wet sample within the XPS entry chamber which can be used to both circumvent and investigate issues associated with sample dehydration. Once a sample is frozen, subsequent exposure to ultra-high vacuum (UHV) at a temperature of approximately -100 °C etches the ice from the surface via sublimation. The sample temperature is then lowered below -120 °C for XPS analysis which would have enabled us to investigate both plasma-induced chemical changes in liquid and the related biomolecular. Since uncontrolled circumstances meant that the XPS and plasma interface (PAD) is still not fully operational, a short literature overview of XPS with relevance to frozen water will be presented in CH3 along with detail of the experimental achievements to date.

2.9 Plasma-liquid applications

2.9.1 Miscellaneous applications

The study of plasma-liquid interactions (PLIs) has a wide range of applications due to the high reactivity of the system such as applications in nanomaterial processing, water and wastewater purification and biomedical and medicine applications etc. In this section a brief discussion on the most common applications will be provided. The plasma nanomaterial applications are promising and has been greatly expanded. There are many available methods for nanoparticle (NP) synthesis depending on reduction of metal ions in solutions and chemical reduction using a reducing agent into the solution. Although they are considered effective methods in NP synthesis, they suffer from long time processing which takes usually several few hours [65]. Plasma-liquid interface offers many advantages for NP synthesis over traditional techniques such as removal of reducing agents, simpler experimental design and the continuity of the synthesis process during the plasma operation, with the key advantage being the possibility of producing much more effective reducing agents, i.e. free electrons, compared to conventional techniques during NP synthesis using plasma-liquid interactions [66–70]. There are many studies and simulations on the plasma-liquid interface and their impact on material processing applications results [71–73] as well as many comprehensive review studies on the PLIs applications on nanoscience filed [74–76].

Water and wastewater treatment have been always of a high interest for many researchers and applications for their importance in our life. The impurities in water range between debris, organic, inorganic and biological waste [77]. There are many traditional techniques for purification depending on the impurities such as primary and secondary treatment which entails filtration and biological methods. However, these techniques suffer from low removal efficiency of many hazardous pollutants. Even though the tertiary treatment can improve the removal efficiency by the addition of chemicals or using advanced separation technologies or oxidation processes, they consume high energy and have a wide range of side effects. Consequently, plasma treatment is a promising method as it has wide range of reactors providing flexible design and avoiding the use of chemicals as well as it is potential in producing wide

range of reactive species such as ozone, hydrogen peroxide, UV photons, and possibly hydroxyl radicals, in the treated liquid [65]. Various plasma studies have been performed for water purification targeting many different impurities including organic compounds [78,79].

2.9.2 Plasma medicine applications

Non-thermal plasmas (NTPs) offer promising potential in biomedicine as they have shown interesting effects in many application areas such as oncology, skin disease treatment, tissues regeneration, cancer therapy, dental care etc. It has been proposed that NTPs can achieve the desired results with minimal effect on the surrounding tissues [80]. Gas plasma creates electric fields and mixture of electrons, ions, UV photons, reactive oxygen and nitrogen species (RONS) such as H_2O_2, ozone, hydroxyl radical, NO, nitric oxide, peroxyacyl nitrates, Peroxynitrite in addition to other components. Reactive species play a pivotal role in plasma medicine applications as many of RONS have biological functions, therefore, they opened the door for redox biology interpreting gas plasma's biological effects in RONS based therapy. NTPs demonstrated outstanding performance in bacterial inactivation such as treatment of *E. faecalis* by plasma for two minutes resulted in 90% of bacteria reduction [81]. In addition, NTPs showed promising results in improving the therapeutic effect when used for treating 12 patients with advanced cancer stage in neck and head [82].

Although gas plasmas have been proposed as treatment method to improve recovery and reduce treatment complications, there are possible disadvantages and many challenges. There is a possibility for plasmas to also damage healthy cells. However, the small area of typical plasma jets may allow focussing on the target area but where necessary, may be scaled using multiple plasma jets to cover larger areas. Most important is combining these devices with a real-time monitoring of the plasma parameters and gas temperature to insure safety of use [83]. NTPs treatment is a surface technique so it is harder to use where access is difficult and the applications are then limited mostly to accessible tumors [84]. The chemical reactions in the gas plasmas induce dozens of RONS but with different concentrations and various reactivity therefore they have diverse travel and diffusion distances. In addition, some species have fast reaction rate in both the gas phase and the treated tissues resulting in

a complex system. It is also challenging to identify individual species quantities and types in such complex environment in particular when they interact with tissues. Furthermore, it is not possible to split the components of RONS to distinguish between the contribution of each RONS or to provide action for one of them only without interference of other species making it difficult to control the dose an to understand the mechanism between gas RONS and tissues. Therefore further and more detailed experimental and simulation studies are required in this field [83].

Wound healing and blood coagulation is one of the promising applications of NTPs [85–88]. Controlled production of RONS may have potential in promoting wound healing where the presence of oxygen related species such as hydrogen peroxide and superoxide was reported as essential factor in wound healing processes [83]. The efficiency of using gas plasma in wound healing can be demonstrated by clinical trials and observations in patients. For example, SteriPlas device was applied in a research to 36 patients with chronic wounds and a reduction in microbial burden was observed [89] along with significant reduction in many other wound parameters were detected in another 70 patients [90]. PlamsaDerm is another device which has been used for wound healing providing a significant decrease in the wound size and microbial load when tested on 14 patients [91]. Gas plasma wound healing treatment most commonly applied three times per day or per week and sometimes once a week depending on the wound and the device used for the application. In addition, wound size and volume are another factors influencing the process whereas the wound location is a critical factor that inhibit the application of many devices [83]. Bleeding control is also vital in medicine application providing that the most common devise used to control bleeding in endoscope's surgery is using Ar thermal plasma coagulator [92,93]. However, this devise cannot be used in external applications due to its high temperature and small treatment area. Therefore, it is important for wound healing and surface applications to operate in low temperature plasma to avoid any damage to the surrounding tissues which has been investigated in many recent researches [85,94–96]. NTPs have been also used in other dermatological applications such as infectious diseases, inflammatory skin treatment [97,98] as well as skin regeneration in many cosmetic medicine where no side effects were reported after the treatment [99,100]. Heinlin et al. [101] provided a comprehensive review on plasma medicine applications and recent studies on skin diseases. Dentistry is another application of NTPs for the

purpose of bacteria removal [102], microbial biofilms removal [103], whitening and tooth bleaching [104,105] where a general review of recent NTPs applications in dentistry has been provided by Arora et al. [106].

Cancer therapy is another promising application of NTPs [107–110]. By comparison, non-plasma cancer treatments such as chemotherapy and radiotherapy, and surgery, can have many drawbacks along with their benefits in treating cancer. Chemotherapy has some adverse effects and toxicities which were linked to cytostatics producing free radicals. Radiotherapy works by radiating cancer cells with high energy photons (or charged particles, e.g. proton therapy), with the aim of killing them or severely damaging their DNA to slow their growth [111]. Radiotherapy is lethal to normal tissues as it damages blood vessels in the treated area causing reduction in the blood supply to the healthy cells and resulting in their death therefore, it requires a high control on the dose amount, distribution and timing administration [112]. The major side effects of both radiotherapy and chemotherapy were linked to the formation of free radicals and their oxidative damaging effect on healthy cells. In a review study, 80% of radiotherapy patients were reported suffering from mucositis while 50 % of them experienced sever mucositis form in addition to other possible acute side effects such as diarrhoea and enteritis. Lymphoedema was reported as adverse effect for breast, ear, nose and throat cancer patients treated by surgery and radiotherapy whereas patients with Lymphoedema in neck and head may suffer a substantial impairment. Also oedema is another advert effect of surgery and radiotherapy which may lead to airway obstruction [113].

The DNA damage in radiotherapy occurs either by direct ionization or indirect one which is a result of ionising water and the production of free radical in particular, hydroxyl radical and solvated electrons [84]. Villamena et al. [114] reported that OH radical has a high influence in attacking the cell membrane, inducing apoptosis and lipid peroxidation. Therefore, there are some similarities between gas plasma and radiotherapy due to the generation of the reactive species and the induction of DNA strand breaks, demonstrating the high potential of using gas plasma as an effective cancer treatment. Lafontaine et al. [115] reported a detailed comparison between using NTPs and radiotherapy in breast cancer treatment. Using gas plasma as a cancer treatment has many advantages over radiotherapy not only because it has no

immunosuppressive effect or risk of bacterial infection but also encourage the immunostimulatory effect. In addition, radiotherapy requires very high energy to enable the radiation to penetrate through the body whereas the plasma uses very low energy and can be applied to a small area using focused-small size plasma such as plasma jet so less likely to cause side effects. Radiotherapy may also affect healthy cells where there is some preliminary evidence that normal cells react differently from cancer cells when exposed to plasmas [84] and demonstrated a killing effect on cancer cell lines than compared to normal cells [116] i.e. there is a possibility for selective treatment. Using NTPs as a cancer therapy requires high control and understanding of the mechanism so as to produce enough hydroxyl radicals for treatment while meeting safety considerations e.g. avoiding potential risks resulting from electric fields or high gas temperature. As most of NTPs are surface technique, further investigations are necessary to find a method to deliver the plasma treatment inside the body. Using plasma during surgeries or delivering the activated droplets through a tube in a keyhole surgery to the target area are potential solutions that require further study of the mechanism and the lifetime of the hydroxyl radical to judge their ability to reach the tumour inside the body.

There are two types of plasma medicine treatments. These are either direct or indirect where the former involves direct exposure of the biological target to the plasma source and the plasma reactive species generated interact directly with the target [117]. Alternatively, indirect plasma treatment requires pre-treatment of a liquid solution to generate plasma activated liquid (PAL) containing reactive species which can be stored and applied later to tissues or cells [118,119] e.g. via injection. Note that in most of the applications between the plasma and tissues involve liquid i.e. most interactions between plasma and tissues or biological cells will involve moist or aqueous phase [80]. Up to now, there are many challenges in understanding the plasma interactions with liquids for both direct and indirect methods. The damage of living mammalian cells using direct plasma has been investigated by Kieft et al. [109] and demonstrated the high importance of the amount of liquid covering the cell samples on the necrosis rate as it is influence the penetration depth of the reactive species in the liquid. Reactive species were reported as the main factor in causing cellular damage and cell [120,121]. Joh et al [122] studied the effect of reactive oxygen species (ROS) generated using APPJ on the apoptosis human cancer cells and deduced that

the plasma treatment induce genetic signalling from DNA damage and non-genetic damage in cellular membranes. ROS was also identified as a major factor in inducing apoptosis and increasing the concentration of the ozone could enhance the DNA damage [123].

Development and studies of NTPs on some preclinical applications in particular for cancer treatment are vital for achieving final clinical applications. In-vitro studies have been performed on many types of cancer such as brain, lung, head, neck, breast, skin etc. [124,125]. Where the basic cellular responses were used to understand the effect of plasma anti-cancer treatment in vitro and provide some observations for in vivo studies. Limanowski et al. [112] summarised these observations in their review paper as follow:

- Large dose use of NTPs results in cellular death, via apoptosis, necrosis and immunogenic cell death.
- Physical factors such as electromagnetic emissions of plasma has effect in some NTPs experiments and may have impact on some cells such as bacteria and mammalian cells.
- Reactive species have a vital role in liquid-based experiments.
- The presence of aqueous medium in the plasma system plays significant role in transporting the reactive species to the target.
- NTPs result in increase in the intracellular ROS which has crucial rule in triggering cellular damage such as DNA and cellular damage, cellular membrane and mitochondrial damage, cell death etc.

In-vivo studies are the major approach in understanding the tissues response to NTPs and some animal models have been used to study the anti-tumour efficiency of NTPs mostly using subcutaneous models [126]. A significant reduction in the tumour volume of more than 50% and a corresponding increase in the model's survival length using two different NTPs setups and mice models has been reported [127,128]. Some clinical trials of using NTPs in cancer therapy have been performed such as a clinical trial on colon cancer by the US Medical innovation company to kill post surgical residual cancer cells as well as killing liver tumour cells [112] in addition to another study in Germany on 12 patients providing significant improvement in the therapeutic

effect while a reduction in pain medication request was also noted with advanced cancer stage in neck and head [82].

Plasma liquid interactions studies for biomedical applications have focused on direct contact and most plasma reactive species interact initially with the biomolecules through the liquid layer. Therefore it is essential to understand this interaction including with samples containing amino acids, DNA, proteins etc as these are the building blocks of cells and organs [80]. For the PAL approach, Gorbanev et al. [129] have demonstrated that the parameters of the plasma process used to generate the PAL have a high influence on the concentration of the reactive species and their biological impacts. PAL will initially contain many different species with a wide range of reactivities and lifetimes. Degradation of some of the PAL reactive species over time has been observed. Even when frozen immediately after generation, the most reactive species with much greater reactivity e.g. the $OH^{\bullet}$ radical have decayed in less than milliseconds leaving only the longer life species such as hydrogen peroxide and ozone [80] so there is still a major question as to the likely effectiveness of PAL.

In-vitro and in-vivo studies on the influence of using PAL on the growth of cancer cells or tissues in cancer treatment applications have been performed and showed ability to inhibit the growth of tumorous tissues [130,131]. With in-vitro studies, PAL has demonstrated killing cancer cells in pancreas, lung, melanoma [132–134]. Utsumi et al. [135] studied the potential use of in-vivo PAL in cancer therapy using a mouse model by injecting PAL into subcutaneous tumors of chronic paclitaxel/cisplatin-resistant ovarian cancer cells as a chemo-resistance cells. PAL demonstrated anti-tumour efficiency where the viability of NOS2 cells decreased by 30 % after 120 s treatment time and this percentage increased to 52 % with the addition of ROS inhibitor to PAL. Harley et al. [84] reviewed the potential use of PAL in cancer treatment and demonstrated its possible problems in clinical trials. PAL was shown to have effectiveness in some mouse models for treating different types of cancers such as pancreatic, ovarian, gastric and melanoma cancers. For example, PAL study on melanoma tumours demonstrated a reduction in tumour size by 78.8% after treatment. Also PAL was assessed in pancreatic cancer, the tumour size and weight were reduced by 21% and 31%, respectively.

Each experiment used different plasma setup, different treated solution, different treatment volume, and different dosing. The treatment dose is a key factor in therapeutic treatments as extra dose my have detrimental effect, however, there is no regimen yet for using PAL. Therefore, it is important to know the concentration of the reactive species to deliver the consistent concentrations to the patient [84]. Note that detecting the reactive species and determining their concentration is challenging in particular, short life span species and more challenging when many agents were used in the treated liquid and requires a depth study to facilitate in vivo studies and support the use of NTPs in clinical therapy [127,136,137]. Harley et al. [84] mentioned that long term side effects of PAL still need further studies and no available researches have yet investigated this. They also recommended further evaluation of treatments protocols and optimisation of PAL plasma systems before using for clinical trials. It is also important to have a common set of solutions and clear procedures to enable effective therapeutic effect in clinical applications. Although in-vivo studies revealed promising results on mouse models, there are still many unanswered questions and further investigation studies are then required before moving PAL to clinical applications

2.9.3 Microdroplets in plasmas

The interaction between plasma and aerosol has many advantages over that between liquid and plasma due to increasing the exposed surface area of liquids to the plasma that would remarkably increase its reactivity. The following is the major benefits of plasma aerosol over plasma-liquid interactions [138]

- The species is produced on the surface of droplets which improves the energy transfer to the liquid
- Droplets can be represented as microreactors which allows better control of the liquid reactivity
- Aerosol can be used as a carrier for micro and nanomaterials in the discharge supporting many relevant applications
- Aerosol plasma can work as a source and a carrier of solvated electrons as well as short lived species to the target from the discharge in a short timescale of milliseconds

- Plasma aerosol is an environmentally friendly technique that produces less contamination compared to batch processes and saves more energy by having more control over the process [138]

Hence, studying the plasma with aerosol would have a great benefit in many applications such as agriculture, nanomaterial synthesis, 3D printing and in particular plasma medicine, delivering activated droplets and treatments to tissues and organs remotely with high efficiency and minimal side effects [49].

2.9.3.1 Plasma-droplets chemical reactions

Plasma aerosol has a high number of chemical reactions and travels for long distances leading to rapid changes in its dynamic behaviour. In addition, charging of aerosol particles causes changes in the electric field which triggers disturbance in the discharge that makes maintaining the plasma's stability is challenging. Figure 2-6 demonstrates plasma aerosol interaction including the mutual influence of droplets and plasma on each other as well as the species transfer between them. As a result, the system becomes complex making studying and modelling the system more challenging and requires deep understanding [138]. Chemical reactions were proven to have enhanced rates, often by orders of magnitude [43,139,140], in gas-phase microdroplets compared to bulk liquids and has led to many research interests [141]. The higher reaction rate in microdroplet is attributed to their smaller confined volume compared to bulk-liquid which drives faster chemical reactions. The small surface to volume ratio affects the special chemical and physical conditions inside these microdroplets to act as microreactors. For instance, microdroplet surface has excess charge accumulation, higher pH value, and fast desolvation rate [142–144]. Quantum mechanical calculations have been used to elaborate this fast reaction rate in which the author also attributed the enhanced rate to the droplets small volume [145]. The research field can be considered from a number of perspectives including microdroplets as reaction chambers, the effects of interfacial electric fields on chemistry, the acquisition of net charge and the nature of the charge. For charging techniques such as electrospray, the imbalance of ions and counterions within the liquid formed during the charging process leads to a net charge. However, plasma charging is due to a net initial free electron flux from plasma to droplet surface. Enhanced reaction rates in droplets passing through a gas plasma was observed in a

recent study using a similar setup to our experiment [43]. In addition, a net charge is expected from a continuous flux of electrons arriving at the droplet surface where interfacial electric field and surface reduction reactions were thought to be a result of these electrons solvation. Quantitative measurements of electron flux or acquired charge within a high-pressure plasma, however, have never been attempted and such measurements represent an essential first step in understanding the nature of enhanced reaction mechanisms in such systems.

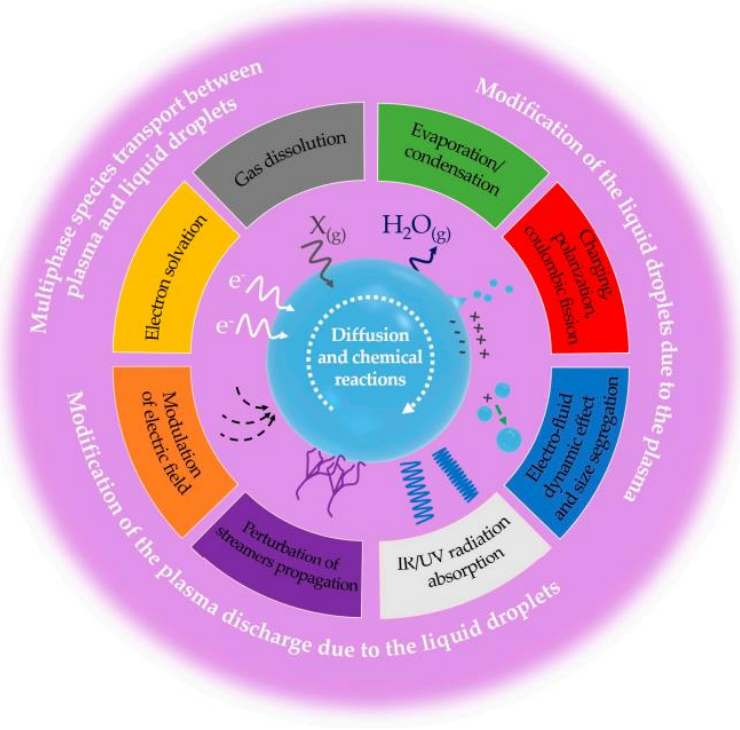

Figure 2-6: Aerosol-plasma interactions demonstrating the modifications of the plasma discharge due to liquid droplets and the changes to droplets due to plasma as well as species transportation between both of them [138]

In a similar RF plasma system to that used in this thesis, a study on droplets in RF microplasmas demonstrated droplets velocity and size distribution with plasma parameters and gas temperature, with and without plasma. Figure 2-7, shows the droplets diameter against the droplet's velocity where the plus sign at the middle of each plot indicates the average value of the demonstrated distributions, where the x-axis represents the normalized droplets velocity with gas velocity and y-axis

represents the droplets diameter. The coordinates of the center of each distribution have values of (0.55, 19) and (0.65, 16) for plasma off and on, respectively. Taking the average gas velocity as 32 ms^{-1}, the average droplet diameter is higher by 3µm when the plasma is off while the average droplet velocity ratio is increased by 20% when the plasma is on. It was suggested that the evaporation of slow droplets, which is more likely due to being exposed to the plasma for a longer time, was a potential reason for the velocity increase when the plasma is on, since these smaller droplets may escape detection i.e. below the imaging threshold, or be fully evaporated. The gas temperature was also estimated in this study to be below 400 K from the nitrogen atomic lines using a spectrometer [49]. Microdroplet transport through plasma jets can generate beneficial enhancement and transport of radical species (e.g., $OH^{\bullet}$, H_2O_2), important electron reduction reactions and rapid nanomaterials synthesis. The chemical kinetics are thought to depend on droplet evaporation which in turn is sensitive to gas temperature.

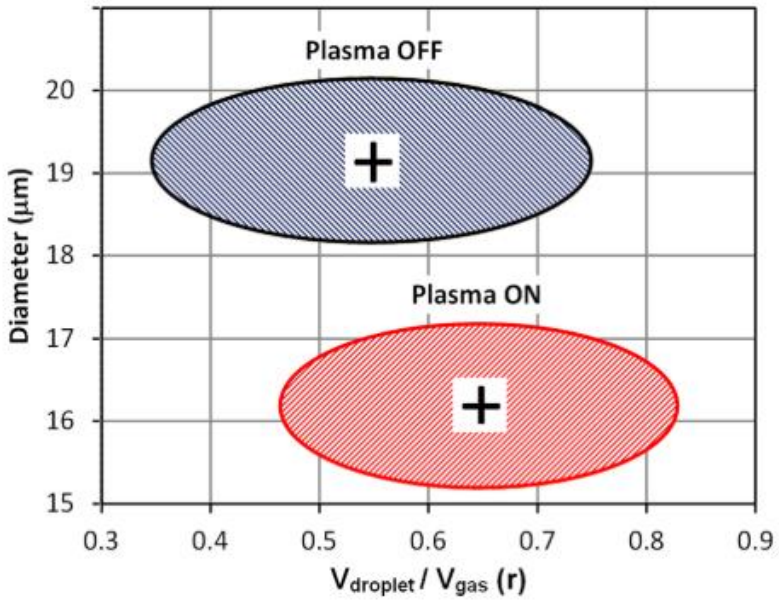

Figure 2-7: Droplet diameter versus normalised droplet velocity distribution with gas velocity for with and without plasma [49].

Liquid droplets were also used in material processing such as nanoparticle deposition using direct writing technique so that plasma deposition is processed using

direct plasma and without extra steps such as printing. The first technique is introducing the aerosol generated by atomization into a microplasmas jet and followed by scanning the substrate. Another technique is to spray the nanoparticles through the plasma using the liquid droplets then the deposition step on the substrate. Liquid droplets have been utilised also in replacing vapor precursors by liquid ones to be introduced into microplasmas as well as introducing non-equilibrium precursors and other new types of precursors for modification and reaction. Printing is another application of plasma droplet technique showing faster treatment time compared to heat treatment by post-deposition [51]. Furthermore, synthesis of small (~4 nm) gold nanoparticles (Au) using APPJ with droplets has been successfully achieved and it has proved a higher rate of synthesis within the droplets than that of radiolysis and irradiation of electron beam. These findings support applications of nanomaterial synthesis and fast delivery to target which is required in medicine applications such as cancer treatment and wound healing. In addition, the production of ultralow energy electrons of below 0.1 eV, supports studying and improving many cancer therapies [43].

The possibility of providing green chemistry has significantly been maximised by studying many reactions of microdroplets. This can be achieved by enabling the electrochemical activity of water molecules without any added reducing agent or applied potential [146] and could represent a potential example of on-water catalysis [147,148]. Accelerated reactions have been observed for a wide range of chemistries [43,149–152] and the spontaneous nature of the acceleration, without catalyst, radiation or applied field, has often been claimed [146,150,153]. Routes to reaction scale-up using gas-phase microdroplets are now being explored [38,154–156]. However, the several mechanisms leading to reaction acceleration in aqueous microdroplets are still unclear despite extensive investigation [157]. Reaction acceleration is known to be significantly impacted by the presence of internal electric fields [158,159]. H_2O_2 can be spontaneously generated in droplets, with the production yield inversely proportional to microdroplet size. A possible mechanism involves spontaneous oxidation of water by a strong intrinsic electric field at the water−gas interface [160], generating $OH^{\bullet}$ from OH^- which recombines to form H_2O_2.

In aqueous droplet microfluidic systems, it has long been thought that high electric fields at the water – oil interface drives reaction acceleration in such systems however, challenges of complicated measurements have halted the accurate measurements of field values at the droplet surface. Xiong et al. recently reported the measurement of high electric fields (~10^9 Vm^{-1}) at droplet surfaces using Raman excited fluorescence microscopy [161]. These fields were thought to be generated via the separation of charges and the high affinity of negatively charged ions at the interface. For water droplets in gas, H_3O^+ accumulates at the surface while the pH increases in the droplet core, which also leads to high electric fields [162]. Various theoretical studies of water – vapour interfaces also demonstrate high interface electric fields, attributed to ordered orientation of surface water molecules. It is observed that the removal of bonded electrons induces spontaneous oxidation and reduction and may occur because of such fields. Moreover, external fields acting on aligned reactant molecules are reported to substantially change the energy profile of chemical reactions resulting in catalysis [29].

2.9.3.2 Influence of plasma on droplets

Droplets delivery, which may contain particles, to the target is affected by the droplet's evaporation. Heinisch et al [163] studied the evaporation rate of single droplet and the factors affecting this rate. The droplet evaporation rate was linked through mathematical models to the gas velocity, viscosity, heat flux and conductivity, in addition to other factors such as droplets diffusion, surface tension, water mass density gradient. The vapour of the adjacent droplets and collision with the capillary tube wall may influence the process. Furthermore, the increase in the gas temperature and the attributed KE of the gas molecules, led to an increase in the evaporation rate. A drop in the droplet's temperature by 17K was reported due to the evaporation using Raman spectroscopy. The droplet evaporation rate in the Heinisch study was lower than that measured in NIBEC system, which is like our experiment setup, by 2-3 orders of magnitude showing that evaporation is enhanced in plasma compared to gas. However, most droplets, except the smallest diameters (< 4 μm) survived transport through the plasma without total evaporation [49]. In our case of plasma aerosol, convection is another factor that helps enhancing the evaporation and may take place in plasma if there is a speed difference between the gas and the droplet. The plasma

itself may affect the evaporation rate due to the presence and collisions of energetic species. In particular, positive ions would accelerate towards the droplets leading to an increase in their KE and may cause an increase in the droplets evaporation rate if the ion collision energy with the droplet is > T_{gas}. Plasma reactive species hits the droplets when they enter the plasma where some of these species dissolve in the droplet producing ROS and leads to many reactions. However, plasma factors and their influence on the droplet evaporation rate and the production of the ROS need further investigation.

2.9.3.3 Impact of droplets on plasma

Plasma characterisation can be achieved by understanding and controlling its main parameters that divide into internal parameters such as n_e, T_e, T_g and absorbed power, and external parameters e.g., gas flow and type, delivered power, geometry, configuration, and size. Whereas electron density and electron temperature are the most essential parameters because higher electrons loss causes an increase in T_e to compensate for this loss and a corresponding potential decrease in n_e which affects the ionisation and excitation processes in the plasma. Electrons loss can take many forms such as electrons loss due to charging of droplets and being part of creating ROS processes in plasma. Molecules have electronic excitation states as well as rotational and translational excited states which allows low energy electrons (LEE) to be absorbed, representing another form of electron loss. The absorbed electrons release energy and cause the molecules to vibrate and rotate. There is also some electrons energy loss due to the momentum exchange collisions with gas atoms and molecules leading to a potential increase in the gas temperature (T_g) where this electron energy loss is more common in collisional APP plasmas compared to LPP. Electron attachment to molecules happens if the electrons have a specific energy creating negative molecular ions and forms another mechanism for electrons loss. Ions are much heavier and slower than electrons and do not contribute to gas ionisation like electrons therefore, the creation of negative ions increases the plasma impedance which adds more resistivity to the plasma and may lead plasma to extinguish. Droplets evaporation is another potential reason for plasma to extinguish by increasing the water content in the plasma over a specific level. The total amount of water released into plasma per droplet can be calculated from the evaporation rate per droplet and

droplet rate [49]. Increasing the input power result in increasing the electron energy (T_e) that may compensate for various forms of electrons loss. Although it is unlikely that the number of electrons lost in charging droplet, to have a remarkable number compared to the total number of electrons in plasma, estimation of the flux of charged species to the droplet would be required to quantify the contribution of electrons in creating ROS.

2.10 Focused applications of this research

Significant attention has been recently paid to non-thermal atmospheric pressure plasma medical science for the delivery of reactive oxygen and nitrogen species. It has been used in treating heat-sensitive and vulnerable materials such as tissues and biological cell due to their low operating gas temperature. RONS has a high biological activity e.g. anti-cancer, anti-microbial and wound healing as they are responsible for majority of the plasma-induced chemical reactions on both tissues and cells. One of the major advantages of direct plasma treatment is the high flux of positive and negative charged species that interact with the target surface liquid, creating high concentrations of RONS locally to use their high reactivity immediately despite the lifetime of these short-lived species [118]. There are many other applications where the plasma interacts with liquid leading to an increase in the liquid reactivity. However, the plasma only interacts on the surface and its effect can be significantly diluted if the volume of liquid is large. Also, it take time for radicals to transport through liquid layers to cells and this could result in loss of reactivity. The plasma interaction with very small volume microdroplets is expected to significantly improve this liquid reactivity due to the high surface to volume ratio but measurement of concentrations in such small volumes if not directly possible. Therefore, the measurement of surface charge and estimation of the flux of these charged species, which create radicals in the liquid, as well as other radical species arriving from the plasma, is essential for liquid chemical simulation. However, the measurement of charge on microparticles or microdroplets has not yet been achieved at atmospheric pressure plasma.

Plasma gas temperature measurements is vital for temperature sensitive applications as it affects chemical, surface and composition reactions and also needs

to be controlled directly. Many biomedical and material applications are heat sensitive surfaces e.g. wound tissue and polymers where a controlled heat load is required for the treatment [164]. The traditional in-situ and lab techniques for temperature measurement have many limitations such as analysis and measurements complexity, high cost and some of them causes plasma disruption. The investigation of a small focal-spot IR sensor in this study to measure plasma gas temperature aims to provide high accurate and continuous measurements without disrupting the plasma and without any complex analysis, ie giving instant temperature values repeatedly. In addition, the plasma gas temperature with microdroplets has not been measured before and the IR sensor would provide these measurements for the first time. Consequently, plasma with and without microdroplets can be used safely in heat sensitive applications such as wound healing and cancer treatment by avoiding causing damage to the surrounding tissues.

Despite of the wide range of applications that may benefit from the results of our research, our main prospective application is cancer treatment inside the body using inflight of low-temperature plasma activated microdroplets. This may deliver high concentration of the most reactive species to the target while the plasma source is kept far away from the patient, allowing the highest possible benefits to the target area without being affected by any of the plasma drawbacks such as arcs, erosion, high electric field, UV photons, high gas temperature etc. Investigating the radical concentrations inside droplets and their lifetimes experimentally or by simulation is critical and has not been carried out up to now. However, adding water vapour to a plasma often leads to rapid increases in gas temperature. It is not known how much water vapour is evaporated from the droplets or its effect on gas temperature. Therefore, continuous measurements of plasma gas temperature with microdroplets would be of high importance to keep it under control. In addition, the study of the charged droplets and the measurements of the electron flux would support liquid simulation models to prove the validity of this idea. Developing the XPS-PAD system would support this application by allowing plasma treatment, instant freezing and then the measurement of plasma – induced chemical reactions at the droplet surface, without environmental contamination or species decay.

2.11 References

[1] N.S.J. Braithwaite, Introduction to gas discharges, Plasma Sources Sci. Technol. 9 (2000) 517–527. https://doi.org/10.1088/0963-0252/9/4/307.

[2] M. Keidar, I.I. Beilis, Plasma Engineering, 2013. https://doi.org/10.1016/C2010-0-67266-X.

[3] S. Nijdam, J. Teunissen, U. Ebert, The physics of streamer discharge phenomena, Plasma Sources Sci. Technol. 29 (2020). https://doi.org/10.1088/1361-6595/abaa05.

[4] P.J. Bruggeman, F. Iza, R. Brandenburg, Foundations of atmospheric pressure non-equilibrium plasmas, Plasma Sources Sci. Technol. 26 (2017). https://doi.org/10.1088/1361-6595/aa97af.

[5] X. Lu, G. V. Naidis, M. Laroussi, S. Reuter, D.B. Graves, K. Ostrikov, Reactive species in non-equilibrium atmospheric-pressure plasmas: Generation, transport, and biological effects, Phys. Rep. 630 (2016) 1–84. https://doi.org/10.1016/j.physrep.2016.03.003.

[6] A. V. Phelps, The Diffusion of Charged Particles in Collisional Plasmas: Free and Ambipolar Diffusion at Low and Moderate Pressures, J. Res. Natl. Inst. Stand. Technol. 95 (1990) 407. https://doi.org/10.6028/JRES.095.035.

[7] D.X. Liu, J.F. Li, A.J. Yang, X.H. Wang, M.Z. Rong, M.G. Kong, Comparison between electropositive and electronegative cold atmospheric-pressure plasmas: A modelling study, High Volt. 1 (2016) 81–85. https://doi.org/10.1049/hve.2016.0019.

[8] and A.J.L. Liebermann, M. A., Principles in plasama discharges and material processing, John Wiley&Sons, 1994.

[9] R. Moulick, M.K. Mahanta, K.S. Goswami, Effect of collision parameters in electronegative plasma sheath with two species of positive ions, Phys. Plasmas. 20 (2013). https://doi.org/10.1063/1.4820803.

[10] P. Swiderek, Electron-induced chemical reactions for surface functionalization,

Encycl. Interfacial Chem. Surf. Sci. Electrochem. (2018) 702–710. https://doi.org/10.1016/B978-0-12-409547-2.13876-4.

[11] Gas temptrure @ www.grc.nasa.gov, (n.d.). https://www.grc.nasa.gov/www/k-12/airplane/temptr.html#:~:text=The temperature of a gas,increased velocity of the molecules.

[12] R. Nave, Kinetic Temperature, Thermal Energy, (2001). http://hyperphysics.phy-astr.gsu.edu/hbase/Kinetic/kintem.html (accessed May 5, 2022).

[13] H. Dreicer, Electron and Ion Runaway in a Fully Ionized Gas. I, Phys. Rev. 115 (1959) 238. https://doi.org/10.1103/PhysRev.115.238.

[14] Ž. Mladenović, S. Gocić, Z. MladenovicáMladenovicá, S. sa Gocic, Influence of air and water vapor on EEDF, plasma parameters, and the main RONS in atmospheric pressure low temperature helium plasmas: Global model approach, Phys. Plasmas. 29 (2022) 103504. https://doi.org/10.1063/5.0110151.

[15] J.S. Boisvert, F. Montpetit, F. Vidal, J. Margot, L. Stafford, Time and space-resolved experimental investigation of the electron energy distribution function of a helium capacitive discharge at atmospheric pressure, J. Phys. D. Appl. Phys. 52 (2019) 245202. https://doi.org/10.1088/1361-6463/AB0FD4.

[16] P.J. Bruggeman, N. Sadeghi, D.C. Schram, V. Linss, Gas temperature determination from rotational lines in non-equilibrium plasmas: A review, Plasma Sources Sci. Technol. 23 (2014). https://doi.org/10.1088/0963-0252/23/2/023001.

[17] C. Riccardi, R. Barni, Chemical Kinetics in Air Plasmas at Atmospheric Pressure, Chem. Kinet. (2012). https://doi.org/10.5772/38396.

[18] A.M. Hirst, F.M. Frame, N.J. Maitland, D. O'Connell, Low temperature plasma: A novel focal therapy for localized prostate cancer?, Biomed Res. Int. 2014 (2014). https://doi.org/10.1155/2014/878319.

[19] M.M. Turner, Uncertainty and sensitivity analysis in complex plasma chemistry models, Plasma Sources Sci. Technol. 25 (2015). https://doi.org/10.1088/0963-

0252/25/1/015003.

[20] S.Y. Yoon, C. Yi, S. Eom, S. Park, S.B. Kim, S. Ryu, S.J. Yoo, Effects of gas temperature in the plasma layer on RONS generation in array-type dielectric barrier discharge at atmospheric pressure, Phys. Plasmas. 24 (2017). https://doi.org/10.1063/1.5003205.

[21] J. Diatczyk, J. Pawlat, H.D. Stryczewska, Diagnostic of temperature distribution in the chamber of ga plasma reactor, J. Ecol. Eng. 17 (2016) 79–83. https://doi.org/10.12911/22998993/65449.

[22] H.D. Stryczewska, J. Diatczyk, J. Pawlat, Temperature distribution in the gliding arc discharge chamber, J. Adv. Oxid. Technol. 14 (2011) 276–281. https://doi.org/10.1515/jaots-2011-0213.

[23] and A.P. Jyoti Kumar, Drinking Water Disinfection Techniques, (n.d.). https://books.google.co.uk/books (accessed August 3, 2021).

[24] H.-H. Cheng, S.-S. Chen, Y. Wu, D. Ho, NON-THERMAL PLASMA TECHNOLOGY FOR DEGRADATION OF ORGANIC COMPOUNDS IN WASTEWATER CONTROL: A CRITICAL REVIEW, J. Environ. Eng. Manag. 17(6) (2007) 427–433.

[25] C. Tendero, C. Tixier, P. Tristant, J. Desmaison, P. Leprince, Atmospheric pressure plasmas: A review, Spectrochim. Acta - Part B At. Spectrosc. 61 (2006) 2–30. https://doi.org/10.1016/j.sab.2005.10.003.

[26] V. V. Shumova, D.N. Polyakov, L.M. Vasilyak, Electrophysical Parameters of Plasma with a Charged Dust Cloud, Russ. J. Phys. Chem. B. 14 (2020) 959–963. https://doi.org/10.1134/S1990793120060275.

[27] H. Kersten, H. Deutsch, G.M.W. Kroesen, Charging of micro-particles in plasma-dust interaction, Int. J. Mass Spectrom. 233 (2004) 51–60. https://doi.org/10.1016/j.ijms.2003.10.018.

[28] B. Van Minderhout, J.C.A. Van Huijstee, B. Platier, T. Peijnenburg, P. Blom, G.M.W. Kroesen, J. Beckers, Charge control of micro-particles in a shielded plasma afterglow, Plasma Sources Sci. Technol. 29 (2020).

https://doi.org/10.1088/1361-6595/ab8e4f.

[29] H. Kersten, H. Deutsch, M. Otte, G.H.P.M. Swinkels, G.M.W. Kroesen, Micro-disperse particles as probes for plasma surface interaction, Thin Solid Films. 377–378 (2000) 530–536. https://doi.org/10.1016/S0040-6090(00)01439-5.

[30] D.A. Mendis, Progress in the study of dusty plasmas, Plasma Sources Sci. Technol. 11 (2002) A219. https://doi.org/10.1088/0963-0252/11/3A/333.

[31] J. Berndt, E. Kovačević, I. Stefanović, O. Stepanović, S.H. Hong, L. Boufendi, J. Winter, Some Aspects of Reactive Complex Plasmas, Contrib. to Plasma Phys. 49 (2009) 107–133. https://doi.org/10.1002/CTPP.200910016.

[32] T. Trottenberg, A. Melzer, A. Piel, Measurement of the electric charge on particulates forming Coulomb crystals in the sheath of a radiofrequency plasma, Plasma Sources Sci. Technol. 4 (1995) 450–458. https://doi.org/10.1088/0963-0252/4/3/015.

[33] J. Beckers, T. Ockenga, M. Wolter, W.W. Stoffels, J. Van Dijk, H. Kersten, G.M.W. Kroesen, Microparticles in a collisional rf plasma sheath under hypergravity conditions as probes for the electric field strength and the particle charge, Phys. Rev. Lett. 106 (2011) 115002. https://doi.org/10.1103/PHYSREVLETT.106.115002/FIGURES/5/MEDIUM.

[34] C.H. Su, S.H. Lam, Continuum theory of spherical electrostatic probes, Phys. Fluids. 6 (1963) 1479–1491. https://doi.org/10.1063/1.1710971.

[35] I.M. Cohen, Asymptotic Theory of Spherical Electrostatic Probes in a Slightly Ionized, Collision-Dominated Gas, Phys. Fluids. 6 (2004) 1492. https://doi.org/10.1063/1.1710972.

[36] S.A. Khrapak, G.E. Morfill, An interpolation formula for the ion flux to a small particle in collisional plasmas, Phys. Plasmas. 15 (2008). https://doi.org/10.1063/1.3035913.

[37] S. Askari, I. Levchenko, K. Ostrikov, P. Maguire, D. Mariotti, Crystalline Si nanoparticles below crystallization threshold: Effects of collisional heating in non-thermal atmospheric-pressure microplasmas, Appl. Phys. Lett. 104 (2014).

https://doi.org/10.1063/1.4872254.

[38] X. Yan, Y.H. Lai, R.N. Zare, Preparative microdroplet synthesis of carboxylic acids from aerobic oxidation of aldehydes, Chem. Sci. 9 (2018) 5207–5211. https://doi.org/10.1039/c8sc01580e.

[39] L. Patacchini, I.H. Hutchinson, Continuum-plasma solution surrounding nonemitting spherical bodies, Phys. Plasmas. 16 (2009). https://doi.org/10.1063/1.3143038.

[40] L.H. Fisher, G.L. Weissler, The apparent breakdown of meek's streamer criterion in divergent gaps due to the failure of Townsend's ionization function, Phys. Rev. 66 (1944) 95–102. https://doi.org/10.1103/PhysRev.66.95.

[41] D. Mariotti, R.M. Sankaran, Microplasmas for nanomaterials synthesis, J. Phys. D. Appl. Phys. 43 (2010). https://doi.org/10.1088/0022-3727/43/32/323001.

[42] S. Samukawa, M. Hori, S. Rauf, K. Tachibana, P. Bruggeman, G. Kroesen, J.C. Whitehead, A.B. Murphy, A.F. Gutsol, S. Starikovskaia, U. Kortshagen, J.P. Boeuf, T.J. Sommerer, M.J. Kushner, U. Czarnetzki, N. Mason, The 2012 plasma roadmap, J. Phys. D. Appl. Phys. 45 (2012). https://doi.org/10.1088/0022-3727/45/25/253001.

[43] P. Maguire, D. Rutherford, M. Macias-Montero, C. Mahony, C. Kelsey, M. Tweedie, F. Pérez-Martin, H. McQuaid, D. Diver, D. Mariotti, Continuous In-Flight Synthesis for On-Demand Delivery of Ligand-Free Colloidal Gold Nanoparticles, Nano Lett. 17 (2017) 1336–1343. https://doi.org/10.1021/acs.nanolett.6b03440.

[44] P. Bruggeman, R. Brandenburg, Atmospheric pressure discharge filaments and microplasmas: Physics, chemistry and diagnostics, J. Phys. D. Appl. Phys. 46 (2013). https://doi.org/10.1088/0022-3727/46/46/464001.

[45] X. Li, N. Yuan, P. Jia, Investigation of a plasma jet generated by high voltage discharge at atmospheric pressure, Adv. Mater. Res. 383–390 (2012) 5907–5911. https://doi.org/10.4028/www.scientific.net/AMR.383-390.5907.

[46] S. Hofmann, A.F.H. Van Gessel, T. Verreycken, P. Bruggeman, Power

dissipation, gas temperatures and electron densities of cold atmospheric pressure helium and argon RF plasma jets, Plasma Sources Sci. Technol. 20 (2011). https://doi.org/10.1088/0963-0252/20/6/065010.

[47] J.Y. Kim, S.O. Kim, Y. Wei, J. Li, A flexible cold microplasma jet using biocompatible dielectric tubes for cancer therapy, Appl. Phys. Lett. 96 (2010) 1–4. https://doi.org/10.1063/1.3431392.

[48] T. Verreycken, A.F.H. Van Gessel, A. Pageau, P. Bruggeman, Validation of gas temperature measurements by OES in an atmospheric air glow discharge with water electrode using Rayleigh scattering, Plasma Sources Sci. Technol. 20 (2011). https://doi.org/10.1088/0963-0252/20/2/024002.

[49] P.D. Maguire, C.M.O. Mahony, C.P. Kelsey, A.J. Bingham, E.P. Montgomery, E.D. Bennet, H.E. Potts, D.C.E. Rutherford, D.A. McDowell, D.A. Diver, D. Mariotti, Controlled microdroplet transport in an atmospheric pressure microplasma, Appl. Phys. Lett. 106 (2015). https://doi.org/10.1063/1.4922034.

[50] P.J. Bruggeman, M.J. Kushner, B.R. Locke, J.G.E. Gardeniers, W.G. Graham, D.B. Graves, R.C.H.M. Hofman-Caris, D. Maric, J.P. Reid, E. Ceriani, D. Fernandez Rivas, J.E. Foster, S.C. Garrick, Y. Gorbanev, S. Hamaguchi, F. Iza, H. Jablonowski, E. Klimova, J. Kolb, F. Krcma, P. Lukes, Z. MacHala, I. Marinov, D. Mariotti, S. Mededovic Thagard, D. Minakata, E.C. Neyts, J. Pawlat, Z.L. Petrovic, R. Pflieger, S. Reuter, D.C. Schram, S. Schröter, M. Shiraiwa, B. Tarabová, P.A. Tsai, J.R.R. Verlet, T. Von Woedtke, K.R. Wilson, K. Yasui, G. Zvereva, Plasma-liquid interactions: A review and roadmap, Plasma Sources Sci. Technol. 25 (2016). https://doi.org/10.1088/0963-0252/25/5/053002.

[51] Y. Sui, C.A. Zorman, R.M. Sankaran, Plasmas for additive manufacturing, Plasma Process. Polym. 17 (2020) 1–25. https://doi.org/10.1002/ppap.202000009.

[52] H. Zeghioud, P. Nguyen-Tri, L. Khezami, A. Amrane, A.A. Assadi, Review on discharge Plasma for water treatment: mechanism, reactor geometries, active species and combined processes, J. Water Process Eng. 38 (2020).

https://doi.org/10.1016/j.jwpe.2020.101664.

[53] M. Moreau, M.G.J. Feuilloley, N. Orange, J.L. Brisset, Lethal effect of the gliding arc discharges on Erwinia spp., J. Appl. Microbiol. 98 (2005) 1039–1046. https://doi.org/10.1111/j.1365-2672.2004.02535.x.

[54] N. Shirai, S. Uchida, F. Tochikubo, Influence of oxygen gas on characteristics of self-organized luminous pattern formation observed in an atmospheric dc glow discharge using a liquid electrode, Plasma Sources Sci. Technol. 23 (2014). https://doi.org/10.1088/0963-0252/23/5/054010.

[55] N. Shirai, K. Ichinose, S. Uchida, F. Tochikubo, Influence of liquid temperature on the characteristics of an atmospheric dc glow discharge using a liquid electrode with a miniature helium flow, Plasma Sources Sci. Technol. 20 (2011). https://doi.org/10.1088/0963-0252/20/3/034013.

[56] M.H. Lee, H.C. Lee, C.W. Chung, Comparison of pressure dependence of electron energy distributions in oxygen capacitively and inductively coupled plasmas, Phys. Rev. E - Stat. Nonlinear, Soft Matter Phys. 81 (2010) 046402. https://doi.org/10.1103/PHYSREVE.81.046402/FIGURES/8/MEDIUM.

[57] M. Bazavan, M. Teodorescu, G. Dinescu, Confirmation of OH as good thermometric species for gas temperature determination in an atmospheric pressure argon plasma jet, Plasma Sources Sci. Technol. 26 (2017). https://doi.org/10.1088/1361-6595/aa723c.

[58] B. Ghimire, E.J. Szili, B.L. Patenall, P. Lamichhane, N. Gaur, A.J. Robson, D. Trivedi, N.T. Thet, A.T.A. Jenkins, E.H. Choi, R.D. Short, Enhancement of hydrogen peroxide production from an atmospheric pressure argon plasma jet and implications to the antibacterial activity of plasma activated water, Plasma Sources Sci. Technol. 30 (2021) 035009. https://doi.org/10.1088/1361-6595/ABE0C9.

[59] G. Dilecce, Optical spectroscopy diagnostics of discharges at atmospheric pressure, Plasma Sources Sci. Technol. 23 (2014). https://doi.org/10.1088/0963-0252/23/1/015011.

[60] S. Schröter, A. Wijaikhum, A.R. Gibson, A. West, H.L. Davies, N. Minesi, J. Dedrick, E. Wagenaars, N. De Oliveira, L. Nahon, M.J. Kushner, J.P. Booth, K. Niemi, T. Gans, D. O'Connell, Chemical kinetics in an atmospheric pressure helium plasma containing humidity, Phys. Chem. Chem. Phys. 20 (2018) 24263–24286. https://doi.org/10.1039/c8cp02473a.

[61] D.X. Liu, P. Bruggeman, F. Iza, M.Z. Rong, M.G. Kong, Global model of low-temperature atmospheric-pressure He + H2O plasmas, Plasma Sources Sci. Technol. 19 (2010). https://doi.org/10.1088/0963-0252/19/2/025018.

[62] R. Sander, MODELING ATMOSPHERIC CHEMISTRY : INTERACTIONS BETWEEN GAS-PHASE SPECIES AND LIQUID CLOUD / AEROSOL PARTICLES Although the liquid phase occupies only a very small fraction of the total volume of air (about 0 . 0001 % in clouds), it is recognized that it, Surv. Geophys. 20 (1999) 1–31. http://www.ncbi.nlm.nih.gov/entrez/query.fcgi?db=pubmed&cmd=Retrieve&dopt=AbstractPlus&list_uids=14438491200596500785related:MWEooD_TX8gJ.

[63] J.H. Yan, C.M. Du, X.D. Li, B.G. Cheron, M.J. Ni, K.F. Cen, Degradation of phenol in aqueous solutions by gas-liquid gliding arc discharges, Plasma Chem. Plasma Process. 26 (2006) 31–41. https://doi.org/10.1007/s11090-005-8723-6.

[64] J. Grzechulska, M. Hamerski, A.W. Morawski, Photocatalytic decomposition of oil in water, Water Res. 34 (2000) 1638–1644. https://doi.org/10.1016/S0043-1354(99)00275-4.

[65] F. Rezaei, P. Vanraes, A. Nikiforov, R. Morent, N. De Geyter, Applications of Plasma-Liquid Systems : A Review, (2019).

[66] C. Richmonds, R.M. Sankaran, Plasma-liquid electrochemistry: Rapid synthesis of colloidal metal nanoparticles by microplasma reduction of aqueous cations, Appl. Phys. Lett. 93 (2008) 131501. https://doi.org/10.1063/1.2988283.

[67] L. Chen, C. Iwamoto, E. Omurzak, S. Takebe, H. Okudera, A. Yoshiasa, S. Sulaimankulova, T. Mashimo, Synthesis of zirconium carbide (ZrC)

nanoparticles covered with graphitic “windows” by pulsed plasma in liquid, RSC Adv. 1 (2011) 1083–1088. https://doi.org/10.1039/C1RA00194A.

[68] S. Sato, K. Mori, O. Ariyada, H. Atsushi, T. Yonezawa, Synthesis of nanoparticles of silver and platinum by microwave-induced plasma in liquid, Surf. Coatings Technol. 206 (2011) 955–958. https://doi.org/10.1016/J.SURFCOAT.2011.03.110.

[69] J. Hieda, N. Saito, O. Takai, Exotic shapes of gold nanoparticles synthesized using plasma in aqueous solution, J. Vac. Sci. Technol. A Vacuum, Surfaces, Film. 26 (2008) 854. https://doi.org/10.1116/1.2919139.

[70] I.G. Koo, M.S. Lee, J.H. Shim, J.H. Ahn, W.M. Lee, Platinum nanoparticles prepared by a plasma-chemical reduction method, J. Mater. Chem. 15 (2005) 4125–4128. https://doi.org/10.1039/B508420B.

[71] T. Shirafuji, Y. Noguchi, T. Yamamoto, J. Hieda, N. Saito, O. Takai, A. Tsuchimoto, K. Nojima, Y. Okabe, Functionalization of multiwalled carbon nanotubes by solution plasma processing in ammonia aqueous solution and preparation of composite material with polyamide 6, Jpn. J. Appl. Phys. 52 (2013) 125101. https://doi.org/10.7567/JJAP.52.125101/XML.

[72] T. Shirafuji, J. Ueda, A. Nakamura, S.P. Cho, N. Saito, O. Takai, Gold nanoparticle synthesis using three-dimensionally integrated micro-solution plasmas, Jpn. J. Appl. Phys. 52 (2013) 126202. https://doi.org/10.7567/JJAP.52.126202/XML.

[73] T. Shirafuji, Y. Himeno, Generation of three-dimensionally integrated micro-solution plasma and its application to decomposition of methylene blue molecules in water, Jpn. J. Appl. Phys. 52 (2013) 11NE03. https://doi.org/10.7567/JJAP.52.11NE03/XML.

[74] G. Saito, T. Akiyama, Nanomaterial Synthesis Using Plasma Generation in Liquid, J. Nanomater. 2015 (2015). https://doi.org/10.1155/2015/123696.

[75] W.G. Graham, K.R. Stalder, Plasmas in liquids and some of their applications in nanoscience, J. Phys. D. Appl. Phys. 44 (2011) 174037.

https://doi.org/10.1088/0022-3727/44/17/174037.

[76] T.A. Kareem, A.A. Kaliani, Glow discharge plasma electrolysis for nanoparticles synthesis, Ionics (Kiel). 18 (2012) 315–327. https://doi.org/10.1007/s11581-011-0639-y.

[77] V.K. Gupta, I. Ali, T.A. Saleh, A. Nayak, S. Agarwal, Chemical treatment technologies for waste-water recycling - An overview, RSC Adv. 2 (2012) 6380–6388. https://doi.org/10.1039/c2ra20340e.

[78] J. ZHANG, J. CHEN, X. LI, Remove of Phenolic Compounds in Water by Low-Temperature Plasma: A Review of Current Research, J. Water Resour. Prot. 01 (2009) 99–109. https://doi.org/10.4236/jwarp.2009.12014.

[79] B. Jiang, J. Zheng, S. Qiu, M. Wu, Q. Zhang, Z. Yan, Q. Xue, Review on electrical discharge plasma technology for wastewater remediation, Chem. Eng. J. 236 (2014) 348–368. https://doi.org/10.1016/j.cej.2013.09.090.

[80] G. Fridman, G. Friedman, A. Gutsol, A.B. Shekhter, V.N. Vasilets, A. Fridman, Applied plasma medicine, Plasma Process. Polym. 5 (2008) 503–533. https://doi.org/10.1002/ppap.200700154.

[81] Y.T. Chang, G. Chen, Oral bacterial inactivation using a novel low-temperature atmospheric-pressure plasma device, J. Dent. Sci. 11 (2016) 65–71. https://doi.org/10.1016/J.JDS.2014.03.007.

[82] H.R. Metelmann, D.S. Nedrelow, C. Seebauer, M. Schuster, T. von Woedtke, K.D. Weltmann, S. Kindler, P.H. Metelmann, S.E. Finkelstein, D.D. Von Hoff, F. Podmelle, Head and neck cancer treatment and physical plasma, Clin. Plasma Med. 3 (2015) 17–23. https://doi.org/10.1016/J.CPME.2015.02.001.

[83] S. Bekeschus, T. von Woedtke, S. Emmert, A. Schmidt, Medical gas plasma-stimulated wound healing: Evidence and mechanisms: Mechanisms of gas plasma-assisted wound healing, Redox Biol. 46 (2021) 102116. https://doi.org/10.1016/j.redox.2021.102116.

[84] J.C. Harley, N. Suchowerska, D.R. McKenzie, Cancer treatment with gas plasma and with gas plasma–activated liquid: positives, potentials and problems

of clinical translation, Biophys. Rev. 12 (2020) 989–1006. https://doi.org/10.1007/s12551-020-00743-z.

[85] S.P. Kuo, Air plasma for medical applications, J. Biomed. Sci. Eng. 05 (2012) 481–495. https://doi.org/10.4236/jbise.2012.59061.

[86] S.P. Kuo, O. Tarasenko, J. Chang, S. Popovic, C.Y. Chen, H.W. Fan, A. Scott, M. Lahiani, P. Alusta, J.D. Drake, M. Nikolic, Contribution of a portable air plasma torch to rapid blood coagulation as a method of preventing bleeding, New J. Phys. 11 (2009) 115016. https://doi.org/10.1088/1367-2630/11/11/115016.

[87] C.Y. Chen, H.W. Fan, S.P. Kuo, J. Chang, T. Pedersen, T.J. Mills, C.C. Huang, Blood clotting by low-temperature air plasma, IEEE Trans. Plasma Sci. 37 (2009) 993–999. https://doi.org/10.1109/TPS.2009.2016344.

[88] G.C. Gurtner, S. Werner, Y. Barrandon, M.T. Longaker, Wound repair and regeneration, Nat. 2008 4537193. 453 (2008) 314–321. https://doi.org/10.1038/nature07039.

[89] G. Isbary, G. Morfill, H.U. Schmidt, M. Georgi, K. Ramrath, J. Heinlin, S. Karrer, M. Landthaler, T. Shimizu, B. Steffes, W. Bunk, R. Monetti, J.L. Zimmermann, R. Pompl, W. Stolz, A first prospective randomized controlled trial to decrease bacterial load using cold atmospheric argon plasma on chronic wounds in patients, Br. J. Dermatol. 163 (2010) 78–82. https://doi.org/10.1111/J.1365-2133.2010.09744.X.

[90] G. Isbary, J. Heinlin, T. Shimizu, J.L. Zimmermann, G. Morfill, H.U. Schmidt, R. Monetti, B. Steffes, W. Bunk, Y. Li, T. Klaempfl, S. Karrer, M. Landthaler, W. Stolz, Successful and safe use of 2 min cold atmospheric argon plasma in chronic wounds: results of a randomized controlled trial, Br. J. Dermatol. 167 (2012) 404–410. https://doi.org/10.1111/J.1365-2133.2012.10923.X.

[91] F. Brehmer, H.A. Haenssle, G. Daeschlein, R. Ahmed, S. Pfeiffer, A. Görlitz, D. Simon, M.P. Schön, D. Wandke, S. Emmert, Alleviation of chronic venous leg ulcers with a hand-held dielectric barrier discharge plasma generator (PlasmaDerm® VU-2010): results of a monocentric, two-armed, open,

prospective, randomized and controlled trial (NCT01415622), J. Eur. Acad. Dermatology Venereol. 29 (2015) 148–155. https://doi.org/10.1111/JDV.12490.

[92] R. Tucker, Commentary on Clinical Applications of Argon Plasma Coagulation in Endoscopy, Gastroenterol. Nurs. 30 (2007) 129–130. https://doi.org/10.1097/01.SGA.0000267935.82490.C9.

[93] J. Raiser, M. Zenker, Argon plasma coagulation for open surgical and endoscopic applications: State of the art, J. Phys. D. Appl. Phys. 39 (2006) 3520–3523. https://doi.org/10.1088/0022-3727/39/16/S10.

[94] K. Priya Arjunan, A. Morss Clyne, Hydroxyl Radical and Hydrogen Peroxide are Primarily Responsible for Dielectric Barrier Discharge Plasma-Induced Angiogenesis, Plasma Process. Polym. 8 (2011) 1154–1164. https://doi.org/10.1002/PPAP.201100078.

[95] J. Raiser, M. Zenker, Argon plasma coagulation for open surgical and endoscopic applications: state of the art, J. Phys. D. Appl. Phys. 39 (2006) 3520. https://doi.org/10.1088/0022-3727/39/16/S10.

[96] R. Tucker, Commentary on Clinical Applications of Argon Plasma Coagulation in Endoscopy, Gastroenterol. Nurs. 30 (2007) 129–130. https://doi.org/10.1097/01.SGA.0000267935.82490.c9.

[97] T. Maisch, T. Shimizu, Y.F. Li, J. Heinlin, S. Karrer, G. Morfill, J.L. Zimmermann, Decolonisation of MRSA, S. aureus and E. coli by Cold-Atmospheric Plasma Using a Porcine Skin Model In Vitro, PLoS One. 7 (2012) e34610. https://doi.org/10.1371/JOURNAL.PONE.0034610.

[98] R. Tiede, J. Hirschberg, G. Daeschlein, T. von Woedtke, W. Vioel, S. Emmert, Plasma Applications: A Dermatological View, Contrib. to Plasma Phys. 54 (2014) 118–130. https://doi.org/10.1002/ctpp.201310061.

[99] M.A. Bogle, K.A. Arndt, J.S. Dover, Evaluation of Plasma Skin Regeneration Technology in Low-Energy Full-Facial Rejuvenation, Arch. Dermatol. 143 (2007) 168–174. https://doi.org/10.1001/ARCHDERM.143.2.168.

[100] W.K. Foster, R.L. Moy, E.F. Fincher, Advances in plasma skin regeneration, J. Cosmet. Dermatol. 7 (2008) 169–179. https://doi.org/10.1111/j.1473-2165.2008.00385.x.

[101] J. Heinlin, G. Isbary, W. Stolz, G. Morfill, M. Landthaler, T. Shimizu, B. Steffes, T. Nosenko, J.L. Zimmermann, S. Karrer, Plasma applications in medicine with a special focus on dermatology, J. Eur. Acad. Dermatology Venereol. 25 (2011) 1–11. https://doi.org/10.1111/j.1468-3083.2010.03702.x.

[102] E. Pennisi, A mouthful of microbes, Science (80-.). 307 (2005) 1899–1901. https://doi.org/10.1126/SCIENCE.307.5717.1899/ASSET/0A08E653-9194-458F-B983-6BF374126BE6/ASSETS/GRAPHIC/1899-5.GIF.

[103] W.E.C. Moore, L.V.H. Moore, The bacteria of periodontal diseases, Periodontol. 2000. 5 (1994) 66–77. https://doi.org/10.1111/j.1600-0757.1994.tb00019.x.

[104] S.H. Nam, H.W. Lee, S.H. Cho, J.K. Lee, Y.C. Jeon, G.C. Kim, High-efficiency tooth bleaching using non-thermal atmospheric pressure plasma with low concentration of hydrogen peroxide, J. Appl. Oral Sci. 21 (2013) 265–270. https://doi.org/10.1590/1679-775720130016.

[105] K. Kawamoto, Y. Tsujimoto, Effects of the hydroxyl radical and hydrogen peroxide on tooth bleaching, J. Endod. 30 (2004) 45–50. https://doi.org/10.1097/00004770-200401000-00010.

[106] V. Arora, Cold Atmospheric Plasma (CAP) In Dentistry, Dentistry. 04 (2013) 1–5. https://doi.org/10.4172/2161-1122.1000189.

[107] J. Schlegel, J. Köritzer, V. Boxhammer, Plasma in cancer treatment, Clin. Plasma Med. 1 (2013) 2–7. https://doi.org/10.1016/j.cpme.2013.08.001.

[108] G. Fridman, A. Shereshevsky, M.M. Jost, A.D. Brooks, A. Fridman, A. Gutsol, V. Vasilets, G. Friedman, Floating electrode dielectric barrier discharge plasma in air promoting apoptotic behavior in Melanoma skin cancer cell lines, Plasma Chem. Plasma Process. 27 (2007) 163–176. https://doi.org/10.1007/s11090-007-9048-4.

[109] I.E. Kieft, D. Darios, A.J.M. Roks, E. Stoffels, Plasma treatment of mammalian vascular cells: A quantitative description, IEEE Trans. Plasma Sci. 33 (2005) 771–775. https://doi.org/10.1109/TPS.2005.844528.

[110] E. Stoffels, A.J.M. Roks, L.E. Deelman, Delayed effects of cold atmospheric plasma on vascular cells, Plasma Process. Polym. 5 (2008) 599–605. https://doi.org/10.1002/ppap.200800028.

[111] National Cancer Institute, Radiation Therapy for Cancer - NCI, Radiat. Ther. to Treat Cancer Was Orig. Publ. by Natl. Cancer Inst. (2019). https://www.cancer.gov/about-cancer/treatment/types/radiation-therapy (accessed November 15, 2022).

[112] R. Limanowski, D. Yan, L. Li, M. Keidar, Preclinical Cold Atmospheric Plasma Cancer Treatment, Cancers (Basel). 14 (2022). https://doi.org/10.3390/cancers14143461.

[113] G. Dennert, M. Horneber, Selenium for alleviating the side effects of chemotherapy, radiotherapy and surgery in cancer patients, Cochrane Database Syst. Rev. 2017 (2006). https://doi.org/10.1002/14651858.CD005037.pub2.

[114] Molecular Basis of Oxidative Stress: Chemistry, Mechanisms, and Disease ... - Frederick A. Villamena - Google Books, (2013). https://books.google.co.uk/books?hl=en&lr=&id=iOXjBEWnieIC&oi=fnd&pg=PT10&dq=Villamena+FA+(2013)+Molecular+basis+of+oxidative+stress:+chemistry,+mechanisms,+and+disease+pathogenesis.+Wiley&ots=b3q5hECfCn&sig=HEWmbTDcIs1gx9Muz07Q-Uo3FxA&redir_esc=y#v=onepa.

[115] J. Lafontaine, J.S. Boisvert, A. Glory, S. Coulombe, P. Wong, Synergy between Non-Thermal Plasma with Radiation Therapy and Olaparib in a Panel of Breast Cancer Cell Lines, Cancers 2020, Vol. 12, Page 348. 12 (2020) 348. https://doi.org/10.3390/CANCERS12020348.

[116] D. Yan, A. Horkowitz, Q. Wang, M. Keidar, On the selective killing of cold atmospheric plasma cancer treatment: Status and beyond, Plasma Process. Polym. 18 (2021) 2100020. https://doi.org/10.1002/ppap.202100020.

[117] D. Dobrynin, G. Fridman, G. Friedman, A. Fridman, Physical and biological mechanisms of direct plasma interaction with living tissue, New J. Phys. 11 (2009) 115020. https://doi.org/10.1088/1367-2630/11/11/115020.

[118] Y. Gorbanev, D. O'Connell, V. Chechik, Non-Thermal Plasma in Contact with Water: The Origin of Species, Chem. - A Eur. J. 22 (2016) 3496–3505. https://doi.org/10.1002/chem.201503771.

[119] D. Xu, Q. Cui, Y. Xu, B. Wang, M. Tian, Q. Li, Z. Liu, D. Liu, H. Chen, M.G. Kong, Systemic study on the safety of immuno-deficient nude mice treated by atmospheric plasma-activated water, in: Plasma Sci. Technol., 2018. https://doi.org/10.1088/2058-6272/aa9842.

[120] D.B. Graves, Reactive species from cold atmospheric plasma: Implications for cancer therapy, Plasma Process. Polym. 11 (2014) 1120–1127. https://doi.org/10.1002/ppap.201400068.

[121] S.H. Ki, K. Masur, K.Y. Baik, E.H. Choi, UV Absorption Spectroscopy for the Diffusion of Plasma-Generated Reactive Species through a Skin Model, Appl. Sci. 2021, Vol. 11, Page 7958. 11 (2021) 7958. https://doi.org/10.3390/APP11177958.

[122] H.M. Joh, S.J. Kim, T.H. Chung, S.H. Leem, Reactive oxygen species-related plasma effects on the apoptosis of human bladder cancer cells in atmospheric pressure pulsed plasma jets, Appl. Phys. Lett. 101 (2012) 053703. https://doi.org/10.1063/1.4742742.

[123] G.J. Kim, W. Kim, K.T. Kim, J.K. Lee, DNA damage and mitochondria dysfunction in cell apoptosis induced by nonthermal air plasma, Appl. Phys. Lett. 96 (2010) 021502. https://doi.org/10.1063/1.3292206.

[124] M. Keidar, Plasma for cancer treatment, Plasma Sources Sci. Technol. 24 (2015) 033001. https://doi.org/10.1088/0963-0252/24/3/033001.

[125] D. Yan, J.H. Sherman, M. Keidar, D. Yan, J.H. Sherman, M. Keidar, Cold atmospheric plasma, a novel promising anti-cancer treatment modality, Oncotarget. 8 (2016) 15977–15995.

https://doi.org/10.18632/ONCOTARGET.13304.

[126] D. Yan, A. Malyavko, Q. Wang, L. Lin, J.H. Sherman, M. Keidar, Cold Atmospheric Plasma Cancer Treatment, a Critical Review, Appl. Sci. 2021, Vol. 11, Page 7757. 11 (2021) 7757. https://doi.org/10.3390/APP11167757.

[127] M. Keidar, R. Walk, A. Shashurin, P. Srinivasan, A. Sandler, S. Dasgupta, R. Ravi, R. Guerrero-Preston, B. Trink, Cold plasma selectivity and the possibility of a paradigm shift in cancer therapy, Br. J. Cancer 2011 1059. 105 (2011) 1295–1301. https://doi.org/10.1038/bjc.2011.386.

[128] M. Vandamme, E. Robert, S. Pesnel, E. Barbosa, S. Dozias, J. Sobilo, S. Lerondel, A. Le Pape, J.M. Pouvesle, Antitumor Effect of Plasma Treatment on U87 Glioma Xenografts: Preliminary Results, Plasma Process. Polym. 7 (2010) 264–273. https://doi.org/10.1002/PPAP.200900080.

[129] Y. Gorbanev, A. Privat-Maldonado, A. Bogaerts, Analysis of Short-Lived Reactive Species in Plasma-Air-Water Systems: The Dos and the Do Nots, Anal. Chem. 90 (2018) 13151–13158. https://doi.org/10.1021/ACS.ANALCHEM.8B03336/ASSET/IMAGES/LARGE/AC-2018-03336C_0007.JPEG.

[130] H. Tanaka, S. Bekeschus, D. Yan, M. Hori, M. Keidar, M. Laroussi, R.O.S. Rns, R.O.S. Rns, R.O.S. Rns, Plasma-Treated Solutions (PTS) in Cancer Therapy, (2021) 1–19.

[131] D. Yan, J.H. Sherman, M. Keidar, The Application of the Cold Atmospheric Plasma-Activated Solutions in Cancer Treatment, Anticancer. Agents Med. Chem. 18 (2017) 769–775. https://doi.org/10.2174/1871520617666170731115233.

[132] K.R. Liedtke, S. Bekeschus, A. Kaeding, C. Hackbarth, J.P. Kuehn, C.D. Heidecke, W. Von Bernstorff, T. Von Woedtke, L.I. Partecke, Non-thermal plasma-treated solution demonstrates antitumor activity against pancreatic cancer cells in vitro and in vivo, Sci. Reports 2017 71. 7 (2017) 1–12. https://doi.org/10.1038/s41598-017-08560-3.

[133] T. Adachi, S. Nonomura, M. Horiba, T. Hirayama, T. Kamiya, H. Nagasawa, H. Hara, Iron stimulates plasma-activated medium-induced A549 cell injury, Sci. Reports 2016 61. 6 (2016) 1–12. https://doi.org/10.1038/srep20928.

[134] K. Saito, T. Asai, K. Fujiwara, J. Sahara, H. Koguchi, N. Fukuda, M. Suzuki-Karasaki, M. Soma, Y. Suzuki-Karasaki, K. Saito, T. Asai, K. Fujiwara, J. Sahara, H. Koguchi, N. Fukuda, M. Suzuki-Karasaki, M. Soma, Y. Suzuki-Karasaki, Tumor-selective mitochondrial network collapse induced by atmospheric gas plasma-activated medium, Oncotarget. 7 (2016) 19910–19927. https://doi.org/10.18632/ONCOTARGET.7889.

[135] F. Utsumi, H. Kajiyama, K. Nakamura, H. Tanaka, M. Mizuno, K. Ishikawa, H. Kondo, H. Kano, M. Hori, F. Kikkawa, Effect of indirect nonequilibrium atmospheric pressure plasma on anti-proliferative activity against chronic chemo-resistant ovarian cancer cells in vitro and in vivo, PLoS One. 8 (2013) e81576. https://doi.org/10.1371/journal.pone.0081576.

[136] Y. Binenbaum, G. Ben-David, Z. Gil, Y.Z. Slutsker, M.A. Ryzhkov, J. Felsteiner, Y.E. Krasik, J.T. Cohen, Cold Atmospheric Plasma, Created at the Tip of an Elongated Flexible Capillary Using Low Electric Current, Can Slow the Progression of Melanoma, PLoS One. 12 (2017) e0169457. https://doi.org/10.1371/JOURNAL.PONE.0169457.

[137] N. Chernets, D.S. Kurpad, V. Alexeev, D.B. Rodrigues, T.A. Freeman, Reaction Chemistry Generated by Nanosecond Pulsed Dielectric Barrier Discharge Treatment is Responsible for the Tumor Eradication in the B16 Melanoma Mouse Model, Plasma Process. Polym. 12 (2015) 1400–1409. https://doi.org/10.1002/PPAP.201500140.

[138] A. Stancampiano, T. Gallingani, M. Gherardi, Z. Machala, P. Maguire, V. Colombo, J.M. Pouvesle, E. Robert, Plasma and aerosols: Challenges, opportunities and perspectives, Appl. Sci. 9 (2019). https://doi.org/10.3390/app9183861.

[139] X. Yan, R.M. Bain, R.G. Cooks, Organic Reactions in Microdroplets: Reaction Acceleration Revealed by Mass Spectrometry, Angew. Chemie - Int. Ed. 55

(2016) 12960–12972. https://doi.org/10.1002/anie.201602270.

[140] S. Banerjee, E. Gnanamani, X. Yan, R.N. Zare, Can all bulk-phase reactions be accelerated in microdroplets?, Analyst. 142 (2017) 1399–1402. https://doi.org/10.1039/c6an02225a.

[141] Z. Wei, Y. Li, R.G. Cooks, X. Yan, Accelerated reaction kinetics in microdroplets: Overview and recent developments, Annu. Rev. Phys. Chem. 71 (2020) 31–51. https://doi.org/10.1146/annurev-physchem-121319-110654.

[142] T. Rainer, R. Eidelpes, M. Tollinger, T. Müller, Microdroplet Mass Spectrometry Enables Extremely Accelerated Pepsin Digestion of Proteins, J. Am. Soc. Mass Spectrom. 32 (2021) 1841–1845. https://doi.org/10.1021/jasms.1c00126.

[143] S. Mondal, S. Acharya, R. Biswas, B. Bagchi, R.N. Zare, Enhancement of reaction rate in small-sized droplets: A combined analytical and simulation study, J. Chem. Phys. 148 (2018) 244704. https://doi.org/10.1063/1.5030114.

[144] H. Wei, E.P. Vejerano, W. Leng, Q. Huang, M.R. Willner, L.C. Marr, P.J. Vikesland, Aerosol microdroplets exhibit a stable pH gradient, Proc. Natl. Acad. Sci. U. S. A. 115 (2018) 7272–7277. https://doi.org/10.1073/pnas.1720488115.

[145] N. Narendra, X. Chen, J. Wang, J. Charles, R.G. Cooks, T. Kubis, Quantum Mechanical Modeling of Reaction Rate Acceleration in Microdroplets, J. Phys. Chem. A. 124 (2020) 4984–4989. https://doi.org/10.1021/ACS.JPCA.0C03225/ASSET/IMAGES/MEDIUM/JP0C03225_0005.GIF.

[146] J.K. Lee, D. Samanta, H.G. Nam, R.N. Zare, Micrometer-Sized Water Droplets Induce Spontaneous Reduction, J. Am. Chem. Soc. 141 (2019) 10585–10589. https://doi.org/10.1021/jacs.9b03227.

[147] M.F. Ruiz-Lopez, J.S. Francisco, M.T.C. Martins-Costa, J.M. Anglada, Molecular reactions at aqueous interfaces, Nat. Rev. Chem. 4 (2020) 459–475. https://doi.org/10.1038/s41570-020-0203-2.

[148] S. Narayan, J. Muldoon, M.G. Finn, V. V. Fokin, H.C. Kolb, K.B. Sharpless, “On water”: Unique reactivity of organic compounds in aqueous suspension, Angew. Chemie - Int. Ed. 44 (2005) 3275–3279. https://doi.org/10.1002/anie.200462883.

[149] H. Nie, Z. Wei, L. Qiu, X. Chen, D.T. Holden, R.G. Cooks, High-yield gram-scale organic synthesis using accelerated microdroplet/thin film reactions with solvent recycling, Chem. Sci. 11 (2020) 2356–2361. https://doi.org/10.1039/c9sc06265c.

[150] J.K. Lee, D. Samanta, H.G. Nam, R.N. Zare, Spontaneous formation of gold nanostructures in aqueous microdroplets, Nat. Commun. 9 (2018) 1–9. https://doi.org/10.1038/s41467-018-04023-z.

[151] H. Cheng, S. Tang, T. Yang, S. Xu, X. Yan, Accelerating Electrochemical Reactions in a Voltage-Controlled Interfacial Microreactor, Angew. Chemie - Int. Ed. 59 (2020) 19862–19867. https://doi.org/10.1002/anie.202007736.

[152] Y. Li, X. Yan, R.G. Cooks, The Role of the Interface in Thin Film and Droplet Accelerated Reactions Studied by Competitive Substituent Effects, Angew. Chemie - Int. Ed. 55 (2016) 3433–3437. https://doi.org/10.1002/anie.201511352.

[153] J.K. Lee, K.L. Walker, H.S. Han, J. Kang, F.B. Prinz, R.M. Waymouth, H.G. Nam, R.N. Zare, Spontaneous generation of hydrogen peroxide from aqueous microdroplets, Proc. Natl. Acad. Sci. U. S. A. 116 (2019) 19294–19298. https://doi.org/10.1073/pnas.1911883116.

[154] K. Luo, J. Li, Y. Cao, C. Liu, J. Ge, H. Chen, R.N. Zare, Reaction of chloroauric acid with histidine in microdroplets yields a catalytic Au-(His)2 complex, Chem. Sci. 11 (2020) 2558–2565. https://doi.org/10.1039/c9sc06221a.

[155] C. Liu, J. Li, H. Chen, R.N. Zare, Scale-up of microdroplet reactions by heated ultrasonic nebulization, Chem. Sci. 10 (2019) 9367–9373. https://doi.org/10.1039/c9sc03701b.

[156] D. Liu, S. Cito, Y. Zhang, C.F. Wang, T.M. Sikanen, H.A. Santos, A versatile

and robust microfluidic platform toward high throughput synthesis of homogeneous nanoparticles with tunable properties, Adv. Mater. 27 (2015) 2298–2304. https://doi.org/10.1002/adma.201405408.

[157] K.R. Wilson, A.M. Prophet, G. Rovelli, M.D. Willis, R.J. Rapf, M.I. Jacobs, A kinetic description of how interfaces accelerate reactions in micro-compartments, Chem. Sci. 11 (2020) 8533–8545. https://doi.org/10.1039/d0sc03189e.

[158] S. Ciampi, N. Darwish, H.M. Aitken, I. Díez-Perez, M.L. Coote, Harnessing electrostatic catalysis in single molecule, electrochemical and chemical systems: a rapidly growing experimental tool box, Chem. Soc. Rev. 47 (2018) 5146–5164. https://doi.org/10.1039/c8cs00352a.

[159] A.C. Aragonès, N.L. Haworth, N. Darwish, S. Ciampi, N.J. Bloomfield, G.G. Wallace, I. Diez-Perez, M.L. Coote, Electrostatic catalysis of a Diels-Alder reaction, Nature. 531 (2016) 88–91. https://doi.org/10.1038/nature16989.

[160] S.M. Kathmann, I.F.W. Kuo, C.J. Mundy, Electronic effects on the surface potential at the vapor-liquid interface of water (Journal of the American Chemical Society (2008) 130, (16556-16561), J. Am. Chem. Soc. 131 (2009) 17522. https://doi.org/10.1021/ja908142d.

[161] H. Xiong, J.K. Lee, R.N. Zare, W. Min, Strong Electric Field Observed at the Interface of Aqueous Microdroplets, J. Phys. Chem. Lett. 11 (2020) 7423–7428. https://doi.org/10.1021/acs.jpclett.0c02061.

[162] H. Wei, E.P. Vejerano, W. Leng, Q. Huang, M.R. Willner, L.C. Marr, P.J. Vikesland, Aerosol microdroplets exhibit a stable pH gradient, Proc. Natl. Acad. Sci. U. S. A. 115 (2018) 7272–7277. https://doi.org/10.1073/pnas.1720488115.

[163] C. Heinisch, J.B. Wills, J.P. Reid, T. Tschudi, C. Tropea, Temperature measurement of single evaporating water droplets in a nitrogen flow using spontaneous raman scattering, Phys. Chem. Chem. Phys. 11 (2009) 9720–9728. https://doi.org/10.1039/b908555f.

[164] A. Schmidt-Bleker, S. Reuter, K.D. Weltmann, Quantitative schlieren diagnostics for the determination of ambient species density, gas temperature and calorimetric power of cold atmospheric plasma jets, J. Phys. D. Appl. Phys. 48 (2015) 175202. https://doi.org/10.1088/0022-3727/48/17/175202.

3 X-ray photoelectron spectroscopy (XPS) - PAD system

3.1 The characterisation of the XPS technique

XPS uses ultrahigh vacuum chamber where the sample is placed in and exposed to X-ray of a chosen wavelength producing XPS spectra [1]. Photoelectrons are released from the sample surface as a result of X-rays adsorption and have energies with high sensitivity to their chemical states. Notably, photoelectrons ejected from a specific place have intensities which are proportional to the element concentration [2]. These photoelectrons are collected and get analysed according to its energy spectrum where each element has a unique energy that could be matched with the photoelectron spectrum. Thus, XPS is able to measure the elemental composition, empirical chemical formula, electronic state and chemical state of the elements that exist within a material [2,3].

XPS has been applied to various bioengineering and biological field due to the common characteristics between the nanomaterials and the biomolecules for example: some of the biomedical molecules and organisms have the same size of the nanoparticle as well as cells nanostructures influence significantly the interaction between the cells and their environment [4]. In addition, XPS has the ability to characterise the chemistry of materials, providing an advantage over other conventional techniques such as quartz crystal microbalance (QCM), atomic force microscopy (AFM), and surface plasmon resonance (SPR). These techniques are able to provide analysis of the interactions between materials and biomolecules and the interaction kinetics of protein-protein without giving any chemical information [2]. XPS has various advantages characteristics which qualify it to be used for frozen water analysis and other biomedical techniques such as XPS freezing hydration capability, it covers wide range of elements, its surface sensitivity, and its ability to map and make a spatial control.

3.1.1 XPS freeze hydration

Most of biological molecules and bioengineering materials are hydrated, therefore the ability of XPS to freeze wet samples has been investigated. XPS can apply a quick freezing of a sample in its first (load-lock) chamber before moving to

the UHV one. Exposing the sample to UHV at temperature of around -100 ^{o}C causes etching of the ice formed on the surface before lowering the sample temperature to -120 ^{o}C for analysis [2].

3.1.2 The wide range of elements covered

XPS can detect all elements excluding hydrogen and helium. Generally, to identify the existence of proteins and its quantity on a surface, the content of nitrogen on the sample is used as indicator beside detecting other elements such as Zn, Fe, and S [2].

3.1.3 XPS surface sensitivity and depth profiling

XPS sampling depth is indicated by around three times of the inelastic mean free path of the element in case the sample is perpendicular to the detector. This makes XPS a sensitive technique for surfaces investigations and suitable for water contained samples and for biomedical applications. Consequently, XPS can detect overlayers of proteins and biomolecules in addition to determining the thickness of the absorbed films from the element attenuation from the substrate. XPS profile depth depend also on the angle between the sample and the X-ray source. By changing the sample stage angle of inclination, we can get depth profile merely from 2 to 10 nm. This feature enables the uses of XPS in detecting compositional changes with depth in a sample without any destructive effect [2,5].

3.1.4 XPS mapping and spatial control

There is a necessity to put more spatial control on biomolecules for various applications. XPS is capable of mapping chemical state and providing small spot analysis as well as its small spatial resolution below 10 μm, making it more suitable for tissue engineering and other array technologies. To get a reliable measurement, the signal from area around the spot required needs to be reduced. This can be achieved by using a transfer lens to control the area where the photoelectrons are ejected or by focusing a monochromatic X-ray beam on the area of interest [2].

Although all these advantages, characterising nanomaterials, biological samples, water samples and the interaction between them are challenging. These challenges include sample preparation, sample handling, the effect of the environment

and time on the samples, issues attributed to samples susceptible to damage, and other challenges to identify and understand the structure of nanoparticle samples. Consequently, more attention should be paid while preparing, handling, and studying the bionanomaterial samples [4].

3.2 Applications on liquid and samples under humid conditions

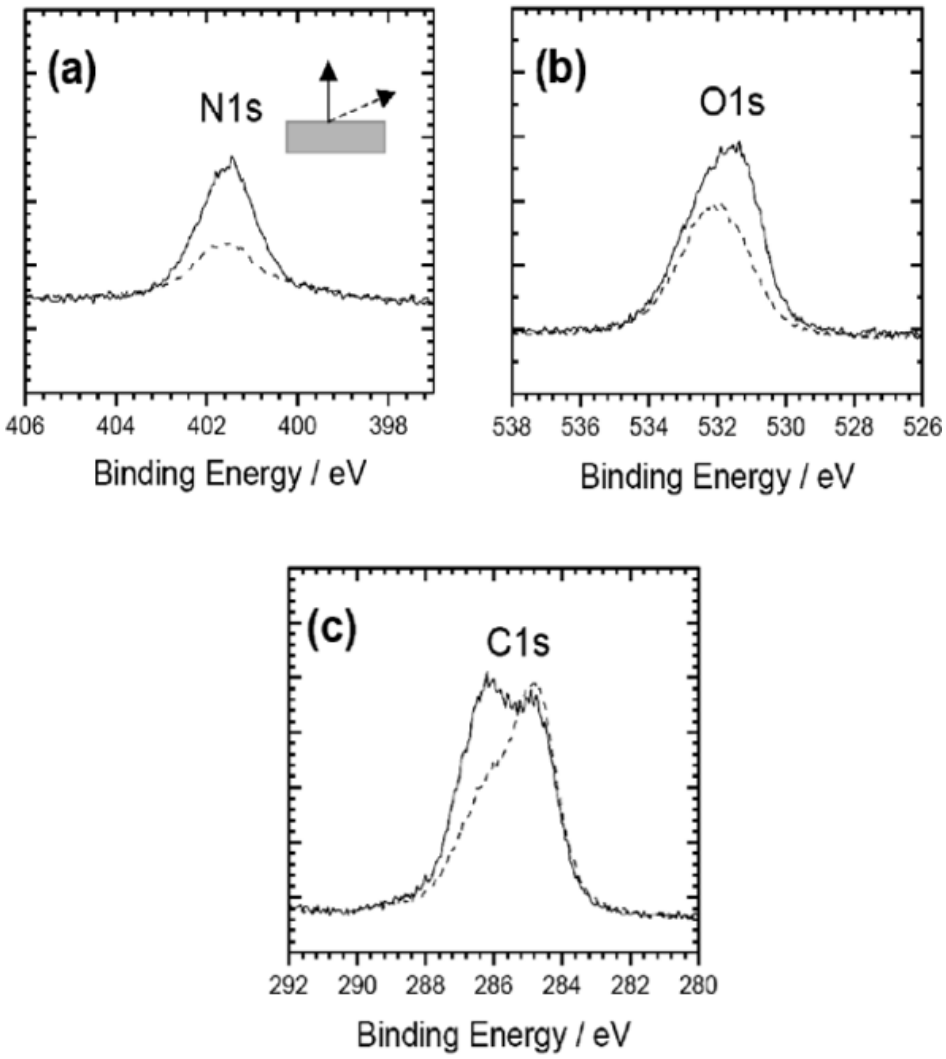

Figure 3-1: The spectrum of XPS for ionic liquid sample (1-ethyl-3-methylimidazolium ethyl sulfate) where the solid and dash lines indicate the 0º and 70º emission angles, respectively [5].

Analysis of liquid solution has a high importance due to the presence of liquid in different materials which interfere in various scientific fields such as biological field analytical chemistry, and porous material applications [6]. XPS was utilised to study

the characteristics of condensed water films on a surface including its structure, thickness, and hydrogen bond changes with the surface and with itself. Owing to XPS ability to measure the chemical properties of the sample, the hydroxyl groups were used for measuring the adsorbed molecular water [7,8]. In addition, the reaction of surfaces with water vapour was investigated. It was found that this reaction changes mostly the properties of the surface such as its reactivity and absorptivity. Moreover, when the humidity increases, this leads to the formation of thin water layer which changes more properties such as the electrical and ionic properties of the surface. Atmospheric pressure XPS (APXPS) is a new XPS technology that operates at elevated pressure and provides high resolution of surface analysis [9,10]. Experimental method was used to study APXPS and the control of the thermodynamic conditions, wettability of water, dissociation, and adsorption. In addition, examples of using APXPS in the applications of water films on oxides and metals were also provided [7,8].

One of low pressure XPS liquid-surface applications is studying the surface composition of ionic liquids, salts with a melting point lower than 100 ^{o}C in a liquid state, at room temperature because of their low vapour pressure [5,11]. The influence of inorganic elements as well as contaminated silicon on the composition of the surface were also investigated. XPS was able to provide the molecular composition of the top ion layer at the UHV/ionic liquid interface by angle-dependant XPS as well as indicating even tiny amounts of impurities by showing surface activity in ionic liquids. Figure 3-1 reveals the ability of XPS to measure liquid surfaces and indicate the dependency of the spectrum intensity on the emission angle, showing that with the bigger angle (70^{o}) XPS gives more details about the surface elemental structure than that of (0^{o}). This indicates that when X-ray beam is perpendicular to the sample, it penetrates therefore, it does not provide much information about the surface. In contrast to the case of higher beam angle, it allows more rays to bounce of the surface providing more details about the sample. This also indicates the possibility of attaining depth profile of the sample by changing the inclination angle of the X-ray beam [5].

Other studies were performed on solid-liquid interfaces in which there were a need to investigate the properties of each part individually: the solid part, the liquid one and the layer between them. XPS was an appropriate tool for this study because

of its chemical and elemental sensitivity with a need to balance between maintaining the surface pressure of the sample above 90-95% of the chamber pressure and constraining the scattering of electrons from the molecules in the gas phase. The AP-XPS studies of solid-liquid interfaces was challenging in adjusting the experimental conditions such as the energy of photons to get a better signal of the photoelectrons coming from the interface as well as preparing the liquid films which need to be thick enough to represent the liquid and thin enough to allow the ejected photoelectrons from the layer in between the solid and the liquid to pass from the liquid to the analyser. XPS was used to examine the solid-liquid interfaces and to get the best range of photon energy which indicates the highest sensitivity of the interface. This range was obtained from the simulation of photoelectron intensities emitted from TiO_2 covered by a thin layer of water using a method called ‟dip and pull″. In addition to a study of the effect of changing the electrolyte pH on the band-bending and the chemical composition of the functionalized TiO_2 surface was performed [12]. AP-XPS is a very new and expensive technique that shows great promise. However, for standard XPS, liquids can only be measured by freezing. For water, this is normally termed crystalline water (ice) or amorphous solid water (ASW) and some XPS studies have been carried out [2,5,7,8]. For biological samples, freeze drying techniques which preserve the biological structure and properties is well developed. For plasma treated water we wish to study not only water (ASW), but the surface chemical conditions induced by the plasma. For this we need fast freezing of the plasma treated liquid. This may be difficult with bulk water but may be possible with microdroplets since their volume is so small.

3.3 Droplet freezing

Ice crystals can be formed when ice nucleation take place in water droplets which involves less existence of particles. Ice nucleation can be categorised as heterogeneous nucleation when the freezing is at a temperature from 0 to -36 ^{o}C and ice nuclei is presented whereas homogeneous nucleation occurs at temperature below -36 ^{o}C, in this case ice is formed automatically without forming ice nuclei [13]. Water droplet freezing has four stages when in contact with a cold surface. First stage is the pre-cooling when the temperature decreases to the nucleation temperature; then the

droplet temperature increases abruptly due to the latent heat released. This is followed by droplet freezing while maintain almost a constant temperature. Finally the droplet temperature decreases further to a temperature close to ambient, i.e. cold surface [14]. The probability of ice nucleation increases by decreasing the temperature where ice can be formed in a droplet due to crystallisation in the presence of a single nucleation event.

Murray et al. [15] developed an experiment to study the kinetics of water freezing where the water phases were monitored by optical microscopy. Video recordings were used to capture the freezing which takes and image every ~40 ms. An equation was provided to calculate the number of droplets remaining in a liquid state with time based on nucleation rate and droplet volume. From this equation and the provided nucleation rate, R_N, at T = 235 K and for droplet volume of 10 μm, an estimate of 40% droplets would be frozen in 1 sec while almost 0% of droplets get frozen in 1 μs. This leads to the conclusion that the freezing rate due to nucleation and crystallisation is slow and not suitable for freezing treated-water droplets for studying short-lived reactive species. Therefore, rapid freezing with a rate faster than their short lifetime would be required. Recent experiments suggest that homogeneous nucleation may not be the only mechanism of freezing at these low temperatures but also surface induced heterogeneous nucleation, i.e. the freezing occurs from the outside [16]. This could be a key factor since XPS studies would only need a surface layer <10 nm thick to be frozen quickly. Estimating timescales for this from [15], the volume is reduced by a factor of 6×10^{-3} and the timescale for freezing 50% of droplets is, ~1 ms, obtained from $t = -\ln(0.5) R_N \times Vol_{surf}$ where R_N is 10^{15} m^{-3} s^{-1} and the surface volume is 3×10^{-18} m^{-3} (10 nm surface layer on a 10 μm diameter droplet). To reach 1 μs, the frozen surface layer thickness would be <0.05 nm. However overall rates could be much faster since freezing occurs by heterogeneous nucleation where the rates are unknown.

There is another option for water freezing which is amorphous solid form of water (ASW) providing non-crystalline ice. The major difference between crystalline and non-crystalline ice is that the molecules in the former are arranged in a regular hexagonal lattice which does not exist in non-crystalline ice. ASW is formed by either rapid freezing of water or by compressing crystalline ice at low temperature. The fast-

cooling rate in the range of milliseconds as well as low temperature below ~130 K are principal factors in producing ASW so as not to allow time for crystals to form. As with crystalline ice for XPS-analysis of short-lived species, freezing the surface first where the plasma liquid chemistry has occurred could be a solution for fast enough freezing. For ASW, a lower temperature is required than for ice. Otherwise, cryoprotectants should be added to the water to increase its viscosity and to prevent crystals formations. The flux of water droplets is another factor affecting the formation of ASW known as the deposition rate where ice crystals are formed on a substrate if the water deposition rate is less than the critical flux which depends on the temperature [17].

The PAD is a specially designed chamber attached to a standard XPS-analysis and sample loadlock chamber. It is meant to allow different plasma systems to be installed to treat solids or liquids and then transfer them directly to the XPS analysis chamber without exposing samples to environment. This is a unique system never built before by any XPS manufacturer. In the design specification for the PAD, it was specified by Ulster design team that the PAD sample stage for plasma treatment and the transfer arm be cooled sufficiently, at atmospheric pressure, so that on arrival at the ultra-high vacuum XPS stage, the water sublimation rate of the sample would be below the allowed leak rate at XPS pressure. This was calculated to require a solid water temperature at the XPS entrance of < -83 ^{o}C. The temperature rise that would occur during transfer from PAD to XPS was then to be determined by manufacturer to establish the maximum temperature allowed at the PAD sample stage. A number of options for active cooling of PAD sample stage via miniature Stirling coolers or biological cryocoolers were requested. The objective was to investigate droplet freezing in flight using cold background gas and deposition onto cold sample stage at its lowest possible temperature or a mixture of both. A second objective was to plasma treat already frozen bulk liquid at various temperatures. However, the manufacturers approved tender only guaranteed the required cold temperatures using a passive liquid nitrogen (LN2) probe design based on their standard product which was specified to reach -150 ^{o}C. Unfortunately, the supplied LN2 probe was unable to reach a temperature below 0 ^{o}C and samples could not be frozen at all due to manufacturing issues leading to be provided a probe not matching with the design specifications. The revised objective was to find a method to obtain bulk liquid sample freezing at

atmospheric pressure inside the PAD for plasma treatment and transfer to XPS. Then the possibility of rapid droplet freezing was to be investigated after that.

3.4 The characterisation of the plasma attachment (PAD)

PAD is a custom-designed vacuum chamber capable of installing different atmospheric plasma devices and samples. It is connected via a gate valve load-lock to the standard sample preparation entry stage, known as Preplock, and from there to the XPS analysis chamber. It is designed as an additional specialised sample preparation stage where samples can be plasma treated and transferred directly to XPS without coming into contact with airborne impurities for the lab. This preparation will be via atmospheric pressure plasma (APP) exposure, either directly or through plasma-liquid interactions, the latter in the form of bulk liquid or in-flight microdroplets. Interchangeable APPs sources can be installed in the PAD leading to a highly versatile facility capable of handling a large variety of samples including inorganic materials, organic, composite, liquid, and biological samples under high-quality environmental control. Our main strategy for overcoming the failure of supplied cooling system to allow for plasma – liquid droplet study is to cool the background chamber gas to as low temperature as possible as well as use the sample cooling stage provided by the manufacturer. Adding the water sample to the cooling stage under atmospheric pressure was not a successful option because the chamber filled with warm gas will halt the formation of ice. Therefore, it is necessary to get rid of this warm gas by pumping and cooling the sample stage as low as possible simultaneously. When minimum temperature reached, pump is turned off and the chamber is backfilled with chilled gas. If water sample is present during pumping it will evaporate so there is a need to find a method of adding water without it leaking into vacuum pump while chamber is at low pressure. Several attempts were made for water sample delivery, but these caused problems with the chamber leak rate and pumping. Finally, injecting a ridiculously small volume of water using a syringe and a Swagelok valve to prevent the leak path was the most successful method. After water sample delivery, plasma treatment can be initiated with a small flow of warm He while maintaining the cooling of the substrate using LN2 and the presence of the cold background gas to increase the probability of keeping the water sample frozen.

3.5 The experimental achievements to date

3.5.1 Droplet freezing PAD configuration

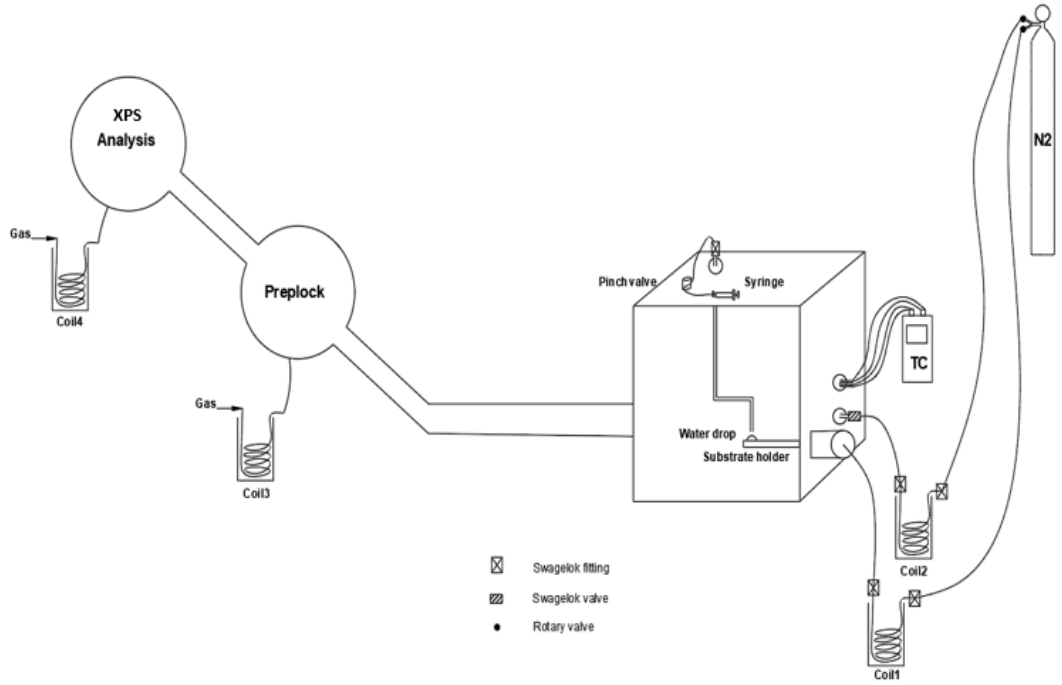

Figure 3-2: Diagram of the PAD-XPS setup and the main components including gas bottle, cooling coils, thermocouples, water sample delivery system and substrate holder.

Diagram, Figure 3-2, for x4 coils and the components involved from bottle to end, including connections and valves also, location of thermocouples. Where "Preplock" is a moderate vacuum load-lock chamber for standard sample entry aiming at ensuring that XPS can remain at UHV (ultra-high vacuum) without exposure to atmosphere. The coils are made of copper and the ones used in the preliminary measurements were provided by the manufacture and have 10 turns each. I later developed the coil design to improve their cooling performance by making handmade coils with higher number of turns formed by a double helical coil of smaller diameter coil inside a larger diameter one. Figure 3-3 shows a picture of the sample stage in the PAD with the block, when PAD is used, samples on the block are transferred using two arms through preplock into XPS as indicted in Figure 3-4. PAD-preplock arm is docked to the block in the PAD, Figure 3-5, and then pulled with the block to the

preplock where the block is docked to the cooled Rotational Stage, Figure 3-6. The Rotational stage should be rotated about 90 ^{o}C then the analysis arm can be docked to the block in the preplock and moved to XPS for analysis.

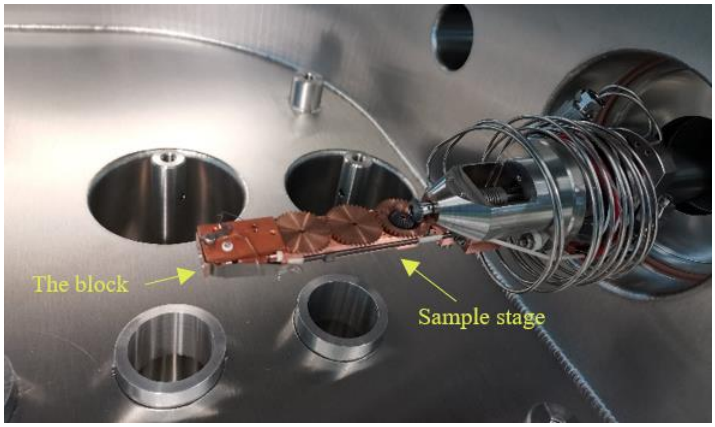

Figure 3-3: The sample stage in the PAD with the block.

Figure 3-4: A photo for the XPS-PAD system including two transfer arms between them and three cooling stages.

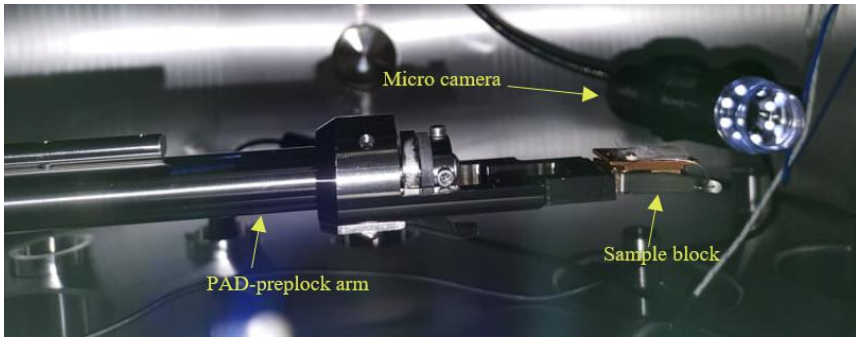

Figure 3-5: Photo of the micro camera and the block docked to the PAD-preplock arm holding a frozen liquid sample .

Figure 3-6: The Rotational Stage of the preplock chamber with a vernier and two sample view points.

3.5.2 Liquid nitrogen (LN2) cooling coils

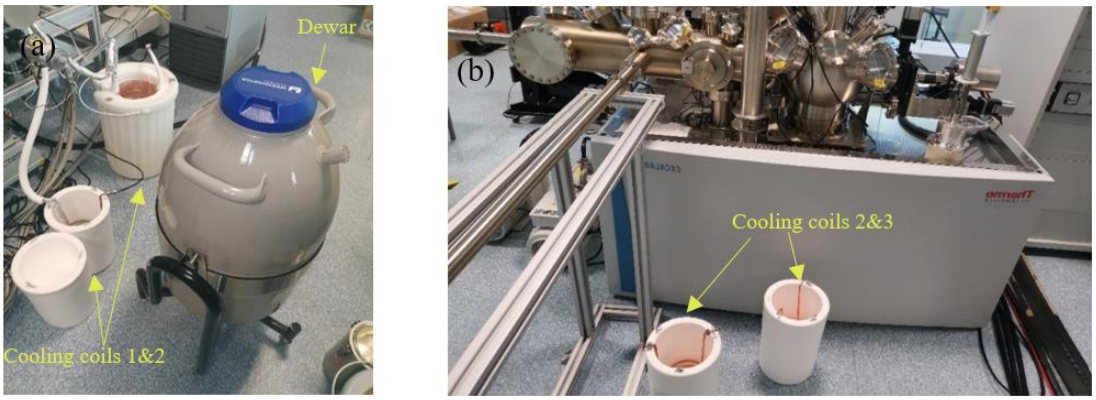

Figure 3-7: The photo in a) is location for coil 1&2 and the dewar with trolly while the photo in b) is for coil 3&4.

- Coil 1: for cooling the substrate.
- Coil 2: for N2 backfill cooling.
- Coil 3: for cooling the preparation chamber.
- Coil 4: for cooling the analysis chamber.

Small hollow cooling coils were supplied with the system to cool the sample on the PAD sample holder, to maintain the sample cold in preplock and in XPS analysis chamber. To chill the background gas another cooling coil system (Coil 2) was designed and evaluated.

For copper coil immersed in LN2, the gas cooling rate is approximately

$$T(t) = T_A + (T_0 - T_A)e^{-t/\tau} \qquad \textit{Equation 5}$$

where T_A is the temperature of the coil (-196 ^oC) and T_0 is the initial temperature of the gas. The time constant, τ, is given by [18]

$$\tau = \frac{m_{gas}c_{gas}}{A_{coil}}\frac{x_{coil}}{2k_{Cu}} \qquad \textit{Equation 6}$$

where c_{gas} is the heat capacity of the gas, k_{cu} is the copper thermal conductivity, x_{coil} is the thickness of the coil wall and A_{coil} is the cross-section area of the coil. The cooling time is the residence time of the gas in the coil in contact with LN2 which depends on the flow velocity and m_{gas} is the mass of N2 gas within the cooled section of coil. From Equation 6, τ = 7184.4 ^{o}C for m_{gas} = 28.02 g/mol = 627.65 g/L = 265161 g, c_{gas} = 1.04 J/ g k, A_{coil} = 2.83 x 10^{-5} m where R= 0.003 m, x_{coil} = 15 x 10^{-5} m and k_{cu} = 98 W/m•K. T(t) from Equation 5 and for T_0 (room temperature) = 23 ^{o}C is:

$$T(t) = -196 + (219)e^{-t/7184.4} \qquad \textit{Equation 7}$$

Where t = $\frac{L_{coil}\, x\, A_{coil}}{Q}$ knowing that L_{coil} is 1.5π m and 7.5π m for a coil with 10 and 50 turns for comparison, respectively where the diameter is 15 cm and Q is the N2 flow rate in m^3/s. Figure 3-8 shows the effectiveness of increasing the flow rate of the cooled N2 gas in changing the cooling probe temperature and provides a comparison between the performance of the actual coil of 10 turns to the performance of a predicted coil with 50 turns using Equation 7. The figure demonstrates negligible effect of increasing the gas flow on the cooling of the probe and the sample. Therefore, increasing the N2 gas flow rate is not advisable option to speed up the cooling rate of the probe and the sample, especially since this option would significantly increase the gas consumption. In addition, for the provided coil with 10 turns at the smallest flow rate of 1 slm, it would take approximately one hour to fill the PAD chamber with N2 (650 mm x 650 mm x 1000 mm, 420 litres).

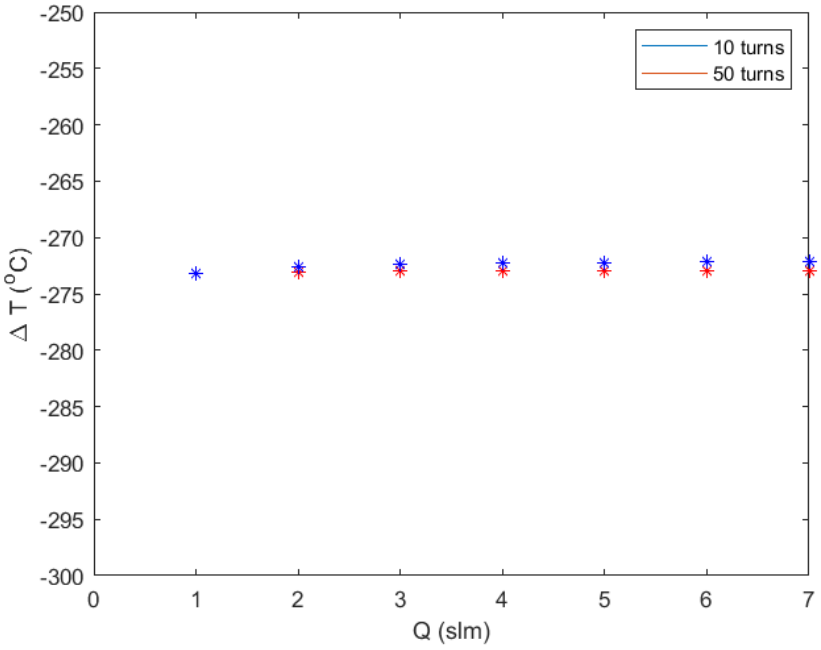

Figure 3-8: The change in copper coils temperature versus cooled N2 gas flow rate for coils with 10 turns and 50 turns.

I made custom-designed double helical coils with higher number of turns (~50 turns), Figure 3-9, as a trial to speed up the cooling and reduce the LN2 consumption. The cooling stage temperature was monitored using both 10 turns and 50 turns coils and a drop from room temperature to -35 ^{o}C and -110 ^{o}C using each of them, respectively was observed. This indicates a significant increase in the cooling rate when using 50 turns compared to 10 turns coil. Therefore, I changed the coils provided with the system (coil 1 and coil 2) by the custom-designed coil with 50 turns and used in all the following measurements. Monitoring the performance of the new coil 2 in changing the PAD chamber's temperature, the temperature decreased 8 ^{o}C from room temperature with the cooled LN2 backfill in 15 minutes. As per the above measurements, increasing the number of coils is expected to increase the cooling rate however, this means a higher consumption rate of LN2 which is not a cost effective option.

Figure 3-9: A handmade custom-design double helical coil with 50 turns.

If the final cooling rate is not good enough it may be necessary to try (i) have multiple double coils in series in individual dewars, needing a much larger amount of LN2 (ii) operate at much lower flow - therefore many hours required to fill chamber and more LN2, (iii) add insulating jacket to the PAD chamber, (iv) use microbore piping – very small diameter which would reduce mass and area in equation 2 but might allow much higher number of turns so longer. Another solution originally considered was to place/inject liquid N2 into PAD chamber, then pump down. The LN2 volume after evaporating would be enough to bring chamber to atmospheric pressure with cold gas. This would also reduce the need for a large volume of coil LN2. To do this, the safety aspects would need to be evaluated carefully and safety systems installed. This was not possible up to now. Finally the ultimate (and expensive) solution would be to install a miniature high performance Stirling cooler as originally request (e.g. **https://www.sunpowerinc.com/products/stirling-cryocoolers/cryotel-cryocoolers**). This would require design to allow make/break contact with travelling sample stage and if possible, locate within chamber so that travelling vacuum port is not needed.

3.5.3 Notes on thermocouples

Figure 3-10: The photo shows the white wire as TC1 and the blue wire as TC2.

- TC 1: for temperature measurements of the room inside the PAD (changes with backfill), Figure 3-10.
- TC 2: connected to the block via the PAD port as a secondary technique to measure the substrate temperature knowing that the primary device is the Eurotherm controller, Figure 3-10.

3.5.4 Experimental methods

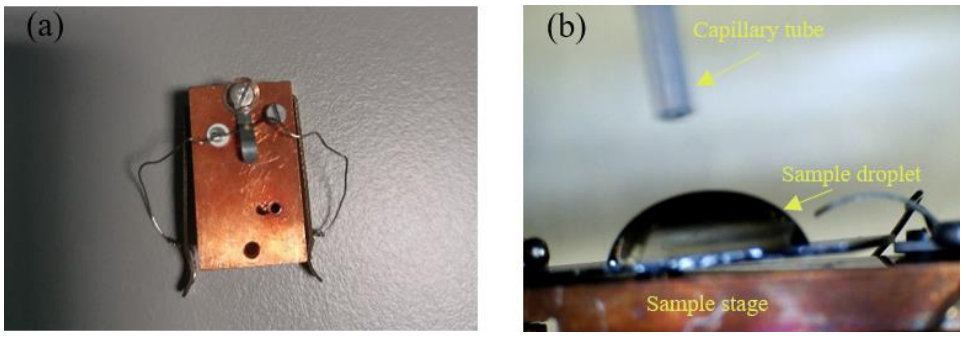

Figure 3-11: a) The sample stage while outside the PAD and b) is the sample stage with a water sample inside the PAD.

The experiment starts by turning on the backing pump with target pressure 1 - 10 mbar and start cooling the sample stage with LN2 simultaneously. The backing pump is turned off after reaching the lowest possible temperature for the sample stage then PAD chamber backfilling is started through cooled LN2 (coil 2) with minimum possible flow value to increase the filling time and to minimise the increase in the sample stage temperature as a result of the backfilling gas. Backfilling is then off followed by the water sample transfer to the sample stage, Figure 3-11. The water sample is loaded manually to the block by opening the pinch valve and pushing the required water amount by a syringe. A microcamera is installed inside the PAD to monitor the frozen sample and x2 pressure relief valves were installed for safety. Once a frozen sample is achieved, the PAD should be pumped down again to vacuum by turning on the backing pump to the target pressure (1 -10 mbar) then the turbo pump until reaching pressure ($1x10^{-5}$ - $10x10^{-5}$ mbar) or lower. This pressure allows opening the gate between the PAD and the preplock to prepare the sample for the transfer to the preplock then the XPS analysis chamber while both at the standard pressure of ~10^{-7} mbar. The pressure in the PAD is a critical factor and if it did not reach 10^{-5} mbar or lower, this indicates a leak in the chamber which should be checked and fixed before opening the gate between the PAD and the preplock.

The leak was one of the major challenges in our system, it was recognised from the PAD pressure measurements with the turbo pump which had higher pressure than its specifications (10^{-5} -10^{-7}mbar) in addition to the turbo interface which indicated its working capacity of 70%. The minimum pressure with turbo was 1.7x 10^{-3} mbar after an hour which is an indication for a leak. Reaching lower pressure is important to reduce the pressure on the preplock turbo when opening the gate valve between the PAD and preplock. The proposed solution was by removing all items inside the PAD as well as removing all installed ports and replacing them by blanks. The system was assessed while all ports have blanks and the turbo indicated working capacity of 99%. Each port was installed individually while other ports have blanks and pressure measurements were taken to identify the source of the leak. Pressure measurements indicated the water feedthrough as the major reason for the leak. Therefore, a change in the design was required and a Swagelok valve was added to the port to prevent the leak.

3.6 Results

In this section experimental results will be presented for the different attempts to achieve a frozen water sample.

3.6.1 Experiment with cooling at higher pressure near atmospheric (ATP).

Initial measurement of the block temperature while the PAD chamber is near ATP were taken. Figure 3-12 demonstrates the response of the LN2 probe at the sample stage and shows a minimum temperature reached of 15 ºC after an hour. This trial did not work for cooling the sample stage to a freezing temperature due to the large mass of block to be cooled, Figure 3-13, and the effect of the warm chamber air resisting the cooling process.

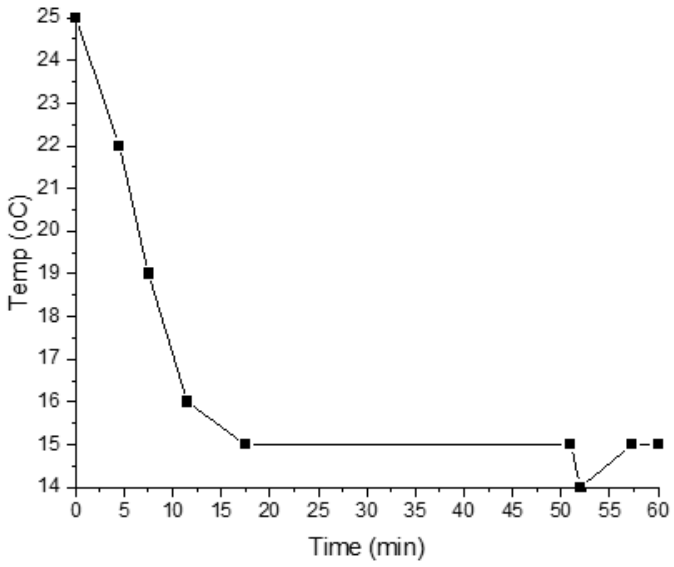

Figure 3-12: Initial measurements of the block temperature vs time at ATP.

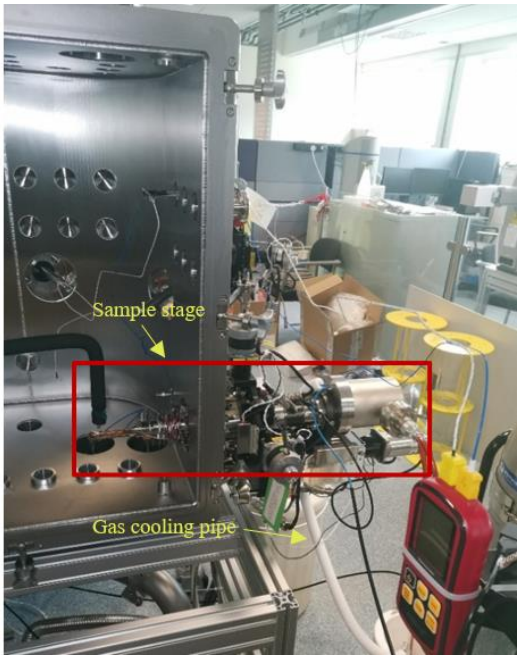

Figure 3-13: A picture of the sample stage and the gas cooling pipe.

3.6.2 Experiment with cooling while the PAD under vacuum

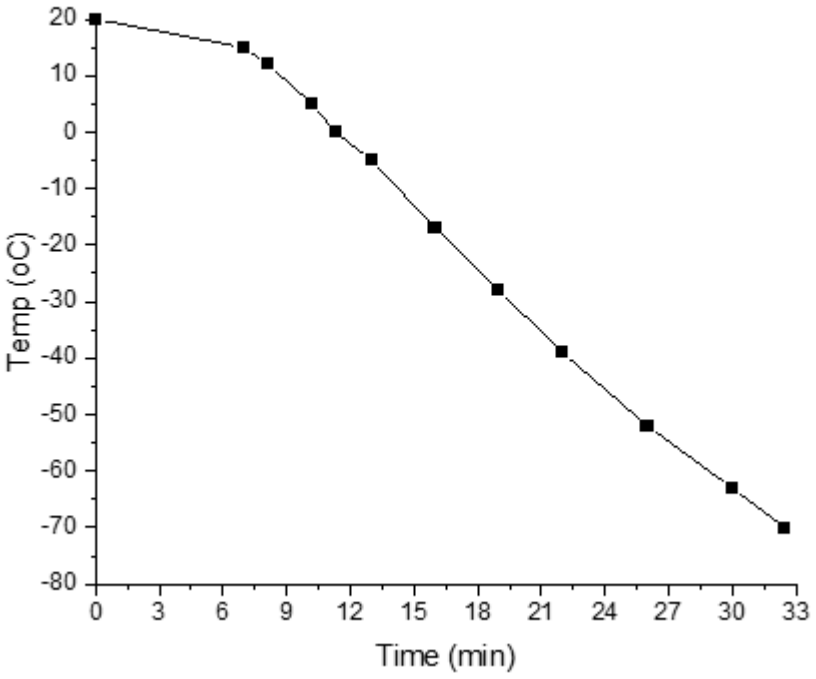

Figure 3-14: The block temperature vs time under vacuum of around 1mbar.

The LN2 probe response to the cooling was monitored when the PAD chamber was pumped down. Figure 3-14 shows the block temperature versus time at pressure near 1mbar where the temperature reached -70 ^{o}C after around 30 mins. This pressure was achieved by using both backing pump and turbo pump. The comparison between the cooling time at ATP and 1mbar demonstrates that the large volume of gas in the chamber is a major factor and even pumping it out is not enough to reach a low cooling temperature results also the chamber walls would heat the gas. In addition, this comparison shows that LN2 probe performance is unsatisfactory at ATP and not performing to specification (i.e., 190K when entering the XPS chamber) even under vacuum. So next, there are few options to be conducted:

1. Cool the background gas to get minimum temperature at ATP.
2. For transfer, perform additional cooling under vacuum then transfer to preplock and in preplock cool further to 190K if necessary.

3.6.3 Experiment of backfilling the PAD

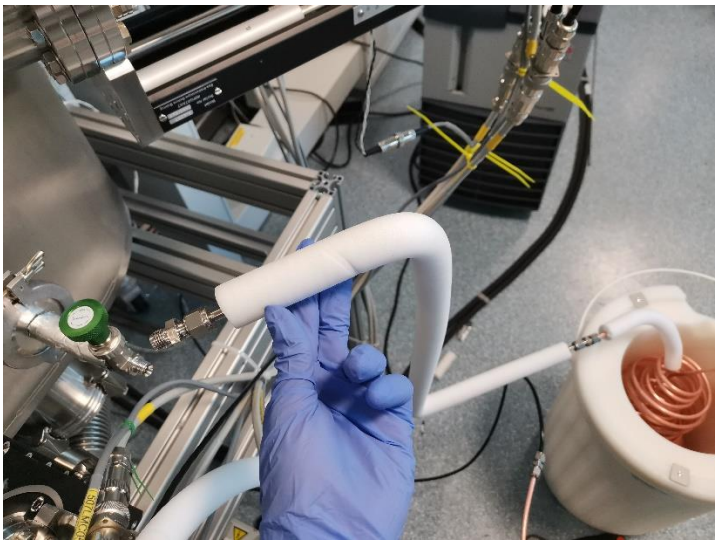

Figure 3-15: The backfill connections and the LN2 coil container.

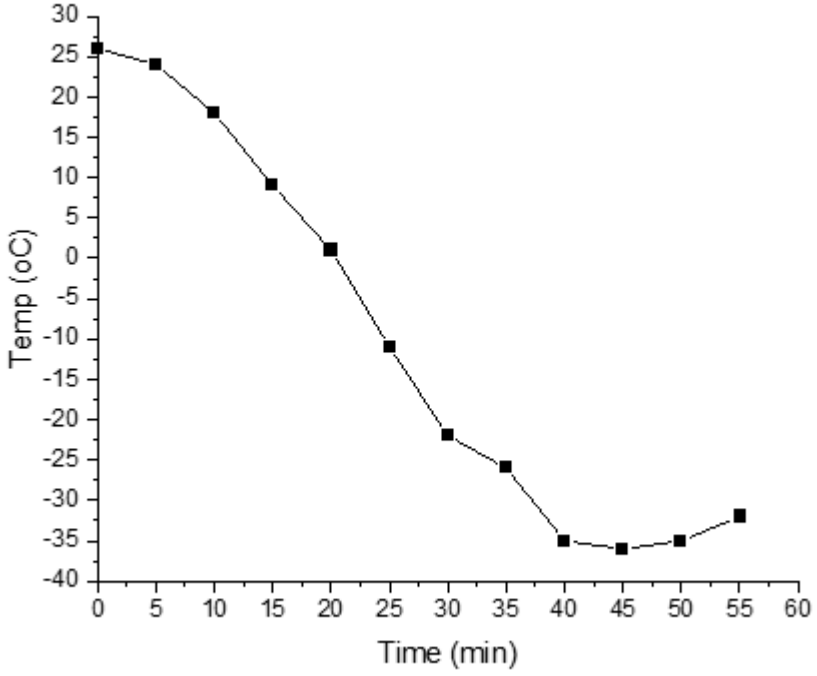

Figure 3-16: Temperature vs time after installing the backfilling port.

By the end of each experiment run, there is a need to bring the chamber up to ATP and to be able to open the door for further experiments. After turning off both pumps, the PAD is very slow returning back to ATP naturally as it took ~15 mins for the pressure to rise by 0.01 mbar. Even when the PAD reach ATP, the door cannot be opened and may need to be left overnight before opening it. This shows the need for connecting a port that can be used for backfilling the chamber to speed up the process of opening the door at ATP and to cool the background gas. Figure 3-15 shows the connections used between the LN2 containers and the PAD port which includes cooling coil of copper (coil 2), a metal tube connection and a valve.

An attempt was made to operate at higher pressure (lower vacuum), which affects the experiment running time, and experiment the cooled background gas. The pressure of the PAD reached 8.7 mbar after 40 mins by the backing pump and then cooling of the block was turned on. Temperature measurements were taken for the block, Figure 3-16, and minimum temperature observed was -36 ^{o}C after ~45 mins. After 1hour, backing pump was turned off and cooling substrate was continuing

while starting backfilling with cooled gas passing through LN2 via the new port, Figure 3-15. The backfill took around 6 mins to reach ATP and caused an increase in the block temperature by ~10 ^{o}C. This comes to a conclusion that the high vacuum is essential for reaching lower temperatures and the effect of the cooled background gas in negligible compared to the LN2 cooling for the sample block.

3.6.4 Introduction of water sample

a	b	c	d	e	f	g	h	k
14.05	24.03	1.2	2.34	8.95	14.00	23.96	19.06	6.87

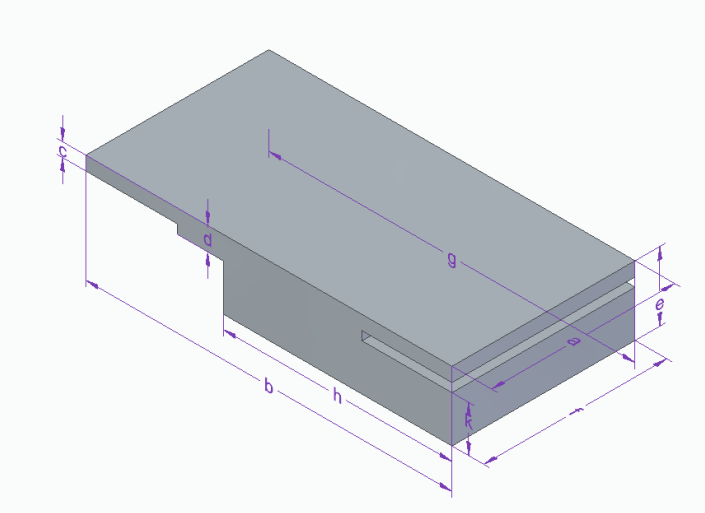

Figure 3-17: The block dimensions in mm.

The procedure for introducing a water sample on the block inside the PAD is:

1. Pump down.
2. Sample cooling via LN2 probe to minimum temperature.
3. Pump off.
4. Add cold gas while still cooling with LN2 probe.
5. Add small volume water to container on sample stage.
6. Continue cooling until water freezes.
7. Turn off cold gas and pump down – ready for transfer.
8. Transfer to preplock.

The design of connections for water sample delivery had many challenges such as:

(i) Need to inject a small volume but need a long tube to get from inlet to sample stage.

(ii) Need to seal the water port and pipe when chamber under vacuum. The syringe does not provide a vacuum seal.

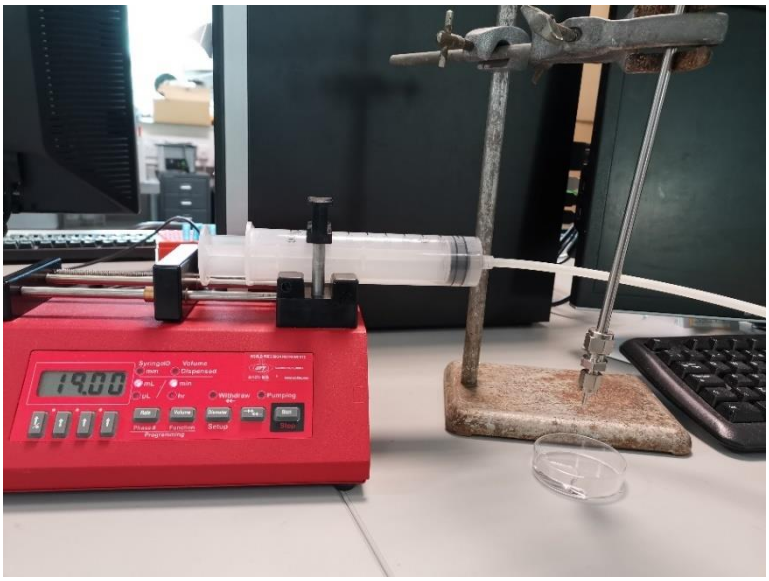

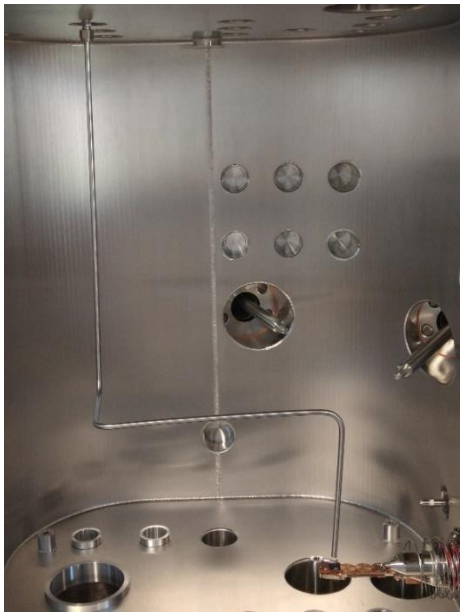

Figure 3-18: the top photo is for a syringe pump for water sample delivery and lower is a 6 mm SST tube from inside positioned over the block.

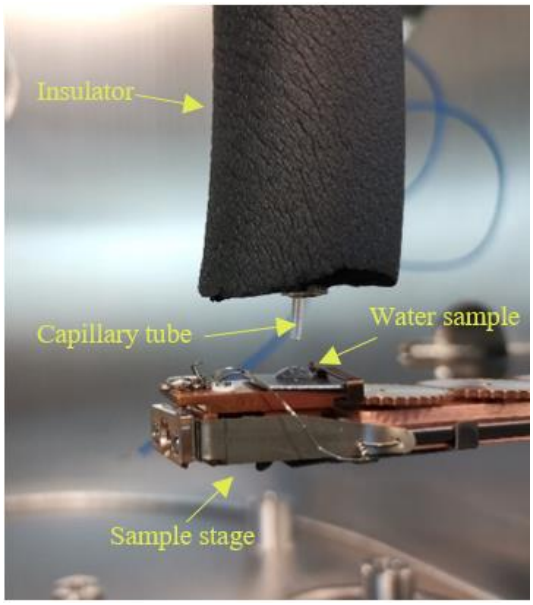

Figure 3-19: The water sample delivered by a teflon capillary tube inside the 6 mm SST tube which is surrounded by heat insulator.

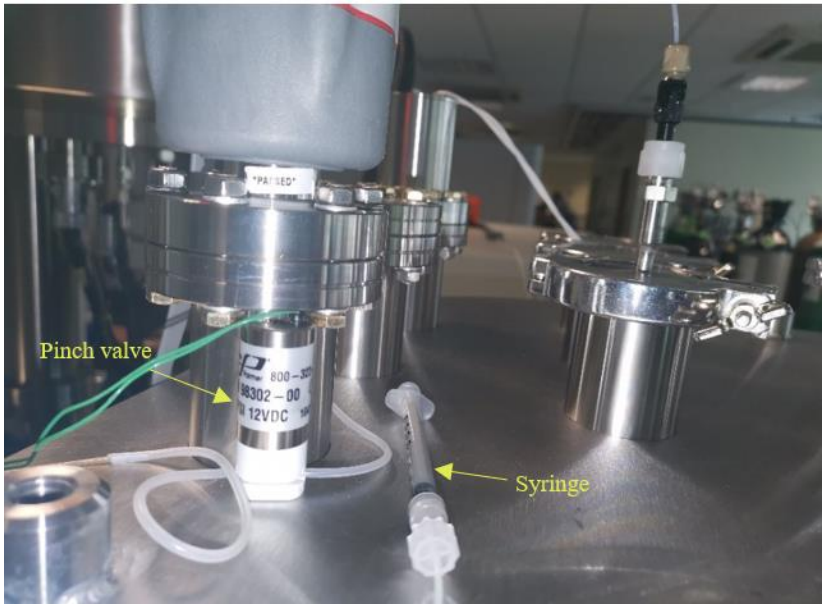

Figure 3-20: A syringe to load the water sample and a pinch valve to control the flow.

Figure 3-21: Swagelok valve to control the leak.

The initial design was attaching a valve from outside to a port with 6mm pipe and connecting a flexible tube on inside. This design was not suitable practically because the cooling block has a small dimension of 14 x 24 mm, Figure 3-17, and it is not possible to fix a flexible tube exactly above the block especially with the high vacuum. Another design was applied by using a syringe pump outside and a SST 6 mm tube inside the chamber, Figure 3-18. This was better in positioning the SST exactly above the block, however, the 6 mm pipe was big and caused a splash of the water on the block and in the chamber. In addition, getting only one droplet using the syringe pump was hard and not easy to control. Less control over the water amount delivered inside the chamber may cause additional unneeded water to be added to the chamber which would affect the vacuum and the functionality of the pumps. Other number of different approaches were attempted but these resulted in either poor vacuum, less control, and/or poor temperature results. The final solution is having a very narrow capillary tube of 0.02in inner diameter passing through the 6 mm SST tube inside the PAD to reduce the water exit diameter and to control the water to be on the block, Figure 3-19. The SST pipe is connected to a pinch valve outside the PAD to control the flow leak and is connected to a syringe which has been tested and experimented to load only the exact amount of water required as shown in Figure 3-20. A final modification was made on the design was by adding a Swagelok valve on the

port from outside to control the leak, Figure 3-21. Then the temperature of the docking stage in the PAD was recorded using external TC2 inserted in the centre of the rotating gear, Figure 3-22. The temperature dropped from room temperature to -115 ^{o}C in two hours but after this, the temperature started to increase slowly again during the third hour and that might be due to saturation. However, the target is to achieve a frozen liquid sample which can be obtained at any temperature below zero. Therefore, the recommended cooling running time is below 1 hour to achieve a frozen liquid sample, Figure 3-23, without wasting extra unnecessary time or high amount of liquid nitrogen.

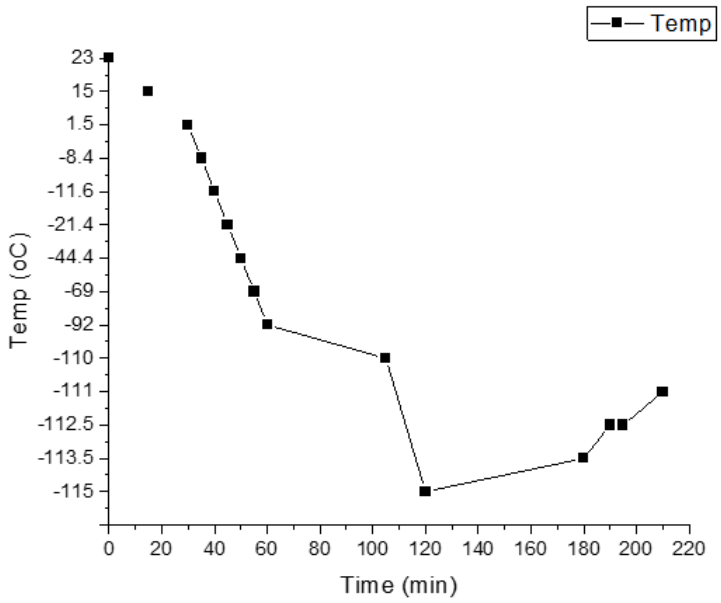

Figure 3-22: Temperature measurements after removing the water feedthrough indicating drop in the temperature to -115 ^{o}C in two hours followed by a slow increase in the temperature, most likely, due to saturation.

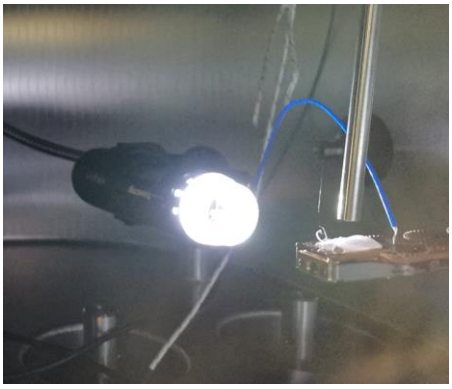

Figure 3-23: A frozen water sample inside the PAD and the blue wire is a thermocouple for measuring the block's temperature.

3.6.5 Pressure – time chart

The PAD reaches 1 mbar from ATP when backing pump is on after around 30 mins, followed by vacuum increase by turning the turbo pump on. After ~ one hour from the start of the experiment, the pressure decreased to 4.7 x 10^{-5} mbar, Figure 3-24.

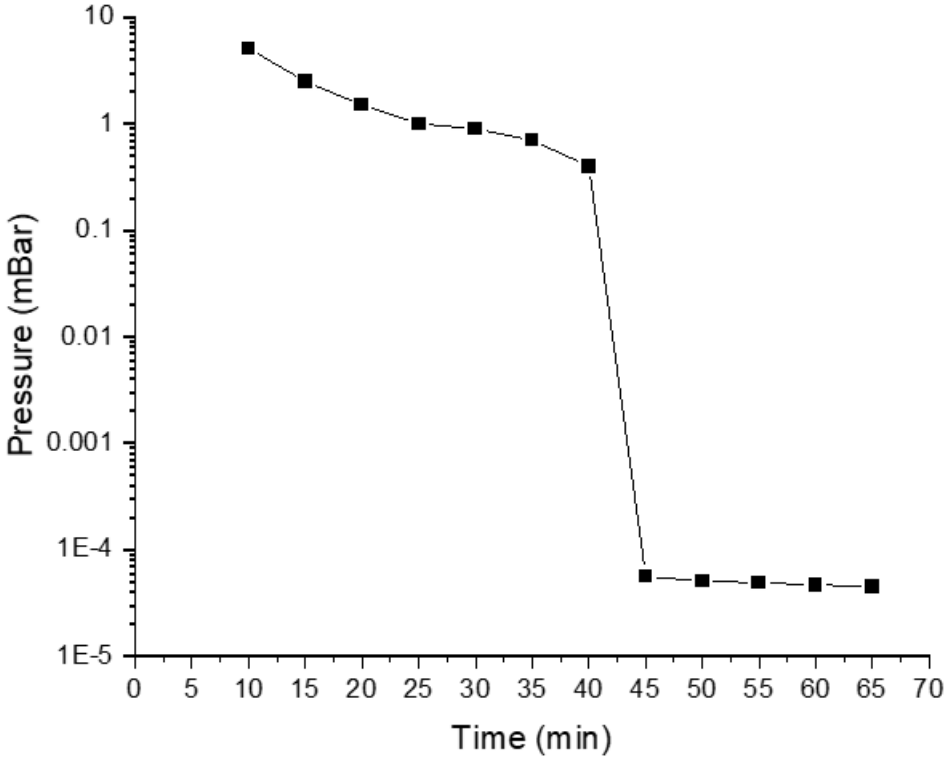

Figure 3-24: PAD pressure vs. time with both backing pump and turbo pump.

3.6.6 Sample transfer to preplock

Figure 3-25: A trial of measuring the temperature inside the preplock using IR probe and BAF2 transparent window.

Sample transfer to the preplock encountered many challenges including:

(i) The transfer arm is not actively cooled except by the cold gas therefore the liquid will start heating up once step the transfer is commenced
(ii) No internal temperature measurement possible from when sample is undocked from PAD cold stage until it reaches XPS

An attempt to use an IR probe through an IR transparent window (MgF2) fixed on a preplock port for temperature measurement inside the preplock, Figure 3-25, was carried out. This trial was unsuccessful, and the temperature measured was around room temperature which is not an indication of the block temperature. Another proposed solution was to insert a thermocouple into preplock; however, this was not attempted as it was not allowed under warranty conditions. Alternatively, experimental trials were carried out to judge whether the frozen sample will exist when it is been moved to preplock or not. Although the PAD-preplock transfer arm cannot be cooled, it can keep the water sample frozen for around 15 mins or a little longer. This result has been proven by a picture of the frozen sample from the preplock window as depicted in Figure 3-26.

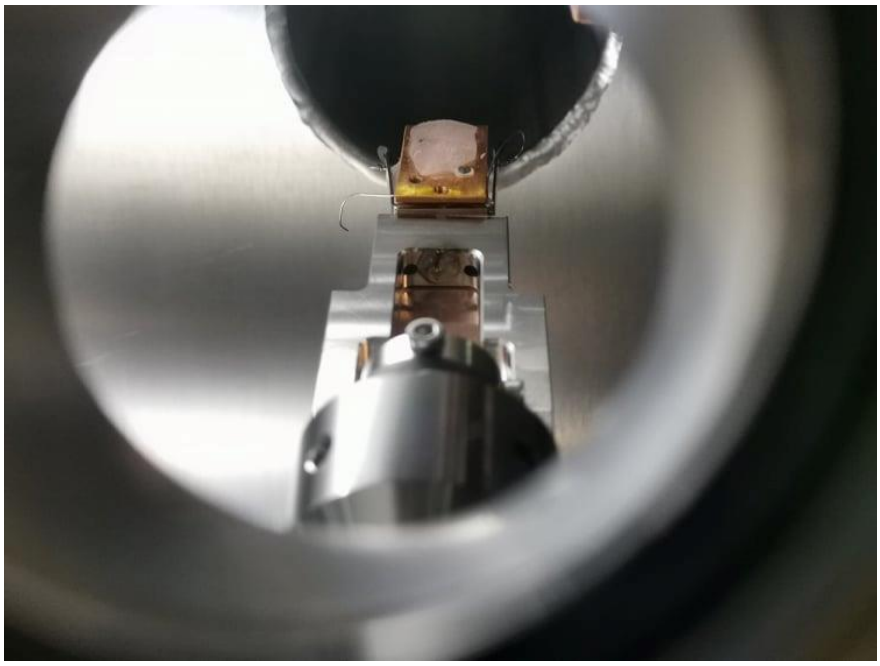

Figure 3-26: A picture of the frozen water sample taken from the preplock window.

3.7 Conclusion

In conclusion, after many attempts, a successful design has been achieved to provide a frozen water sample while the PAD was under high vacuum. The minimum temperature obtained on PAD was ~ -115 ^{o}C and can be achieved after an hour, approximately. In addition, the frozen sample has been successfully transferred to the preplock and proven to stay frozen for around half an hour from the minute it leaves the cooling stage in the PAD which should be enough time to be docked on the rotational stage and to be transferred to the XPS analysis unit. However, the transfer time should be kept as minimum as possible to reduce the possibility of the sample to get melt. The plasma treatment time are estimated to be in minutes, with the transfer time an overall estimate of the entire process time will be below an hour and half. The full process would consume around 25L of LN2 that would be used in the four coils.

Next step would start by fixing the transfer arm. The cooling in the preplock and XPS have been assumed to be working properly, however experimental trials should be done to check their cooling efficiency. Installation of the plasma system may encounter few challenges such as locating the plasma capillary tube exactly above the sample. Also, a high control on the plasma parameter such as gas flow and power are important to maintain the plasma temperature under control in order to keep the sample frozen during and after the treatment. Although the final design presented of water sample delivery to the cooling stage in the PAD was successful, it requires a high control over the amount of water pushed by the syringe. Further improvement can be done by changing the 6 mm SST with a smaller diameter and using the suitable fittings to connect it with the 6 mm water feedthrough port.

3.8 References

[1]XPS Basics - The XPS Library of Monochromatic XPS Spectra, (n.d.). https://xpslibrary.com/xps-basics-2/ (accessed July 25, 2022).

[2]S.L. McArthur, G. Mishra, C.D. Easton, Applications of XPS in biology and biointerface analysis, Surf. Anal. Tech. Biol. (2014) 9–36. https://doi.org/10.1007/978-3-319-01360-2_2.

[3]Thermo Fisher Scientific Inc., Thermo Scientific XPS: What is XPS, Thermo Sci. XPS Simpl. (2013) 1–4. https://xpssimplified.com/_whatisxps.php (accessed May 16, 2022).

[4]D.R. Baer, M.H. Engelhard, XPS analysis of nanostructured materials and biological surfaces, J. Electron Spectros. Relat. Phenomena. 178–179 (2010) 415–432. https://doi.org/10.1016/j.elspec.2009.09.003.

[5]J.M. Gottfried, F. Maier, J. Rossa, D. Gerhard, P.S. Schulz, P. Wasserscheid, H.P. Steinrück, Surface studies on the ionic liquid 1-ethyl-3-methylimidazolium ethylsulfate using X-ray photoelectron spectroscopy (XPS), Zeitschrift Fur Phys. Chemie. 220 (2006) 1439–1453. https://doi.org/10.1524/zpch.2006.220.10.1439.

[6]D. Shah, D.I. Patel, S. Bahr, P. Dietrich, M. Meyer, A. Thißen, M.R. Linford, Liquid water, by near-ambient pressure XPS, Surf. Sci. Spectra. 26 (2019) 024003. https://doi.org/10.1116/1.5119259.

[7]H. Bluhm, Photoelectron spectroscopy of surfaces under humid conditions, J. Electron Spectros. Relat. Phenomena. 177 (2010) 71–84. https://doi.org/10.1016/j.elspec.2009.08.006.

[8]Héloïse Tissot, Thesis of: Beyond the gap of pressure : XPS studies of interfaces at near ambient pressures, l'UNIVERSITE PIERRE ET MARIE CURIE, 2014.

[9]C. Matter, A. Manuscript, Ambient pressure photoelectron spectroscopy : Practical considerations and experimental frontiers Manuscript version : Accepted Manuscript Ambient Pressure Photoelectron Spectroscopy : Practical

Considerations and Experimental Frontiers, (2017) 0–71.

[10] V. Pfeifer, M. Hävecker, R. Wang, A. Centeno, A. Zurutuza, Atmospheric pressure X-ray photoelectron spectroscopy apparatus : Bridging the pressure gap, (1835).

[11] S. Seo, J. Park, Y.C. Kang, Chemical Analysis of Ionic Liquids Using Photoelectron Spectroscopy, Bull. Korean Chem. Soc. 37 (2016) 355–360. https://doi.org/10.1002/bkcs.10683.

[12] S. Seo, J. Park, Y.-C. Kang, Chemical Analysis of Ionic Liquids Using Photoelectron Spectroscopy, Bull. KOREAN Chem. Soc. Chem. 220 (2006) 1439–1453. https://doi.org/10.1524/zpch.2006.220.10.1439.

[13] Formation of Ice Crystals, (n.d.). http://data.cas.manchester.ac.uk/micc/formation of ice crystals.htm (accessed July 13, 2022).

[14] A. Wei, Z. Yang, L. Tang, B. Xiong, P. Wang, Z. Jin, Temperature measurements in the freezing supercooled water droplet by utilizing molecular tagging thermometry technique, Rev. Sci. Instrum. 93 (2022) 074901. https://doi.org/10.1063/5.0090429.

[15] B.J. Murray, S.L. Broadley, T.W. Wilson, S.J. Bull, R.H. Wills, H.K. Christenson, E.J. Murray, Kinetics of the homogeneous freezing of water, Phys. Chem. Chem. Phys. 12 (2010) 10380–10387. https://doi.org/10.1039/c003297b.

[16] H. Xue, Y. Fu, Y. Lu, D. Hao, K. Li, G. Bai, Z.C. Ou-Yang, J. Wang, X. Zhou, Spontaneous Freezing of Water between 233 and 235 K Is Not Due to Homogeneous Nucleation, J. Am. Chem. Soc. 143 (2021) 13548–13556. https://doi.org/10.1021/jacs.1c04055.

[17] K.P. Stevenson, G.A. Kimmel, Z. Dohnálek, R.S. Smith, B.D. Kay, Controlling the morphology of amorphous solid water, Science (80-.). 283 (1999) 1505–1507. https://doi.org/10.1126/science.283.5407.1505.

[18] S.P. Sukhatme, A TEXT-BOOK ON HEAT, Lancet. 223 (1934) 116.

https://doi.org/10.1016/S0140-6736(01)03154-3.

4 Plasma gas temperature

Work is published [1]

4.1 Introduction

Continuous and reliable measurement of gas temperature in atmospheric pressure plasmas (APP) is critical for future applications in plasma medicine, food, and agriculture as well as nanomaterials synthesis. APP systems cover a wide variety of configurations, geometries, and temperature ranges. In non-thermal equilibrium APPs, there is generally a desire to maintain temperatures as low as possible. However, there is also an understanding that gas temperature can be sensitive to several factors that are rarely well-characterised or controlled, especially with the inclusion of molecular gases and water as environmental feedback factors. Gas temperature increase in APPs is due to the high electron and particle collisionality of these systems [2]. Most chemical and combustion reactions are strongly dependent on gas temperature [3], as are surface reactions and neutral radical distributions and their kinetic [4,5]. Additionally in many biomedical and material applications a controlled heat load is required for the treatment of heat sensitive surfaces e.g. wound tissue and polymers [6]. Issues such as feedback process control, process stability/repeatability, regulatory, or end-user approval, require a capability for inline monitoring of temperature and rapid response to fluctuations or thermal runaway. The various techniques to measure gas temperature include optical emission spectroscopy (OES) [1], [6]–[15], infrared thermometry [2,17–19], millimetre wave interferometry [20] Schlieren [2,6], Rayleigh scattering [21,22], thermocouple [2,11,23,24], and fibre optic based thermometry [25,26]. These have been applied to a varying degree in different plasma systems including plasma torch [15,27,28], dielectric barrier discharge [2,14,16,19,20], plasma jet, [6,8,9,17,21,25,28,29], gliding arc discharge [3,18,26], and glow discharge [22].

4.2 Measurement of plasma gas temperature

The main techniques and principles used to obtain estimates of the gas temperature divide into lab and in-situ techniques. The main lab techniques are measurement of line profiles technique, Raman and Rayleigh scattering and optical emission spectroscopy (OES). While the major in-situ techniques are thermocouples (TC), fibre optic probes (FO), and thermal imaging by IR sensors and IR cameras.

4.2.1 The main lab techniques

4.2.1.1 The line profile measurement technique

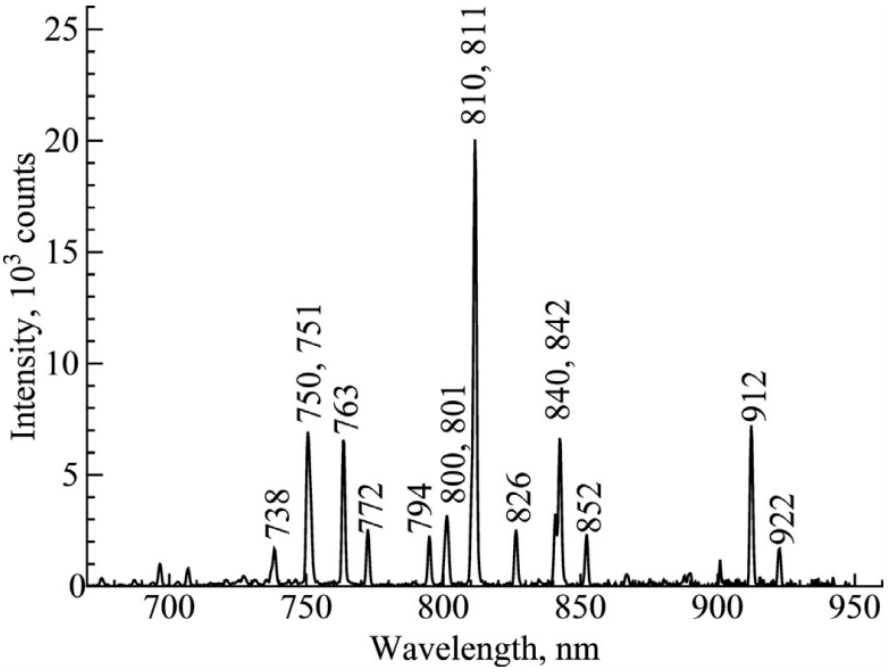

Figure 4-1: Standard spectral emission of Ar plasma [30].

The line profile measurement technique considers the radiation emitted due to the energy difference between two levels at a specific wavelength in molecular and atomic transitions which provides a range of frequencies with nonzero linewidth. Many external conditions may affect the atomic radiation such as atomic collisions and movement of particles around the atom causing shift in the spectral line from the wavelength centreline [31]. Changes in the intensity of the spectral lines is mainly

caused by changes in electron temperature. While the change in the electron temperature affects the electron energy distribution function which changes the electron densities at the specific energy relevant to each line therefore, higher number of electrons result in higher excitations. Spectral line intensity also depends on the electron density and excitation energy as the excited electrons within the atom at high energy state release energy moving to the lower energy state. The released energy equals to the energy difference between the two states and result in emission line. The intensity of emission at a specific line is higher if the electron density and electron temperature are higher which lead to excitation of more electrons. Atomic lines were used to provide an estimate of argon (Ar) plasma temperature variation with RF power at wavelengths 810.37 nm and 811.53 nm from the standard spectral emission of Ar plasma [32]. All OES measurements mentioned in this chapter have been referenced from the literature, including from the same plasma device as used here, in order to compare with the IR sensor technique developed for measuring the gas temperature.

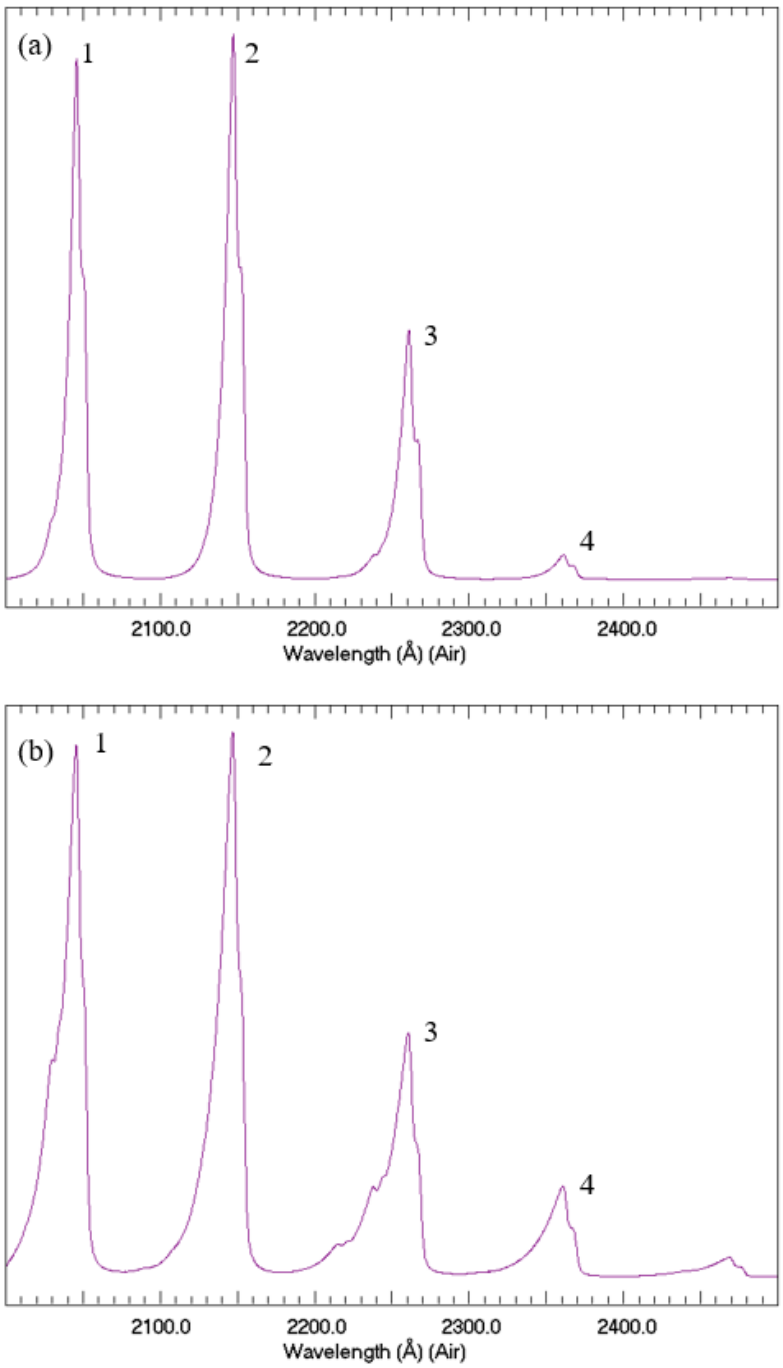

Figure 4-2: The NO (A-X) spectrum versus wavelength generated from LIFBASE software a) for set temperature of 300 K and b) 2000 K, showing width increase for each peak by increasing the temperature and indicates the importance of having high resolution spectrometer for accurate temperature measurements [33].

Figure 4-1 is an example of Ar plasma spectral emission indicating the wavelengths of most intense Ar atomic lines [30]. Both atomic and molecular lines were used in helium (He) atmospheric pressure microwave plasma to predict the gas temperature which had a value of 1700 ± 100 K from the rotational vibrational OH transitions for a power of ~180 ± 10 W

[34]. Excited molecules in microplasmas emit visible (VIS) and close to UV emissions and there are different plasma processes which can form excited species such as electron impact and dissociative excitation. This technique requires a spectrometer with high resolution to be able to analyse the line broadening at high accuracy [3]. The collisions in atmospheric pressure thermalize the gas temperature with the rotational temperature $T_{rot} = T_g$. Also, the collisions with the background gas are not high enough to make transitional-rotational equilibrium so the lowest rot levels are the only thermalized ones even in collisional system. Therefore, rotational temperature has been used extensively as a representation of gas temperature [3]. LIFBASE is a spectroscopic software of diatomic molecules which provides spectral simulation, thermal and non-thermal population distribution and line boarding, allowing changing simulation parameters such as set temperature and rotational and vibrational temperatures [33]. Figure 4-2 depicts the NO (A-X) spectrum for a set temperature of 300 K in (a) and 2000 K in (b) indicating an increase in the peaks' widths by increasing the set temperature. This demonstrates the need for a high-resolution spectrometer in Angstrom scale or higher resolution to be able to capture the changes in temperature and provide accurate measurements.

Atoms such as He and Ar can be excited electronically when provided with high energy resulting from collisions of highly energetic electrons where the energy of the excited states depends mainly on the element's nature. Electronic excited states are existing also in the case of molecules such as N_2. In addition, the collisions between a molecule and heavy gas molecules result in additional vibrational and rotational excited states, whereas no vibrational nor rotational states exist in the case of atoms. In Figure 4-3 the curved lines represent the electronic states where the horizonal lines correspond to both vibrational and rotational states by adding more energy to the electronic states due to the vibration and rotation of the molecule. The energy difference between the two curved energy levels represents the excitation energy. Therefore, there is only one emission line for atoms compared to several emission lines for molecules. High accuracy spectrometer will be required to perform the measurements accurately otherwise, those peaks may get merged forming a broad peak and causing inaccurate measurements. In molecular rotational distribution technique, the VIS and UV emission from excited molecules can be detected by

spectrometry and diagnosed by techniques such as Raman scattering and laser-induced fluorescence (LIF).

Laser-induced fluorescence is a laser gas temperature measuring techniques and can be applied to different plasma system used in various applications [4]. It works by detecting the fluorescence which arises when high energy photons are absorbed causing molecular excitation, at wavelength of about 550 nanometre, and lower energy photons are emitted at different wavelength. Molecular transition is being excited by a laser pointed to it then the excited state produces the fluorescence, see Figure 4-3 an illustration of both the fluorescence and excited spectra formation. LIF can be used to determine T_{rot} for both the ground and excited states depending on the experiment conditions. This technique has been widely used in plasma physics knowing that the molecular excitation is initiated by plasma not a laser source [3]. A modern approach of using a two-photon absorption LIF to measure gas temperature in oxygen plasma was reported. The inaccuracy in gas temperature measurements was estimated by ±10 K when the wave meter resolution was 5MHz FWHM [35].

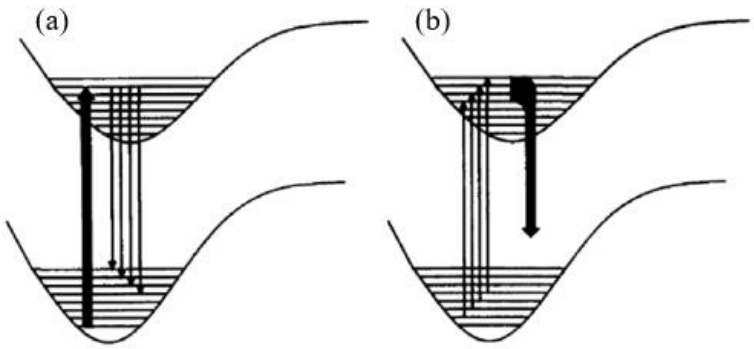

Figure 4-3: Illustration of both a) fluorescence and b) excitation spectra energy levels [3].

4.2.1.2 Raman scattering

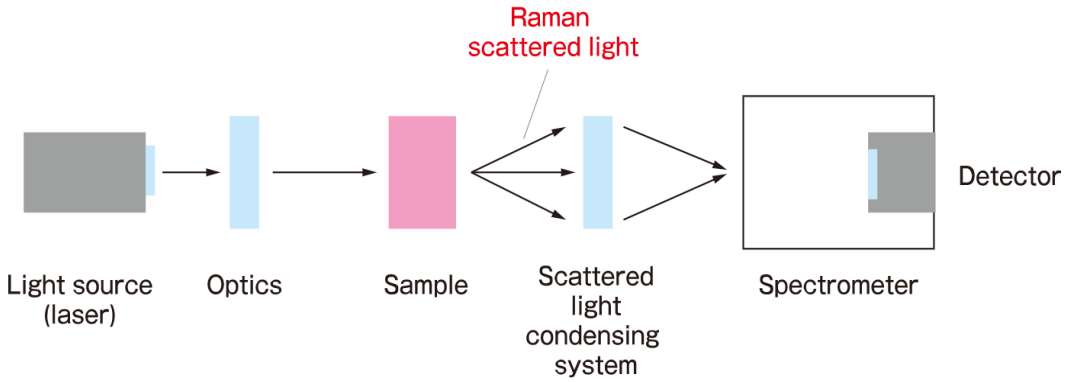

Figure 4-4: Raman spectroscopy technique schematic diagram including the main components of laser source, optics, condensing system and spectrometer [36].

Raman scattering represents photons inelastic scattering from a molecule. Both rotational and vibrational modes, that are attributed to the symmetrical structure of the molecule, can be determined by Raman scattering to get distinctive molecular spectrum. Therefore, Raman is used to provide the molecular composition in many experiments. In addition, Raman scattering can be used to obtain the rotational temperature of the gas that can be indicated from the vibrational ground state of the molecules. Calibration of Raman spectroscopy components such as laser source of light (in the range of VIS, UV or IR), detectors and the laser beam power, Figure 4-4, is essential for providing accurate gas measurements [37]. However, the spectrum from the vibrational ground state is very close to rotational line of the stray light, Rayleigh signal and the laser beam hence, a filter should be used to avoid the interference of these signals. Nevertheless, filtration of inelastic scattered light is challenging due to the weakness of the spontaneous Raman scattering. Raman scattering was used to indicate gas temperature by measuring carbon dioxide (CO_2) vibrational ground state in DBD plasma using a spectrometer with paper filter while IR camera was used to measure the wall temperature (T_{wall}). T_{rot} was assumed to be an indication for T_g while the validity of this assumption was studied by Brehmer et al [37] depending on some indications such as the relaxation of collisions in the rotational states and the low probability to observe filament. The gas temperature was estimated by varying the plasma power (0-60) W and the gas heating had a value of 160 K at power of 33 W with observed deviation in the measurements' accuracy of about 5% [37].

4.2.1.3 Rayleigh scattering

In neutral density technique, Rayleigh scattering can be used to measure the neutral density directly since the scattering cross section depends on the neutral species type and density, therefore the scattered light is proportional to the density of the neutrals found in the scattered volume. Assuming ideal gas law conditions, the gas temperature is then inversely proportional to the scattered light at constant pressure [3]. Gas temperature was measured using Rayleigh scattering and Raman scattering in APP glow discharge using air as the feeding gas and water electrode at 15 mA, Figure 4-5. The measurements using Rayleigh and Raman were almost the same except having higher error using Raman scattering at the middle of the discharge due to the lower signal intensity at higher temperature [22]. Raman and Rayleigh scattering techniques may be used to measure the gas temperature due to the temperature dependence of the scattered light intensity/ wavelength. Nonetheless, it is considered expensive methods for most of lab work or industrial applications. Moreover, laser techniques need to be used carefully to keep the plasma parameters without any changes as a result of, for instance, photoionization [21]. There is also a major difficulty in using these techniques with microplasmas because there are many objects in the pathway between the light source and the detector need to be carefully considered e.g. optics, condensers etc. In addition the accuracy of the measurements depends mainly on the pathlength exposed to the light beam, determined by the volume of the sample, and a minimum pathlength is required to ensure absorbance values are within the dynamic range of the detector . That is very hard task with small volumes such as the case of microplasmas. Therefore, these techniques are complex and unable to provide in situ and continuous measurements as required for many applications such as medical and material applications so they are not recommended in our research.

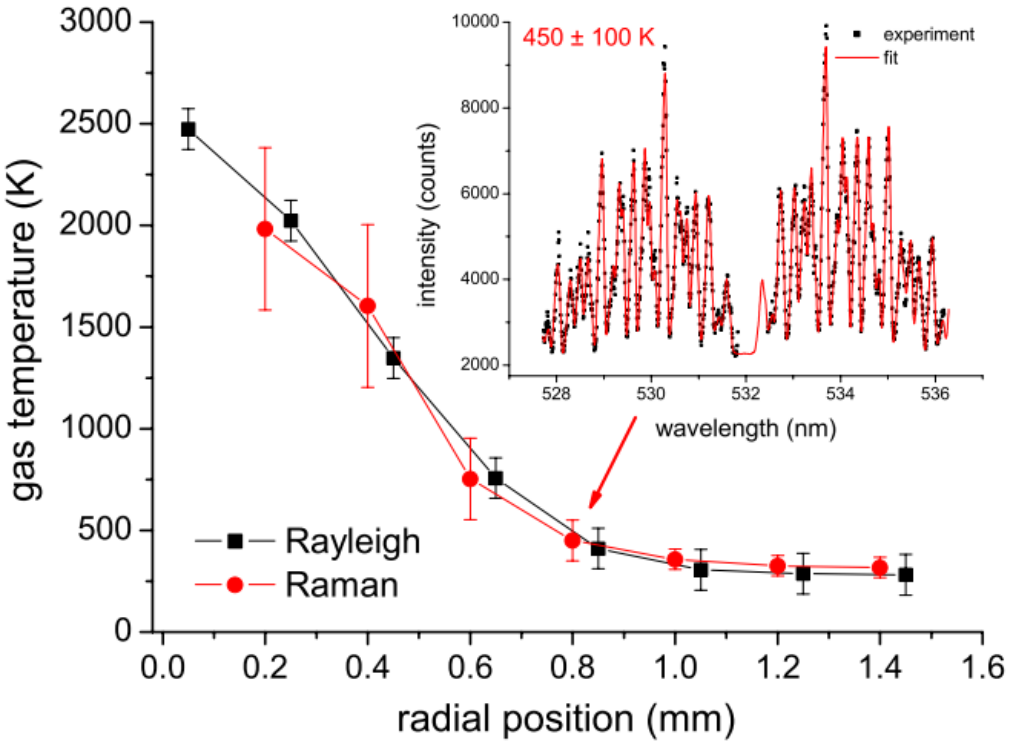

Figure 4-5: Gas temperature measurements vs. plasma radial position using Rayleigh scattering and Raman scattering at 15 mA and inset plot of Raman spectrum at 0.8 mm radial position [22].

4.2.1.4 Schlieren technique

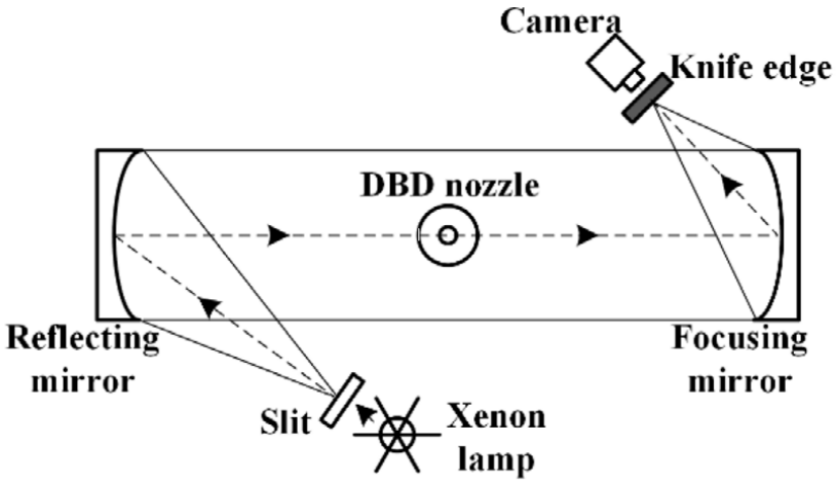

Figure 4-6: Schlieren imaging setup technique for DBD plasma including light source, mirrors and a camera [2].

Schlieren is an imaging technique to study plasma diagnostics by visualising the flow in a transparent media. The main setup components of Schlieren experiment are light source such as Xenon/ LED lamp, slit to get homogeneous lighting from the light source, two mirrors working as focusing lenses, knife edge to reduce the intensity of light collimated by the focusing mirror, and a high-resolution camera (e.g., CCD, Canon camera) to provide Schlieren signal imaging. Plasma source is placed between the two mirrors so that reflected light from the lamp passes through the plasma and imaged by the camera. Figure 4-6 illustrates Schlieren experiment setup for AC DBD plasma [2]. According to the ideal gas law, gas density is inversely related to the gas temperature. Therefore, Schlieren has been also utilised in measuring gas temperature by monitoring the flow patterns to evaluate density gradients. Maximum gas temperature recorded using Schlieren in non-thermal APP jet operated by argon in the effluent was 328 K [6]. While uncertainty of Schlieren gas temperature measurements, in a different study, was expected to be ±2.5% [38]. Schmidt-Bleker et al [6] mentioned that the state of the gas flow should be constant with no laminar-turbulent transitions to get accurate measurements. Also mixing gases caused change in the refractive index and a consequent change in the temperature. Therefore, adjustments in the Schlieren contrast should be considered when mixing various gases. Although Schlieren imaging method is an accurate gas temperature measuring technique but in microplasma, like our case, it is impossible to perform a Schlieren measurement inside the capillary, making Schlieren inappropriate technique for microplasmas [6]

4.2.1.5 Optical emission spectroscopy

While some methods offer high accuracy, they are not suitable for continuous measurement due to size and cost and have generally been used to provide a calibrated reference for other techniques, particularly OES, which is a routine and non-invasive technique. OES obtains a gas temperature estimate by fitting the experimental spectra to theoretical spectra of chosen molecular species, for example N_2, NO, OH or CN [21,28]. However the population of the rotational energy levels, derived from the observed emission cannot automatically be assumed to be in equilibrium with the translational states i.e. gas temperature [3,29]. Iseni et al. [39] compared the analysis of broadening (line, resonance and Van der Waals) of specific isolated lines with the analysis of the rotational distribution of diatomic molecules as methods to determine

neutral gas temperatures. They provide estimates of uncertainties of 3% - 6% and 4% respectively [3,28]. In spectroscopic, rotational spectra can be fitted to the original line profile as it has many resolved rotational lines then Boltzmann plot can be used to represent the spectra. Fitting rotational temperature with Boltzmann plot is an iterative process and, in some cases, may not result in a good fit. Results showed that fitting with single temperature does not yield to good match with experimental data and using two Boltzmann plots showed better fit. However, temperature measurements are more realistic and accurate when they are been aligned to the wavelength. Knowing that not using the wavelength fitting may result in inaccuracies in temperature by 10 K along with potential inaccuracies due to other sources [3].

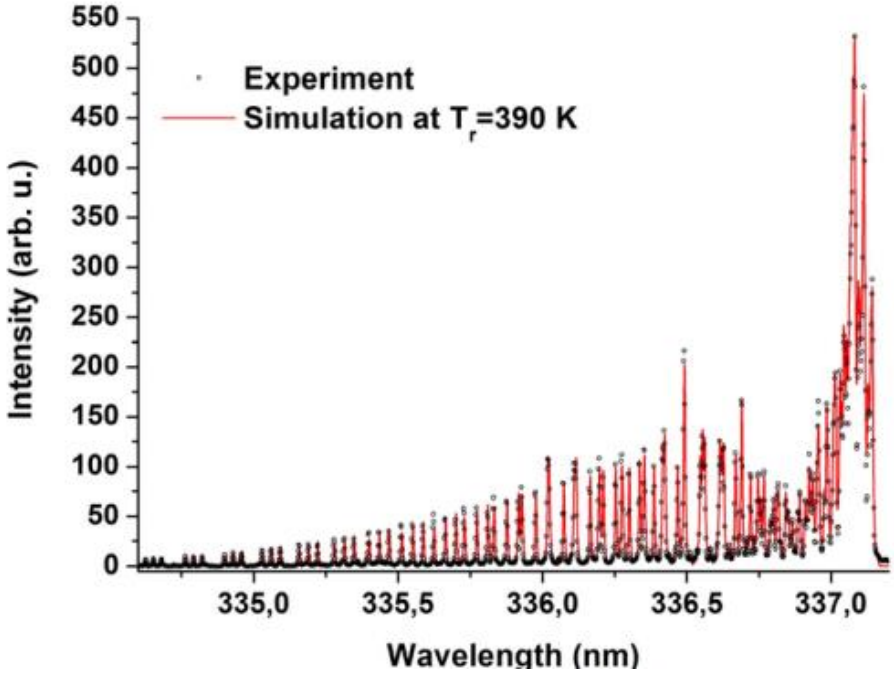

Figure 4-7: Results of experiment and simulation of rotational Spectrum of N_2 (C–B; 0–0) vibrational band [3].

N_2(C–B), OH(A–X) and N^+_2(B–X) are the transitions that has been widely used in determining T_g by OES. Most emissions occur in plasma comprising N_2 or can be represented by the N_2 positive system. The wavelength for N_2 positive vibrational branches lay between 280-500 nm. The (0,0) and (0,2) transitions at 337nm and 380 nm, respectively has mostly been used for the determination of T_g. Figure 4-7 is an example of Rot. Spectrum of N_2(C–B; 0–0) vibrational band recorded with high

resolution of RF APP glow discharge plasma with He–H_2O. In another example of APP micro-glow plasma with a high-resolution rotational temperature measurement of N_2(*C-B*), the temperature difference of afterglow discharge was found to be between 800 -1450 K. OES was not possible for many cases such as filamentary plasmas with small size because of the difficulties in obtaining accurate inline measurements. The fitting accuracy is so important because an error in the rotational temperature of roughly 200 K may result from a small deviation in the fit. In the case of N_2(C-B) function, fluctuation of 10% result in difference of 50 K in the rotational temperature was found when using Boltzmann fit at 350 K [3]. OES was applied to many experiments to measure different temperatures such as rotational and vibrational temperatures (T_{rot} and T_{vib}). Although analysis of nitrogen gas rotational lines is most common in determining T_g, adding N_2 to the experiment, if it is not one of the gases used, may lead to changes in the discharge characteristics [37].

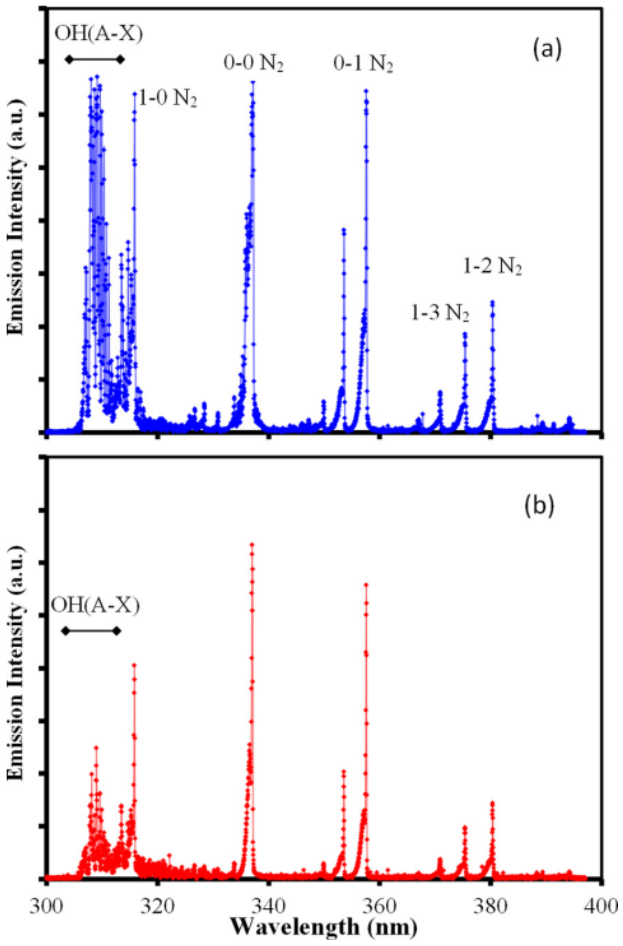

Figure 4-8: N_2 and OH(A-X) optical emission spectral lines for a) plasma without aerosol and b) with aerosol [7].

In a previous work in NIBEC which has the same system for droplets, gas temperature was measured by portable OES to determine the impact of APP heating on nanoparticle synthesis. The gas temperature was estimated by fitting the experimental measurements with theoretical N_2 and OH spectral lines generated from Specair software. For He plasma with 0.1% N_2, maximum T_g measured from N_2 lines was below 400K with an estimated fit error of ±50 K due to difficulty of fitting, for temperatures around 600 K in dry Ar [40]. A comparison between N_2 and OH spectra is presented in Figure 4-8 (a) for plasma with aerosol and Figure 4-8 (b) for without aerosol, showing a noticeable reduction in the intensity of OH(A-X) line with the introduction of aerosol. Therefore with added water, the use of the OH lines leads to heightened error margins due to electronic quenching of OH (A-X) emission by H_2O molecules [41]. This effect becomes noticeable at 100 – 300 ppm H_2O and above [42]. Microdroplet transport through plasma jets can generate beneficial enhancement and transport of radical species (e.g. $OH^{\bullet}$, H_2O_2), important electron reduction reactions and rapid nanomaterials synthesis [43,44]. The chemical kinetics are thought to depend on droplet evaporation which in turn is sensitive to gas temperature. However the OES derived temperature estimates, obtained using OH lines, exhibit significant differences compared to using the N_2 lines, once droplets are introduced into the plasma [7].

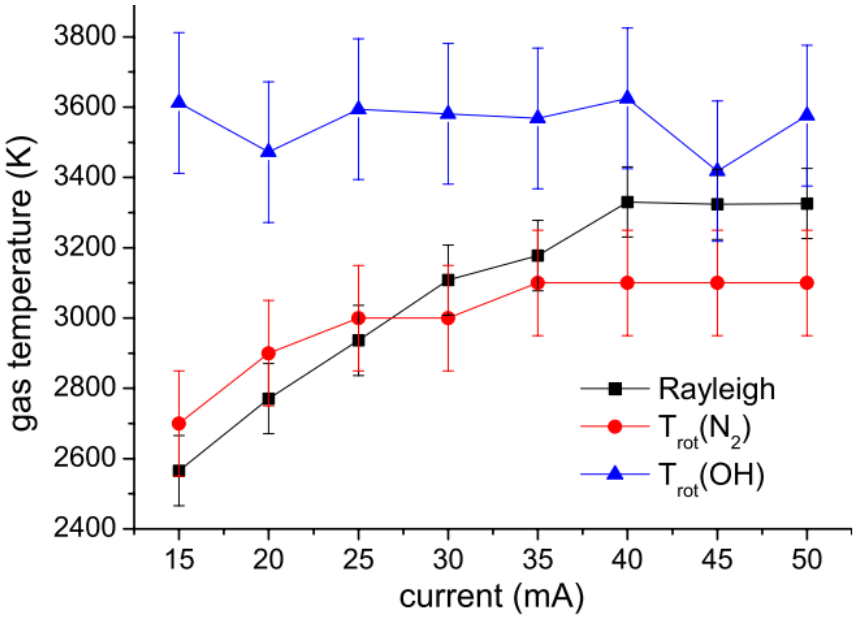

Figure 4-9: Comparison of gas temperature using Rayleigh scattering and OES for (N_2 and OH) vs. current [22].

The gas measurements using Rayleigh scattering were compared with T_{rot} obtained by OES using OH(A-X) and N_2(C-B) lines, Figure 4-9. Gas temperatures determined from Rayleigh scattering, OH(A) and N_2(C) emission were 2600 ± 100 K, 3600 ± 200 K, and 2700 ± 150 K, respectively. The difference between T_{rot} (OH) and T_g from Rayleigh scattering was estimated by 1000 K. While T_{rot} from N_2(C) represents a much closer fit to that obtained from Rayleigh [22]. The lack of accuracy in the temperature measurement using OH(A) was also observed at low temperatures using the NIBEC aerosol system [7]. Since high resolution spectrometer instrumentation is not viable for continuous sensing, the inability to resolve the rotational structures leads to a fitting process which can be complex, slow, difficult to automate, and with accuracy levels strongly dependent on apparatus parameters [3,28]. Temperature resolution is of the order ≥ 50 K in cold plasmas unless high resolution spectra are available. However, high resolution OES would have a bigger size and a higher cost therefore, OES is not suitable for field measurements nor suitable for continuous measurement due the complicated manual calculation. In addition, OES cannot provide instant measurement which is required for many applications such as medical ones.

4.2.2 In-situ sensors for continuous monitoring

4.2.2.1 Thermocouples

Metal wire thermocouples can be used in various applications although challenging to use in microplasmas due to the geometrical restrictions and because thermocouple measurements can be significantly affected by plasma interference. Furthermore, thermocouples affect the properties of plasma when obstructing the plasma outlet [3].

4.2.2.2 Fibre Optic Thermometer

Fibre optic thermometer (FOT) is another method to measure gas temperature that consists of optical fibre with GaAs probe on its tip with connections to source of light and a spectrometer. The idea of this device is that the gas temperature variation is attributed to the probe band gap edge shifting [3]. Figure 4-10 demonstrates the changes in temperature and absorption edge wavelength according to the change in the energy band gap of GaAs which have been measured from a mathematical

equation. From the plot, FOT shows unsensitivity to temperature variation and the wavelength has a slight change, below 10 nm, for a rise of 50 K in temperature [45].

T (K)	Eg(GaAs) (eV)	λg (nm)
0	1.519	816
50	1.514	819
100	1.501	826
150	1.485	835
200	1.465	846
250	1.445	858
300	1.422	872
350	1.399	886
400	1.376	901
450	1.352	917
500	1.327	934

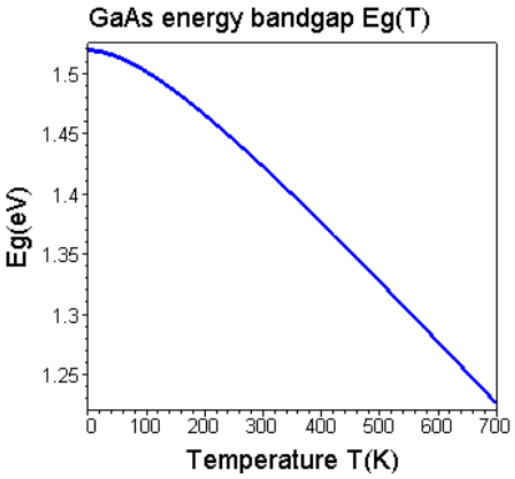

Figure 4-10: The relation between band gap, temperature and wavelength for GaAs where the wavelength changes slightly similar to the energy of the band gap with big increase in the temperature [45].

To conduct the measurements, fibre optic and a monitoring system will be required. Alternatively, a spectrometer with wavelength range of about 350 nm – 1 μm and resolution of about 1.34 nm FWHM can be used. However, both options are costly and are not suitable for microplasmas. Since the fibre optic system is based on measuring the intensity of light, it could potentially show false readings if specific wavelengths penetrated through the probe. Both thermocouple (TC), fibre optic (FO) thermal indicators are problematic [46]. Permanently locating the TC or FO into the gas stream is often inhibited by geometric restrictions, flow disruption, contamination and electrical coupling concerns. Moreover, the finite size of the temperature probe may lead to slight smoothing of the temperature.

4.2.2.3 IR thermal imaging

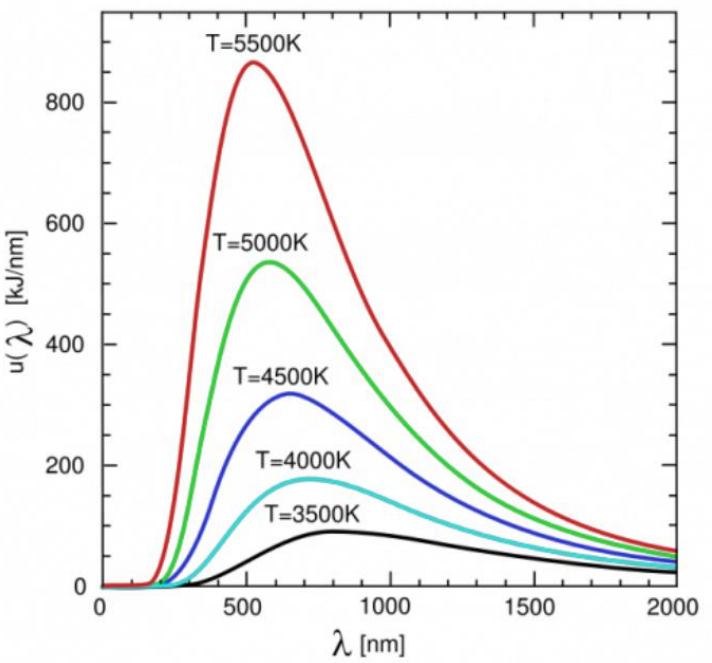

Figure 4-11: Blackbody spectrum with various temperatures [47].

A blackbody (BB) is a perfect absorption body that absorbs all the radiation falls on it and emits radiation at frequencies depending on its temperature. The radiation emitted by a heated blackbody is known as electromagnetic radiation or photons and is limited to infrared spectrum at room temperature. Blackbody radiation is a theoretical concept that can be used in determining objects temperature by assuming that these objects are behaving as perfect blackbodies. Figure 4-11 shows the blackbody spectrum according to its temperature and demonstrates that more light is emitted for blackbodies with higher temperature than the light emitted from lower temperature blackbodies. In addition, the spectrum is continuous and has a peak with a shorter wavelength when the blackbody gets hotter [47].

4.2.2.3.1 IR sensors

IR sensors are contactless IR thermometers used in measuring objects temperatures depending on the infrared energy emitted from them. The infrared sensor uses wavelength range of 1-20 μm for measuring the thermal radiation. The radiation intensity depends on the object's material which is defined by material's emissivity. The emissivity of an object describes its ability to emit IR energy and has a range of

0.0 to 1.0 where 0.1 represent a mirror and 1.0 represent a blackbody. The accurate value of emissivity depends on the material thickness, dimension, surface constitution and transmittivity while the materials range of emissivity are available in tables in the manufacture manuals.

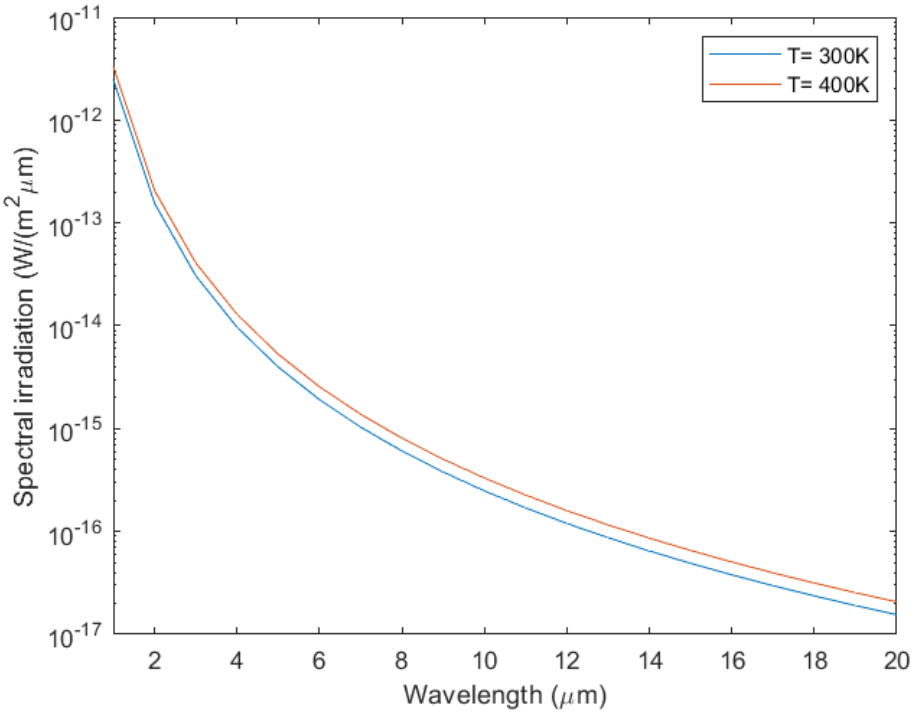

Figure 4-12: BB radiation for both T= 300K and 400K.

The main components of IR thermometers are lens, detector, spectral filter, and controller. The temperature is collected by the lens that passes through the spectral filter which select the range of wavelength. Both controller and detector are responsible for converting the collected IR radiation into electrical signals [48]. Hence the temperature can be calculated from mathematical equations depending on the emissivity of the object and the generated voltage [49]. For instance, the IR sensor can read the difference in BB spectra for two temperatures from the voltage generated in the circuit, Figure 4-12.

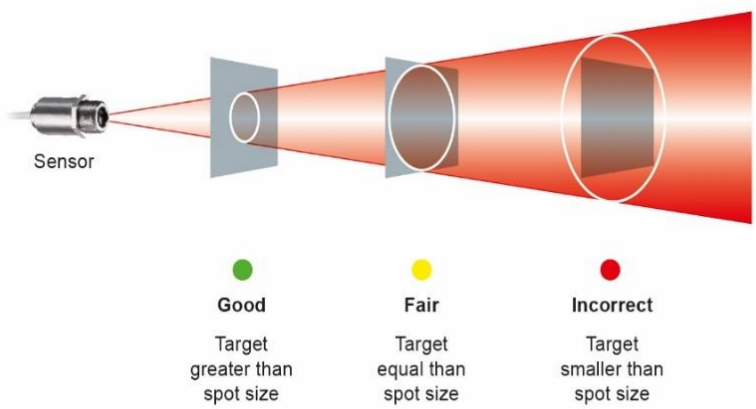

Figure 4-13: A photo of a manufactured IR sensor with FoV and the best location of target for accurate temperature measurements [50].

The field of view (FoV) of IR sensor is the visual angle of its lens and it has different shapes for different manufacturing models. The optical resolution of IR sensor depends on its FoV and the object location with respect to the focal spot size. Figure 4-13 shows an example of IR sensor to demonstrate the target various locations with respect to its FoV. If the target is smaller than the spot size, average background will be considered in the temperature measurement and average temperature will be calculated including both the target and the background. Therefore it is important to make sure that the target is at a point where it is all included in the FoV i.e. the target has the same size or larger than the focal spot size in the FoV [50]. Normal IR probes offer arrange of focal area sizes vs. distance e.g. Calex IR sensor which offers a small focal spot size of 5 mm at distance of 100 mm [51]. However, it is not suitable in our case of microplasma with a small capillary tube size of 2 mm and a small distance between the two electrodes of 2 mm. Therefore, an IR sensor with a smaller focal spot size will be essential to perform a high accuracy temperature measurement in microplasmas. The model of the IR sensor used in our study is “CT-SF22 + CF lens”. Figure 4-14 shows a photo of the IR sensor and the manufacturing dimensions [52]. The optical chart, Figure 4-15, reveals the ratio between the measuring spot diameter “S” and the distance “D” between the sensor and the object where the spot size represents 90% of the object’s radiated energy. It is having a small focal spot of 0.6 mm @ 10 mm stand-off distance which is suitable for microplasmas applications. For accurate measurements, the optical path should be always kept clear.

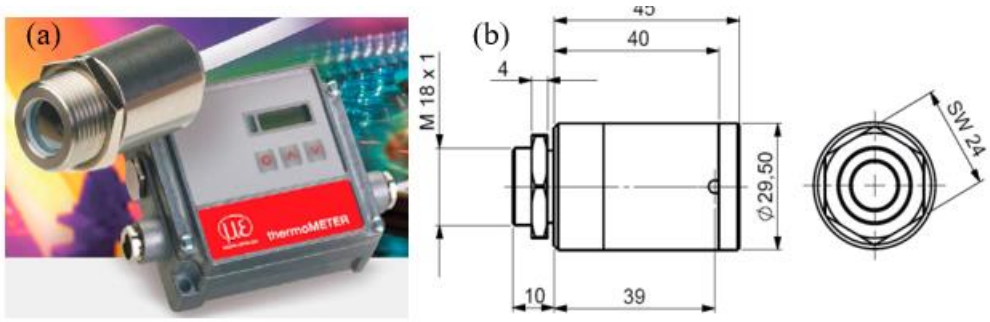

Figure 4-14: IR sensor photograph in a) and dimensions in b) in mm, not to scale [52].

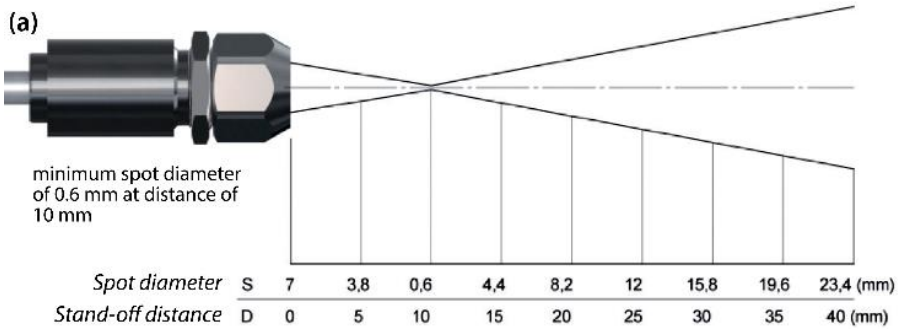

Figure 4-15 Optical chart of spot diameter vs. the stand-off distance for the FoV [52].

4.2.2.3.2 Thermal cameras

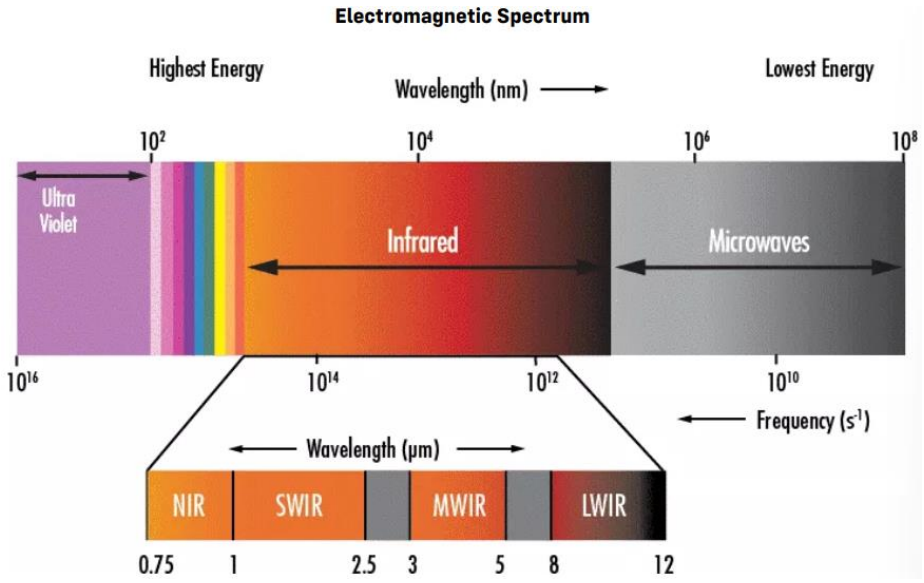

Figure 4-16: Electromagnetic spectrum range from ultra violet spectrum to infrared and microwave spectrums identifying also the energy of each range [53].

The object's radiation can also be detected by a thermal camera at various wavelengths in the range of infrared spectrum using infrared sensors. It provides temperature measurements in the form of coloured image hence IR cameras can be utilized as thermographic cameras [53]. Noting that for thermal cameras, a mass of photons will be required to produce electrical signal, representing the temperature measurements [54]. The electromagnetic spectrum includes Ultraviolet, Infrared and Microwave radiation, Figure 4-16. Where the IR radiation can be divided to various wavelength Long, Medium, and Short -Wave IR that have wavelength of (LWIR) (7.5-14 µm), (MWIR) (3-5 µm) and (SWIR) (1-3 µm), respectively. Knowing that the LWIR range is the most common between modern thermal cameras [53].

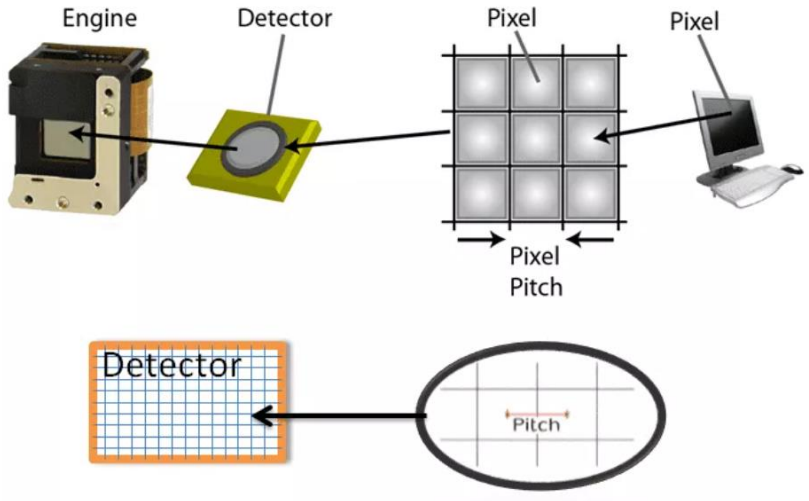

Figure 4-17 IR camera detector composition of pixels [55].

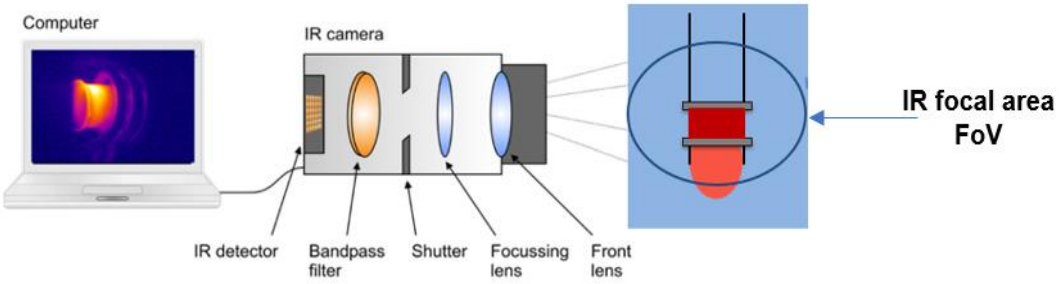

Figure 4-18: Schematic diagram of microplasma traditional infrared imaging system with camera inner components and the associated field of view which is bigger than the microplasma dimensions and includes cooler background.

The resolution of the camera is determined by the number of pixels whereas high resolution IR cameras have 640 × 480 detectors which is equivalent to 307,200 pixels. The pixel size is in micron and the distance between the centre of two adjacent pixel is called the pitch, Figure 4-17. The signal is formed from the photons collected by number of pixels where each pixel acts like a single IR probe hence, it has a focal spot size versus distance [55]. The spatial resolution of each camera describes pixel's spot size at a specific distance and the field of view of each pixel is measured in milliradian (mrad). For example, FLIR A320 camera has a minimum focus distance of 0.4m and a spatial resolution of 1.36 mrad, equivalent to a pixel view area of 1.36 mm at distance of 1 m [56]. However, at large enough distance the focal spots of neighbouring pixels will overlap and these signals interpolate to form the thermal image which may not provide an accurate measurement of microsize applications like our case of microplasmas [57]. Figure 4-18 depicts traditional IR measurements for microplasmas. It provides an average wall temperature value over the field of view (FoV) and at typical sensor stand-off distances, the FoV is unsuitable for many plasma systems because of size or temperature non-uniformity. Thermal imaging using cooled high resolution IR cameras can improve the spatial resolution but this technique is reserved for stand-alone experiments, often at high temperatures [58–62].

Infrared camera (FLIR, A320) was used to measure the temperature of the quartz wall and gas temperature of dielectric barrier discharges experiment, estimating the temperature between 320-480 K [19]. While infrared camera (GUIDE M8) with 160x120 resolution was utilised in measuring gas temperature in a gliding arc reactor and was found to be below 70 C for various flow rates [18]. The following are some of the major advantages of IR sensor over IR camera, IR sensor has a small focal spot that can be focused on a small area such as microplasmas applications, IR sensor is much cheaper than IR camera, it can be left in place to obtain continuous measurements, provides continuous monitoring (readings every 1 ms) and IR measurements are not affected by aerosol plasmas. Zhou et al [2] used different techniques of measuring gas temperature and compared between them. K-type thermocouple was used to measure the air jet temperature in DBD reactor while the wall temperature was measured by infrared thermometer. The gas temperature measurements using the thermocouple showed inaccuracy range of 1.0 K compared to 1.8 K of using the IR thermometer for wall temperate measurements. While the use of

IR thermal camera to observe the temperature in the plasma area revealed inaccuracy range of 2%. OES, using N_2 positive/ negative systems, was used for providing temperature distribution and gas temperature verification by using LIFBASE software spectrum simulation. The comparison between the T_{rot} from OES measurements with gas temperature measurements using IR thermometer indicated a close approximate and demonstrated that T_{rot} of plasma can represent the gas discharge temperature [2]. Also, gas temperature was measured in atmospheric pressure microwave plasma running by helium gas inside a 13 mm diameter tube using thermocouple and the excitation of the plasma was studied by OES. Measurements reported gas temperature to be 1208 K inside the tube while the optical emission of N_2 rotational spectrum provided gas temperature measurements in the range 1000 to 2000 K for similar operating conditions [11].

4.3 Experimental setup and methods for gas temperature measurements

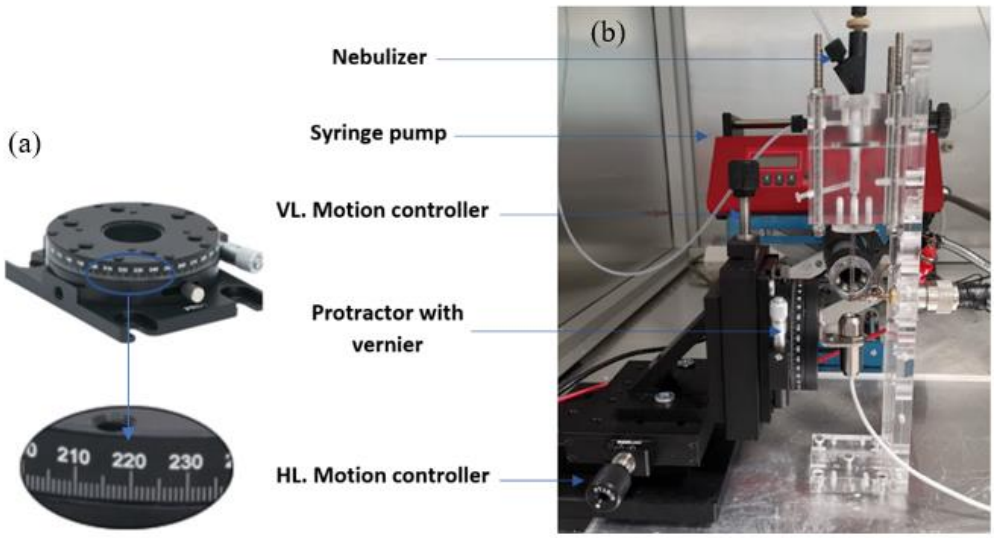

Figure 4-19: a) 360° of Coarse Rotation and Vernier Scale Provide ±5° Fine Adjustment and b) is a photo of all experiment components.

Here the use of a small form factor IR sensor for continuous monitoring of gas temperature of a RF plasma jet contained in a narrow quartz capillary tube is investigated, a photo of the experimental apparatus is shown in Figure 4-19. The plasma region is defined by two outer ring electrodes which are separated by a distance

≥ 2 mm. The sensor FoV diameter is 0.6 mm at a stand-off distance of 10 mm. It is expected that the inner wall temperature of the capillary in contact with the plasma will rapidly reach equilibrium with the plasma gas temperature and represent a close approximation. To determine the temperature gradient across the quartz, i.e., between inner and outer walls, first the temperature of the inner wall in contact with the plasma with the sensor placed at the capillary exit and directed along the capillary axis is measured. Precisely locating the sensor FoV within the plasma region is achieved with reference to a known geometrical setup, by scanning the sensor in XYZ directions and over a range of angles. After obtaining calibration measurements of outer wall against inner wall temperature for varying power, flow, and He/Ar gas mixture, then gas temperature in the presence of microdroplets from the outer wall temperature is determined.

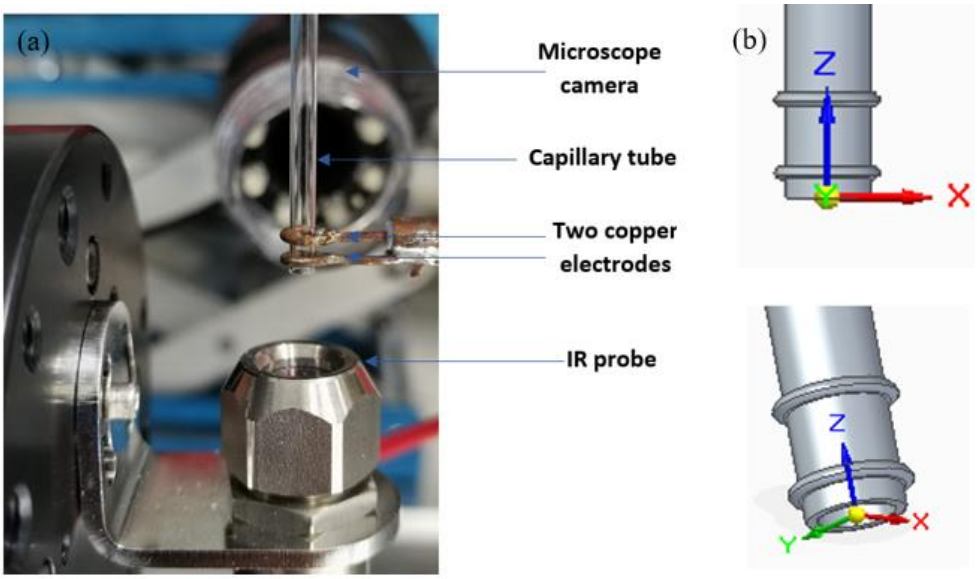

Figure 4-20: a) magnified photo showing the IR sensor, electrodes and capillary tube and b) is 3D drawing of the capillary tube and the two ring electrodes.

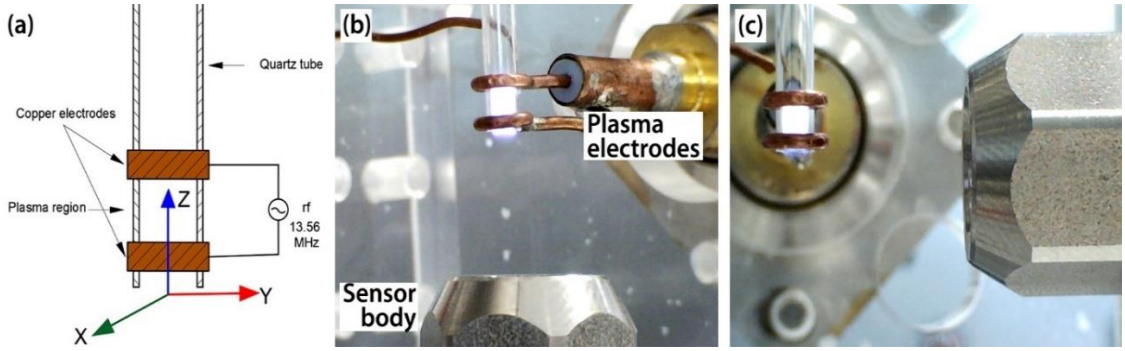

Figure 4-21: (a) Schematic of the plasma setup with axis labels, (b) vertical orientation for inner wall temperature measurement and (c) horizontal orientation for outer wall measurement.

Figure 4-20 shows a closer photo of the IR sensor, electrodes and capillary tube and Figure 4-21 depicts a schematic diagram of them with the horizonal and vertical position of the IR sensor for wall temperature measurements. The plasma is generated inside a capillary quartz tube 2.00 mm inner diameter (0.2 mm thickness). Radio frequency (RF) power at 13.56 MHz is connected to two concentric copper ring electrodes with a 2 mm separation, with the quartz tube extending 1 mm below the lower electrode. He, Ar and Ar/He gas flows from 0.5 to 3.0 slm without droplets were controlled by MKS G-Series mass flow controller. The net RF power, as determined using an Octiv Suite 2.0 VI Probe, is varied from 0.05 W to 0.6 W. For microdroplet studies, microdroplets with average diameters in the range 12 μm – 15 μm was obtained from a Burgener Mira Mist X-175 nebuliser and were injected into a helium gas flow (Q_1) of 0.7 slm upstream of the plasma. The nebuliser was driven by a separate He gas flow (Q_2) and the total plasma gas flow was $Q = Q_1 + Q_2$. The liquid (H_2O) was supplied from a syringe pump at 4 μl/min and an estimated 5×10^4 droplets per second were delivered into the plasma [7,43]. Infrared temperature measurements were obtained using a Micro-Epsilon Thermometer CT precise infrared sensor (CT-CF22-C1 Miniature-Pyrometer) with spectral range 8 - 14 μm and integrated CF lens providing a focal spot diameter of 0.6 mm at a stand-off distance of 10 mm [63].

In normal operation, the sensor face is positioned at a stand-off distance from the outer wall of the quartz tube to collect emission from between the copper electrodes, Figure 4-21 (c). In order to calibrate the temperature gradient across the thin quartz wall, calibration measurements of the inner wall temperature between the electrodes are obtained with the setup shown in Figure 4-21 (b), with the sensor pointing upwards along the capillary axis. The variation in sensor FoV with stand-off distance is given in Figure 4-22 (a) and the sensor position relative to the capillary exit, in the configuration of Figure 4-21 (b), is shown in the CAD drawing of Figure 4-22 (b), with the optic field profile overlaid (red). The 7 mm wide sensor face is inclined at angle θ with its centreline situated X mm and Y mm from the capillary axis and Z mm from the capillary exit. To obtain an optic field intersection with the inner wall, of diameter D, within the region bounded by the two electrodes, the sensor XYZ position and angle θ is varied in increments of 0.25 mm and 0.5 degrees, respectively. The clearance, c, between the upper edge of the optic field and the bottom of the quartz tube determines the limit of sensor vertical movement. Firstly, the precise centreline (axis) of the tube is determined by scanning the sensor in x- and y-directions with a nominal 0^o inclination. The resultant temperature profile when the plasma was on, Figure 4-23 (a) shows two peaks indicating the wall positions and the centreline is assumed to be at the lowest temperature between the walls. The sensor is then positioned at this centreline axis and the temperature is obtained while the inclination is varied using a precision rotation platform (5 arcmin resolution), Figure 4-23 (b). The reference 0^o inclination is taken as the angle at which the minimum temperature occurs. It should be noted that these plots act as a calibration procedure specifically to identify the capillary tube centerline and hence the measurement location point on the capillary, before each set of measurements. The actual gas temperature measurements will be discussed in the next section and represented by series of measurements with error bars.

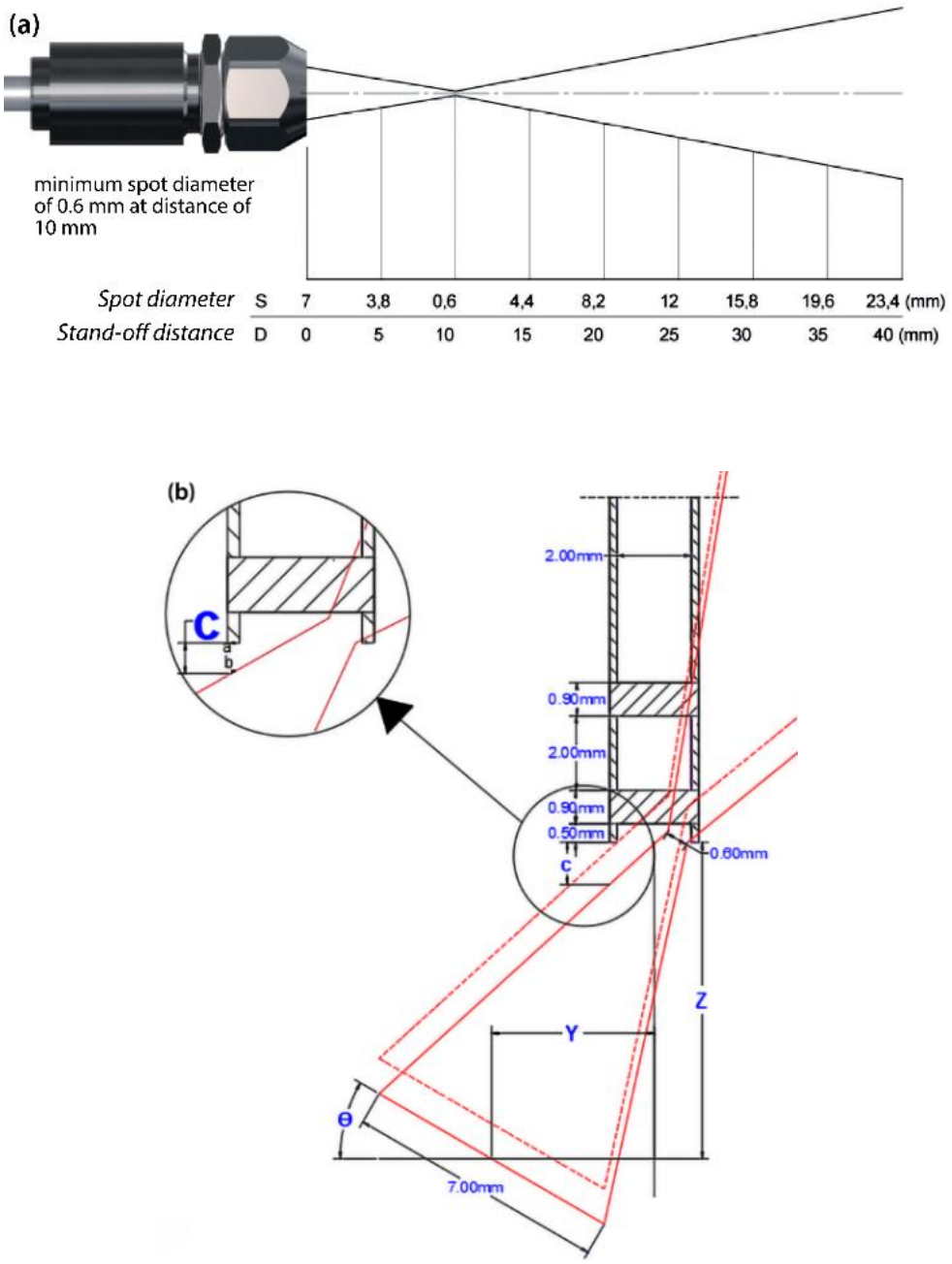

Figure 4-22: (a) IR sensor optic field profile showing spot diameter versus stand-off distance and (b) CAD drawing of the geometric setup of the plasma capillary and IR probe, in vertical configuration for inner wall measurement. Overlay shows the positions of the optic field profile outlines, initially (red, dashed) and after translation in the Z-axis (red, solid), where the initial clearance between upper edge of the optic field and quartz wall is 0 mm and the final clearance is c mm.

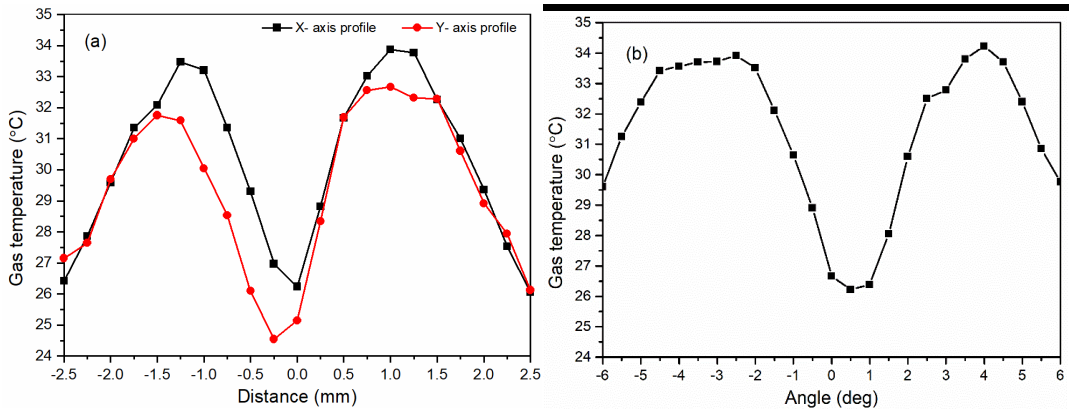

Figure 4-23: Determining the alignment of sensor with respect to the quartz tube axis from temperature profiles across the tube by (a) varying X and Y distances and (b) angle of inclination

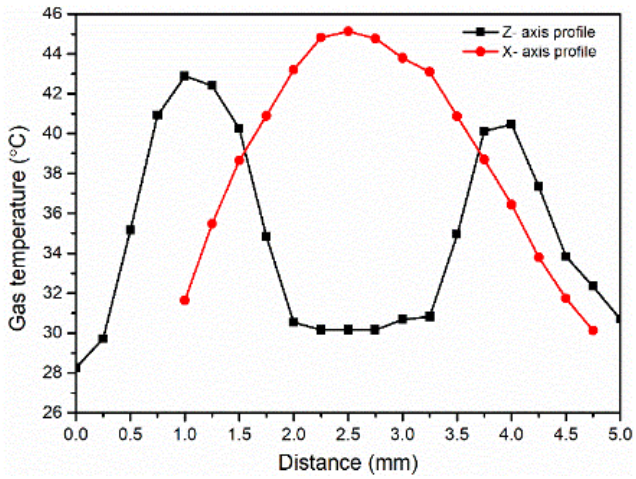

Figure 4-24: Vertical and horizontal temperature profile of the outer surface of the capillary with the IR probe in the horizontal position. The peaks in the z-axis profile indicate the Cu electrode temperature. An emissivity value of 0.93 (quartz) was used and temperature values are valid only for the quartz region. Assuming a Cu emissivity range of 0.5 to 0.8 for unpolished/rolled metal, gives a maximum upper electrode temperature in the range 50 ºC – 80 ºC.

To locate its normal position reading the outer wall temperature at the centre of the plasma, the sensor is set at a stand-off distance of 10 mm, with an FoV diameter at the outer quartz wall of 0.6 mm, Figure 4-21 (c). The sensor is scanned in the horizontal direction (X), to determine the tube limits and central axis, and in the vertical direction to locate the two electrodes and obtain plasma temperatures in the interval. The temperature peaks in the z-axis profile of Figure 4-24 represent the Cu

electrodes. The actual value of temperature is unknown since the emissivity of Cu varies considerably (0.1 to 0.9) based on surface condition. Assuming a Cu emissivity range of 0.5 to 0.8 for unpolished/rolled metal, gives a maximum upper electrode temperature in the range 50 ^{o}C – 80 ^{o}C. The distance between temperature peaks in the vertical (Z) profile, figure 4, is ~3 mm, equivalent to the 2 mm gap between electrodes and accounting for electrode thickness and FoV diameter. The constant temperature valley extends ~1.5 mm and this provides the average plasma temperature.

The IR sensor readings are available every 1 ms. Transient thermal response characteristics are shown in Figure 4-25 for both inner and outer wall measurements. Plasma ignition and extinction points are obtained from a photodiode response to plasma brightness. The rise time to final average value is ~3 s for both. For all temperature measurements, a constant quartz emissivity value of 0.93 was used.

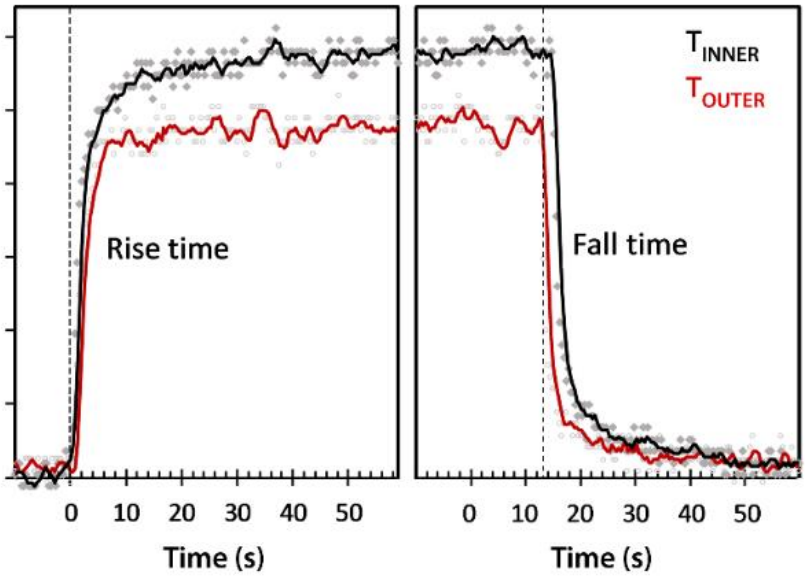

Figure 4-25: Temperature rise and fall times for inner wall (black) and outer wall (red). Dashed lines indicate the plasma ignition and extinction times obtained from photodiode response.

4.4 Validation

4.4.1 Preliminary measurement of the electrode's temperature profile

The electrodes temperature is subjected to an increase due to being connected to a driven power. Therefore, it is important to study the electrodes temperature so that we can judge the factors affecting the capillary tube temperature along with the plasma temperature. Figure 4-26 is the temperature profile of the copper electrode while pointing the focal spot of the IR sensor at the electrode in vertical position. The temperature profile of the electrode is affected by its material and consequently its emissivity. Using emissivity of 0.1 represents the best case as the temperature increases by increasing the emissivity of the material. Figure 4-26 indicates an increase in the electrode's temperature to a maximum value of 44 ^{o}C in the first two minutes followed by a drop to room temperature. Consequently, the electrode temperature can be considered to have a neglectable effect on the quartz tube temperature with respect to the gas temperature.

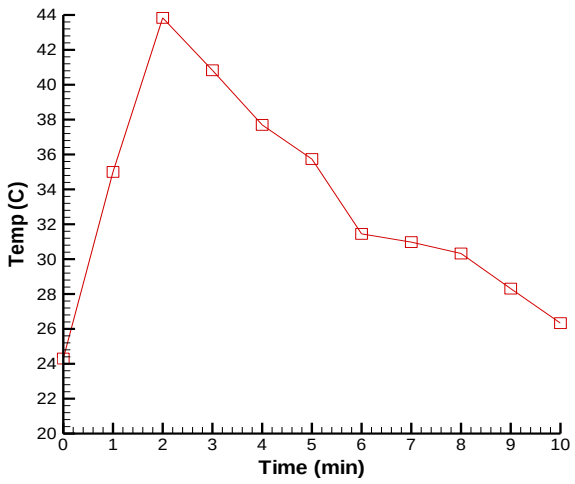

Figure 4-26: The temperature profile of lower electrode vs. time using emissivity of 0.10.

4.4.2 Aerosol temperature measurements

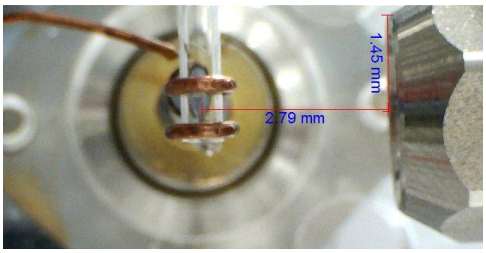

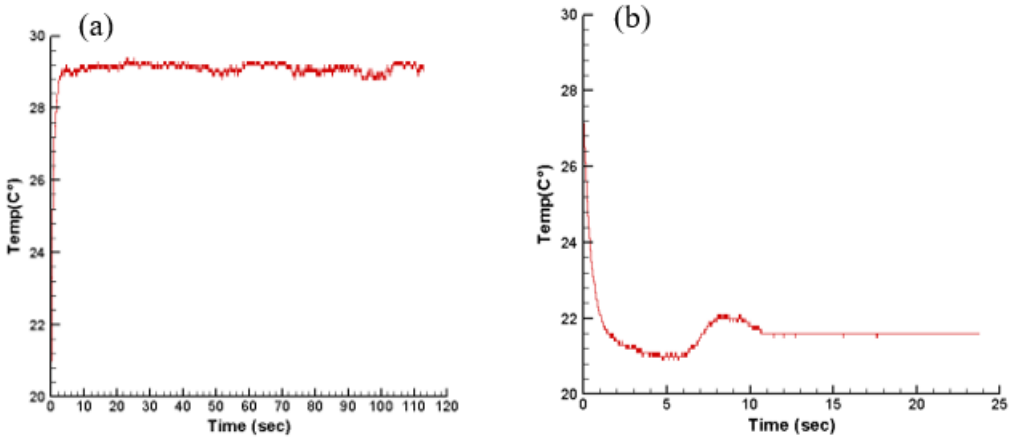

Figure 4-27: a) Temperature measurements at the midpoint between the two electrodes during heating up till saturation and b) during cooling down at He flow rate= 1.5 slm, maximum net power of 0.58 W and droplets flow rate= 4 µl/min.

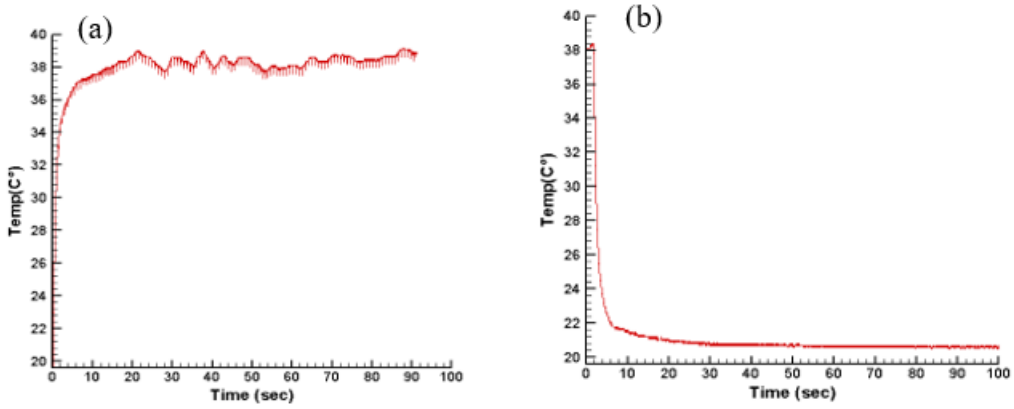

Figure 4-28: a) Temperature measurements at the midpoint between the two electrodes during heating up till saturation and b) during cooling down at He flow rate= 0.5 slm, maximum net power of 0.58 W and droplets flow rate= 4 µl/min.

Aerosol temperature measurements with time were taken at midpoint between the two electrodes to find out the temperature saturation time when the plasma is on and cooling time after turning of the plasma. While using maximum net power of 0.58 W, droplets flow rate 4 µl/min and He gas flow of 1.5 slm in Figure 4-27 and 0.5 slm in Figure 4-28, fast saturation and cooling time within few seconds can be noticed. In addition aerosol temperature measurements were taken at 2.0 mm above the top electrode in Figure 4-29 at the same plasma conditions. When plasma on at 0.5 flow rate, Figure 4-29 (a), the temperature showed a fluctuation between 24 ^{o}C and 29 ^{o}C compared to a rapid saturation with higher flow rate at 1.5 slm as shown in Figure 4-30 while a rapid cooling down was always monitored after turning off the plasma, Figure 4-29 (b). The fluctuation in the top electrode temperature by ±2.5 ^{o}C, Figure 4 29 (a), is probably due to the instability of the afterglow area above the top electrode, which is connected to the power supply and therefore heated by ohmic losses, while impacted by the cooling gas flow in the opposite direction.

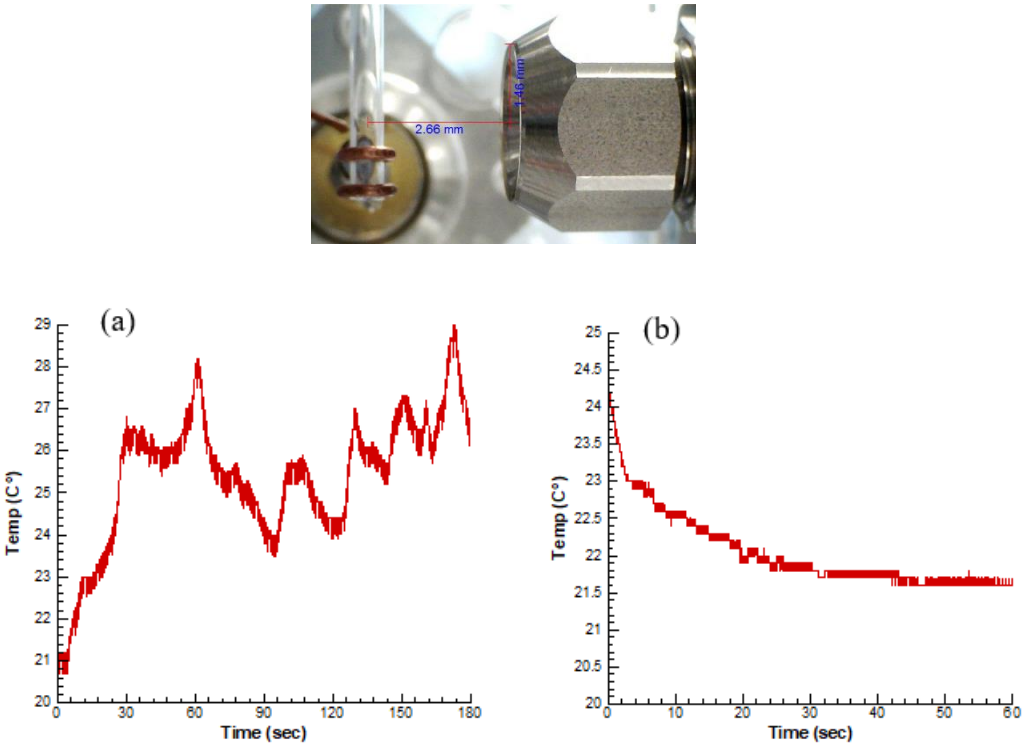

Figure 4-29: a) Temperature measurements 2mm above the top electrode during heating up till saturation and b) during cooling down at He flow rate= 0.5 slm, maximum net power of 0.58 W and droplets flow rate= 4 µl/min.

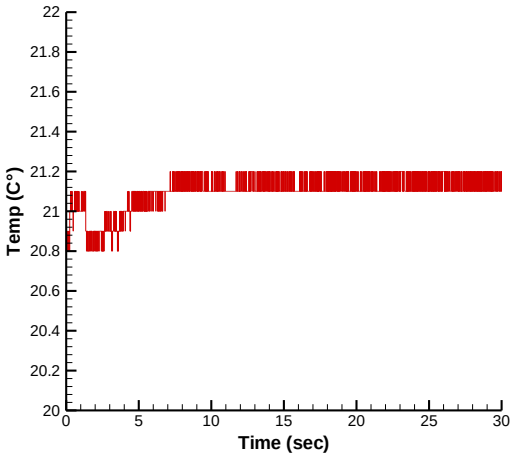

Figure 4-30: Temperature measurements 2mm above the top electrode during heating up till saturation at He flow rate= 1.5 slm, maximum net power of 0.58 W and droplets flow rate= 4 µl/min.

4.4.3 Validation of CAD technique

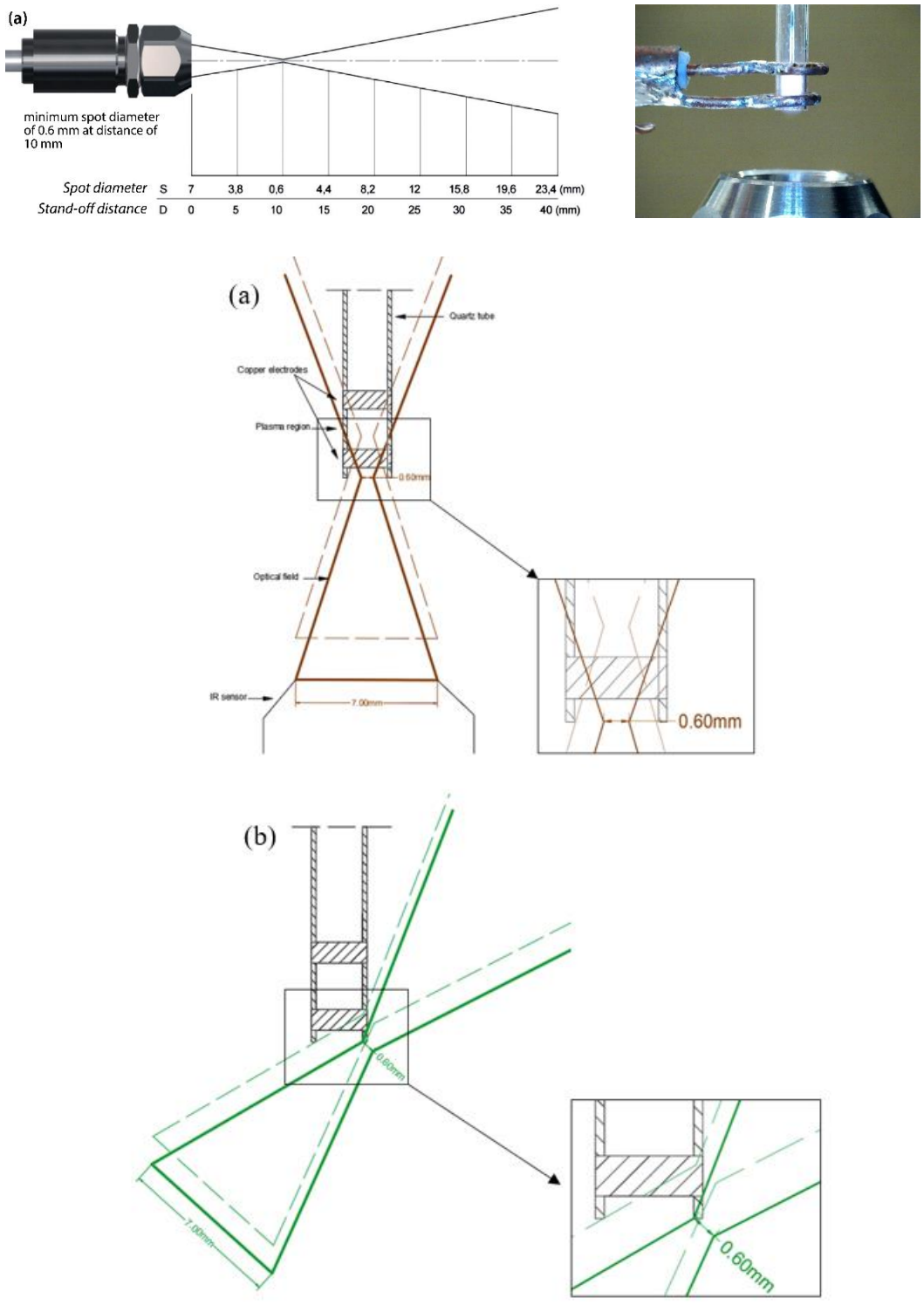

Figure 4-31: Preliminary CAD drawings of initial IR sensor field of view when the sensor is at a) vertical position (θ=0) positions and b) when the FoV has high angle of inclination that results in FoV to lay outside the tube. The optical field profile (solid line) is obtained from manufacturers specifications (see Figure 4-22(a)), the dashed lines indicate maximum Z-axis travel for c > 0.

Figure 4-31 shows a CAD drawing of the capillary tube and the IR sensor FoV when the sensor is vertical, the IR lens has a radius of 7.00 mm and the focal spot is 0.6 mm. At this position, the focal spot does not intersect with the capillary tube in the area between the two electrodes and there is a large area of background included in FoV so an inclined angle is required for accurate measurements. However too much inclination would result in the FoV to lay outside the tube and consequently misleading measurements as shown in Figure 4-31 (b). So, a precise measurement of the geometry and the intersections between the FoV and the plasma tube is essential.

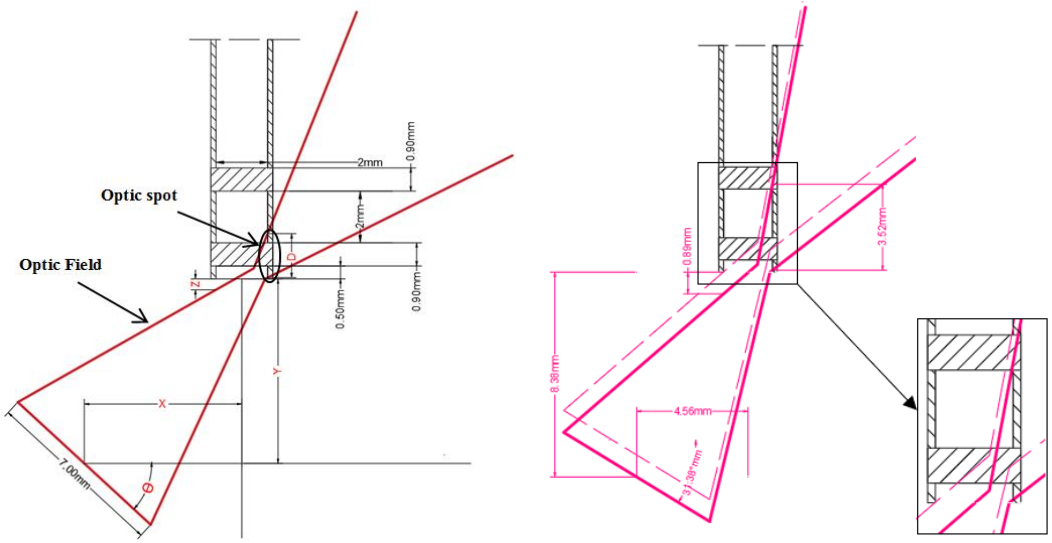

Figure 4-32: CAD drawings IR sensor field of view with all dimension that should be considered where X,Y are the location of the centreline of the IR sensor with respect to tip of the tube, D is optic spot intersection with the tube wall where b) is a trial for locating the FoV with the capillary wall.

Figure 4-32 shows identification of factors and parameters to be considered and Figure 4-32 (b) shows an iteration to locate FoV between the two electrodes where D= 3.52 cm compared to D=2.94 cm in profile B. It indicates that higher D resulted in including part of the electrode in the FoV, so it does not provide an accurate indication of the gas temperature compared to profile B.

4.5 Results of gas temperature

4.5.1 Plasma only

After locating the sensor centreline point of the tube, the aim was to adjust the XYZ and θ positions to achieve an intersection of the optical field with the inner wall that lies between the two electrodes. The sensor starting positions are chosen to ensure the optical edge at the minimum spot size is located as close as possible to the end of the tube inner wall. Three example starting positions are illustrated in Figure 4-33 and Y(0), Z(0) and θ(0) initial values along with the resultant focal spot diameter, D, is given in Table 4. The dashed optic field profile indicates the limit of Z-travel while maintaining c > 0. The inner wall temperature profile, Figure 4-34, was obtained for each starting setup in Figure 4-33, by varying the clearance, c, from zero up to the maximum possible, given in Table 4. Profile A is dominated by the temperature at the lower electrode region and is constant with c. The profile C diameter at the wall is > 4 mm and hence is greater than the plasma area. The temperature increases as the spot moves down since less of the cooler wall above the plasma region is included in the temperature measurement. In profile B, the spot size and location represent the closest match to the plasma region. The temperature decreases as the spot moves away from the powered electrode. The final position is taken therefore from the maximum temperature point of profile B and is given by Y = 4.91 mm, Z = 8.15 mm, θ = 33.75^o, c ~ 0 mm, with a spot diameter of 2.94 mm.

Table 4: Values for initial IR sensor positions and inclinations according to CAD drawings in Figure 4-33. X and Y are the distances (mm) from the capillary centreline, Z is the distance from the sensor to the capillary, c is the clearance before the optic field hits the wall, θ is the angle of inclination with x-axis and D is the diameter of optical spot in mm.

	Y(0) mm	Z(0) mm	θ(0)	c(final) mm	D mm
Profile A	6.10	6.78	42.69^o	0.42	1.75
Profile B	4.91	8.15	33.75^o	0.78	2.94
Profile C	4.37	8.51	30.05^o	0.94	4.05

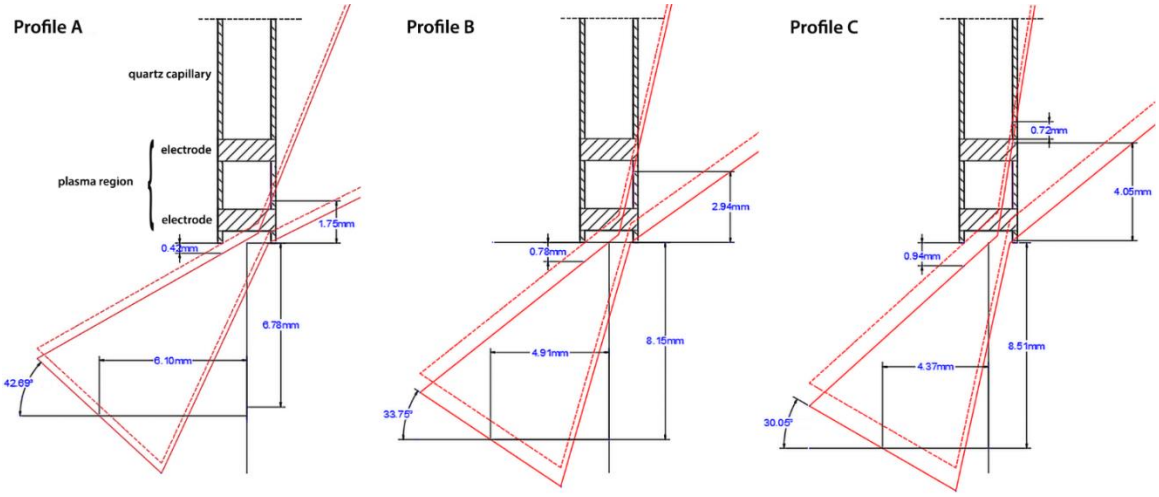

Figure 4-33: CAD drawings of initial IR sensor positions and inclinations showing the intersection of optical field with inner wall. The optical field profile (solid red) is obtained from manufacturers specifications (see Fig 2(a)), the dashed lines indicate maximum Z-axis travel for c > 0.

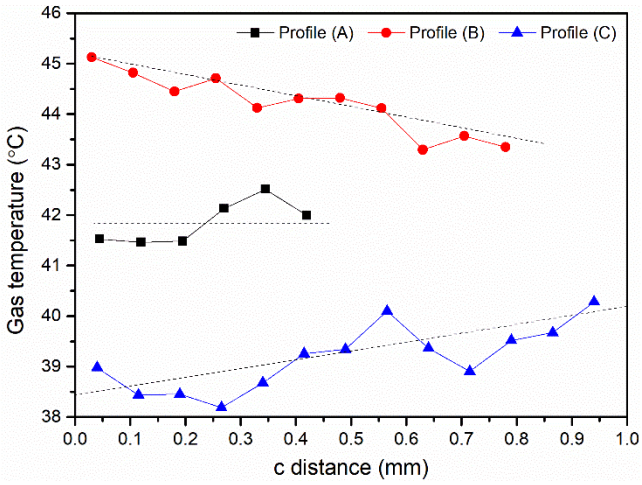

Figure 4-34: Temperature profile of the inner wall of the capillary tube versus clearance, c, between bottom of quartz tube and the upper edge of the optic field profile (see Figure 4-22 (b)). Note in Figure 4-33, the minimum clearance is shown by the dashed profile and maximum by the solid.

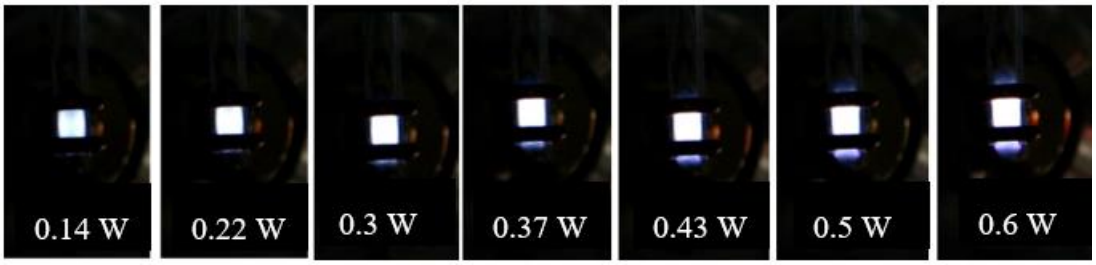

Figure 4-35: Pictures of the plasma with the absorbed RF power variation using He flow rate at 1.00 slm.

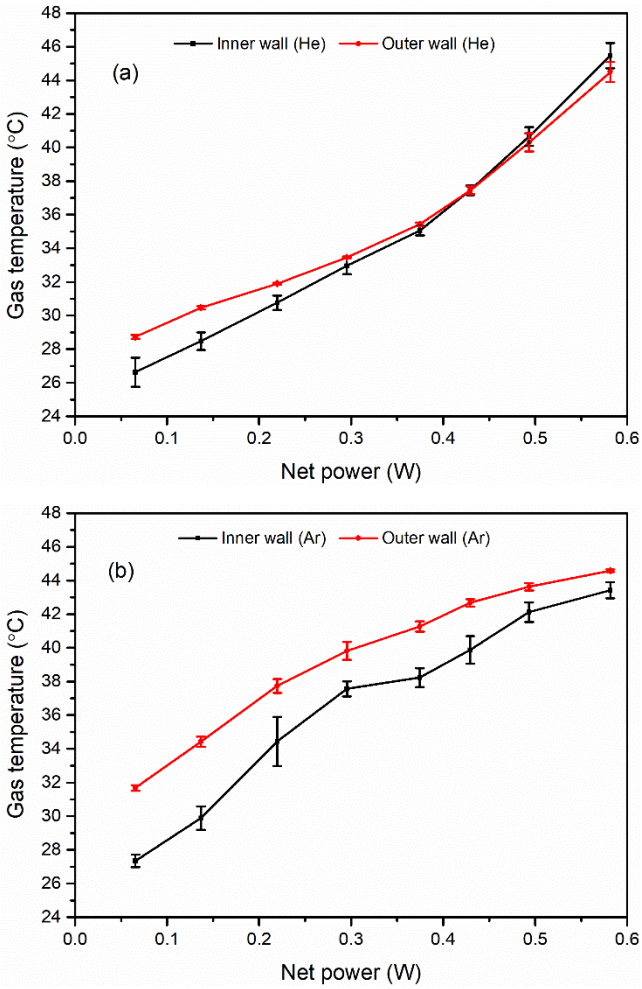

Figure 4-36: Inner and outer wall temperature of the capillary tube against RF net power at a fixed flow rate of 1.0 slm for (a) He and (b) Ar plasmas. Error bars represent the standard error (n = 3).

The delivered power is the total electric power received from the power supply and delivered to the system whereas the absorbed power is the quantity of power consumed by the plasma. The absorbed power can be obtained by the Octiv Suite 2.0 VI Probe installed in the system whereas the difference between the absorbed power and the delivered power is lost in the component of the circuit. In a He plasma, Figure 4-35 depicts the illuminance of the plasma with increasing the power and shows increase in the brightness along with the length of the afterglow areas. As the measurements in Figure 4-29 (a) were taken at maximum power with the longest afterglow area in Figure 4-35, less fluctuation would be anticipated at lower power as the afterglow area gets shorter. The average temperature variation with power, Figure 4-36 (a), follows an almost linear relationship with minimal difference between inner

and outer wall temperatures while for argon, a sub-linear relation is observed and the outer wall temperature is 2 °C – 4 °C higher than the inner. The temperature differences between inner and outer wall are of similar magnitude to error margin of individual readings. Nevertheless, there is evidence that the plasma electrode temperature increases when the plasma is operated with argon. This may cause some external heating of the quartz capillary. With increasing flow, the gas temperature decreases for both gases, Figure 4-37. The introduction of Ar into He changes the plasma impedance and at the lowest flow rate, the gas temperature falls to a minimum when the Ar:He fraction reaches 40:60, Figure 4-38 (a). A plot of net power absorbed against mixture ratio shows the temperature fall is due to a reduction in absorbed power with mixture variation as indicated in Figure 4-38 (b).

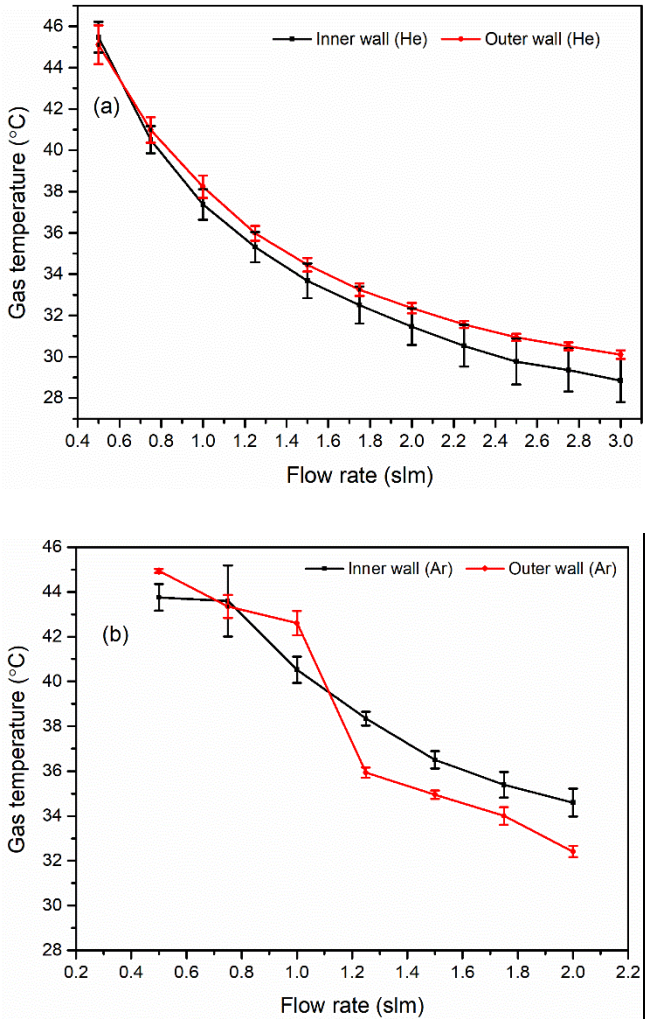

Figure 4-37: Inner and outer wall temperature of the capillary tube against flow rate at a fixed RF net power of 0.3W for (a) He and (b) Ar plasmas. Error bars represent the standard error (n = 3).

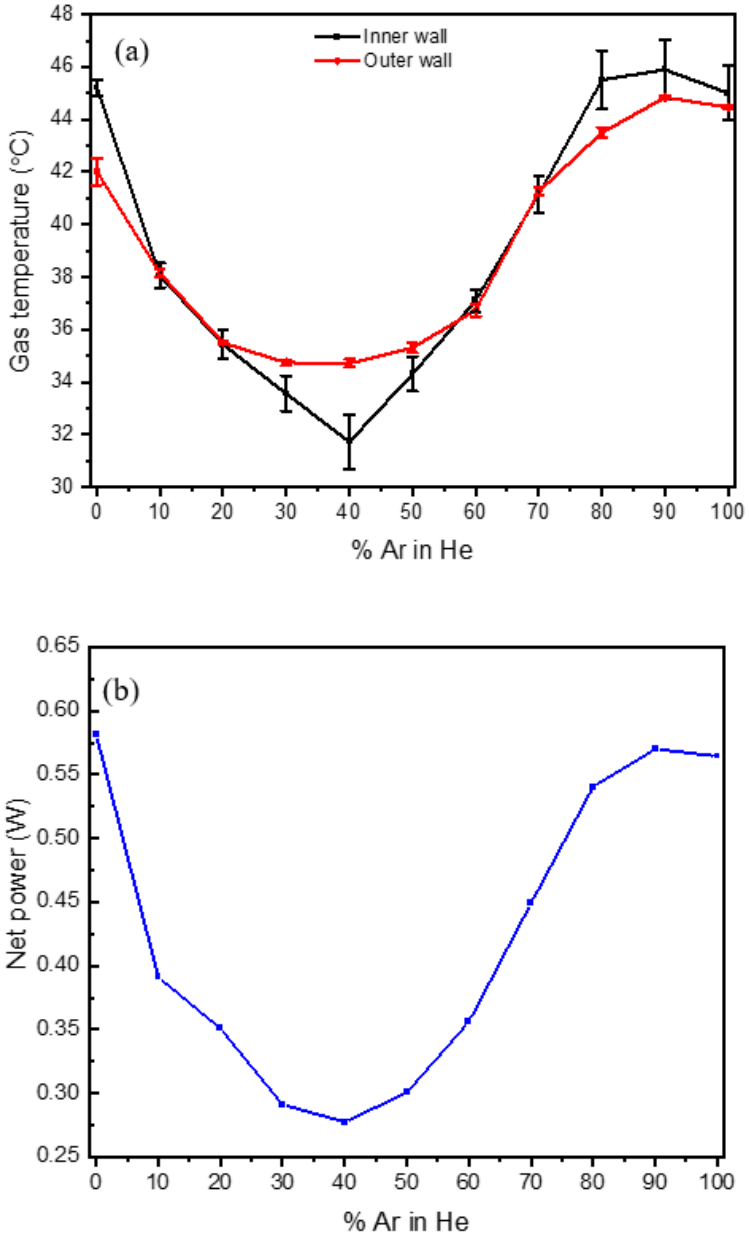

Figure 4-38: a) Inner wall temperature versus Ar:He mixture at total flow rate of 1.5 slm and maximum net power of 0.58 W and b) is the variation in absorbed power with Ar:He ratio. Error bars represent the standard error (n = 3).

Also, thermocouple (TC) measurements close to the gas outlet were obtained. Using an unshielded Type K thermocouple resulted in large inaccuracies due to RF interference. To overcome this an earthed shield was incorporated around the TC tip, which was set ~20 mm from the outlet of a similar plasma configuration which had a greater clearance to accommodate the bulky TC. Measurements required up to 300 s to reach equilibrium and the final measured temperature variation with power at 1 slm

flow was from 34 ^{o}C to 55 ^{o}C. Finally, a number of different insulating probes were placed at the gas outlet and temperature stabilised in the gas flow. One probe consisted of a polymer tube of diameter ~1 mm covered with black tape while the other was a thin 0.5 mm black insulated wire. The IR sensor, in vertical mode, Figure 4-21 (b), was then focussed on these probes and a temperature reading obtained. An emissivity value of 1 was assumed for both. In He (0.58W, 0.5 slm) the measured temperature was 38 ^{o}C and 49 ^{o}C for the tube and wire respectively, while the inner wall temperature at these conditions was 44 ^{o}C to 46 ^{o}C. In Ar (0.58W, 0.5 slm) the measured temperature was 36 ^{o}C and 39 ^{o}C for the tube and wire respectively, while the inner wall temperature at these conditions was 43 ^{o}C to 45 ^{o}C.

4.5.2 Plasma with microdroplets

Inclusion of microdroplets into the plasmas causes a reduction of the gas temperature. For a total He gas flow of 1.5 slm, the absolute temperature decreased by ≥ 6 °C at the lowest power and by 12 °C at the highest power, Figure 4-39. The temperature sensitivity to power variation was also reduced. The reduction in temperature with the addition of microdroplets was most noticeable at the lower flow rates, Figure 4-40. At the highest flow (3 slm) the temperature difference was ~1 °C.

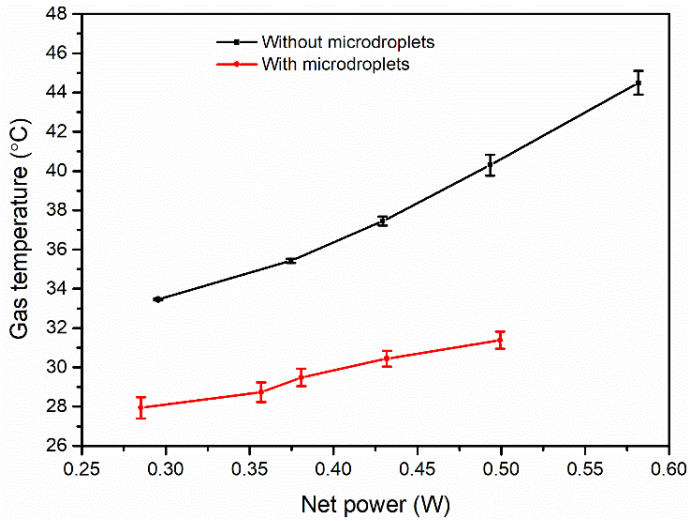

Figure 4-39: Gas temperature against RF net power in He without and with microdroplets at flow rates of 1.5 slm. Error bars represent the standard error (n = 3).

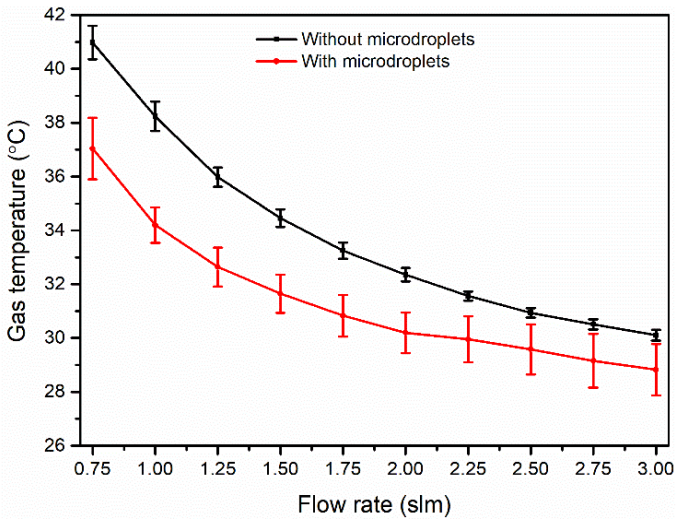

Figure 4-40: Gas temperature versus total He gas flow rate with and without microdroplets, for a fixed RF power of 0.3W. Error bars represent the standard error (n = 3).

4.6 Discussion

The IR sensor demonstrated a promising technique for measuring the plasma gas temperature however, it is necessary for measurements accuracy to precisely locate the centreline of the capillary tube and locate the IR sensor's small focal spot between the two electrodes. Otherwise, cooler background areas will be included and misleading measurements would be expected. CAD drawings was proved to be the most appropriate technique along with temperature scan in the three dimensions as demonstrated in Figure 4-22 and Figure 4-23, respectively. Also, the IR sensor revealed a very fast thermal response, Figure 4-25, to plasma gas temperature in both outer and inner wall measurements and the rise time was indicated as 3 sec when compared with the photodiode response to the plasma brightness. In addition, fast saturation and cooling time within few seconds were noticed when using the maximum power of 0.58 W and various gas flow rates.

The use of plasma-exposed microdroplets has important potential for delivering plasma-activated liquids and on-demand nanoparticles downstream over rapid timescales. Their chemistry, lifetime and transport however will be sensitive to the gas temperature in the plasma. It is well-known that the addition of small quantities of electronegative gases, e.g. O_2 or H_2O, can increase the gas temperature in noble gas plasmas as they tend to attract free electrons to their orbits therefore higher voltage and power will be required to maintain the plasma [3,64]. Hence the possibility exists for accelerated gas heating as the droplet evaporation proceeds. However, under current conditions, the reduction in gas temperature with microdroplet addition indicates that other factors, including evaporative cooling, may be involved. The significance of such cooling depends on droplet number and evaporation rate.

In the same plasma system, the average droplet evaporation rates were estimated by comparing lognormal droplet size and velocity distributions with and without plasma exposure and fitting to a D^2 – time profile [7,43]. For the conditions in this study, the evaporation rate was $\sim 5 \times 10^{-8}$ m^2 s^{-1}. The maximum droplet rate, obtained from the liquid flow rate and the droplet size distribution, is 5×10^4 s^{-1} and the total energy flux (power) required, from the plasma, for this level of evaporation is 18 mW. For the case where droplet and gas travel at same velocity, A simplified

version of the Abramzon and Sirignano model for droplet vaporisation was used which indicated that gas heating supplies a maximum energy flux of 3 mW, i.e. over 80% of the evaporation is due to droplet bombardment by charged species [65] Heinisch et al. observed experimental evaporation rates in flowing dry N_2, without plasma, approximately one order of magnitude lower than found here, supporting the conclusion that evaporation is dominated by charged particle heating of the droplet [66].

A reduction was observed in gas temperature when droplets are introduced while the power absorbed remains constant. From heat capacity considerations, the maximum difference in temperature (10 ^{o}C at 1.5 slm and 0.3 W) is equivalent to a power difference of 200 mW. At the highest flow, the small reduction in temperature is equivalent to ~40 mW. Therefore, across all conditions, the contribution of evaporative cooling (18 mW) is insufficient to account for the full temperature reduction. The introduction of electronegative gases is known to affect power absorption efficiency as the plasma couples less effectively to negative ions. In a separate study, this effect as H_2O content in the plasma reaches ~3000 ppm has been observed. However, with a maximum droplet flow rate of 5 x 10^4 s^{-1}, the evaporation contributes a maximum of 23 ppm to the average H_2O content in the plasma and hence the impact of enhanced humidity is negligible. Although the evaporated water is more likely to diffuse slowly away from the droplet, ~ 100 μm over the plasma flight time, rather than disperse uniformly throughout, most of the plasma volume remains in its original dry and electropositive state.

Plasma ion density variation also impacts on gas temperature through ion – neutral collisions [21,64,66]. Figure 4-36 (a) shows an almost linear relationship between gas temperature and power, for He, and plasma density is expected to scale linearly with absorbed power. In Figure 4-36 (b), Ar, the relationship is sub-linear. In addition, the gas temperature decreased from 46 ^{o}C to 30 ^{o}C with increasing the gas flow rate from 0.2 to 2.0 slm for He and Ar gases, Figure 4-37. The introduction of Ar into He caused the gas temperature to fall to a minimum temperature of ~33 ^{o}C when the ratio between them was 40:60 which can be explained by the change in the plasma impedance and the reduction in the net power with Ar:He mixture ratios. The minimal difference noticed between inner and outer wall measurements demonstrated the

possibility of using the outer wall temperature as an indication of the plasma gas temperature for future applications. On introducing droplets, any reduction in plasma density while constant power is maintained implies that the loss terms in the power balance equation increase; these include collisional energy lost per electron-ion pair created and the mean kinetic energy lost per electron or ion lost, which depends on T_e. Therefore, droplet introduction may lead to a reduction in plasma density and increase in electron temperature, while the absorbed power remains approximately constant.

Successful implementation of droplet in plasma (DiP) technology for application in areas such as plasma medicine, agriculture and microreaction chemistry requires knowledge and control of gas temperature and evaporation kinetics. Future developments include increasing droplet flow rate while reducing diameter, gas velocity and extending the plasma flight time. Under current conditions only the smaller droplets (< 4 μm) evaporated totally, resulting in a loss of ~5% of the total droplet number and ~0.05% of the total liquid flow volume. For a ten-fold increase in droplet rate and a reduction to an average diameter of 5 μm, while maintaining constant gas flow, the added water content increases to 2000 ppm while the evaporative cooling power also increases to ~700 mW. This provides an indication of the future scope for parameter optimisation.

4.7 Conclusions

Continuous gas temperature measurement in plasmas is important for many applications, particularly for verifiable monitoring and control of plasmas for medical treatment. The accurate measurement of gas temperature using a small-spot IR temperature probe focussed on the outer quartz wall have been shown. Calibration was obtained via careful measurement of the temperature of the inner wall in direct contact with the plasma, to account for heat loss across the thin quartz tube. For He plasmas, the temperature difference between inner and outer walls was not detectable, within the error margin. For argon, the outer wall was a few degrees hotter. This may be due to additional heating by the external electrodes since the Ar required greater applied

power for the same net power. While the emissivity of quartz is reasonably constant at 0.93, Cu emissivity can vary widely depending on surface condition of the metal. We estimate the electrode temperature between 50 ^{o}C and 80 ^{o}C. Electrode heating of the quartz outer surface may therefore lead to an overestimation of gas temperature. Plasma gas temperature was observed to increase, as expected, with increasing power and reduced gas flow. The maximum temperature over the full operating range was < 50 ^{o}C and slight difference was observed between pure He and Ar plasmas. For Ar/He mixtures, the fall in temperature on adding Ar is clearly due to the reduction in absorbed power caused by a change in the electrical characteristics of the plasma. The non-invasive low-cost IR probe demonstrated sub-second resolution and performs much better than bulky shielded thermocouple probes that obstruct the gas flow and have a response time of many minutes. Compared to expensive thermal image cameras that can resolve small plasma dimensions, the small-spot IR sensor can be kept in-situ and its output directly used for feedback control. The sensor also provides useful temperature information for more complex plasma configurations. A cooling of the plasma on introduction of a microdroplet stream is observed. Previous estimates of such temperatures using OES fitting had a wide error margin (~50 ^{o}C) and suggested an average of >75 ^{o}C. This is an important parameter in modelling the droplet evaporation rate and the resultant enhancement of overall humidity. The observed fall can be attributed to evaporative cooling and since an increase in humidity generally leads to increased gas heating, these results indicate that the average humidity remains approximately constant and confirms previous droplet measurements which show limited size reduction due to evaporation during transit through the plasma [7].

4.8 References

[1] N. Hendawy, H. McQuaid, D. Mariotti, P. Maguire, Continuous gas temperature measurement of cold plasma jets containing microdroplets, using a focussed spot IR sensor, Plasma Sources Sci. Technol. 29 (2020). https://doi.org/10.1088/1361-6595/aba2aa.

[2] S. Zhou, L. Su, T. Shi, T. Zheng, Y. Tong, W. Nie, X. Che, J. Zhao, Experimental study on the diffusive flame stabilization mechanism of plasma injector driven by AC dielectric barrier discharge, J. Phys. D. Appl. Phys. 52 (2019). https://doi.org/10.1088/1361-6463/ab15cd.

[3] P.J. Bruggeman, N. Sadeghi, D.C. Schram, V. Linss, Gas temperature determination from rotational lines in non-equilibrium plasmas: A review, Plasma Sources Sci. Technol. 23 (2014). https://doi.org/10.1088/0963-0252/23/2/023001.

[4] M. Aramaki, Y. Okumura, M. Goto, S. Muto, S. Morita, K. Sasaki, Measurements of gas temperature in high-density helicon-wave H2 plasmas by diode laser absorption spectroscopy, Japanese J. Appl. Physics, Part 1 Regul. Pap. Short Notes Rev. Pap. 44 (2005) 6759–6763. https://doi.org/10.1143/JJAP.44.6759.

[5] A.A. Fridman, L. Boufendi, T. Hbid, B. V. Potapkin, A. Bouchoule, Dusty plasma formation: Physics and critical phenomena. Theoretical approach, J. Appl. Phys. 79 (1996) 1303–1314. https://doi.org/10.1063/1.361026.

[6] A. Schmidt-Bleker, S. Reuter, K.D. Weltmann, Quantitative schlieren diagnostics for the determination of ambient species density, gas temperature and calorimetric power of cold atmospheric plasma jets, J. Phys. D. Appl. Phys. 48 (2015) 175202. https://doi.org/10.1088/0022-3727/48/17/175202.

[7] P.D. Maguire, C.M.O. Mahony, C.P. Kelsey, A.J. Bingham, E.P. Montgomery, E.D. Bennet, H.E. Potts, D.C.E. Rutherford, D.A. McDowell, D.A. Diver, D. Mariotti, Controlled microdroplet transport in an atmospheric pressure microplasma, Appl. Phys. Lett. 106 (2015). https://doi.org/10.1063/1.4922034.

[8] J.L. Walsh, M.G. Kong, Room-temperature atmospheric argon plasma jet

sustained with submicrosecond high-voltage pulses, Appl. Phys. Lett. 91 (2007) 2005–2008. https://doi.org/10.1063/1.2817965.

[9] M. Bazavan, M. Teodorescu, G. Dinescu, Confirmation of OH as good thermometric species for gas temperature determination in an atmospheric pressure argon plasma jet, Plasma Sources Sci. Technol. 26 (2017). https://doi.org/10.1088/1361-6595/aa723c.

[10] D. Mariotti, Y. Shimizu, T. Sasaki, N. Koshizaki, Gas temperature and electron temperature measurements by emission spectroscopy for an atmospheric microplasma, J. Appl. Phys. 101 (2007) 1–8. https://doi.org/10.1063/1.2409318.

[11] A. Gulec, F. Bozduman, A.M. Hala, Atmospheric Pressure 2.45-GHz Microwave Helium Plasma, IEEE Trans. Plasma Sci. 43 (2015) 786–790. https://doi.org/10.1109/TPS.2015.2403280.

[12] M. Tuszewski, Ion and gas temperatures of 0.46 MHz inductive plasma discharges, J. Appl. Phys. 100 (2006) 0–5. https://doi.org/10.1063/1.2337167.

[13] K.K. Jayapalan, O.H. Chin, Measurement of neutral gas temperature in a 13.56 MHz inductively coupled plasma, AIP Conf. Proc. 1657 (2015). https://doi.org/10.1063/1.4915242.

[14] Y. Hu, J. Yang, C. Feng, C. Jin, W. Wang, L. Zhuge, X. Wu, A Convenient Method to Realize Large-Area APGD for Wool Surface Modification, IEEE Trans. Plasma Sci. 47 (2019) 2629–2636. https://doi.org/10.1109/TPS.2019.2907099.

[15] S.Z. Li, Z.Y. Li, Y. Wu, J. Zhang, Spectroscopic diagnosis of gas temperature in blown-out plasma of atmospheric-pressure microwave oxygen plasma torch, Phys. Plasmas. 25 (2018). https://doi.org/10.1063/1.5009591.

[16] S.Y. Yoon, C. Yi, S. Eom, S. Park, S.B. Kim, S. Ryu, S.J. Yoo, Effects of gas temperature in the plasma layer on RONS generation in array-type dielectric barrier discharge at atmospheric pressure, Phys. Plasmas. 24 (2017). https://doi.org/10.1063/1.5003205.

[17] X. Li, N. Yuan, P. Jia, Investigation of a plasma jet generated by high voltage discharge at atmospheric pressure, Adv. Mater. Res. 383–390 (2012) 5907–

5911. https://doi.org/10.4028/www.scientific.net/AMR.383-390.5907.

[18] J. Sláma, Plasma flow and temperature in a gliding reactor with different electrode configurations, Acta Polytech. 52 (2012) 61–64. https://doi.org/10.14311/1516.

[19] F. Brehmer, S. Welzel, M.C.M. Van De Sanden, R. Engeln, CO and byproduct formation during CO2 reduction in dielectric barrier discharges, J. Appl. Phys. 116 (2014). https://doi.org/10.1063/1.4896132.

[20] X.P. Lu, M. Laroussi, Electron density and temperature measurement of an atmospheric pressure plasma by millimeter wave interferometer, Appl. Phys. Lett. 92 (2008) 2007–2009. https://doi.org/10.1063/1.2840194.

[21] S. Hofmann, A.F.H. Van Gessel, T. Verreycken, P. Bruggeman, Power dissipation, gas temperatures and electron densities of cold atmospheric pressure helium and argon RF plasma jets, Plasma Sources Sci. Technol. 20 (2011). https://doi.org/10.1088/0963-0252/20/6/065010.

[22] T. Verreycken, A.F.H. Van Gessel, A. Pageau, P. Bruggeman, Validation of gas temperature measurements by OES in an atmospheric air glow discharge with water electrode using Rayleigh scattering, Plasma Sources Sci. Technol. 20 (2011). https://doi.org/10.1088/0963-0252/20/2/024002.

[23] T. Oshita, H. Kawano, T. Takamatsu, H. Miyahara, A. Okino, Temperature Controllable Atmospheric Plasma Source, IEEE Trans. Plasma Sci. 43 (2015) 1987–1992. https://doi.org/10.1109/TPS.2015.2428696.

[24] H. Kawano, T. Takamatsu, Y. Matsumura, H. Miyahara, A. Iwasawa, A. Okino, Influence of gas temperature in atmospheric non-equilibrium plasma on bactericidal effect, Biocontrol Sci. 23 (2018) 167–175. https://doi.org/10.4265/bio.23.167.

[25] R. Perekrestov, P. Kudrna, M. Tichý, The deposition of titanium dioxide nanoparticles by means of a hollow cathode plasma jet in dc regime, Plasma Sources Sci. Technol. 24 (2015). https://doi.org/10.1088/0963-0252/24/3/035025.

[26] R. Zhang, G. Luo, The mode of gliding arc discharge and its characteristics, Proc. IEEE Int. Conf. Prop. Appl. Dielectr. Mater. 2018-May (2018) 305–310.

https://doi.org/10.1109/ICPADM.2018.8401270.

[27] A. V. Gerasimov, A.P. Kirpichnikov, L.A. Rachevsky, Determination of gas temperature in the plasmatron channel according to the known distribution of electronic temperature, Therm. Sci. 17 (2013) 1251–1254. https://doi.org/10.2298/TSCI1304251G.

[28] C.J. Chen, S.Z. Li, Spectroscopic measurement of plasma gas temperature of the atmospheric-pressure microwave induced nitrogen plasma torch, Plasma Sources Sci. Technol. 24 (2015). https://doi.org/10.1088/0963-0252/24/3/035017.

[29] P. Bruggeman, R. Brandenburg, Atmospheric pressure discharge filaments and microplasmas: Physics, chemistry and diagnostics, J. Phys. D. Appl. Phys. 46 (2013). https://doi.org/10.1088/0022-3727/46/46/464001.

[30] K.E. Evdokimov, M.E. Konischev, V.F. Pichugin, Z. Sun, Study of argon ions density and electron temperature and density in magnetron plasma by optical emission spectroscopy and collisional-radiative model, Resour. Technol. 3 (2017) 187–193. https://doi.org/10.1016/j.reffit.2017.04.002.

[31] line spectrum | physics | Britannica, (n.d.). https://www.britannica.com/science/line-spectrum (accessed April 28, 2022).

[32] D. Wang, W. Liu, Y. Wu, L. Hang, H. Yu, N. Jin, Characteristics of plasma source for the plasma polishing of super smooth optics, Phys. Procedia. 19 (2011) 412–415. https://doi.org/10.1016/j.phpro.2011.06.184.

[33] LIFBASE 2.0 Download (Free) - Lifbase2.exe, (n.d.). https://lifbase.software.informer.com/2.0/ (accessed April 28, 2022).

[34] M. Santos, C. Nôl, T. Belmonte, L.L. Alves, Microwave capillary plasmas in helium at atmospheric pressure, J. Phys. D. Appl. Phys. 47 (2014). https://doi.org/10.1088/0022-3727/47/26/265201.

[35] J.P. Booth, D. Marinov, M. Foucher, O. Guaitella, D. Bresteau, L. Cabaret, C. Drag, Gas temperature measurements in oxygen plasmas by high-resolution Two-Photon Absorption Laser-induced Fluorescence, J. Instrum. 10 (2015). https://doi.org/10.1088/1748-0221/10/11/C11003.

[36] H. Photonics, Raman spectroscopy | Hamamatsu Photonics, (n.d.). https://www.hamamatsu.com/eu/en/applications/analytical-equipment/raman-spectroscopy.html (accessed April 21, 2022).

[37] F. Brehmer, S. Welzel, B.L.M. Klarenaar, H.J. Van Der Meiden, M.C.M. Van De Sanden, R. Engeln, Gas temperature in transient CO2 plasma measured by Raman scattering, J. Phys. D. Appl. Phys. 48 (2015). https://doi.org/10.1088/0022-3727/48/15/155201.

[38] L. Prevosto, G. Artana, B. Mancinelli, H. Kelly, Schlieren technique applied to the arc temperature measurement in a high energy density cutting torch, J. Appl. Phys. 107 (2010). https://doi.org/10.1063/1.3291099.

[39] S. Iseni, R. Michaud, P. Lefaucheux, G.B. Sretenović, V. Schulz-Von Der Gathen, R. Dussart, On the validity of neutral gas temperature by emission spectroscopy in micro-discharges close to atmospheric pressure, Plasma Sources Sci. Technol. 28 (2019). https://doi.org/10.1088/1361-6595/ab1dfb.

[40] S. Askari, I. Levchenko, K. Ostrikov, P. Maguire, D. Mariotti, Crystalline Si nanoparticles below crystallization threshold: Effects of collisional heating in non-thermal atmospheric-pressure microplasmas, Appl. Phys. Lett. 104 (2014). https://doi.org/10.1063/1.4872254.

[41] P. Bruggeman, F. Iza, P. Guns, D. Lauwers, M.G. Kong, Y.A. Gonzalvo, C. Leys, D.C. Schram, Electronic quenching of OH(A) by water in atmospheric pressure plasmas and its influence on the gas temperature determination by OH(A-X) emission, Plasma Sources Sci. Technol. 19 (2010). https://doi.org/10.1088/0963-0252/19/1/015016.

[42] O. Motret, C. Hibert, S. Pellerin, J.M. Pouvesle, Rotational temperature measurements in atmospheric pulsed dielectric barrier discharge - gas temperature and molecular fraction effects, J. Phys. D. Appl. Phys. 33 (2000) 1493–1498. https://doi.org/10.1088/0022-3727/33/12/311.

[43] P. Maguire, D. Rutherford, M. Macias-Montero, C. Mahony, C. Kelsey, M. Tweedie, F. Pérez-Martin, H. McQuaid, D. Diver, D. Mariotti, Continuous In-Flight Synthesis for On-Demand Delivery of Ligand-Free Colloidal Gold Nanoparticles, Nano Lett. 17 (2017) 1336–1343.

https://doi.org/10.1021/acs.nanolett.6b03440.

[44] E.D. Bennet, C.M.O. Mahony, H.E. Potts, P. Everest, D. Rutherford, S. Askari, D.A. McDowell, D. Mariotti, C. Kelsey, F. Perez-Martin, N. Hamilton, P. Maguire, D.A. Diver, Precision charging of microparticles in plasma via the Rayleigh instability for evaporating charged liquid droplets, J. Aerosol Sci. 100 (2016) 53–60. https://doi.org/10.1016/j.jaerosci.2016.05.002.

[45] Energy bandgap of AlGaAs, (n.d.). https://www.batop.de/information/Eg_GaAs.html (accessed April 29, 2022).

[46] K. Knoerzer, A.B. Murphy, M. Fresewinkel, P. Sanguansri, J. Coventry, Evaluation of methods for determining food surface temperature in the presence of low-pressure cool plasma, Innov. Food Sci. Emerg. Technol. 15 (2012) 23–30. https://doi.org/10.1016/j.ifset.2012.02.008.

[47] J.A. Dutten, Blackbody Radiation | Astronomy 801: Planets, Stars, Galaxies, and the Universe, (n.d.). https://www.e-education.psu.edu/astro801/content/l3_p5.html (accessed April 29, 2022).

[48] Micro-Epsilon, Operating Instructions - thermoMeter CS, 49 (2021). https://www.micro-epsilon.com/download/manuals/man--thermoMETER-CT--en.pdf.

[49] E. Imaz, R. Alonso, C. Heras, I. Salinas, E. Carretero, C. Carretero, Infrared thermometry system for temperature measurement in induction heating appliances, IEEE Trans. Ind. Electron. 61 (2014) 2622–2630. https://doi.org/10.1109/TIE.2013.2281166.

[50] Optical Resolution, (n.d.). https://www.optris.co.uk/optical-resolution (accessed April 22, 2022).

[51] Measuring Small Objects with Infrared Pyrometers | Calex, (n.d.). https://www.calex.co.uk/measuring-small-objects-with-infrared-pyrometers/ (accessed April 29, 2022).

[52] Infrared pyrometers for universal measurements, (n.d.). https://www.micro-epsilon.com/temperature-sensors/thermoMETER_CT_basic/?sLang=en (accessed April 29, 2022).

[53] Introduction to Infrared (Part 1): The Physics Behind Thermal Imaging - Opgal, (n.d.). https://www.opgal.com/blog/thermal-cameras/the-physics-behind-thermal-imaging (accessed April 20, 2022).

[54] N. Rajic, N. Street, A performance comparison between cooled and uncooled infrared detectors for thermoelastic stress analysis, Quant. Infrared Thermogr. J. 11 (2014) 207–221. https://doi.org/10.1080/17686733.2014.962835.

[55] Opgal, Intro to IR (Part 3): Sensitivity, resolution and frame rate, (n.d.). https://www.opgal.com/blog/thermal-cameras/intro-to-ir-part-3-sensitivity-resolution-and-frame-rate/ (accessed April 20, 2022).

[56] FLIR A320 Tempscreen Fixed-Mount Thermal Camera for EBT Screening | Teledyne FLIR, (n.d.). https://www.flir.co.uk/products/flir-a320/ (accessed April 29, 2022).

[57] Intro to IR (Part 5): Lens - Opgal, (n.d.). https://www.opgal.com/blog/thermal-cameras/intro-to-ir-part-5-lens/ (accessed April 20, 2022).

[58] S. Mazouffre, P. Echegut, M. Dudeck, A calibrated infrared imaging study on the steady state thermal behaviour of Hall effect thrusters, Plasma Sources Sci. Technol. 16 (2007) 13–22. https://doi.org/10.1088/0963-0252/16/1/003.

[59] W. Fu, C. Zhang, C. Nie, X. Li, Y. Yan, A high efficiency low-temperature microwave-driven atmospheric pressure plasma jet, Appl. Phys. Lett. 114 (2019). https://doi.org/10.1063/1.5108538.

[60] C. Engelhard, A. Scheffer, T. Maue, G.M. Hieftje, W. Buscher, Application of infrared thermography for online monitoring of wall temperatures in inductively coupled plasma torches with conventional and low-flow gas consumption, Spectrochim. Acta - Part B At. Spectrosc. 62 (2007) 1161–1168. https://doi.org/10.1016/j.sab.2007.07.010.

[61] D.P. Dowling, M. Donegan, P.J. Cullen, V.J. Law, V. Milosavljevic, Importance of plasma thermal energy transfer for plasma jet systems, IEEE Trans. Plasma Sci. 42 (2014) 2426–2427. https://doi.org/10.1109/TPS.2014.2326962.

[62] J. Jang, W. Choe, B.J. Peterson, D.C. Seo, K. Mukai, R. Sano, S. Oh, S.H. Hong, J. Hong, H.Y. Lee, Tomographic reconstruction of two-dimensional

radiated power distribution during impurity injection in KSTAR plasmas using an infrared imaging video bolometer, Curr. Appl. Phys. 18 (2018) 461–468. https://doi.org/10.1016/j.cap.2018.01.009.

[63] https://www.micro-epsilon.com/temperature-sensors/thermoMETER_CT_basic/?sLang=en, (n.d.).

[64] D. Mariotti, Nonequilibrium and effect of gas mixtures in an atmospheric microplasma, Appl. Phys. Lett. 92 (2008) 2006–2009. https://doi.org/10.1063/1.2912039.

[65] B. ABRAMZON, W. SIRIGNANO, Droplet vaporization model for spray combustion calculations, 32 (1988) 1605–1618. https://doi.org/10.2514/6.1988-636.

[66] C. Heinisch, J.B. Wills, J.P. Reid, T. Tschudi, C. Tropea, Temperature measurement of single evaporating water droplets in a nitrogen flow using spontaneous raman scattering, Phys. Chem. Chem. Phys. 11 (2009) 9720–9728. https://doi.org/10.1039/b908555f.

5 Measurement of plasma charged microdroplets

Work in preparation for submission [1]

Measurement of the charge on individual charged particles had never been accomplished before for systems at high and atmospheric pressure. Over the previous years a research project was instituted in NIBEC (Ulster University) to attempt such measurements. A wide range of techniques were progressively attempted and a database of measurement results were obtained. In this thesis a subset of this data, representing measurements taken using the plate collector and the double ring electrodes were selected. These were critically analysed for accuracy and consistency and a further subset selected from a wide range of plasma conditions, comprising the data with the highest reliability/repeatability and accuracy. The measurement setup for both selected techniques (ring and plate) are given in the experimental methods section of each chapter. Also given are the complete plasma conditions regarding power, gas flow and electrode geometry as well as droplet size range and velocity range.

5.1 Droplet charging

UV [2] and corona discharges [3] can be utilised in non-contact charging from the gas-phase. In the former, analytical and numerical techniques were used to analyse multi-charged particles and study their photoionization, recombination, diffusion and electric field transport. This technique is based on charging aerosol particles in nanometre size range using UV photoionization where particles are charged by absorbing UV photons and emitting electrons which collides with the surrounding gas and produce ions which remain to form an electrostatic field with a positive charge. The average charge for particles was estimated from a numerical model and was found to be controlled by changing the bias voltage [2]. William et al. provided charge distributions by calculating ion-aerosol attachment coefficients and compared theoretical charge predictions with experimental results using corona discharge. They found also that the difference between positive and negative ions physical properties result in high discrepancy in the number of positive and negative charged particles, at larger radius particles, in particular [3]. Steady-state production of droplets of fixed

size and charge distribution is possible with corona assisted electrospray and moderately conductive liquids. However, to achieve high charge to mass levels requires increased flow rates, which also leads to larger droplets, > 100 μm, where the surface to volume advantages is significantly reduced. For low conductivity liquids, the drastic decrease in dielectric relaxation speed result in reduction in the charge to fully charge droplets before they detach [4]. Rayleigh limit of charge (Q_R) is the maximum charge that can be held on a drop before it split into smaller droplets. This limit is also defined by the strength of the electrical breakdown and depend mainly on the size of the droplets as shown in the following equation [5]:

$$Q_R = 8\pi\ (\varepsilon_0 \gamma R^3)^{1/2} \qquad \textit{Equation 8}$$

Where γ is the surface tension and ε_0 is the permittivity. This limit is often used as a benchmark. Theoretical and simulation estimates of diffusion and field charging in unipolar corona discharges are in the range 0.1 – 1% of Q_R [6–8], since they depend on the product of ion density and residence time ($N_i t$) [9]. Also, corona-assisted ES is generally limited to positively charged droplets since operating in negative mode risks high energy ion bombardment of the meniscus, instability and gas breakdown [10,11]. Corona charging depends mainly on ions, of either polarity, as free electrons attach to air molecules quickly, although additional free electron contributions to charging have been achieved in pure electropositive gases [12,13].

5.2 Droplet charging in a plasma

Charge generation by glow discharge plasma sources has an advantage over corona that it can provide higher plasma densities by up to 10^6 times in the gas-phase [14], and there is growing interest in incorporating aerosols for plasma – liquid based applications using various droplet generation sources [15]. In addition, non-contact low-temperature or cold plasma charging, apart from generating an internal electric field, provides more reactive species to the droplet reactor, specifically a high flux of gas-phase electrons striking the surface and likely initiate electron-mediated chemistry at the liquid – gas interface. The reduction of $HAuCl_4$ to form Au nanoparticles in

plasma irradiated microdroplets was demonstrated at synthesis rates up to seven orders of magnitude faster than traditional routes [16]. Enhanced reaction rates have also been observed in other plasma – droplet systems [17–20]. The low energy electrons provided by the gas phase are expected to solvate at the liquid surface and form a thin layer of charge, leading to internal electric fields and solvated electron-initiated reduction reactions. However gold salt reduction in plasma-irradiated microdroplets requires very high electron fluxes to account for observed reaction rates [16].

Particle charging in plasmas has received considerable theoretical attention for many decades. Experiments in low pressure plasma, where gas-phase species collisions are rare, have been performed to validate the particle charging theoretical predictions where acquired particle charge and associated electron flux have been also estimated. However, at atmospheric pressure, the large number of collisions within the plasma adds considerable complexity and to date, measurement of acquired charge has not been achieved. Without knowledge of the surface charge, essential estimates of electron flux to the microdroplet cannot be made. In this chapter, measurements of the average charge acquired by liquid droplets after passing through a low-temperature plasma will be presented. The droplets have diameters in the range 5 μm – 30 μm, sufficiently large to ensure survival while retaining a large area to volume ratio [21].

5.3 Experimental methods

5.3.1 Plasma details

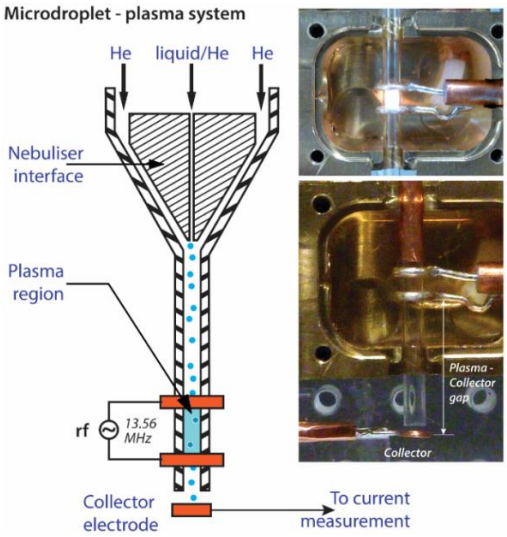

Figure 5-1: RF atmospheric pressure plasma (APP) configuration composed of double copper ring electrodes connected to RF power source, microdroplets and collector configrantion.

An RF-driven (13.56 MHz) atmospheric pressure plasma was generated inside a 2 mm inner diameter quartz tube, between two exterior concentric Cu electrodes, ~2 mm apart and operated in helium at flow rates between 1 – 7 slm. The plasma impedance and net power absorption were monitored continuously using an inline VI probe (Impedans Octiv Suite 2.0). The water vapour content, monitored using an inline Xentaur XTR-100 Dew Point Meter, was maintained below 100 ppm, without droplets present. The gas temperature was monitored using a Micro-Epsilon CT precise infrared sensor (CT-CF22-C1 Miniature-Pyrometer). The focal spot, with a diameter of 0.6 mm at a stand-off distance of 10 mm, was located on the quartz wall between electrodes [22]. Maximum gas temperatures were 46 ^{o}C for a net input power of 0.6 W at the lowest flow rate (0.6 slm) and without droplets. The introduction of microdroplets reduced the gas temperature by up to 10 ^{o}C. Microdroplets with average diameters in the range 12 μm – 15 μm were obtained from a Burgener Mira Mist X-175 nebuliser and were injected into a helium gas flow (Q_1) of 0.7 slm upstream of the plasma. The nebuliser was driven by a separate He gas flow (Q_2) and the total plasma gas flow was $Q = Q_1 + Q_2$. The liquid (H_2O) was supplied from a syringe pump at 5 μL min^{-1} (Q_L).

5.3.2 Plasma droplets details

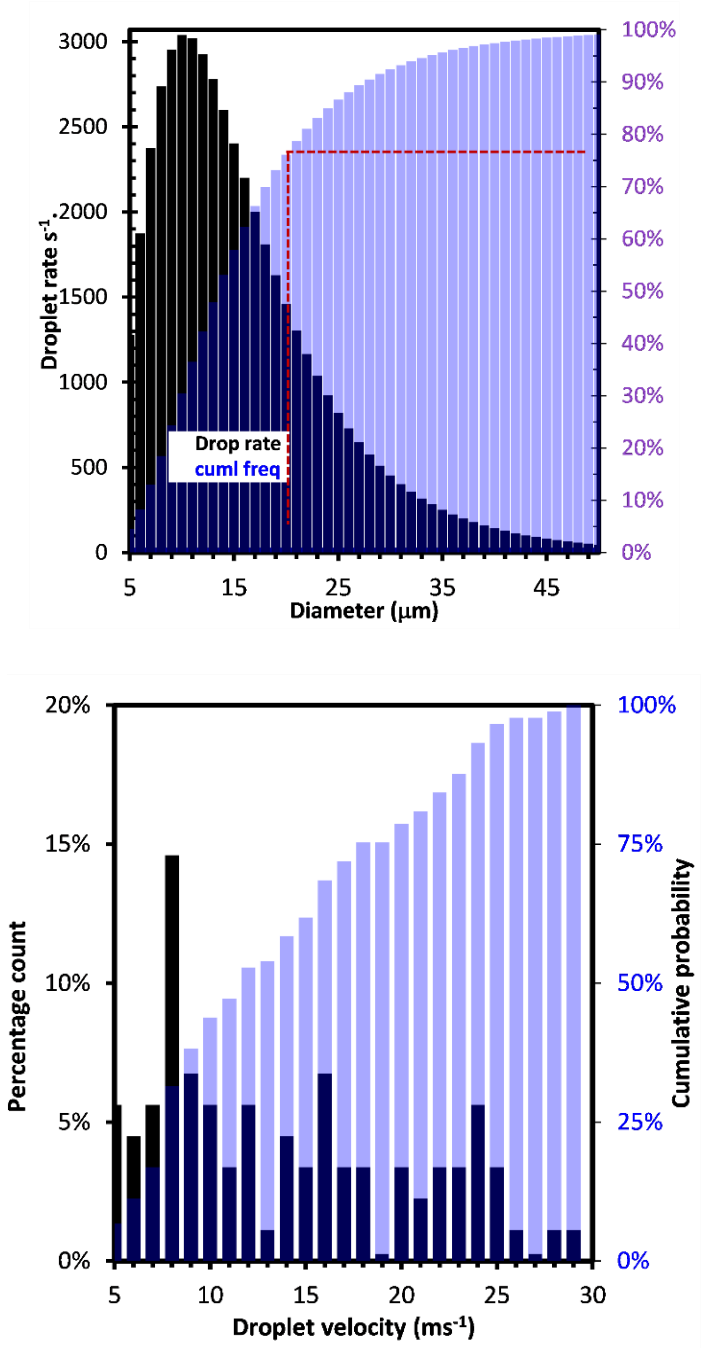

Figure 5-2: (a) Droplet rate versus size for measured lognormal diameter distribution (count median diameter = 13.6 µm, geometric std. deviation = 1.7) for a total droplet rate of 5 x 10^4 s^{-1}, calculated from the measured distribution of droplet diameters and the injected liquid volume (300 µL h^{-1}). Also shown is the cumulative probability. The net plasma power was 1 W, and the total gas flow was 3.5 SLM. (b) Droplet velocity distribution and cumulative frequency distribution showing 50% of droplets travel at ≤ 12 ms^{-1}, and 75% at ≤ 17 ms^{-1}. Measurements were obtained at an average of 1.5 mm from the plasma capillary outlet. The peak and average gas velocities within the capillary are ≤ 16 ms^{-1} and ≤ 32 ms^{-1} respectively, assuming laminar flow.

In-flight measurements of individual droplet diameters and velocities were previously obtained from high resolution droplet imaging using similar experimental setup in NIBEC. A stream of nanodroplets from Burgener Mira Mist X-175 nebuliser was magnified by a Quester QM-100 microscope and imaged by Andor IStar CCD camera for droplets sizes and velocities measurements. The droplet sizes were found to follow a known lognormal distribution which is related to measured size distribution depending on droplets count median diameter (CMD) and geometric standard deviation (GSD). These measurements have a high accuracy due to the high resolution of the measuring techniques which has 1805 x 1805 imaging resolution, equivalent to a limit of 1.7×10^{-6} m per imaged pixel for the microscope imaging while the camera was capable of providing exposure time of 10 μs - 20 μs. The lognormal distribution is based on the experimental sample distribution measurements and the calculated CMD and GSD values [21]. The total droplet rate is $\sim 5 \times 10^{4}$ s^{-1}, equivalent to 1 droplet arriving every ~20 μs. Within the plasma capillary, the gas velocity radial profile is parabolic due to laminar flow conditions with peak and average velocities of 32 ms^{-1} and 16 ms^{-1}, respectively, at a gas flow of 3.5 slm. Therefore, the average droplet spacing is in the range ≤ 340 μm to 680 μm. However, on exiting the plasma capillary, the droplets slow down. Measurements indicate 50% of droplets travel at ≤ 12 ms^{-1} and 75% at ≤ 17 ms^{-1} with an overall average velocity of 13.2 ms^{-1} (SD = 6.7). Under maximum gas flow conditions, 7.5 slm, the average measured velocity is 28.2 ms^{-1} (SD = 15.2). At a gas flow of 3.5 slm, the droplet diameter distribution is lognormal with a count median diameter (CMD) of 13.9 μm and a geometric standard deviation (GSD) of 1.7. Over 75% of droplets have a diameter ≤ 17 μm. A similar size distribution is obtained for other flow conditions. Example size and droplet velocity distributions are demonstrated in Figure 5-2.

5.4 Droplet charge measurement

Our main objective is to measure the average droplet charge using a low-density stream of microdroplets impacting a contact electrode after passing through a short atmospheric pressure plasma region.

5.4.1 Collector electrical response simulation

When a droplet contacts a solid electrode, e.g., a metal wire or sheet, its charge is transferred, and a current is measured. A charged particle approaching a conducting electrode creates an image charge and with a finite collector electrode geometry, where Borzabadi et al. [23] has provided an approximation of the magnitude of the image charge as following:

$$q' = -q\left(1 - \frac{x}{\sqrt{{R_C}^2 + x^2}}\right) \qquad \textit{Equation 9}$$

where x is the distance between the droplet and collector and R_C is the collector radius. At a distance, δx, where $\delta x << R_C$, the induced charge reaches its maximum, $q' \cong q$. The measured current is:

$$i = \frac{dq'}{dt} = \frac{qv{R_C}^2}{\sqrt{\left({R_C}^2 + \delta x^2\right)^3}} \qquad \textit{Equation 10}$$

and for a constant velocity, v, the current due to the particle just arriving at the collector, i.e., $\delta x \sim 0$, is $i = qv/R_C$. If a stream of charged particles, spaced a distance R_C apart, arrives at the collector the second and third particles induce currents $i_2 \cong i_1/3$ and $i_3 \cong i_1/11$ respectively, with particles further away having negligible effect. Figure 5-3 shows the current pulse with a 2 mm radius collector and for a maximum droplet charge typical current pulse amplitudes and lengths are in the 10^{-9} A and 10^{-3} s range. Where Figure 5-4 reveals the relative response of an electrode, of radius R, to the arrival of a charged particle depends on the particle distance, x/R, from the electrode. Therefore, the inter-droplet spacing needs to be $> 2R_C$ to measure individual droplets and to ensure that the current pulses are detectable, R_C must be sufficiently small. However, if R_C is too small, the droplet is carried around it on the gas streamlines and no contact is made.

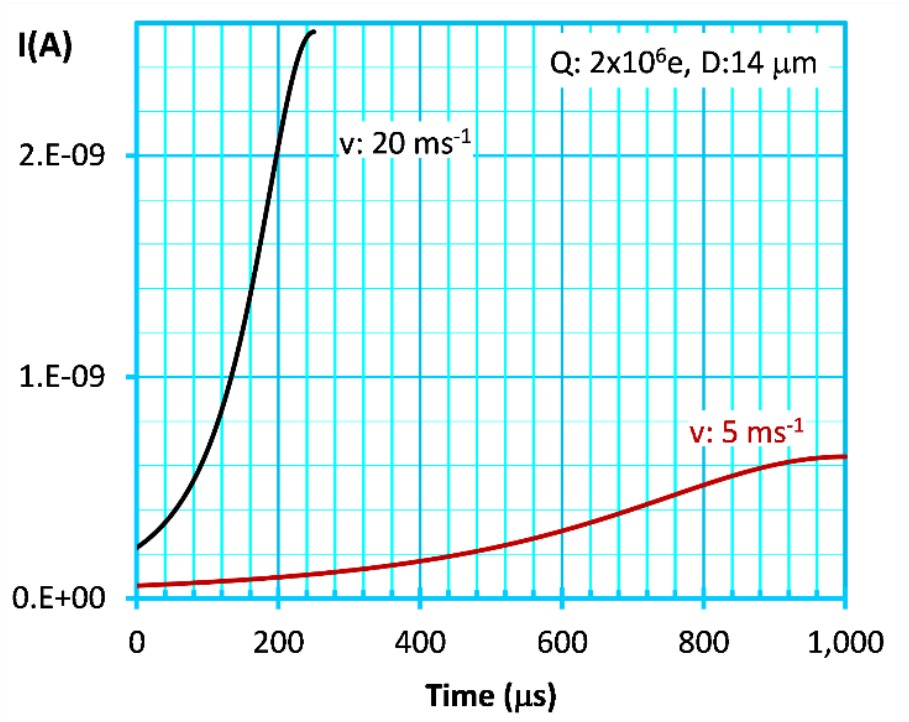

Figure 5-3: Current pulses from Equation 9 for single droplet of diameter 14 µm. The collector radius is 1.5 mm.

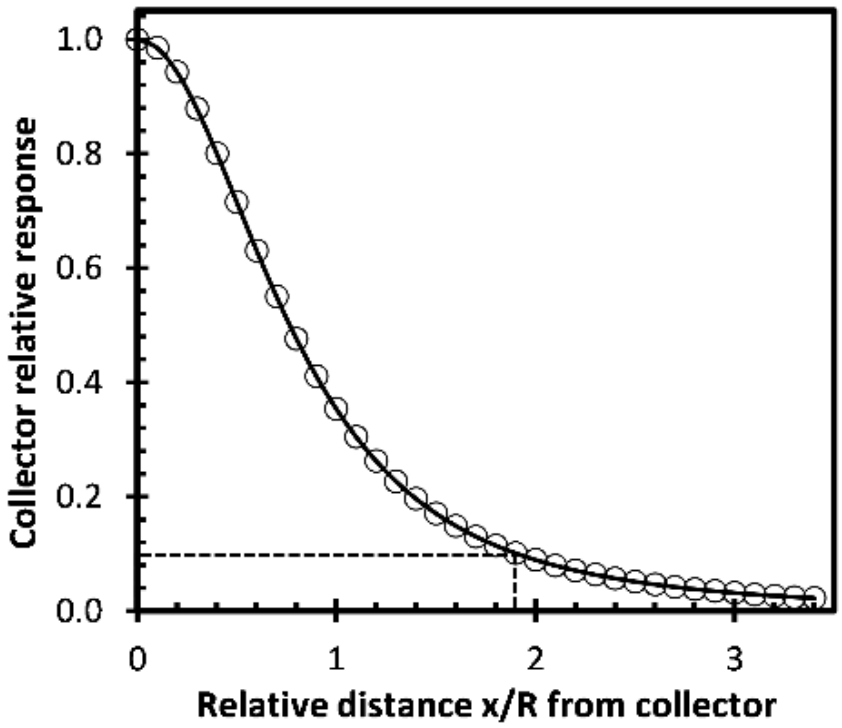

Figure 5-4: Electrode relative response to charged particle flux versus particle distance, normalised to electrode radius, Rc.

5.4.2 Current measurements

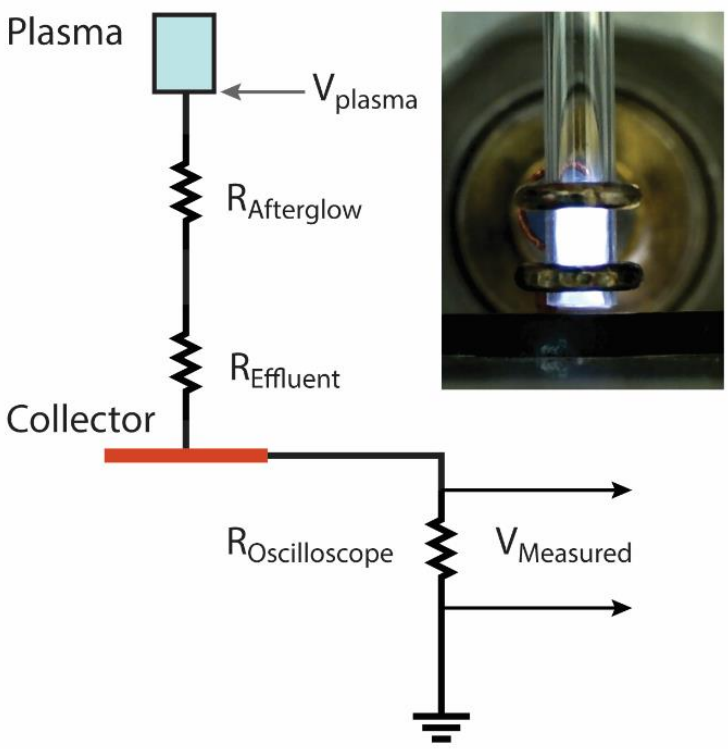

Figure 5-5: Measurement equivalent circuit.

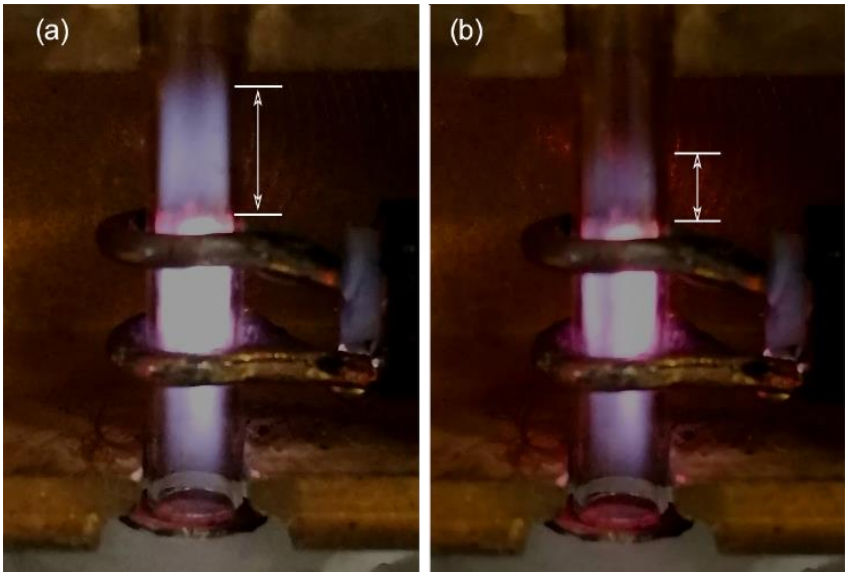

Figure 5-6: (a) without droplets. The length of the luminous afterglow is illustrated by the arrow and compared with (b) when microdroplets are introduced.

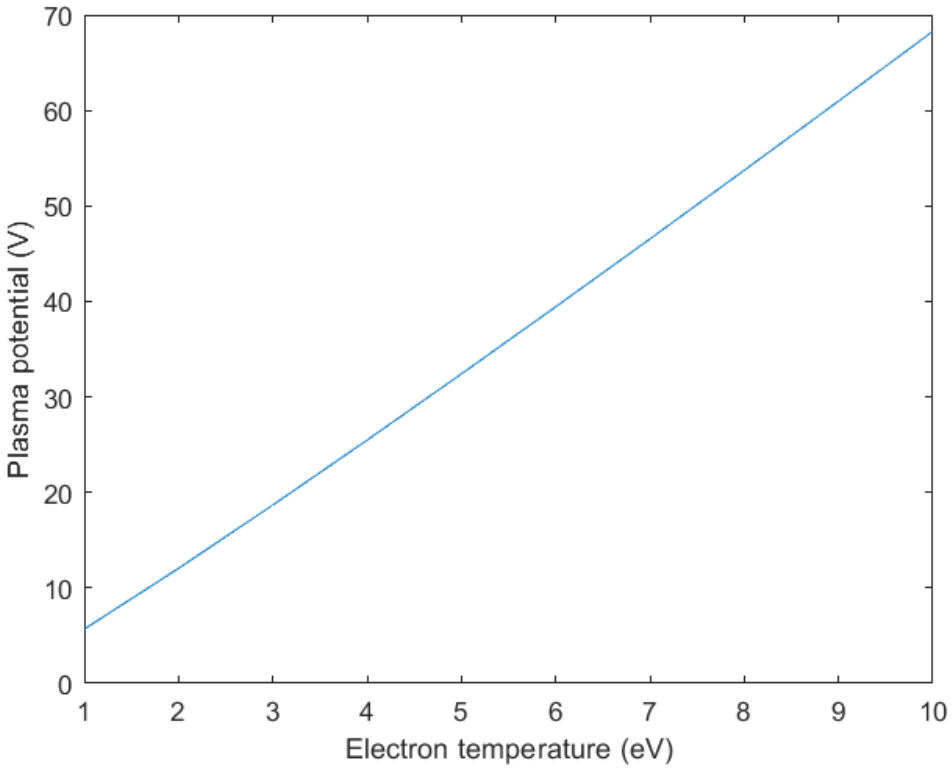

Figure 5-7: Plasma potential versus electron temperature for estimated T_{ion} ~500 K in He.

The electrical equivalent circuit between plasma and collector represents three spatial regions, namely the high conductivity plasma itself between the electrodes, a low resistance plasma region, often labelled "afterglow (R_{Ag})" and a high resistance plasma effluent region (R_{Eff}), Figure 5-5. These three regions are considered plasma but with different electron densities. So, when the plasma is ignited, the area between the two electrodes would have the highest density of reactive species and electrons due to electron trapping [24]. The afterglow corresponds to a plasma with a diminishing carrier density while further away in the effluent, only a small positive ion current is expected. The length of the afterglow region depends on plasma parameters [25]. Therefore, there is always reactive species in the three regions but with different densities. Lu et al. also found that high frequency atmospheric pressure plasma jets to have reactive species not only between the two electrodes but also effluent region [26]. Furthermore, Suk et al. [24] demonstrate that the particles from plasma pass significantly beyond its boundaries. The precise electrical extent of the afterglow is not known, but previous miniature Langmuir probe spatial measurements

indicate a sharp rise in resistance just outside (< 1 mm) the luminous region. Therefore, the afterglow is thought to correspond approximately with this luminous region beyond the electrodes, Figure 5-6 (a), and its length is observed to increase with absorbed power. However, with the addition of microdroplets, the afterglow length is much shorter, Figure 5-6 (b). The measurement circuit is represented by a resistor divider network which comprises the oscilloscope input resistance (R_{osc}) and the plasma – collector path resistance (R_{pc}) determined mainly by the length of the high resistance effluent region. The measured voltage, in the absence of microdroplets, is given by the following equation which is driven from the electric circuit simplification in Figure 5-5 by obtaining the equivalent resistant of the three resistances in series and applying the general equation V= I x R

$$V_{meas} = \frac{V_{plasma}}{1 + \frac{R_{Ag} + R_{Eff}}{R_{Osc}}} \qquad \textit{Equation 11}$$

where V_{plasma} is the plasma potential, given by

$$V_{plasma} = \frac{kT_e}{2e} ln\left(\frac{m_{ion}T_e}{m_e T_{ion}}\right) \qquad \textit{Equation 12}$$

Assuming cold ions and an electron temperature of T_e ~2 eV and T_{ion} ~500 K in He, leads to an estimate of V_p ~12 V. The plasma potential is sufficiently positive in order to trap electrons to main plasma neutrality (ne ~ nion), as the electrons since they are lighter would normally escape must faster than positive ions. These values were obtained based on experimental measurements as well as kinetic models for atmospheric pressure helium plasma [27,28]. Therefore, Figure 5-7 demonstrates the values of plasma potential for T_e in the range of 1-10 eV. There are some analytical models studied the untrapped electrons [29,30] while the study of electron trapping requires models and simulations. Kostyukov et al. used a numerical 3D simulation model to study the electron trapping and their threshold momentum. Where these electrons were trapped in a bubble and accelerated by the plasma field leading to electrons acceleration. They also identified that a large amount of electrons can be

trapped in the downward region of plasma density transition [31]. In addition, a trapping model was used to study electrons from plasma and to indicate the propagation length of the trapped electrons. The density of the trapped particles was also evaluated and the results of this model were compared with other models for validation [32]. Suk et al. studied also the dynamics of trapped electron using a simulation and compared the results with a derived analytical model. In addition, they employed a theoretical model by considering, initially, the electron's position and momentum at the downstream region which has low density electrons. The final phase of the electron after trapping was then achieved using the analytical model [24].

Sample current waveforms are shown in the original oscilloscope trace before and after aerosol injection to form the stream of microdroplets, Figure 5-8. Stable collector output is obtained without aerosol, the introduction of which creates a short period of instability. After settling, the collector signal amplitude has increased, due to the aerosol. The photodiode signal provides a record of continuous plasma operation during measurement. The equivalent charged droplet induced current pulse data are shown in Figure 5-9. The current pulse lengths are 10 – 60 ms which is much longer than expected for the flight time of a single droplet. The capture zone is the farthest distance where a charged droplet will create a signal on the collector. Therefore, each current peak is thought to represent multiple droplets due to the effective length of the collector capture zone which is much longer than the expected distance between droplets. The average pulse length was obtained from a sample of pulses and observed to decrease with increasing gas flow, **Figure** 5-10, as expected. In Figure 5-11, the power spectral density (PSD) plot for the plasma-only exposed electrode (blue) is overlayed onto that for the plasma – aerosol condition (red). According to Fourier analysis, any physical signal can be decomposed into a number of discrete frequencies, or a spectrum of frequencies over a continuous range. The power spectrum of a time varying signal describes the distribution of power into frequency components composing that signal i.e. it indicates the relative importance of each frequency. If the components were due only to the charge on droplets as it reached the collector, then a prominent frequency at 50 kHz, the droplet frequency, would be expected. However, the spectrum of Figure 5-11 shows many frequencies due to noise or experimental artefacts. This plot generated by the oscilloscope connected to the experiment where the large peaks represents spikes due to RF emission noise from the plasma. At low

frequencies, additional features were observed either without plasma or during nebuliser operation in the absence of liquid flow. These are attributed to pulsing of syringe pump and nebuliser operation. Therefore, this plot helps in understanding the influence of the system components on the signal and reveals high noise is expected to influence the droplets charge measurements.

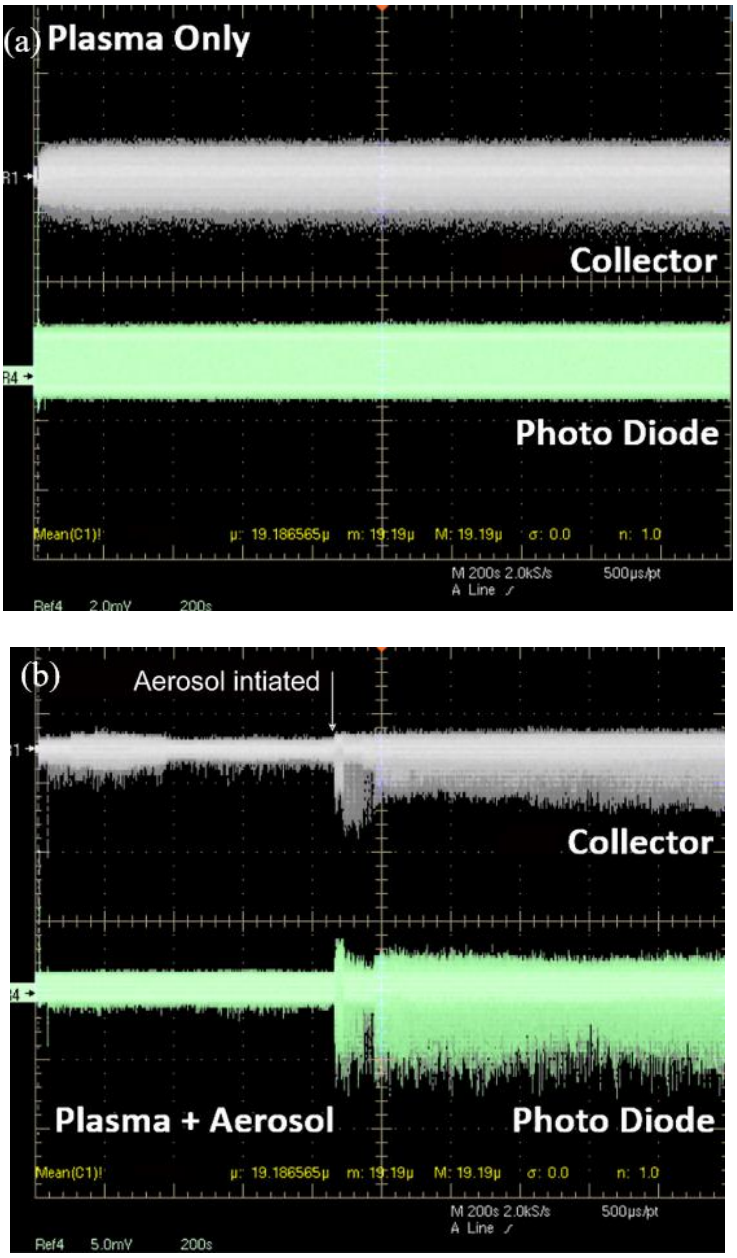

Figure 5-8: Oscilloscope traces of collector current and luminance signals for plasma (a) without and (b) with aerosol. The voltage scale is 2.0 mV/div in (a) and 5.0 mV/div in (b). The total collection time is 200s, 2 kS/s. The input resistance is 1 ΩW.

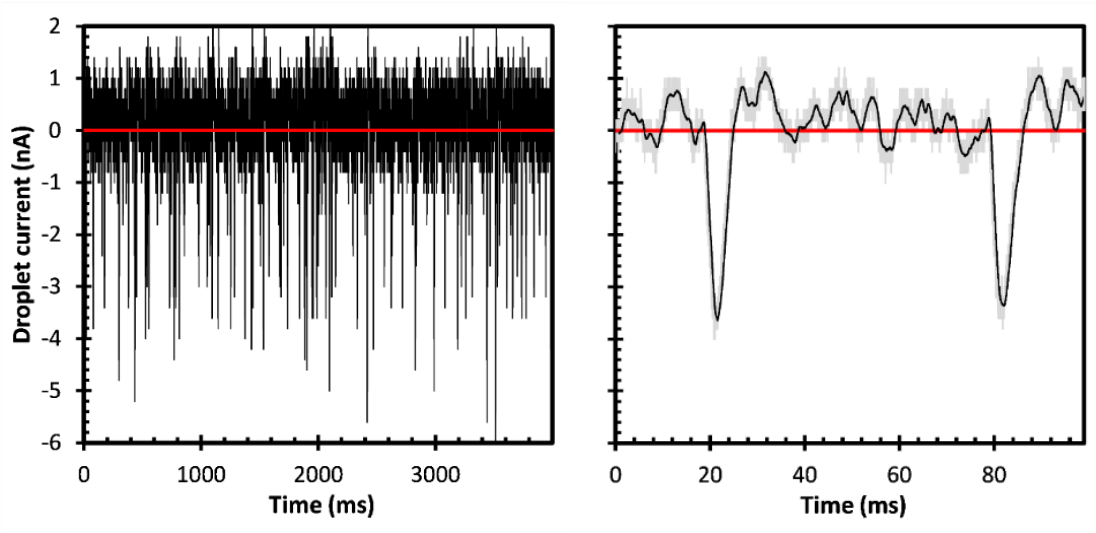

Figure 5-9: (left) Measured collector (radius 3mm) current for plasma power of 1W and total He gas flow of 5 slm. (right) Expanded time axis.

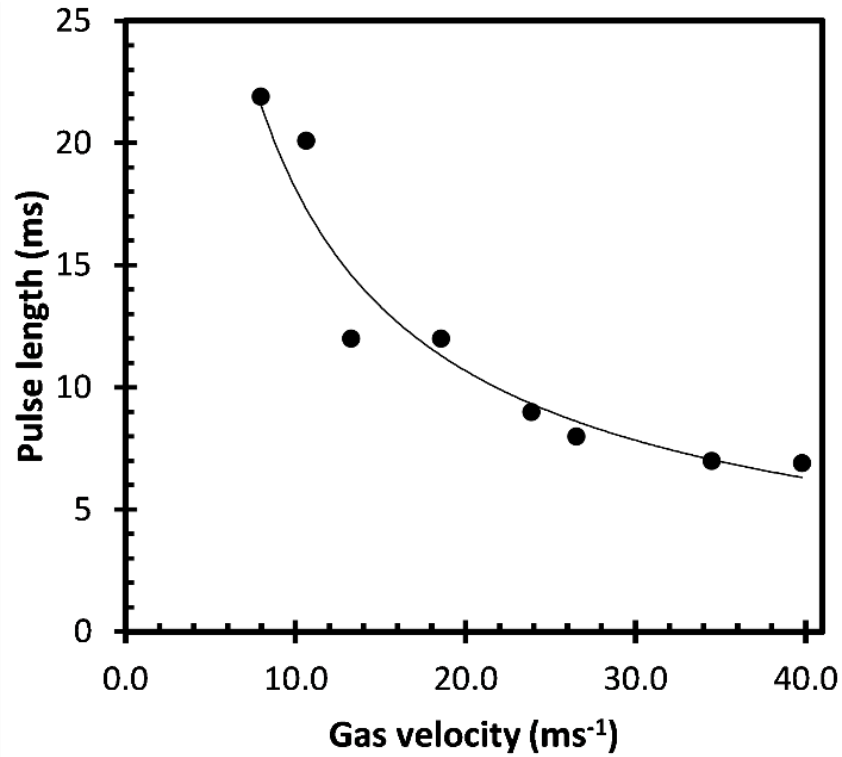

Figure 5-10: Average current pulse length versus gas velocity where the pulse length gets shorter with increasing the gas velocity.

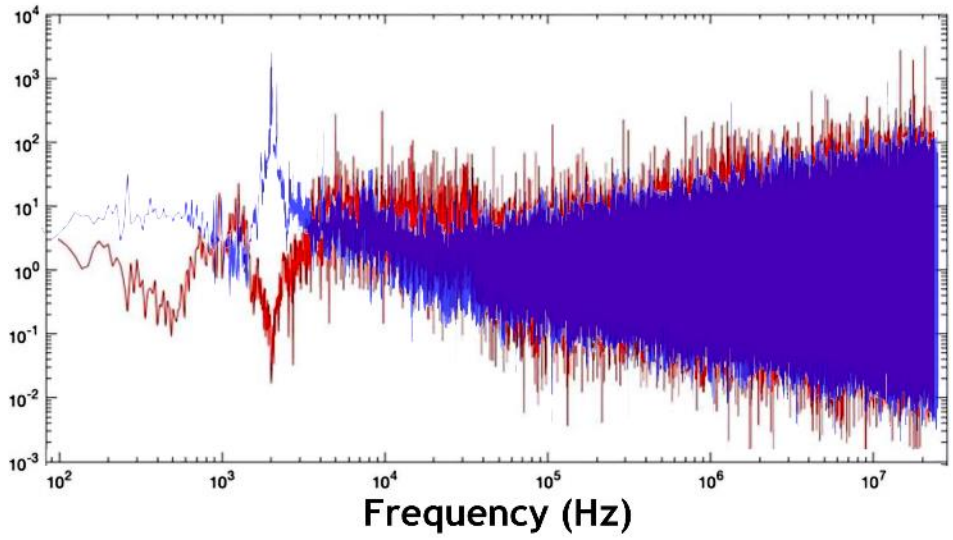

Figure 5-11: Power spectral density plots from plasma exposed 4 mm electrode (blue), superimposed on that of plasma with droplets (red). Where additional features were found at low frequencies as well as RF spikes.

5.4.3 Collector dimension and location for charge detection

A charge measurement electrode, the collector, was placed downstream from the plasma capillary outlet at various locations to determine the minimum distance required to ensure placement beyond the plasma afterglow region and hence minimise interference from plasma currents. While the plasma to collector gap was varied, Figure 5-1 the quartz capillary was adjusted to maintain an air gap of ~1 mm and minimise turbulence effects and droplet loss at its outlet. In an attempt to investigate single droplet current pulses, a number of wire and disk collectors of various dimensions were initially investigated. However, only disk electrodes larger than the outer diameter of the capillary (2.5 mm) were capable of capturing most droplets. For wire electrodes ≤ 100 μm, almost zero droplets were collected. To achieve isolated single droplet measurements under these conditions (large $R_C \geq 2.5$ mm) would require an arrival frequency ≤ 1500 Hz to ensure sufficient inter-droplet spacing. Considering individual droplets with a maximum charge value given by the Rayleigh limit, the expected pulse characteristics, from Equation 10, are in the 10^{-9} A and 10^{-4} s – 10^{-3} s range. While the measured pulse amplitudes are in the expected range (0.1 nA – 10 nA), the observed pulse lengths were much longer (5 ms – 25 ms). With a large collector radius, the electrode response zone contains several droplets with a range of

velocities and charge levels and the observed extended pulses likely represent the superposition of these multiple droplets. All electrical measurements were obtained with the plasma system and nebuliser placed inside a Faraday cage. An additional Faraday shield directly enclosed the plasma electrodes and inline RF, and anti-aliasing filters were installed. Nevertheless, since the electrode is in close electrical proximity to the output of a high-power radio-frequency source, the current pulses may also be subject to interference due to RF spikes as depicted in Figure 5-11. For the above reasons, single droplet analysis was not possible. Instead, the average voltage induced on the collector by a stream of microdroplets was used to estimate the average microdroplet charge. A 3 mm diameter copper disk collector was placed downstream from the plasma capillary outlet and the current signal fed directly to an oscilloscope with an input impedance of 1 MΩ to produce a voltage signal. Data was collected for various values of plasma – collector distance, 3 – 30 mm, and variable gas flows from 1.5 slm to 7.5 slm.

5.4.4 Collector electrode calibration

5.4.4.1 Large droplet experiment

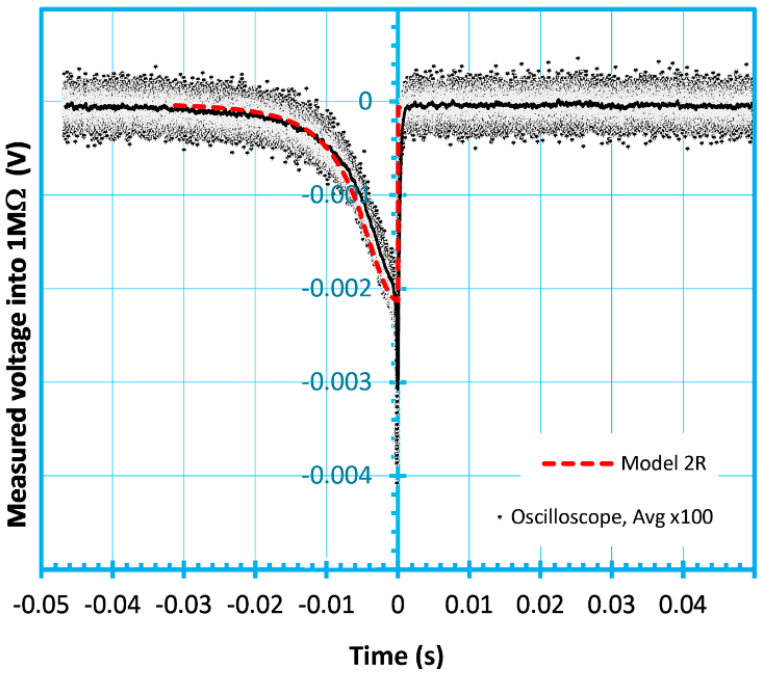

Figure 5-12: Current measurements for a 2 mm diameter droplet impacting a collector electrode.

In earlier experimental work previously conducted in NIBEC, large droplets were obtained from a DC biased hypodermic needle and allow to free fall onto a collector plate. From imaging, the size and velocity of droplets were determined, allowing calculation of the droplet charge. Simultaneous current measurements were then fitted to Equation 9 and Equation 10. Current measurements for a 2 mm diameter droplet impinging a collector electrode are shown in Figure 5-12. The current measurements were taken in comparison with model from Equation 9 for a calculated droplet charge of 10^8 electrons. Knowing that the current spike when droplet impact occurs (at t = 0) is not accommodated by Equation 9.

5.4.4.2 Droplet stream simulation

To calibrate the collector for microdroplets, a number of simulations, based on Equation 10, were carried out using continuous droplet streams with varying values of charge, velocity and droplet spacing. From the measured size and velocity distributions at a gas flow of 3.5 slm, the estimated average distance between droplets is ~300 μm resulting in the presence of ≥ 12.5 droplets within the collector sensitivity zone, ~$2R_C$, with R_C equal to 2 mm. High resolution imaging of the exiting aerosol indicated droplet divergence was small over the relevant distances without the collector in place. However, the presence of a collector is likely to disrupt the gas flow. In particular the low density helium may induce a counterflow due to buoyancy forces, slowing the droplets as they reach the electrode and possibly leading to droplet pileup or deflection away from the electrode [33]. For a fixed diameter (D) of 14 μm, i.e., the Count Median Diameter (CMD) of the aerosol distribution, simulated velocities (v) were varied between 28 ms^{-1}, the maximum observed average velocity, and 1 ms^{-1} which represents possible droplet deceleration due to counterflow conditions.

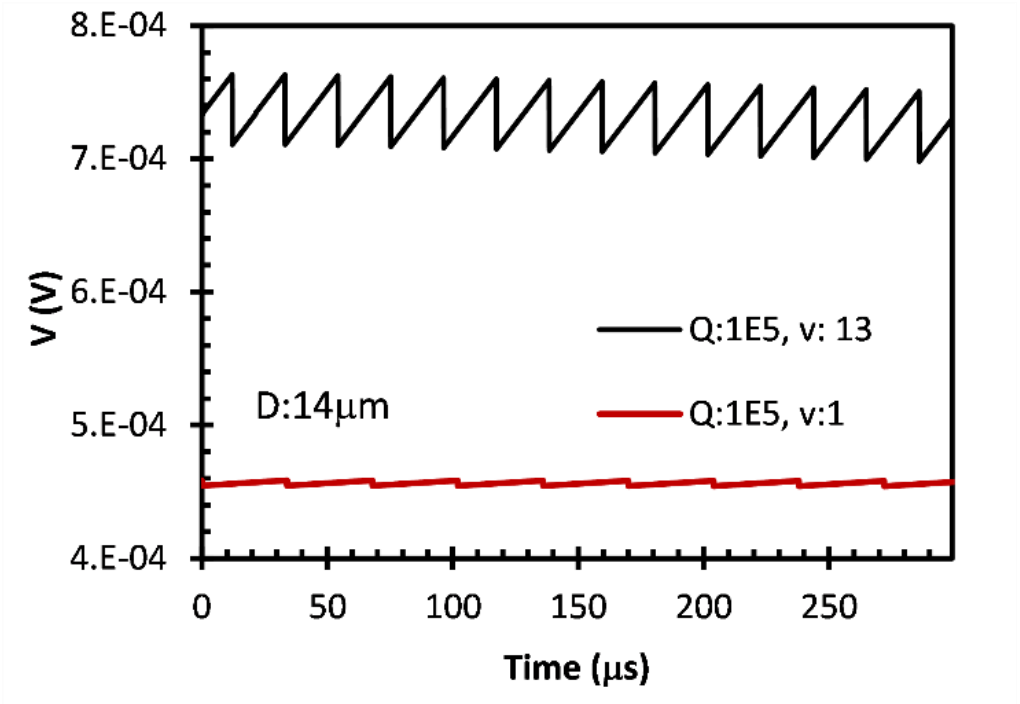

Figure 5-13: Simulation of a droplet stream impacting the collector electrode, using the measured droplet frequency of 5 x 10^4 s^{-1}, a fixed diameter (14 µm), charge (10^5e) and average velocities of 1 ms^{-1} and 13 ms^{-1}.

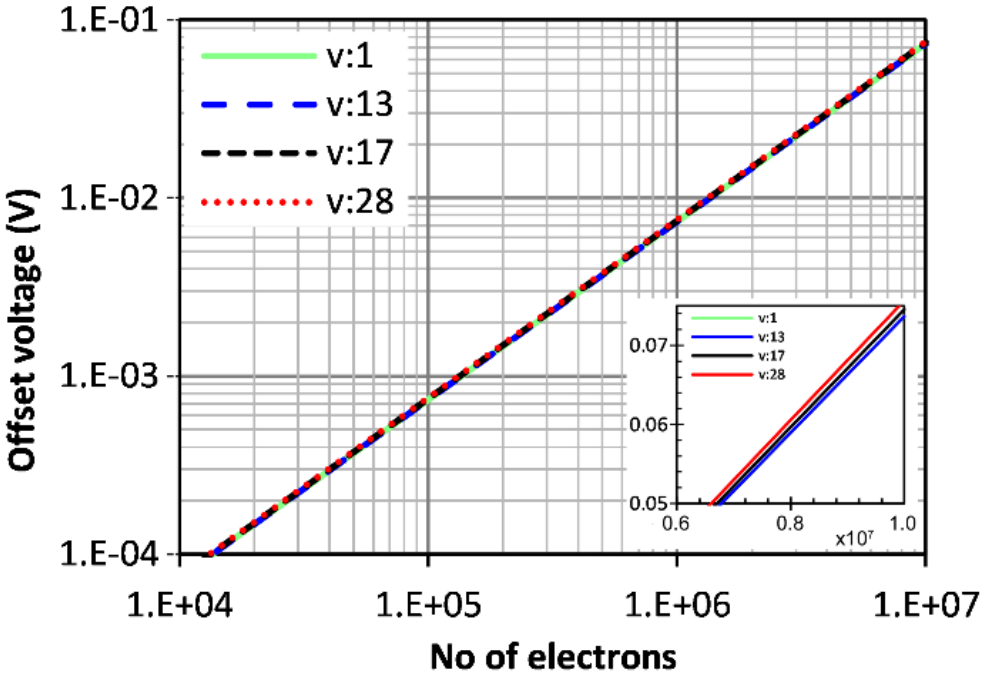

Figure 5-14: Simulation of a droplet stream impacting the collector electrode. Offset voltage dependence on charge and velocity. The inset shows plot on linear scale

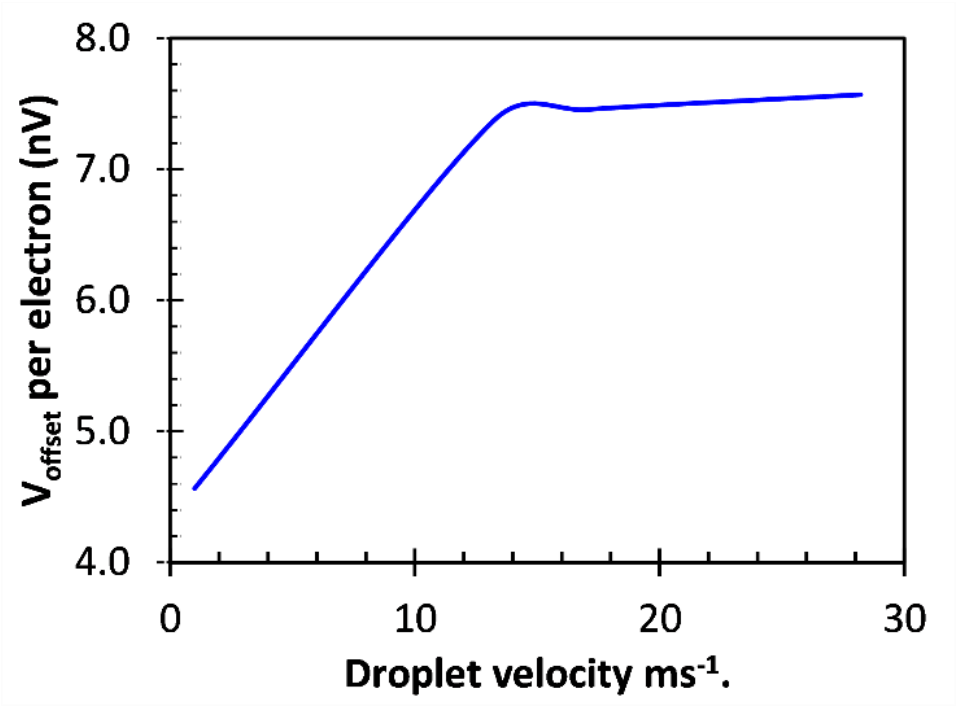

Figure 5-15: Calculated offset voltage per electron charge versus velocity. The simulation range extended a distance 4 x R_C from an electrode of radius R_C. The droplet diameter (D) and spacing (G) was 14 μm and vT_{int} respectively, where T_{int} is the droplet generation interval, 20 μs. The minimum number of droplets was 4R/(D+G).

The simulation range was extended to 16 mm, to fully account for all significant droplet contributions. The gap (G) between droplets was set at vT_{int} where T_{int} is the droplet generation interval, which was observed to be approximately constant at 20 μs, irrespective of plasma gas flow. The total number of droplets in the simulation region, at any instant, was $4R_C/ (D + vT_{int})$. Example simulation of the effect of droplet velocity on induced dc bias and superimposed current pulse amplitudes is depicted in Figure 5-13, considering equivalent current to voltage conversion by the oscilloscope input impedance ($R_{in} = 10^6$ Ω). The simulated waveforms displayed a small ripple voltage due to individual droplets superimposed on a DC offset voltage where the time delay between droplets depends on their generation rate (5×10^4 s^{-1}) and velocity. Across a range of charge values (10^4 e to 10^7 e), simulation indicates the impact of varying velocity, from 1 ms^{-1} to 28 ms^{-1}, is limited, Figure 5-14. The estimated gain factor, from the simulated calibration curve in Figure 5-15, is 5 - 8 nV/electron across the expected velocity range.

5.5 Results

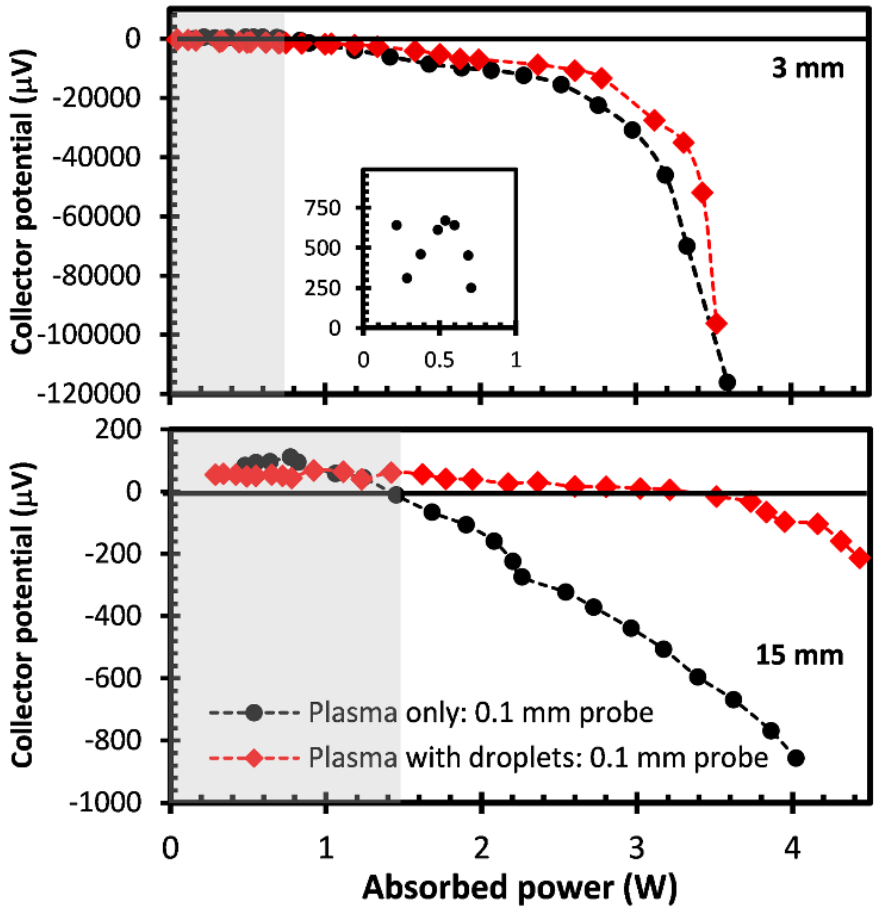

Figure 5-16: Collector potential (V_C) versus absorbed power, with and without droplets at distances of 3 mm and 15 mm from the plasma electrode. The wire collector diameter was < 100 μm. The shaded regions indicate where $V_C > 0$. Inset (3mm) shows magnified shaded region positive potential (plasma only).

To determine the induced current due to charged droplet arrival, it is necessary to subtract the background due to the plasma potential. However, since conditions and hence plasma potential will change on the introduction of microdroplets, the latter needs to be estimated separately from the droplet impact effect. Using a thin (< 100 μm) wire collector, almost zero droplets were collected as they are carried around the wire by the gas flow. Therefore, the contribution of droplets to the collector voltage is considered negligible. The measured collector potential versus power is shown in Figure 5-16 for plasma – collector gaps of 3 mm and 15 mm. At low powers, indicated by the shaded regions, the potential without droplets remains positive and

represents the output expected when a high resistance effluent region exists in the path. Where the shaded area represents $V_c > 0$ and indicates the area where the afterglow region is shorter than the distance between the collector and the capillary tube. Therefore, the plasma is uncouple with the collector for both cases of with and without droplets at 3 mm and for plasma only when the collector is at 15 mm. However, at higher powers, the afterglow region length increases, and the voltage decreases until the collector is, at least, partially situated within the afterglow region where it then assumes a negative floating potential (V_F) determined by the local electron temperature. At the maximum power, V_F is a factor of ~100 greater at 3 mm distance compared to 15 mm.

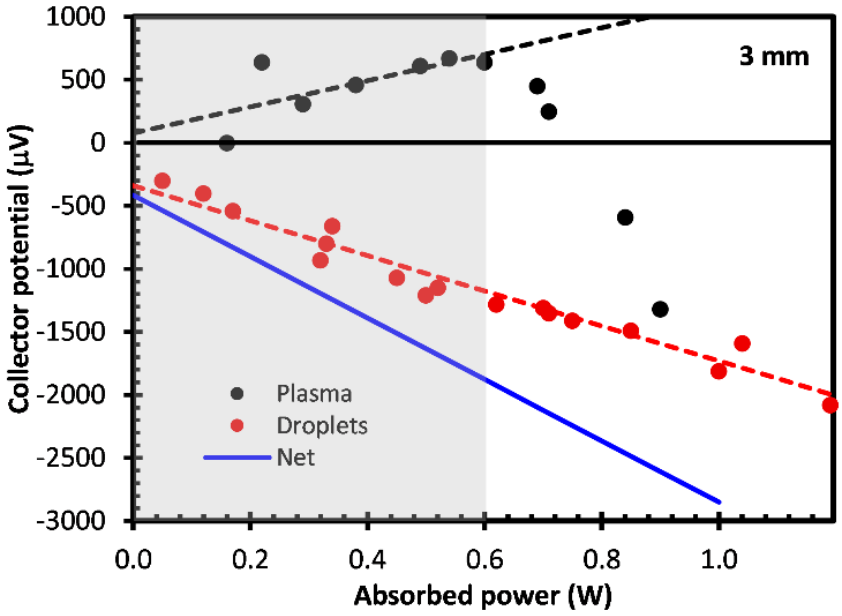

Figure 5-17: Collector potential (V_C) versus absorbed power, with and without droplets at a distance of 3 mm, using a 4 mm diameter disk collector to measure droplet charge. Dashed lines represent least squares fit to measurements over the power range (shaded), representing the decoupled region for plasma without droplets. The net potential due to droplets alone is obtained from subtracting the plasma fitted line from the droplets fitted line.

On the addition of droplets, the characteristics remain similar at 3 mm but at 15 mm, the potential remains positive until a much higher power. This is due to the reduction in the afterglow length, indicated in Figure 5-6. Thus, the collector is either electrically coupled or decoupled to the plasma, via the afterglow region, depending on distance and power. Since bombardment by negatively charged droplets will

decrease the collector potential, it is necessary to operate in decoupled mode to avoid interference from the floating potential. In Figure 5-17, the collector potential versus power is shown for plasmas with and without droplets, at a 3 mm distance from the large collector (4 mm diameter). A least-squares fit to each data set, over the power range appropriate for decoupled mode (shaded) was then used to calculate the net potential on the collector that can be attributed to the charge carried by the droplet stream. From the simulated calibration factor which varies from 4.6 – 7.6 nV per electron, Figure 5-15 the average value of charge per droplet can be obtained from the net potential and is shown in Figure 5-18 for low and high powers.

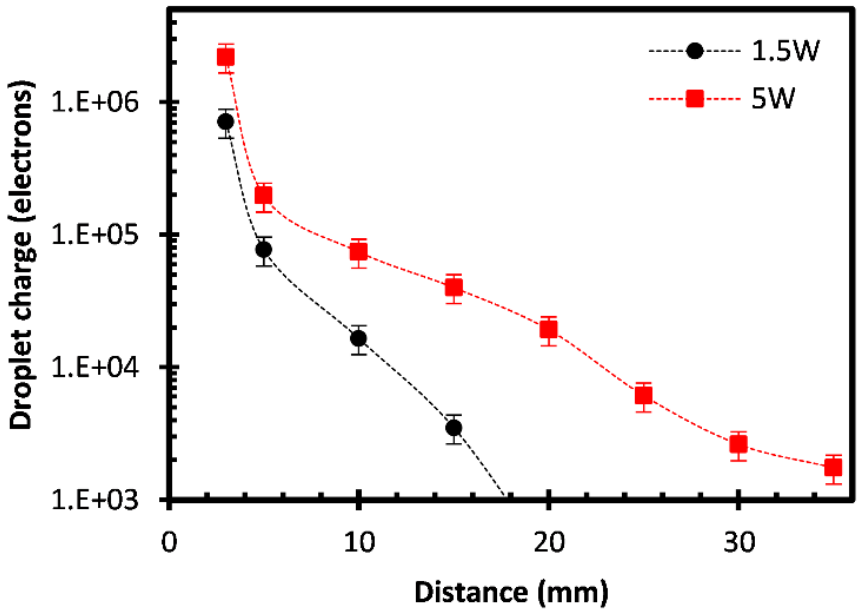

Figure 5-18: Calculated average droplet charge versus distance at low and high powers using the simulated calibration curve. Error bars represent the impact of the variation in calibration factor over the expected velocity range.

The power required to couple plasma with collector was estimated across the range of plasma – collector gaps and is shown in Figure 5-19 (a). In the case of droplets, the onset of coupling is not easily determined and hence a lower bound estimate of the coupling threshold is given. Using a least square fit to each power – distance dataset and estimating the plasma volume from the length of the plasma plus the two afterglow regions, an estimate of the volume power density required with and without droplets is shown in Figure 5-19 (b).

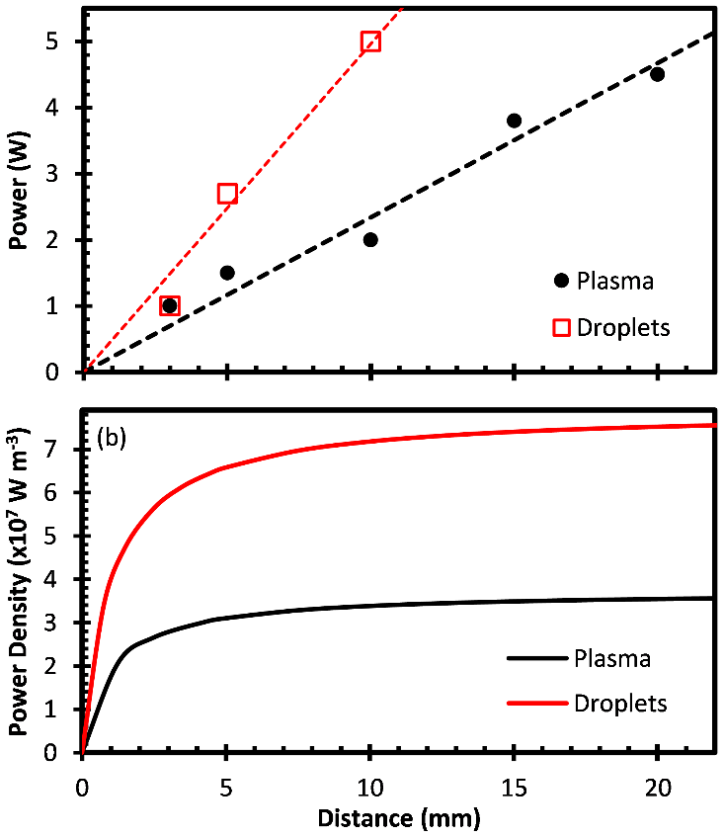

Figure 5-19: (a) Power required to couple plasma to collector versus distance with and without droplets and (b) estimated volume power density.

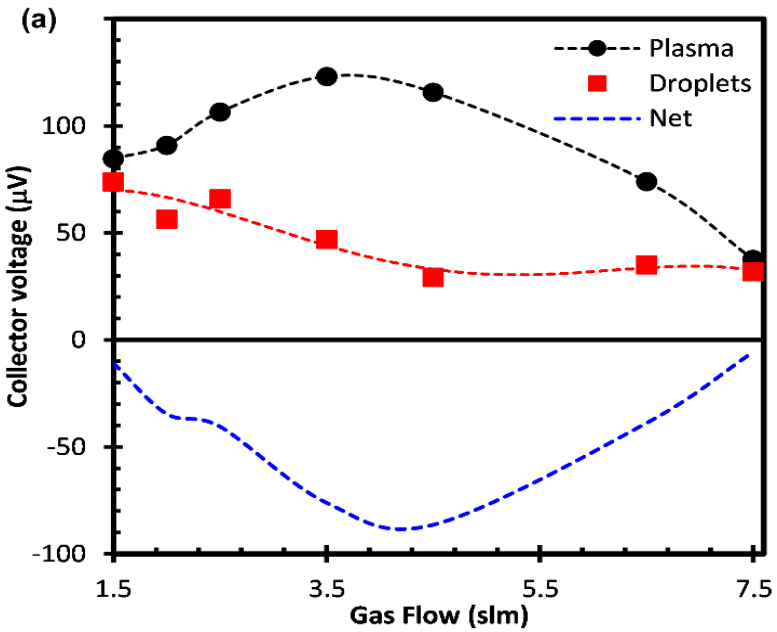

Figure 5-20: (a) Measured collector voltage with and without droplets and resultant net potential versus total gas flow, $Q_1 + Q_2$, with Q_2 constant at 0.7 slm. The plasma – collector gap was 15 mm and 1W power.

The effect of changing plasma gas flow (Q_2) was observed in time-domain pulse signals where the average pulse width decreased and the maximum pulse height increased with increasing gas flow, as expected from Equation 10. The effect of Q_2 is given in Figure 5-20 and maximum collector potential occurs at total gas flow ($Q_1 + Q_2$) of 3.5 slm whereas the actual details about droplet rates and sizes are unknown because these were not measured.

5.6 Discussion

In corona systems, the highest charging rates are found with particle transport through the unipolar region. Here the charge magnitude is dependent on radius, mean ion velocity, the net drift electric field and the ion density – transit time product ($N_i t$) [6,34]. However, even at high electric fields, N_i remains low (~10^{14} m^{-3}). Experimental measurements of corona charged particles are rare, especially for R > 1 μm. Intra et al. reports Q < 100e for 1 μm diameter particles, with $N_i t < 10^{14}$ s m^{-3} [9]. Park et al. report similar charge levels at 1 μm while for 10 μm diameter particles the charge increases to ~7000e ($N_i t$ ~10^{13} s m^{-3}) [6]. Molchanov et al. report ~2000e at 7 μm ($N_i t$ ~10^{13} s m^{-3}) [8]. For comparison, if the plasma charging system were considered similar to a unipolar corona discharge, the mean electron velocity can be determined from the electron temperature and for T_e of 2 eV and N_e of 10^{20} m^{-3}, the predicted charge would be 22,000e for a 10 μm diameter particle [34]. While the equivalent $N_i t$ product is very low (~10^{10} s m^{-3}) compared to the corona systems above, the electron mean velocity is much higher and so therefore is the derived charge. However, the value of predicted charge, assuming a unipolar corona equivalent model for the plasma, is only ~1% of that measured. Therefore, we have obtained the first direct measurements of charge on microparticles in an atmospheric pressure plasma and have shown the level of charge to be very high compared to unipolar corona systems. The amount of charge falls as the distance from plasma increases maybe because the in the plasma effluent, the electrons from the plasma are lost more quickly than the positive ions so the droplets pass through a region of net positive charge which can discharge the droplet. The power density required to maintain the plasma with droplets is higher than without droplets. This maybe because added vapour around droplet due to evaporation may trap electrons by electron attached to molecules e.g., $OH^{\bullet} \rightarrow OH^{--}$.

5.7 Conclusions

The first measurements of average particle charge acquired by microparticles in a fully collisional atmospheric pressure low temperature plasma is reported for the first time. Using a constant stream of liquid microdroplets, delivered at a rate of ~50 kHz, the maximum average charge per droplet was 8×10^5 electrons (128 fC) and 2.5×10^6 electrons (400 fC) for absorbed powers of 1.5 W and 5 W, respectively, at a distance of 3 mm from the downstream plasma electrode. This represents a 2 – 3 orders of magnitude increase in charge levels compared to ion charging in corona systems or electron charging in low pressure plasmas, where electron densities are much lower. Charge decay to $10^3 – 10^4$ electrons per droplet was then observed over a short distance from the plasma (30 mm), likely due to recombination with net positive ions and interaction with air molecules.

5.8 References

[1] N. Hendawy et al., The creation of highly charged micron-sized water droplets, In Preperation. (n.d.).

[2] R.T. Nishida, A.M. Boies, S. Hochgreb, Modelling of direct ultraviolet photoionization and charge recombination of aerosol nanoparticles in continuous flow, J. Appl. Phys. 121 (2017) 023104. https://doi.org/10.1063/1.4972335.

[3] W.A. Hoppel, G.M. Frick, Ion—aerosol attachment coefficients and the steady-state charge distribution on aerosols in a bipolar ion environment, Aerosol Sci. Technol. 5 (1986) 1–21. https://doi.org/10.1080/02786828608959073.

[4] A. Brentjes, A.K. Pozarlik, G. Brem, Estimating droplet charge in numerical simulations of charged sprays, J. Electrostat. 112 (2021) 103591. https://doi.org/10.1016/j.elstat.2021.103591.

[5] L. Konermann, A Simple Model for the Disintegration of Highly Charged Solvent Droplets during Electrospray Ionization, J. Am. Soc. Mass Spectrom. 20 (2009) 496–506. https://doi.org/10.1016/j.jasms.2008.11.007.

[6] J. Park, C. Kim, J. Jeong, S.G. Lee, J. Hwang, Design and evaluation of a unipolar aerosol charger to generate highly charged micron-sized aerosol particles, J. Electrostat. 69 (2011) 126–132. https://doi.org/10.1016/j.elstat.2011.02.001.

[7] J.P. Borra, Charging of aerosol and nucleation in atmospheric pressure electrical discharges, Plasma Phys. Control. Fusion. 50 (2008) 124036. https://doi.org/10.1088/0741-3335/50/12/124036.

[8] O. Molchanov, K. Krpec, J. Horák, L. Kuboňová, F. Hopan, Comparison of methods for evaluating particle charges in the electrostatic precipitation of fly-ash from small-scale solid fuel combustion, Sep. Purif. Technol. 248 (2020) 117057. https://doi.org/10.1016/j.seppur.2020.117057.

[9] P. Intra, Corona discharge in a cylindrical triode charger for unipolar diffusion aerosol charging, J. Electrostat. 70 (2012) 136–143. https://doi.org/10.1016/j.elstat.2011.11.007.

[10] J. Rosell-Llompart, J. Grifoll, I.G. Loscertales, Electrosprays in the cone-jet mode: From Taylor cone formation to spray development, J. Aerosol Sci. 125 (2018) 2–31. https://doi.org/10.1016/j.jaerosci.2018.04.008.

[11] J.P. Borra, Review on water electro-sprays and applications of charged drops with focus on the corona-assisted cone-jet mode for High Efficiency Air Filtration by wet electro-scrubbing of aerosols, J. Aerosol Sci. 125 (2018) 208–236. https://doi.org/10.1016/j.jaerosci.2018.04.005.

[12] P. Bürger, U. Riebel, Electrostatic charging and precipitation of nanoparticles in technical nitrogen: Highly efficient diffusion charging by hot free electrons, J. Aerosol Sci. 141 (2020) 105495. https://doi.org/10.1016/j.jaerosci.2019.105495.

[13] F.J. Romay, D.Y.H. Pui, Free electron charging of ultrafine aerosol particles, J. Aerosol Sci. 23 (1992) 679–692. https://doi.org/10.1016/0021-8502(92)90036-U.

[14] S. Askari, I. Levchenko, K. Ostrikov, P. Maguire, D. Mariotti, Crystalline Si nanoparticles below crystallization threshold: Effects of collisional heating in non-thermal atmospheric-pressure microplasmas, Appl. Phys. Lett. 104 (2014). https://doi.org/10.1063/1.4872254.

[15] A. Stancampiano, T. Gallingani, M. Gherardi, Z. Machala, P. Maguire, V. Colombo, J.M. Pouvesle, E. Robert, Plasma and aerosols: Challenges, opportunities and perspectives, Appl. Sci. 9 (2019). https://doi.org/10.3390/app9183861.

[16] P. Maguire, D. Rutherford, M. Macias-Montero, C. Mahony, C. Kelsey, M. Tweedie, F. Pérez-Martin, H. McQuaid, D. Diver, D. Mariotti, Continuous In-Flight Synthesis for On-Demand Delivery of Ligand-Free Colloidal Gold Nanoparticles, Nano Lett. 17 (2017) 1336–1343. https://doi.org/10.1021/acs.nanolett.6b03440.

[17] B.R. Locke, K.Y. Shih, Review of the methods to form hydrogen peroxide in electrical discharge plasma with liquid water, Plasma Sources Sci. Technol. 20 (2011) 034006. https://doi.org/10.1088/0963-0252/20/3/034006.

[18] G. Oinuma, G. Nayak, Y. Du, P.J. Bruggeman, Controlled plasma-droplet

interactions: A quantitative study of OH transfer in plasma-liquid interaction, Plasma Sources Sci. Technol. 29 (2020) 095002. https://doi.org/10.1088/1361-6595/aba988.

[19] K. Nitta, Y. Shimizu, K. Terashima, T. Ito, Plasma-assisted synthesis of size-controlled monodisperse submicron gold particles using inkjet droplets, J. Phys. D. Appl. Phys. 54 (2021) 33LT01. https://doi.org/10.1088/1361-6463/ac02f8.

[20] I. Sremački, G. Bruno, H. Jablonowski, C. Leys, A. Nikiforov, K. Wende, Influence of aerosol injection on the liquid chemistry induced by an RF argon plasma jet, Plasma Sources Sci. Technol. 30 (2021) 095018. https://doi.org/10.1088/1361-6595/abe176.

[21] P.D. Maguire, C.M.O. Mahony, C.P. Kelsey, A.J. Bingham, E.P. Montgomery, E.D. Bennet, H.E. Potts, D.C.E. Rutherford, D.A. McDowell, D.A. Diver, D. Mariotti, Controlled microdroplet transport in an atmospheric pressure microplasma, Appl. Phys. Lett. 106 (2015). https://doi.org/10.1063/1.4922034.

[22] N. Hendawy, H. McQuaid, D. Mariotti, P. Maguire, Continuous gas temperature measurement of cold plasma jets containing microdroplets, using a focussed spot IR sensor, Plasma Sources Sci. Technol. 29 (2020). https://doi.org/10.1088/1361-6595/aba2aa.

[23] E. Borzabadi, A.G. Bailey, The measurement of charge on microscopic particles, J. Phys. E. 12 (1979) 1137–1138. https://doi.org/10.1088/0022-3735/12/12/005.

[24] H. Suk, N. Barov, J.B. Rosenzweig, E. Esarey, Plasma electron trapping and acceleration in a plasma wake field using a density transition, Phys. Rev. Lett. 86 (2001) 1011–1014. https://doi.org/10.1103/PhysRevLett.86.1011.

[25] S. Hofmann, K. Van Gils, S. Van Der Linden, S. Iseni, P. Bruggeman, Time and spatial resolved optical and electrical characteristics of continuous and time modulated RF plasmas in contact with conductive and dielectric substrates, Eur. Phys. J. D. 68 (2014) 21–23. https://doi.org/10.1140/epjd/e2014-40430-3.

[26] X. Lu, G. V. Naidis, M. Laroussi, S. Reuter, D.B. Graves, K. Ostrikov, Reactive species in non-equilibrium atmospheric-pressure plasmas: Generation, transport, and biological effects, Phys. Rep. 630 (2016) 1–84.

https://doi.org/10.1016/j.physrep.2016.03.003.

[27] E.K. Isakaev, V.F. Chinnov, M.A. Sargsyan, D.I. Kavyrshin, Nonequilibrium state of highly ionized helium plasma at atmospheric pressure, High Temp. 51 (2013) 141–146. https://doi.org/10.1134/S0018151X13020090.

[28] K. Wiesemann, A short introduction to plasma physics, CAS-CERN Accel. Sch. Ion Sources - Proc. (2013) 85–122.

[29] I. Sremački, G. Bruno, H. Jablonowski, C. Leys, A. Nikiforov, K. Wende, Influence of aerosol injection on the liquid chemistry induced by an RF argon plasma jet, Plasma Sources Sci. Technol. 30 (2021). https://doi.org/10.1088/1361-6595/abe176.

[30] J. Kruszelnicki, A.M. Lietz, M.J. Kushner, Atmospheric pressure plasma activation of water droplets, J. Phys. D. Appl. Phys. 52 (2019). https://doi.org/10.1088/1361-6463/ab25dc.

[31] I. Kostyukov, E. Nerush, A. Pukhov, V. Seredov, A multidimensional theory for electron trapping by a plasma wake generated in the bubble regime, New J. Phys. 12 (2010). https://doi.org/10.1088/1367-2630/12/4/045009.

[32] H.A. Rose, D.A. Russell, A self-consistent trapping model of driven electron plasma waves and limits on stimulated Raman scatter, Phys. Plasmas. 8 (2001) 4784–4799. https://doi.org/10.1063/1.1410111.

[33] E. Robert, V. Sarron, T. Darny, D. Riès, S. Dozias, J. Fontane, L. Joly, J.M. Pouvesle, Rare gas flow structuration in plasma jet experiments, Plasma Sources Sci. Technol. 23 (2014). https://doi.org/10.1088/0963-0252/23/1/012003.

[34] H.J. White, Particle Charging in Electrostatic Precipitation, Trans. Am. Inst. Electr. Eng. 70 (1951) 1186–1191. https://doi.org/10.1109/T-AIEE.1951.5060545.

6 Charged droplets measurements using double ring electrodes

6.1 Introduction

Measurements of droplet charge in flight using a pair of ring electrodes outside the quartz capillary have been attempted in the following sections. This double ring electrode setup (SR2) has possible advantages over other collectors such as:

1. Avoids the droplets to impact the collector which may lead to charge loss, noise, and pulse shape artefacts.
2. SR2 are further from the plasma electrodes, to limit its interference with the plasma and also to reduce plasma-related noise.
3. SR2 does not disturb the gas or droplet flow so the droplets are not affected by them.
4. The droplets are maintained within a He environment rather than meeting the laboratory air.
5. The use of thin rings that may be able to detect small fast-moving charges.
6. The use of rings electrodes enables adjustments of variable distance from plasma as well as variable inter-ring distance.

Measurements result in a time series of voltage pulses. The voltage amplitude is expected to relate to droplet charge and other factors according to electrostatic theory applied to each of the ring electrodes individually, although the external circuit and parasitic capacitances are also expected to affect the measured pulse characteristics. A further possible factor is the influence of following droplets on the measured droplet characteristic which may be dependent on geometry, time constants based on self and external capacitance, and the inter-droplet distances. To investigate these factors a numerical model of the ring system was built based on the work of Yan et al. [1] who applied electrostatic theory to the measurement of large scale pneumatically conveyed solids. In addition, the model attempts to match the characteristics of the experimental signal with the simulated output using predicted relationships between main droplet characteristics of size distribution, radial position distribution, velocity distribution and charge distribution. The model by Yan et al has also been used by Hussain et al to measure triboelectric charge on large isolated powder particles [2]. A number of other

electrostatic models were considered, for example the different approaches analysed by Gajewski [3]. Here a simple relationship was developed, given by

$$Q = 4\pi\varepsilon_0\sqrt{v^2t^2 + r^2}V_m(t) \qquad \textit{Equation 13}$$

where $V_m(t)$ is the measured voltage, v is the velocity, ε_0 is permittivity of free space, and r the ring radius. At time t = 0, when the particle passes through the ring, $Q = 4\pi\varepsilon_0 r V_{max}$. Thus, Q could be directly calculated. However, in the analysis there are assumptions that exclude parasitic and external circuit elements and assume particles fill the pipe cross-section with a uniform density. The application is directed at tribocharged turbulent powder transport in large pipes and no relevant information was given and so it was not possible to judge the validity of this approach for plasma microdroplets case. A later review evaluates the history of such charge measurement techniques and highlights the importance of capacitance for voltage induction [4]. While no models truly reflect the experimental situation here, the chosen model (Yan) [1] appeared to be the least affected by external factors, since explicit values of parasitic capacitance was not required. It also considered droplets travelling on trajectories displaced from central axis. However, the Yan model only considers individual isolated droplets.

6.2 Experimental analysis

6.2.1 Experimental setup

Same previous plasma setup described in chapter 5 was used for these measurements. The system was operated in He, Ne, and Ar/Ne gas with controlled flows from 1.5 to 7.5 slm. For droplets studies, a standard liquid aerosol (water) was obtained from a primary droplet source at 300 µL/h flow rate. The spacing between the two plasma electrodes is 2 mm, Figure 6-1. The double ring electrodes are constructed with two rigid rings situated around the outside of the quartz capillary just downstream from the plasma electrodes and spaced by 22 mm, Figure 6-2.

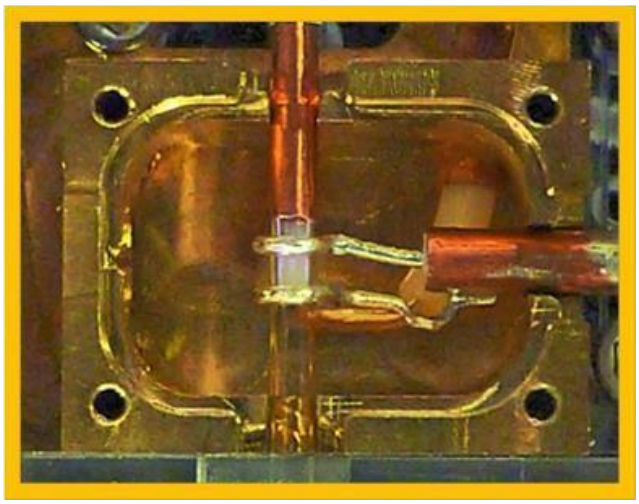

Figure 6-1: Plasma ring electrodes with d = 2.0 mm.

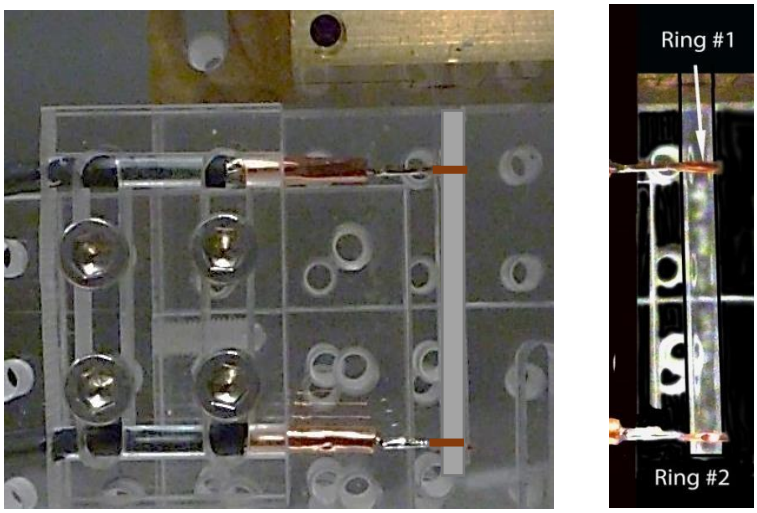

Figure 6-2: Measuring ring electrode with d= 22.0 mm. In left figure, the capillary and rings are indicated by a graphic. Right figure is photograph.

6.2.2 Examples of measured output signal

The profile of droplets signal depends on several factors. If there is only one droplet passing by ring 1, same pulse would be expected on ring 2 but with different amplitude representing decay of the signal and also delay. This delay can be calculated from x_g / v_s where x_g is the gap between the two electrodes (22 mm) and v_s is the droplets velocity. However, the pulse on ring 2 is always different from ring 1 and that is maybe due to charge loss, gas flow disruption, loss of small droplets or plasma interference which has different influence on ring2 than ring1 due to the different location. Consequently, ring 2 cannot be directly compared with ring 1 because of the noisy signals. Comparing two signals is possible using signal processing techniques, for example cross-correlation. It is the similarity measurement between two series by knowing the shift of one of them with respect to the second so when sliding one of the series by this shift, they become identical. The cross-correlation can be calculated using MATLAB to provide the timeshift that ring 2 has from ring 1 by plotting timeshift (t_s) with correction coefficient. This means that if ring 2 signal has been shifted by this value, it would be identical to ring 1. Cross-correlation is expected to show a sharp peak near $t_s = 0$ if ring 2 signal is a copy of that of ring 1 but shifted in time by x_g / v_s. However, for real signal, ring 2 has a smaller amplitude than ring 1 which might cause a problem with cross-correlation. A few experimental signals for different plasma parameters and the cross-correlation between electrode ring 1 and ring 2 are presented below with input power representation. Where the relation between the input power and the absorbed net power can be obtained from the Octiv suite 2.0 VI probe providing net power of 0.05 W to 0.6 W which is corresponding to input power 60 W to 120 W. Below are two samples for fixed input power supply power (P) = 100 W, and different gas flows, Q_{Ne}= 1.00 slm and Q_{He}= 3.5 slm in Figure 6-3 and Q_{He}= 6.0 slm in Figure 6-4. Another four samples for fixed flow, Q_{Ne} = 1.00 slm, Q_{He} = 3.5 slm and different powers P = 80 W in Figure 6-5, P = 105 W in Figure 6-6, P = 110 W in Figure 6-7 and P = 115 W in Figure 6-8. The droplets velocity is calculated from dividing the gap between the two electrodes (22 mm) by the timeshift between ring 1 and ring 2, obtained from the cross-correlation of ring 1 and ring 2 signals, and have values indicated in Table 5. These velocity values are close to those obtained in the previous chapter in Figure 5-2 where the average droplets velocity is < 32 ms^{-1} at 3.5 slm gas flow rate. For example, The droplets velocity in Figure 6-3

has a value of 24.3 ms^{-1} in Table 1 which is slightly lower than the average droplet velocity (< 32 ms^{-1}) provided in the previous chapter. However, in the ring experiment the plasma was operated at lower power and it is known from previous work that the plasma exposure of droplets led to an increase in droplet velocity.

Table 5: Droplets velocity for various power and flow rate.

P (W)	Q_{Ne} (slm)	Q_{He} (slm)	V (m/s)
80	1.0	3.5	24.3
100	1.0	3.5	24.5
105	1.0	3.5	19.6
110	1.0	3.5	19
115	1.0	3.5	19
100	1.0	3.5	24.6
100	1.0	6.0	61.1

Figure 6-8 is the selected experimental signal for analysis and the peaks' locations for the droplets passing by ring 1 is shown in Figure 6-9. The range of peak heights from trough to peak from our experimental sample is 0.17 - 0.76 V from smallest to biggest pulse, Figure 6-10, which equivalent to average amplitude range of 0.09 - 0.38 V. To focus on the major pulses, a threshold of 0.4 was applied, Figure 6-11. MATLAB has been used to provide pulses widths (W_p) obtained from full width at half maximum (FWHM), pulses amplitudes (A) and their time location, Table 6. Peak 2 was chosen as a reference for the simulation, and it has A = 709 mV and W_p = 4.5 ms. Where the whole pulse width of the pulse from start to end point is 10.6 ms as shown in Figure 6-12. These values will be used for comparison between the simulated pulses and the experimental signal. With respect to ring 2, a threshold of 0.2 was applied where major peaks are shown in Figure 6-13 and their pulse width, amplitude and time location is indicated in Table 7.

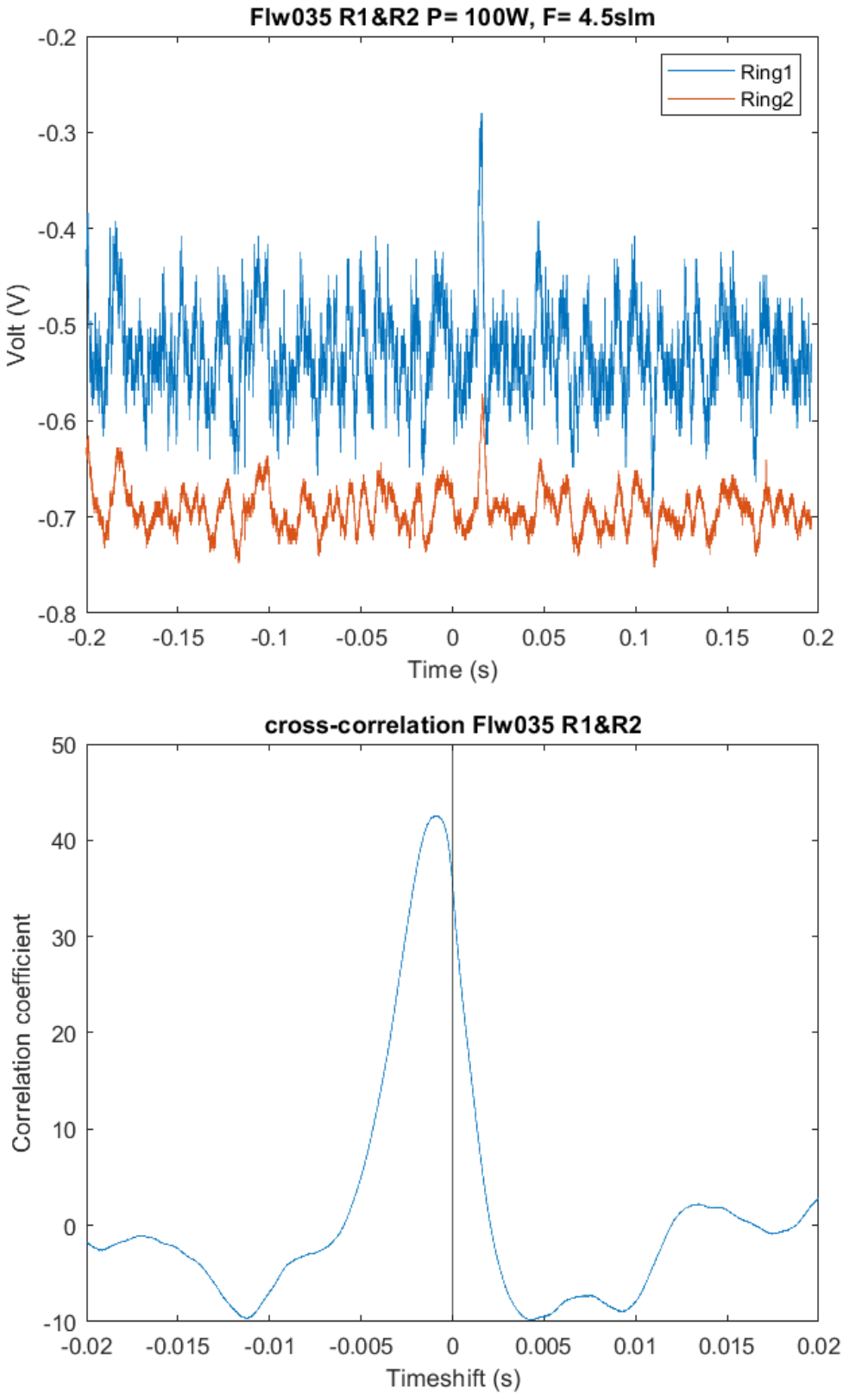

Figure 6-3: a) Amplified volt-time for experimental sample when P= 100 W, Q_{Ne}= 1.00 slm, Q_{He} = 3.5 slm and b) is the cross-correlation between ring 1 and ring 2, Amplifier gain = 1000.

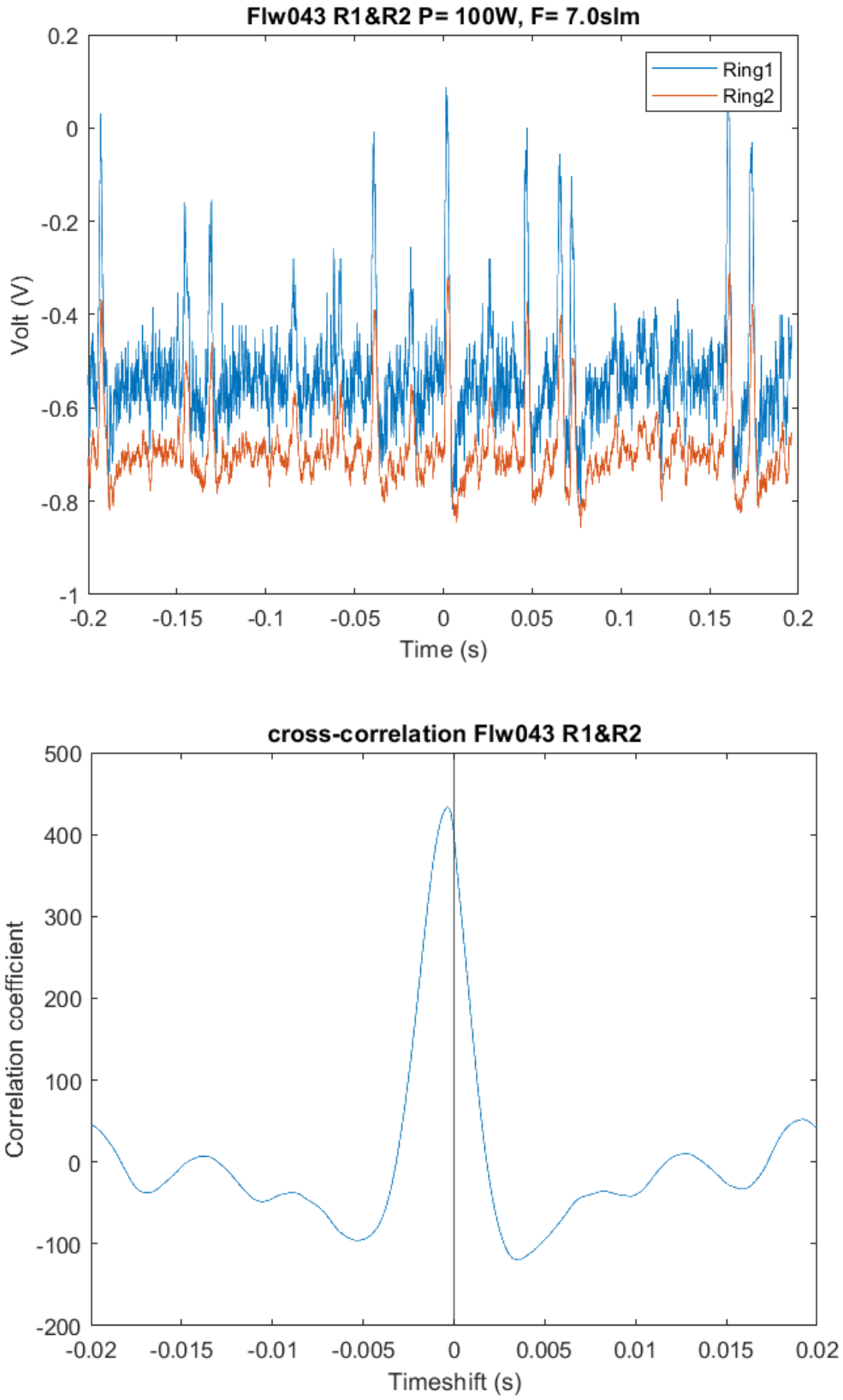

Figure 6-4: a) Amplified volt-time for experimental sample when P= 100 W, Q_{Ne}= 1.00 slm, Q_{He}= 6.0 slm and b) is the cross-correlation between ring 1 and ring 2, Amplifier gain = 1000.

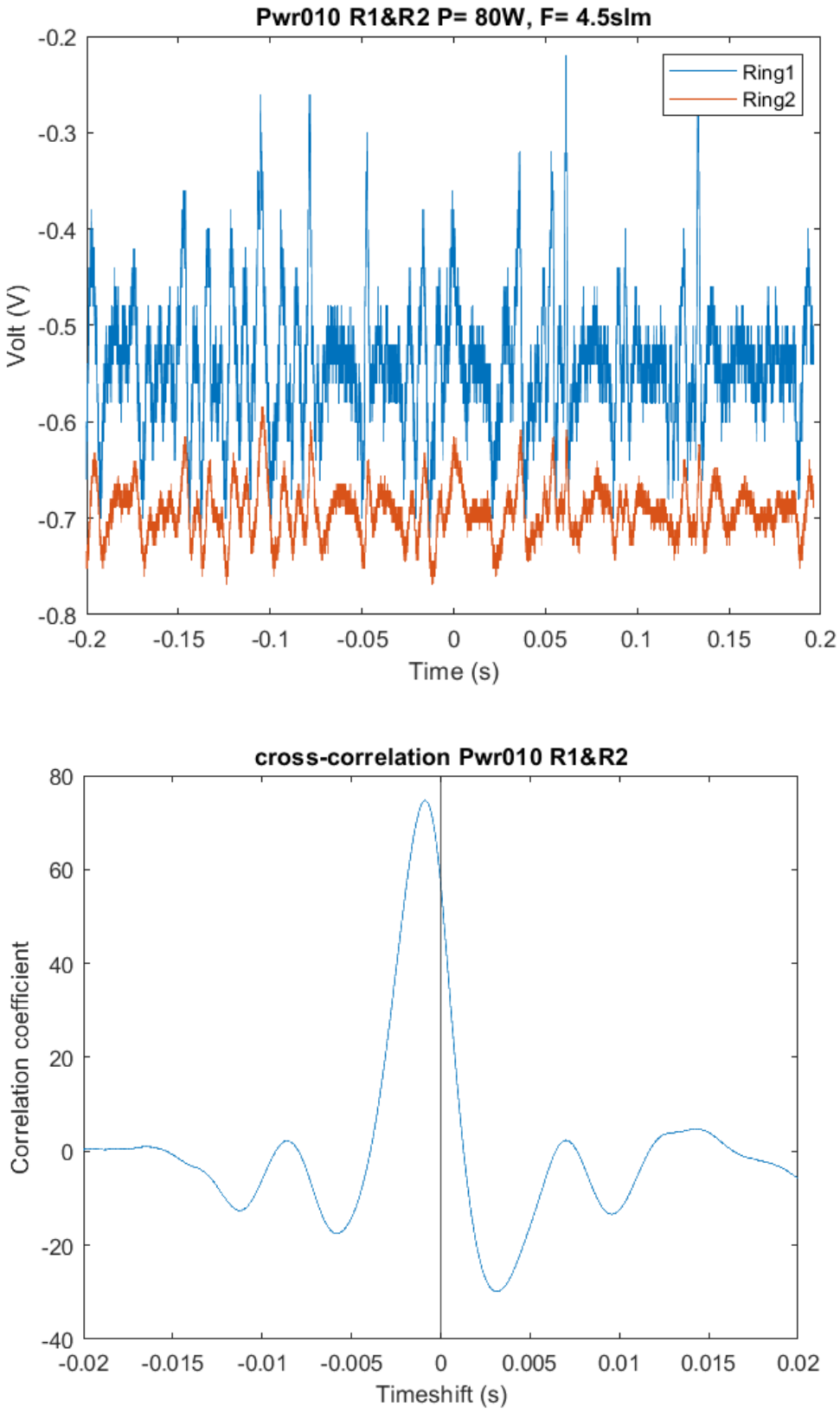

Figure 6-5: a) Amplified volt-time for experimental sample when P= 80 W, Q_{Ne}= 1.00 slm, Q_{He}= 3.5 slm and b) is the cross-correlation between ring 1 and ring 2, Amplifier gain = 1000.

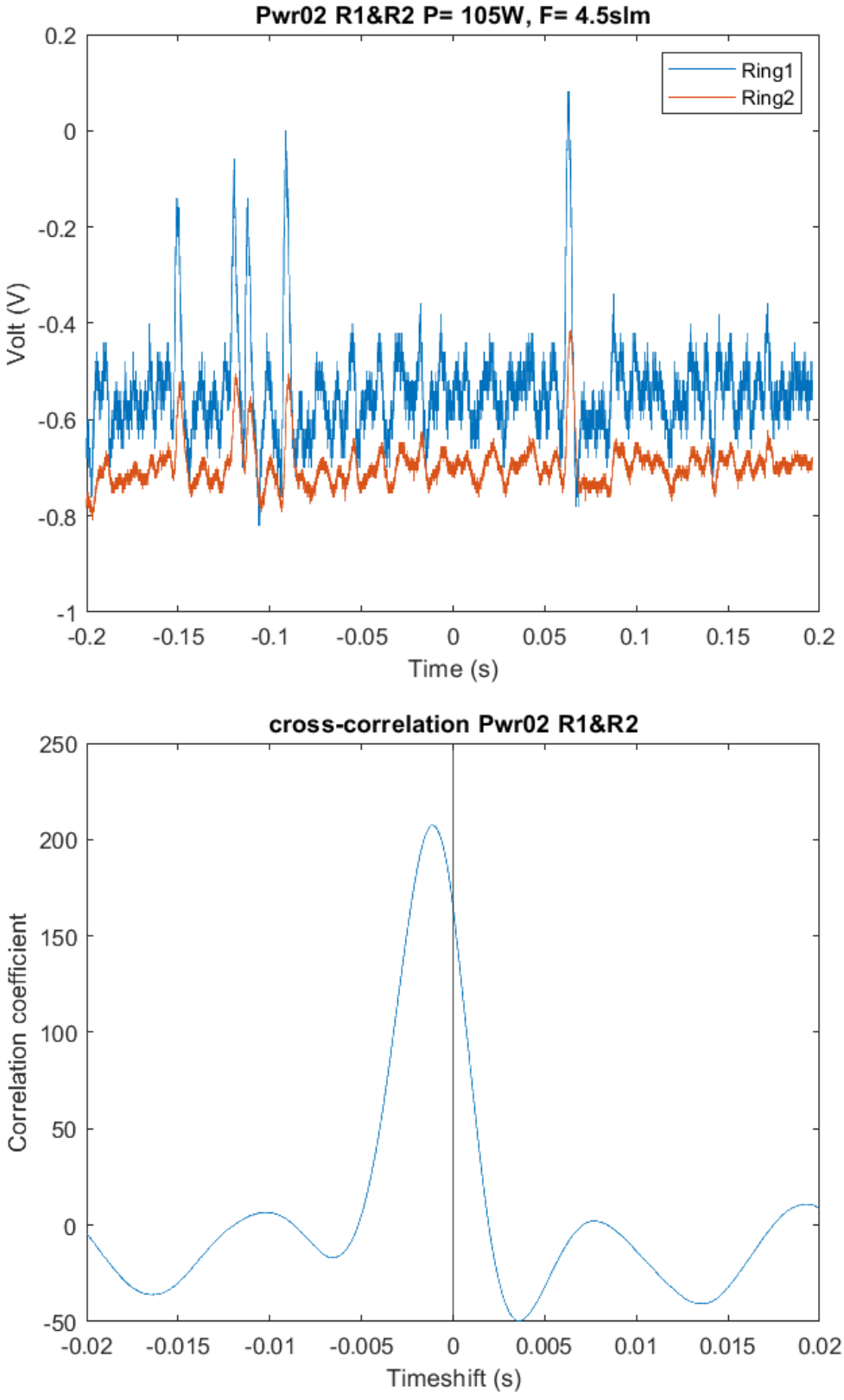

Figure 6-6: a) Amplified volt-time for experimental sample when P= 105 W, Q_{Ne}= 1.00 slm, Q_{He}= 3.5 slm and b) is the cross-correlation between ring 1 and ring 2, Amplifier gain = 1000.

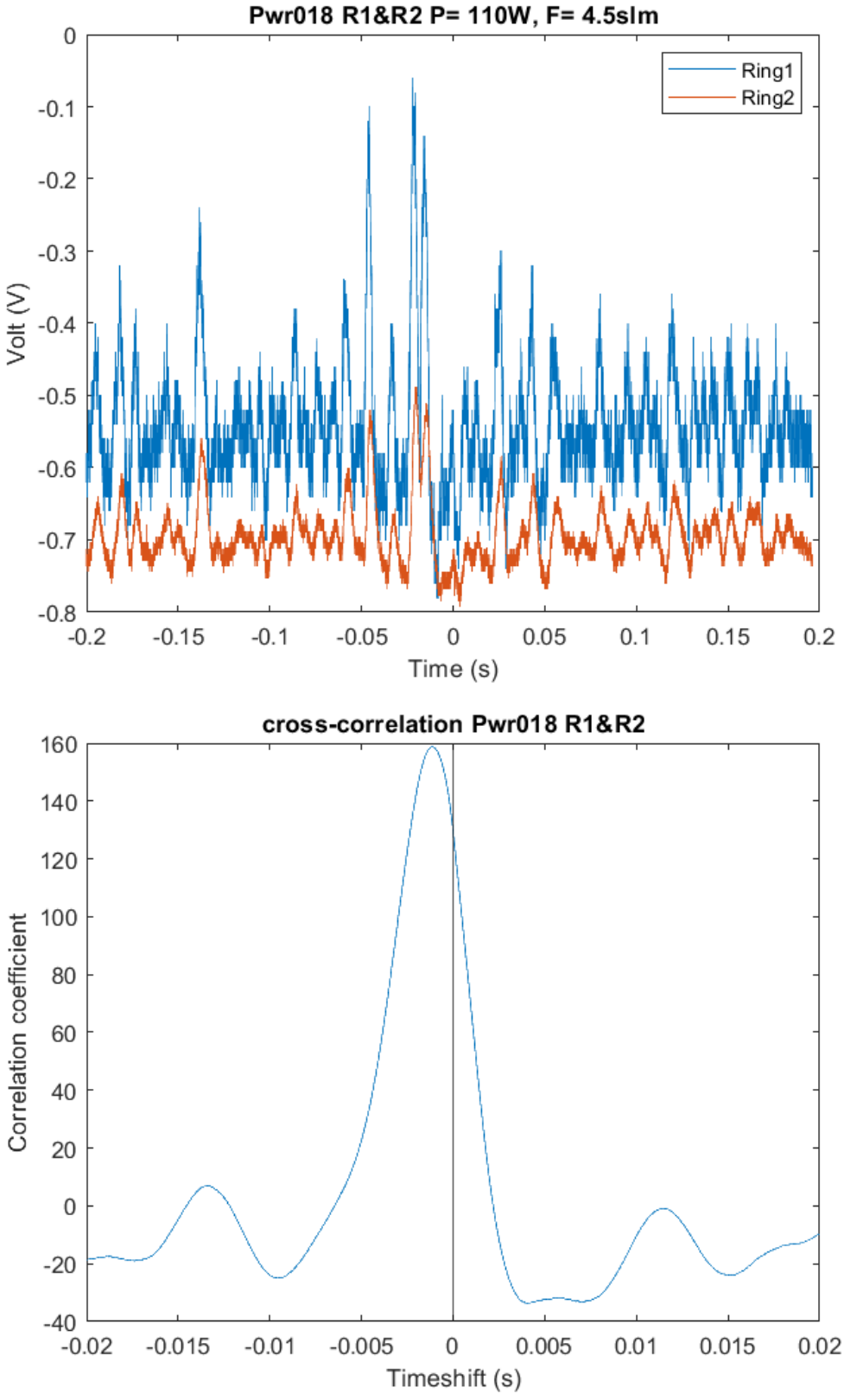

Figure 6-7: a) Amplified volt-time for experimental sample when P= 110 W, Q_{Ne}= 1.00 slm, Q_{He}= 3.5 slm and b) is the cross-correlation between ring 1 and ring 2, Amplifier gain = 1000.

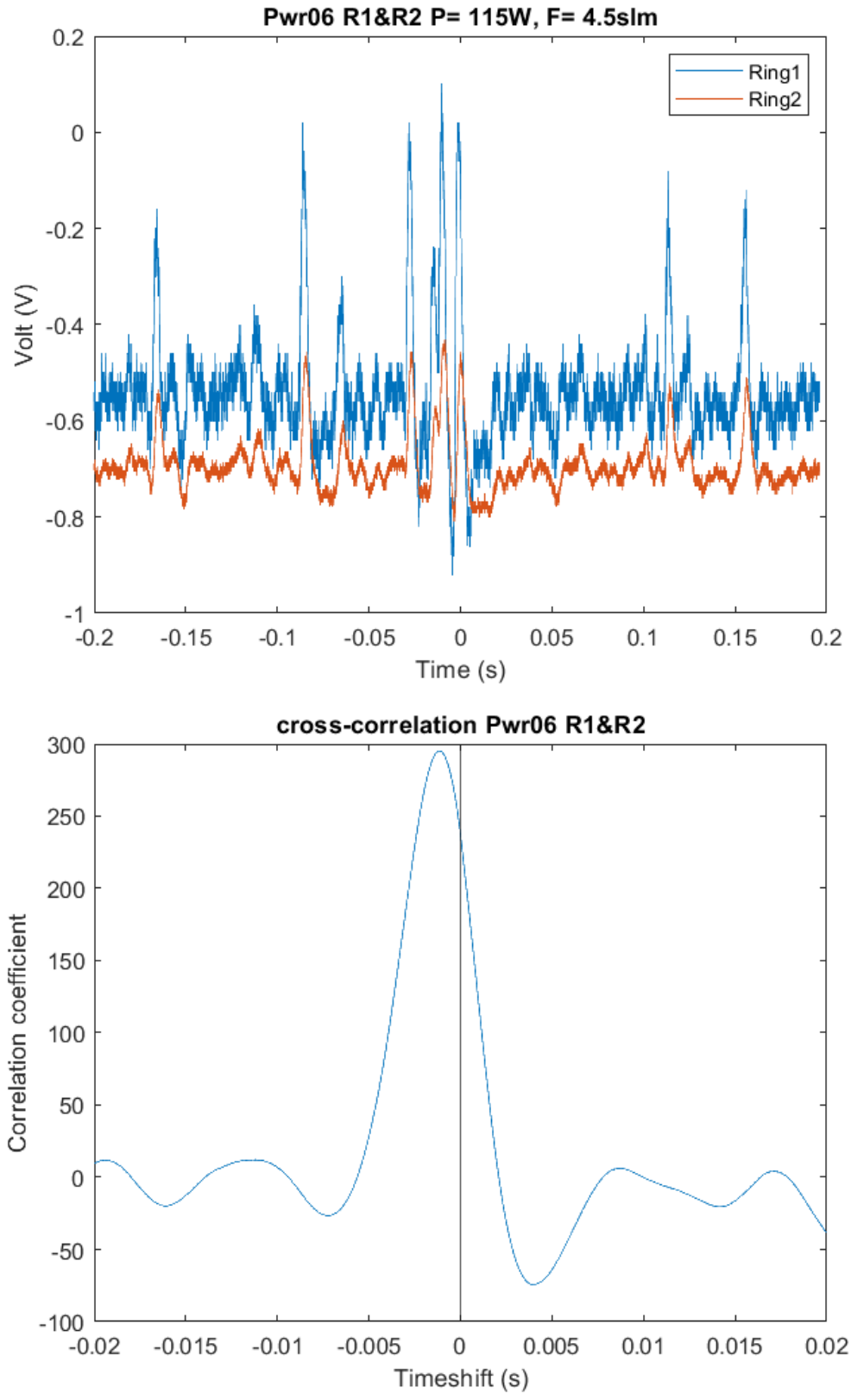

Figure 6-8: a) Amplified volt-time for experimental sample when P= 115 W, Q_{Ne}= 1.00 slm, Q_{He}= 3.5 slm and b) is the cross-correlation between ring 1 and ring 2, Amplifier gain = 1000.

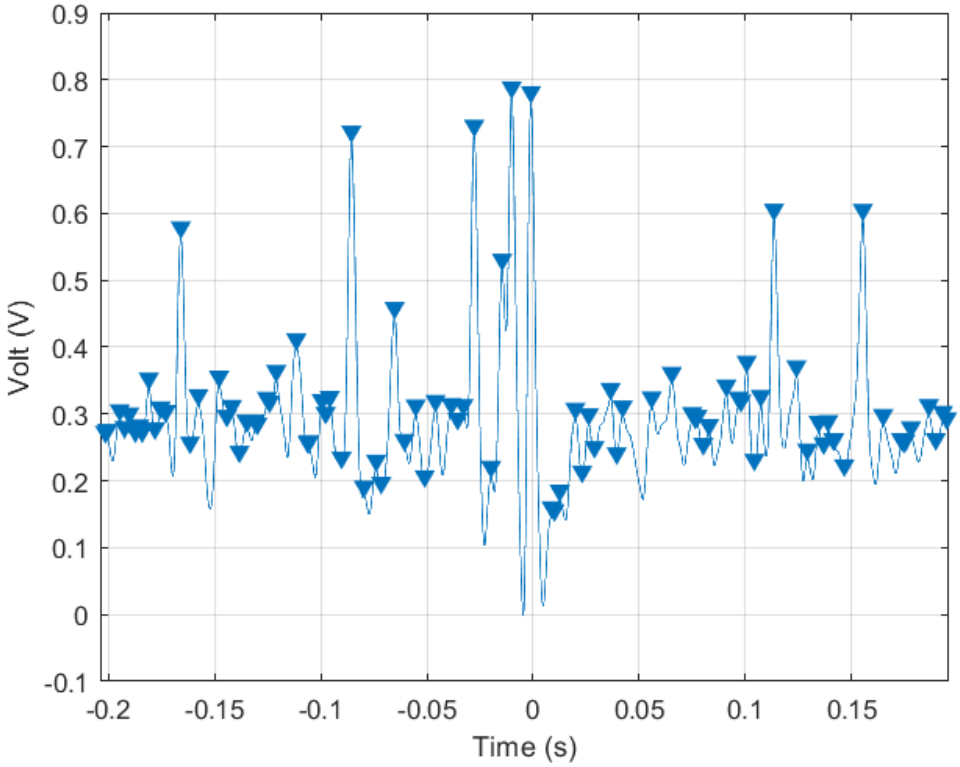

Figure 6-9: Location of signal peaks for ring 1.

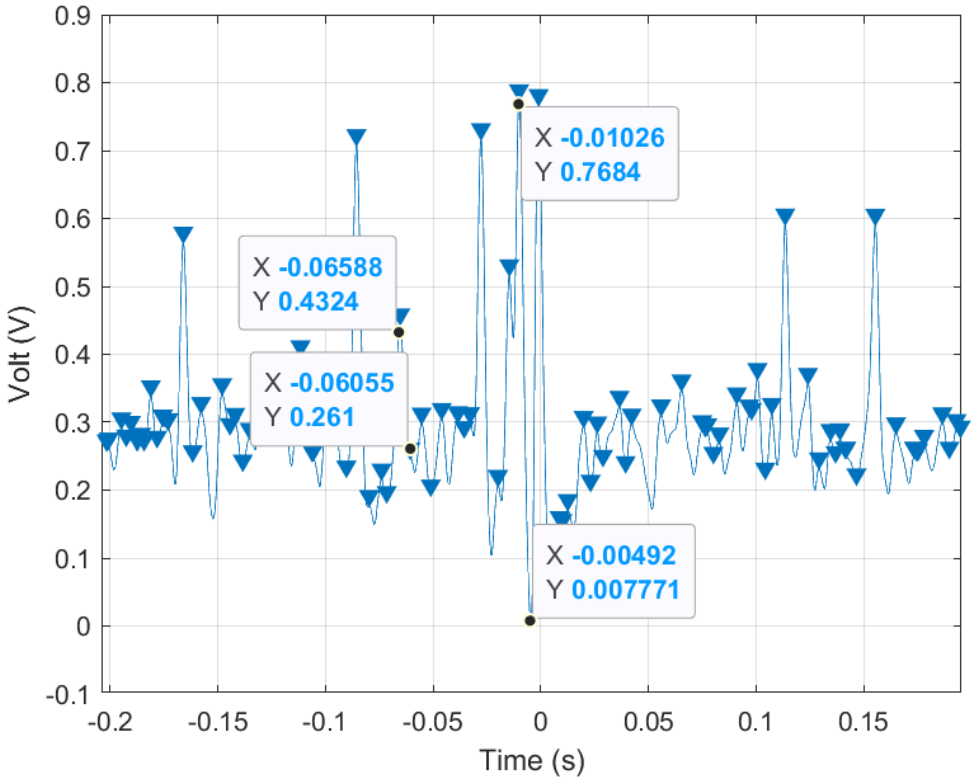

Figure 6-10: Minimum and maximum peak heights from trough to peak from our experimental sample.

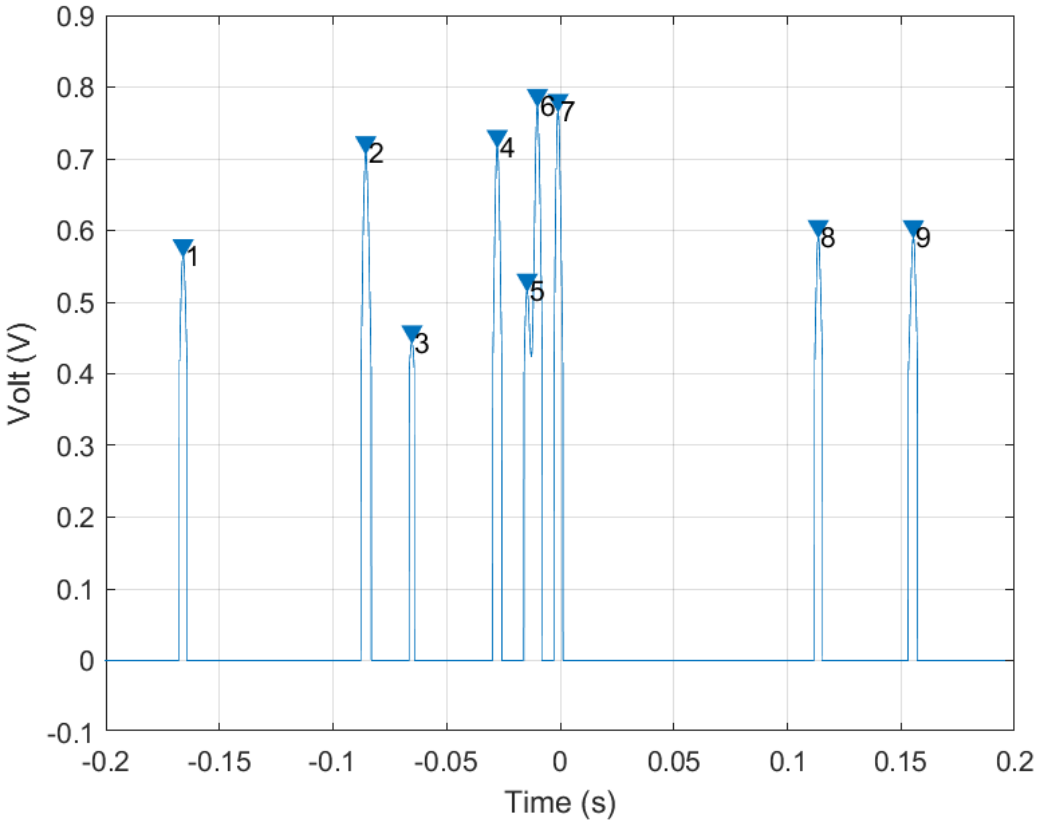

Figure 6-11: Ring 1 volt-time major peaks after applying threshold of 0.4.

Table 6: Amplitude, width, and location of major peaks of ring 1 where amplifier gain was x1000.

	Amplitude	FWHM	Time location
1	0.5651	0.0035	-0.1660
2	0.7086	0.0045	-0.0856
3	0.4448	0.0023	-0.0652
4	0.7174	0.0041	-0.0277
5	0.5169	0.0018	-0.0145
6	0.7746	0.0082	-0.0100
7	0.7676	0.0039	-0.0010
8	0.5917	0.0036	0.1136
9	0.5914	0.0041	0.1555

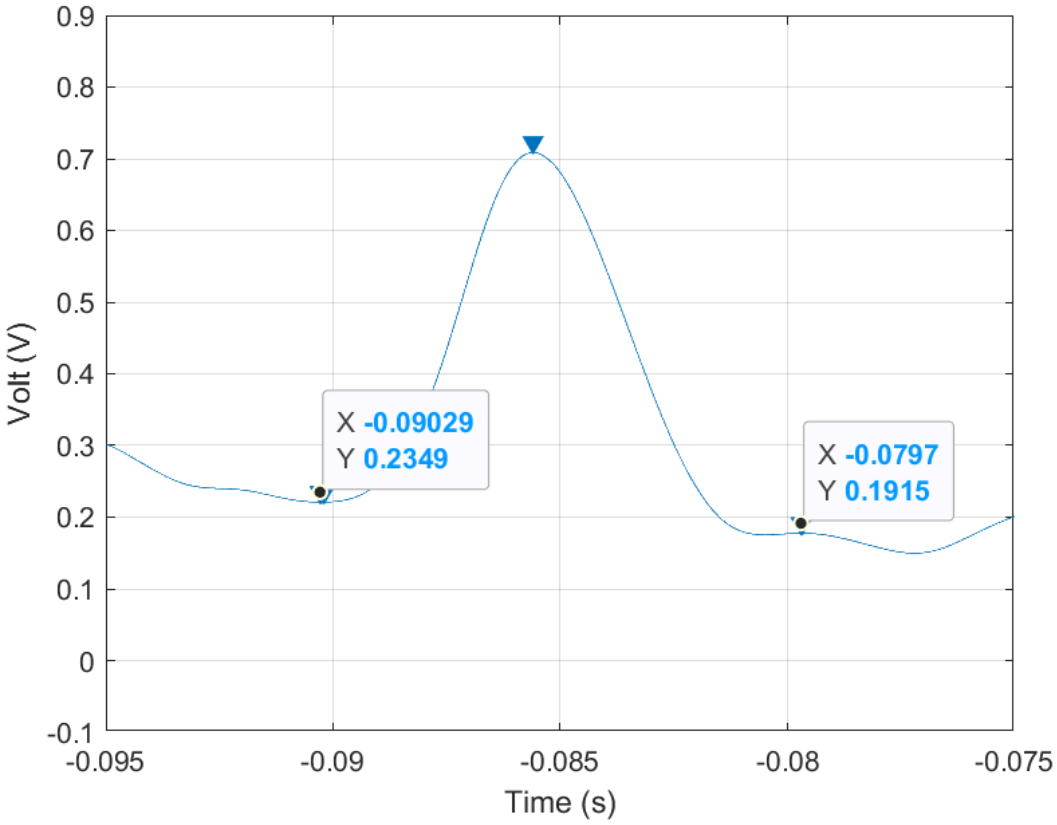

Figure 6-12: The whole pulse width of the selected peak.

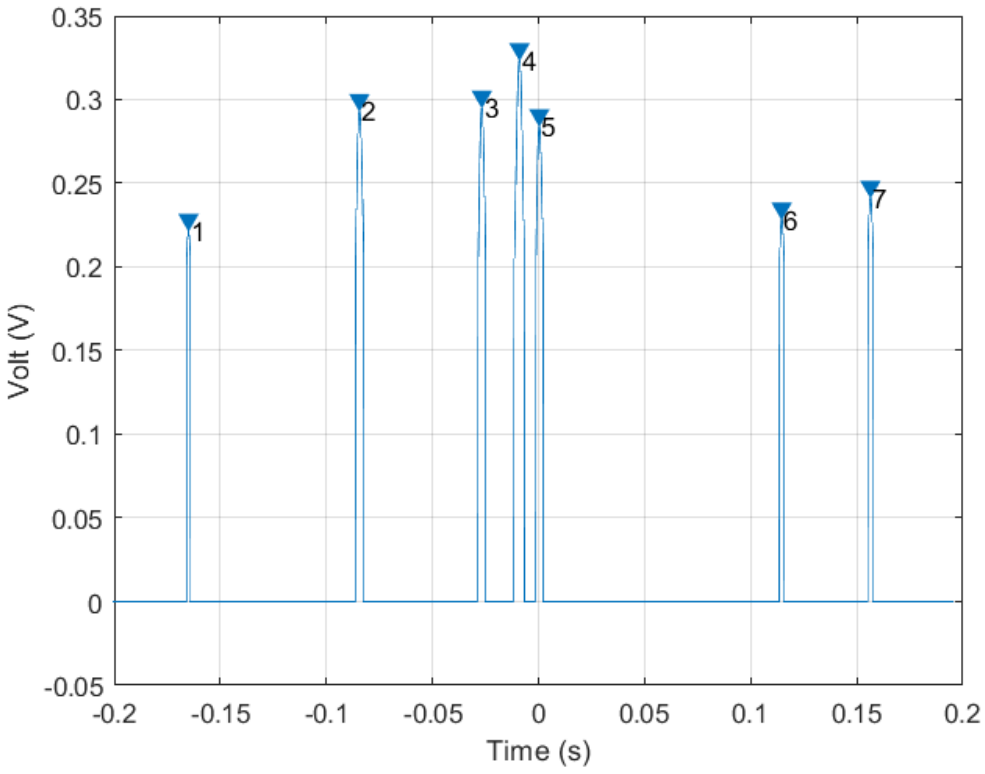

Figure 6-13: Ring 2 volt-time major peaks after applying threshold of 0.2.

Table 7: Amplitude, width, and location of major peaks of ring 2 where amplifier gain was x 1000.

	Amplitude	FWHM	Time location
1	0.2220	0.0020	-0.1650
2	0.2937	0.0040	-0.0844
3	0.2956	0.0036	-0.0267
4	0.3240	0.0049	-0.0090
5	0.2846	0.0035	0.0004
6	0.2288	0.0023	0.1146
7	0.2419	0.0028	0.1565

6.3 Mathematical model of ring electrode data

Figure 6-14 depicts a particle/ droplet carrying a charge (q) at a given location (x, z) from the centreline of the ring where x is the radial distance between droplet to the axial centreline of the ring and z is the distance from ring and can be expressed as function of time (t) and particle velocity (v_s) i.e. $z = v_s t$. D is the ring electrode diameter; W is its axial length and the angle between the electrode radius and the point charge location is θ. The particle induces a charge q` on the electrode's surface where the relation between this charge and the induced current is demonstrated in Figure 6-15.

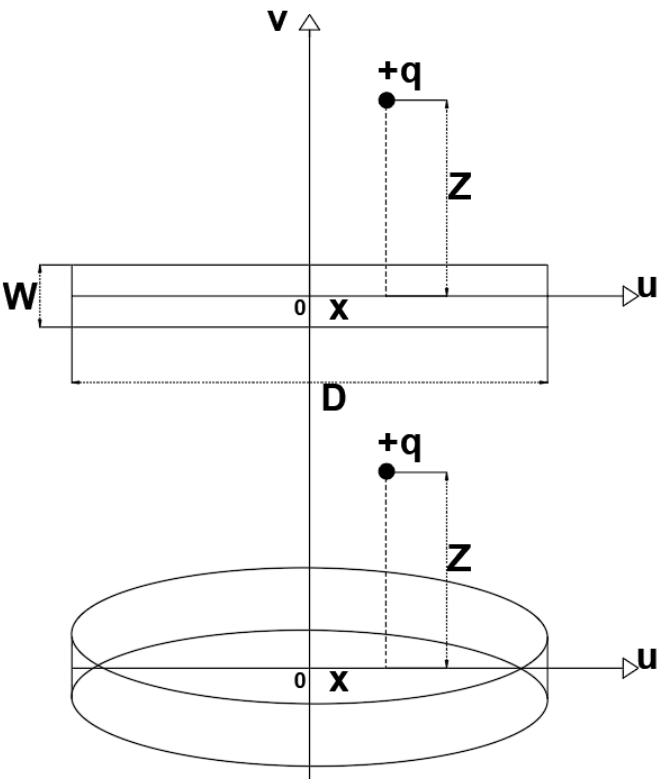

Figure 6-14: Electrodynamic sensor's coordinate system for modelling [1]. Z is the particle distance from ring, x is the radial distance from axis of ring, D is the ring diameter and W its width.

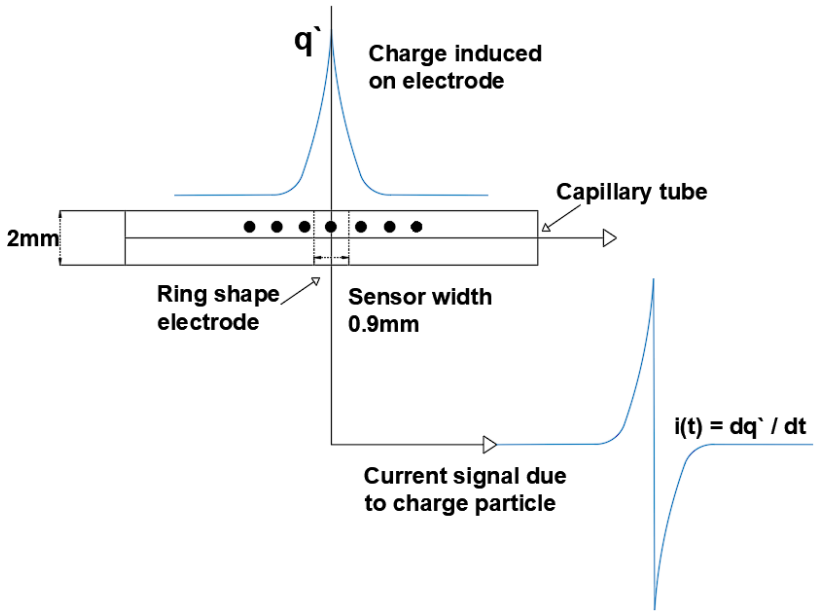

Figure 6-15: Schematic diagram of the relation between the induced charge (q`), current i (t) [2].

The presence of external circuit components such as capacitance or amplifiers may change the shape and amplitude of the signal by integrating the current signal. In the previous chapter, the charge amplifier (Amptek A250F) used in the measurement circuit was found to have a gain value of 1000 and has input capacitance of > 40.000 pF, feedback capacitor of 2 pF, output impedance < 100 Ω, operating voltage of ± 6 V, operating current ± 1.2 mA, and gain bandwidth of > 300 MHz [5]. However, comparison of amplified and unamplified signals showed no difference in pulse decay times i.e., the pulse widths were the same and so the amplifier does not act as an integrator. The same amplifier was used in this experiment and so the observed signal is considered the current signal. Therefore the equation of the actual current output of the ring electrodes due to the movement of a charged droplet has been used for the simulation which is given by [1]:

$$I(t) = -\frac{Dqv}{4\pi}\left(\int_0^{\pi}\left(\frac{0.5D - x\cos\theta}{\left((z+0.5W)^2+F^2(x,\theta)\right)^{\frac{3}{2}}} - \frac{0.5D - x\cos\theta}{\left((z-0.5W)^2+F^2(x,\theta)\right)^{\frac{3}{2}}}\right)d\theta\right) \qquad \textit{Equation 14}$$

where $f(x,\theta)$ is:

$$\left[(0.5D)^2 + x^2 - Dx\cos\theta\right]^{1/2} \qquad \textit{Equation 15}$$

6.4 Simulation procedures

The model by Yan et al. [1] has been selected because it is simpler than other models, does not require knowledge of external circuit components such as stray capacitance and because it contains variables from our experiment setup such as the radius and width of the ring electrode in explicit form. The integration in Equation 14 cannot be obtained analytically therefore a numerical solution is used. Velocity v_s is calculated by laminar flow equation depending on the selected value of x from:

$$v_s(x) = 2v_{av}(1 - x^2/R^2_{ring})$$ *Equation 16*

where v_{av} is the average velocity which is given by the gas flow (Q_g) in m^3s^{-1} divided by the capillary tube area. The unknowns in Equation 14 are x, D, q. We initially assume that droplets pass through the centreline of the tube i.e., x = 0 and that q is a constant value for all droplets. While these interim assumptions are not realistic, the model is progressively improved by using more realistic values of x, D and q. Droplet radial locations, x, and droplet sizes are estimated from their measured distributions, with each individual droplet allocated a random value of x and D so that over a large number of droplets the measured distributions are reproduced. We also assume that q depends on diameter, D, where the dependence comes from a theoretical charging model. This procedure would allow us to validate each step and to judge whether it is correct or not before moving to the next step and increasing the number of variables. In addition, the charge results for this chapter will be compared with the previous chapter results for validation also, the simplified charge approximation Equation 13 from [3]. will be evaluated for comparison. The assumptions development and the simulation procedures are as follow:

- Initial assumptions are assuming q is constant for all droplets and that droplets pass through the centreline of the tube i.e., x = 0.
- followed by estimation of the equivalent droplet charge to match the experimental signal.
- Comparison between droplets at different x locations from the centerline and the original experimental signal.
- Gradual increase to the number of droplets and providing simulation of two pulses and 100 pulses.
- Then droplets radial locations, x, and droplet sizes will be selected randomly from their measured distributions.
- Random q values will be allocated using a polynomial approximation for the droplet charge dependence on the droplet radius.
- The simulation parameters of random droplets with random q, x, v_s will be implemented for 1000 droplets representing ring 1.

- Analysis of ring 2 for 1000 random droplets and random q, x, v_s by implementing charge delay and decay to ring 1.
- Cross-correlation between ring 1 and ring 2 for droplets velocity estimation.

6.5 Simulation parameters

Simulation parameters are droplet size (D) and charge (q), droplet radial location (x) and droplet velocity (v_s). For simulating multi droplets, a random selection of droplet with size D and radial location x is implemented where the droplets velocity and charge will be dependant on these two parameters where the distributions and assumptions used are described in this section:

6.5.1 Droplets location and velocity distributions

Droplets have various locations with respect to the centerline of the capillary tube which is represented by x. The uniform distribution of droplets is represented by a 2D plan taken as an axial section through the centre of a cylinder where the vertical projection of this plan is a line of length equal to the diameter of the cylinder [5]. By splitting the line into equal 10 segments of thickness dx for each, the uniform distribution indicates equal number of droplets in each segment which is at distance x from the centre. When each segment is then integrated with a limit of 360^o, it forms an annulus with average radius x. The total number of droplets in annulus is $\frac{2\,\pi\,x}{W}$ where W is the focal depth of the imaging and represents the width of the segment, then the droplets distribution versus x is the relative number of droplets in each annulus. After selecting a random value of x, the corresponding value of velocity is calculated from the laminar flow equation in Equation 16 depending on the droplet position.

6.5.2 Droplets sizes distributions and charge - radius relationship

Based on previous work by NIBEC team on a similar plasma system [6], the droplet sizes follow a known lognormal distribution which is related to measured size distribution depending on droplets count median diameter (CMD) and geometric standard deviation (GSD). A random selection of droplets radius was simulated using the lognormal distribution for a measured size distribution of CMD = 13.9 x10^{-6} m and

GSD = 1.73. Whereas the charge on a droplet is thought to depend on its size, however the relationship q-r is unknown for plasma charging at atmospheric pressure. There are three different simulation models for particle charging i.e., orbital motion limited (OML) theory [7–9], Allen, Boyd, & Reynolds (ABR) theory [10,11] and Patacchini - Hutchinson model (PH) [12,13]. The former assumes a moving charge with critical radius of approach below which electrostatic forces will ensure collision with the particle and hence determines the effective capture cross-section. For example, if a Langmuir probe with a cylindrical geometry and probe length bigger than its radius collects electrons, then the electrons move in a central field of force where the conservation of energy and angular momentum apply.

ABR assumes radial motion only for cold ions that follow the lines of force and move in straight lines radially toward the particle via electrostatic attraction [8]. For the case of a spherical probe inserted in a plasma, the density of electrons and ions will be equal where the ions moves towards the probe and the potential highly depends on the probe's radius when the cold-ion assumption is valid [11]. The Patacchini-Hutchinson model provided a comprehensive description for electron collection as well as electrons motion in grain sheath in the presence of magnetic fields. They also provided a MATLAB code representing Patacchini-Hutchinson model for particle charging involving the populations of both drifting Maxwellian ion and Maxwellian electron [14]. Each model provides a relationship between charge and droplet radius and a polynomial fit is obtained as demonstrated in Figure 6-16. The polynomial fit to the output of the charge model from Figure 6-16 is:

$$q = a(R^2) + bR + c \qquad \textit{Equation 17}$$

Where radius is in μm and the constant values a, b and c are constants of the second order polynomial equation and depend on the model as following:

- Model PH = [a = 900, b = 900, c = - 25864]
- Model ABR = [0, 3000, 0]
- Model OML = [12949, 11730, - 17570]

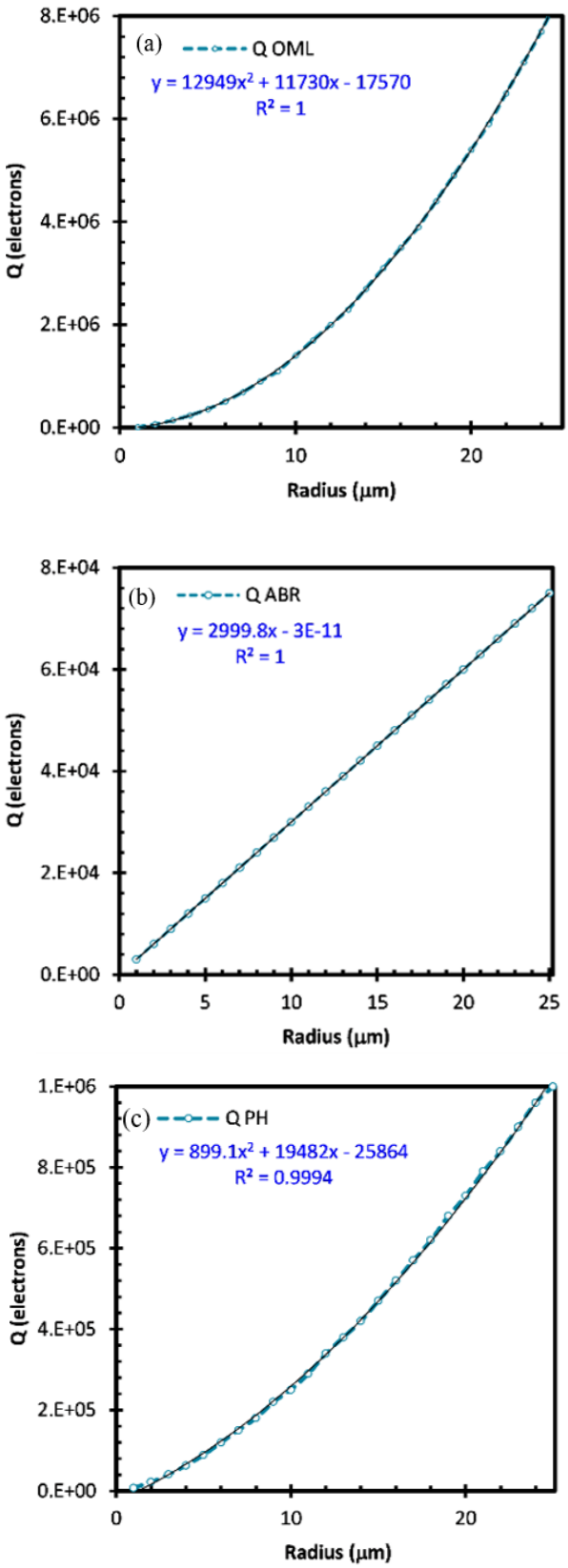

Figure 6-16: Plots of Q vs R calculated for a) OML model, b) ABR model, and c) PH model.

Using the measured size distribution, a charge value is given to each droplet size according to the model fit, such that the average charge is equal to that measured. According to the different simulation models PH, ABR and OML [15] where OML and ABR models are most commonly used in collisionless low pressure plasmas. PH model was developed for collisional plasma and can be used under specific conditions where the charged particle does not perturb the plasma and that is the case when the floating potential is small and the Debye is large which is the case in our plasma [15,16]. At this condition, the perturbation exerted by charged particle is small and on the other hand, plasma does a perturbative effect on the charged particles where the field slightly perturbs the equilibrium motion of the electrons as a result of the applied field and leads to approximate straight-line motion as studied by Neufeld et al. [17] however, this does not affect the selection of our model. If the floating potential is high and the Debye length is small, the plasma experience nonuniformity and as a result, the charged particles perturbs the plasma and forms a Debye sheath around it [16]. In summary, PH model was selected for the charge calculations in this simulation because it was developed for collisional plasma in contrast to OML and ABR. It also offers a complete description for charging by electron in the presence of magnetic fields, including the motion of electrons in the grain sheath [14]. In addition, Patacchini et al. [13] provided a formulas for charged particles current with various radii to understand the dust particles charge and Langmuir probe characteristics. This formulas involves the electron density which was validated and proved to have a small error providing electron flux density using empirical expression and leading to potential profile determination. This model has another advantage over OML and ABR models that it entails the influence of the finite-Larmor radius on the electrons. Where the finite-Larmor radius is the radius of the helix generated by a particle moving in plasma magnetic fields and is function of the applied magnetic field as well as the particle's charge, mass and velocity [14].

6.6 Simulation outputs

6.6.1 Simulation of a single droplet

Simulation of charged droplets using Equation 14 will be presented in this section. Starting by simulation of single droplet with the initial assumptions of a charge q =1.0 e and passing by the centerline of the tube (i.e., x = 0) followed by estimation of the equivalent droplet charge to match the experimental signal. Then a comparison between droplets at different x locations from the centerline and the original experimental signal is shown.

6.6.1.1 Unit value charge at the centre of the tube

Figure 6-17 shows the simulated signal for one single droplet travelling along the capillary centreline (x = 0) and currying a charge of 1 electron (q = 1.0 e). The droplet velocity is 34 m/s from Equation 16 for a selected experimental sample with nominal flow of 4.5 slm and after calibration factor correction was applied, it was 3.2 slm. Applying these values to Equation 14 and for electrode diameter (D) of 2 mm, the result pulse amplitude is 1.7×10^{-15}A and W_p = 32 µs. Our signal from the experiment is amplified where the amplifier gain factor (Ring 1) = 1000 and the oscilloscope input impedance (R_{osc}) is 10^6 Ω therefore, the resultant simulated volt-time pulse is demonstrated in Figure 6-18 and has amplitude of 1.7×10^{-6} V and W_p = 32 µs.

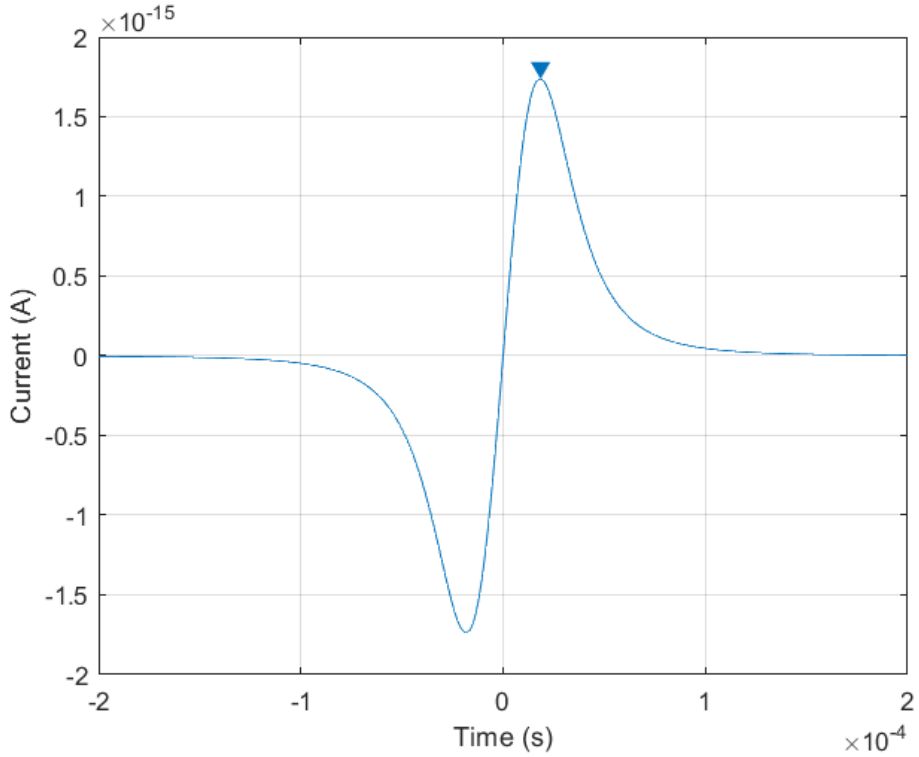

Figure 6-17: Simulated current-time signal for q = 1.0 e.

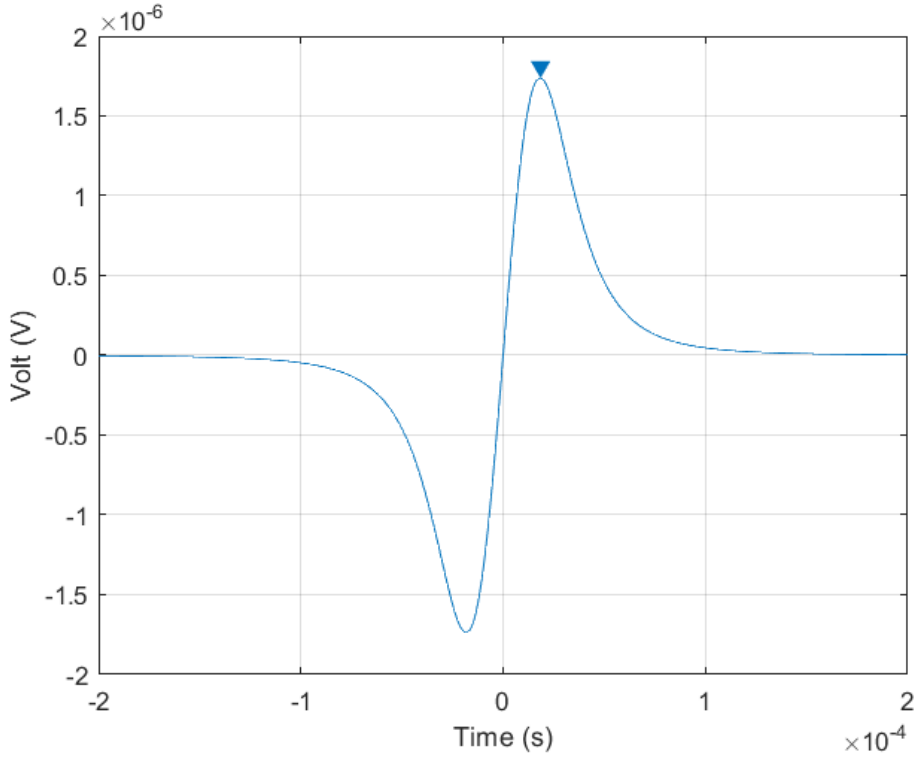

Figure 6-18: Simulated volt-time signal for q = 1.0 e.

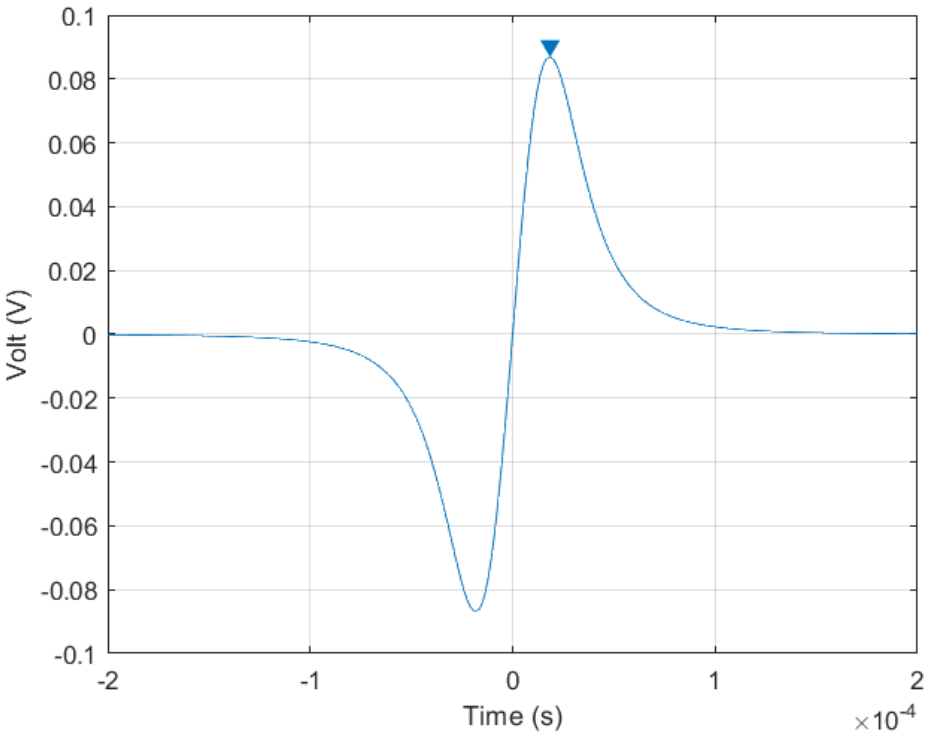

Figure 6-19: Simulated signal volt-time for q = 5.0 x 10^4 e, x = 0.

To match the amplitude of the simulated signal with the average amplitude range of our experimental sample, which is 0.09 - 0.38 V from Figure 6-10, the charge value q would have a value between 5 x 10^4 e - 2.24 x 10^5 e. Figure 6-19 is an example of a simulated pulse for q = 5.0 x 10^4 e with a pulse amplitude of 0.0869 which is a close approximate to that of the smallest experimental peak. This means that if each pulse were a single droplet the value of charge would be in the range of 5.0 x 10^4 e - 2.24 x 10^5 e to match the experimental signal.

6.6.1.2 Simulation of single droplet at various x

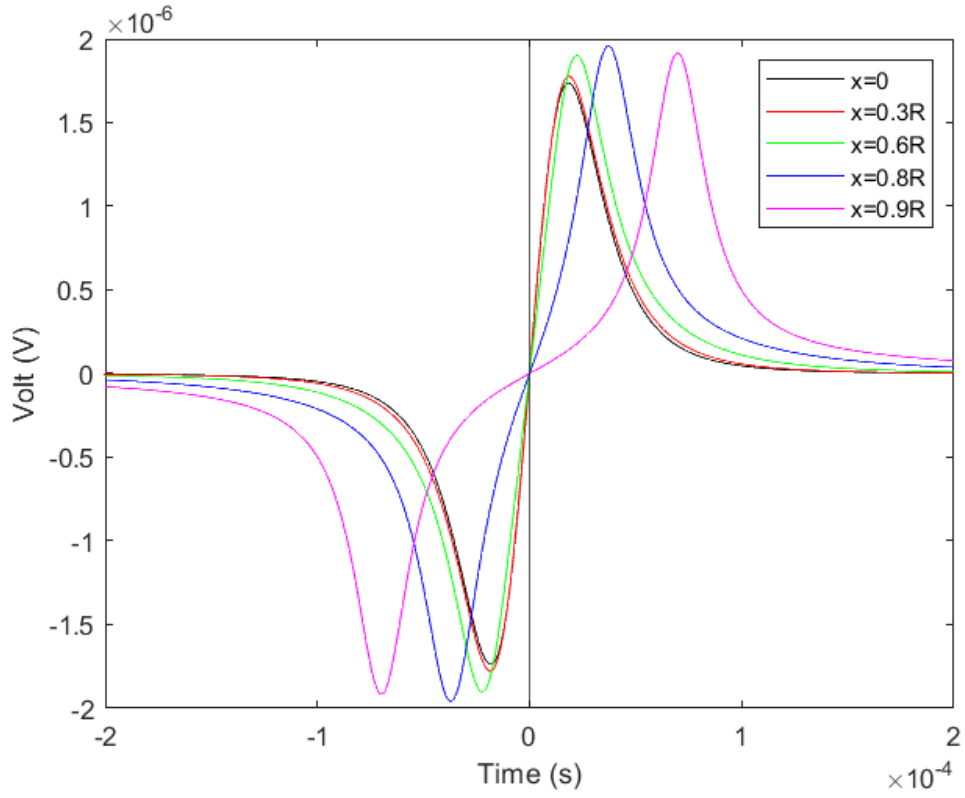

Figure 6-20: Volt-time plot for various x values.

This section aims at understanding the profile of the pulse when the droplet has a location of x between x = 0 and x = 0.9 R from the centerline of the tube (i.e. x = 0) for q = 1.0 e. Figure 6-20 demonstrates that all pulses are same width about 50% level so FWHM has almost equal values of 33 μs however, the pulses of droplets travelling at large x are broader below 50% - so FWHM is not a good indicator. The simulated signal at x = 0.9 R starts at - 200 μs and ends at + 200 μs, which gives a whole pulse width of ~ 400 μs. An approximate range for FWHM observed experimentally is 230 - 820 μs as indicated in Table 6 and the whole pulse width of the experimental selected peak is 10.6 ms, Figure 6-12. By comparing the pulse width of the measured signal with the simulated signal at x = 0.9 R, the simulated pulse width is much smaller than that of the experimental pulse. This may be due to interference by nearby droplets also adding to the experimental signal so that single droplets are not being measured. The next step is to increase the number of pulses by adding more droplets to the simulation to test the interference effect.

6.6.2 Simulation of two pulses (x = 0, q = 1.0 e)

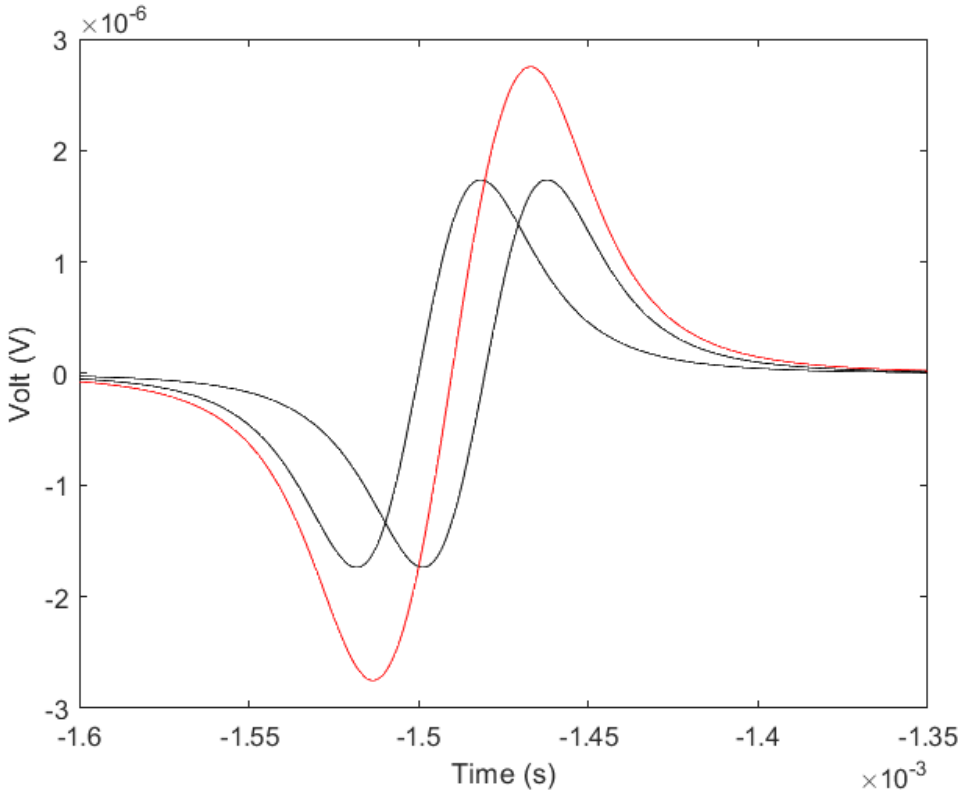

Figure 6-21: Volt-time plot for two pulses at the centre of the tube.

Figure 6-21 shows two separate pulses and their summation for similar value of q and at the centerline of the tube i.e., x = 0. The droplets rate is (freq)= 5 x10^4 droplets/s therefore the timeshift between the two droplets is 20µs. As long as each individual pulse has a width of ~ 33 µs which is bigger than the timeshift, pulses are expected to overlap, as shown in summation which amplitude of 2.75 x10^{-6} V and W_p = 37.5 µs.

6.6.3 Simulation of multi droplets

6.6.3.1 Same charge value at the centerline of the tube (x = 0, q = 1.0 e)

A simulation of 100 droplets passing along the centerline of the tube i.e., x = 0 with timeshift of 20 µs between them and similar charge value of q = 1.0 e is presented in Figure 6-22 and indicates a signal of 1000 µs from start to end. The amplitude is almost zero since the single droplet pulses are exactly same shape and cancel out except near start and end of signal. Where the delay is dependant on the distance between the two electrodes which is constant and equal to 22 mm and on the velocity of each droplet. The signal in Figure 6-22 is not yet similar to the signal of the original experiment presented Figure 6-8 because the real signal is expected to have a composition of droplets sizes with different q values and also different x locations which gives different droplet velocities and therefore timeshifts. This will be implemented in the simulation in the following sections to add randomisation.

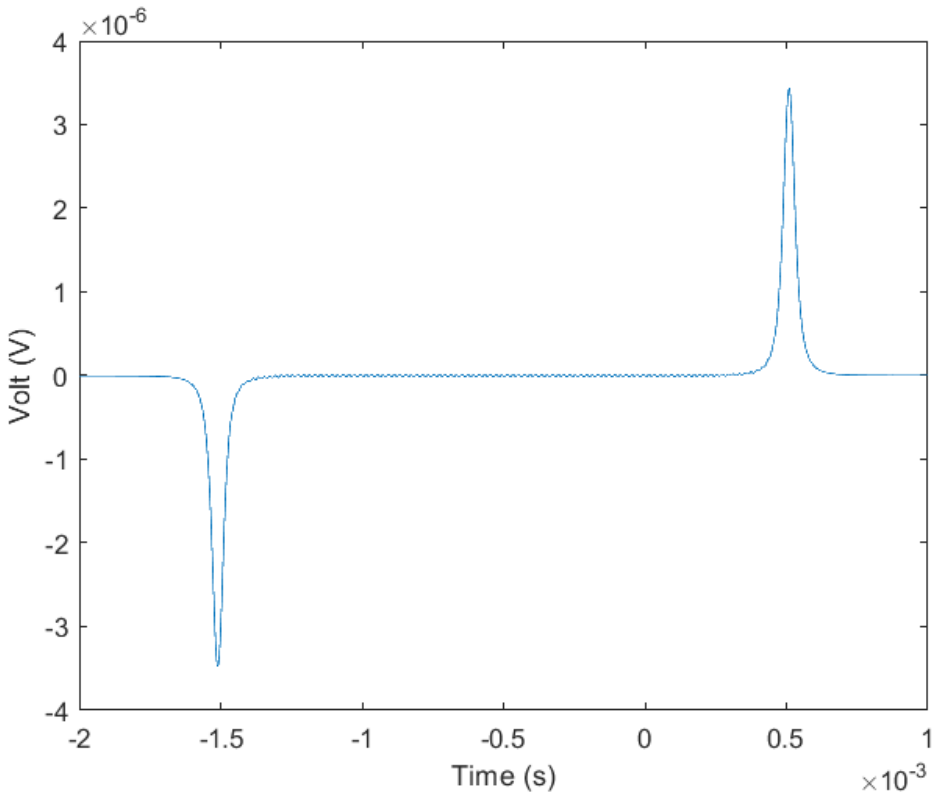

Figure 6-22: Volt-time for 100 droplets at the centerline of the tube and with q = 1.0 e where the amplitude is almost zero in the mid-time range because the single droplet pulses have a similar signal that cancel each other.

6.6.3.2 Simulation of 100 droplets and 1000 droplets with random charge q

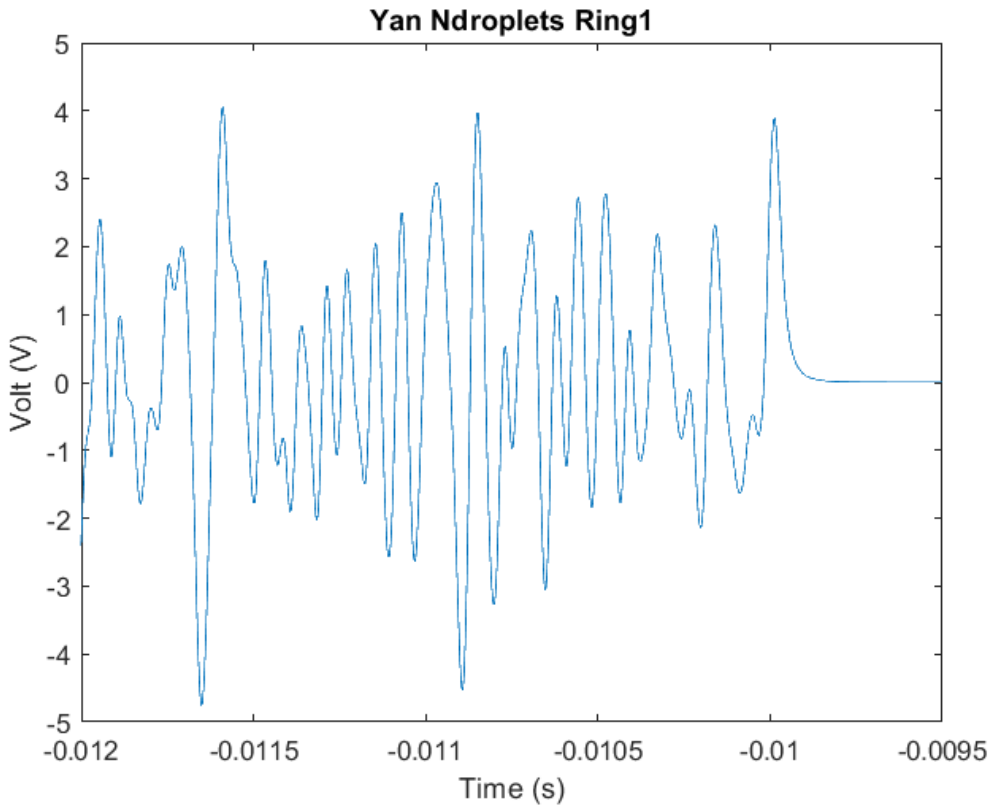

Figure 6-23: Volt-time for 100 droplets with random q at x = 0.

Figure 6-23 shows the simulated signal after implementation of random droplets radius and consequent charge value assuming all droplets pass by the centerline of the tube. Although this signal is closer to the experimental signal than Figure 6-22, droplets have various locations with respect to the centerline of the capillary tube which is represented by x. After selecting a random value of x, the corresponding value of velocity is calculated from the laminar flow equation in Equation 16 depending on the droplet position. The next step is to increase the number of droplets to 1000 droplets in the simulation and the resultant signal for random droplets radius, charge, velocity, and location is shown in Figure 6-24.

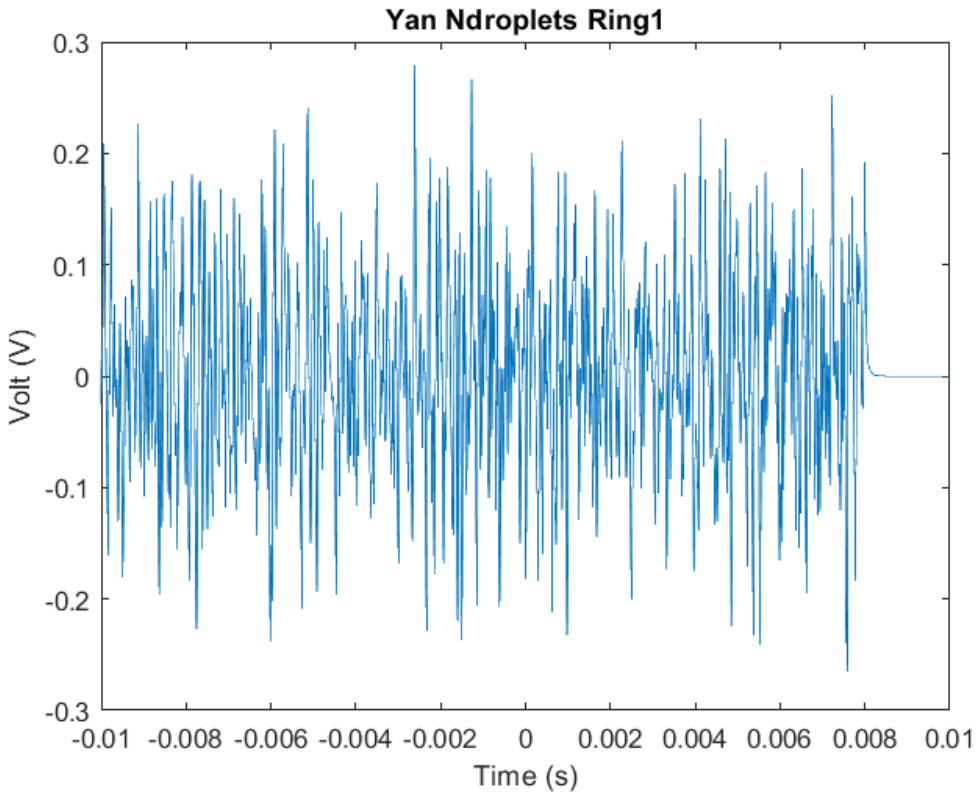

Figure 6-24: Volt-time for simulated 1000 random droplets.

6.6.4 Ring 2 signal

The calculations of ring 2 signal is based on the time taken by the droplets to pass ring 1 in addition to the time to reach ring 2 which is equal to x_g / v_s where x_g is the gap between the two electrode = 22 mm, Figure 6-25.

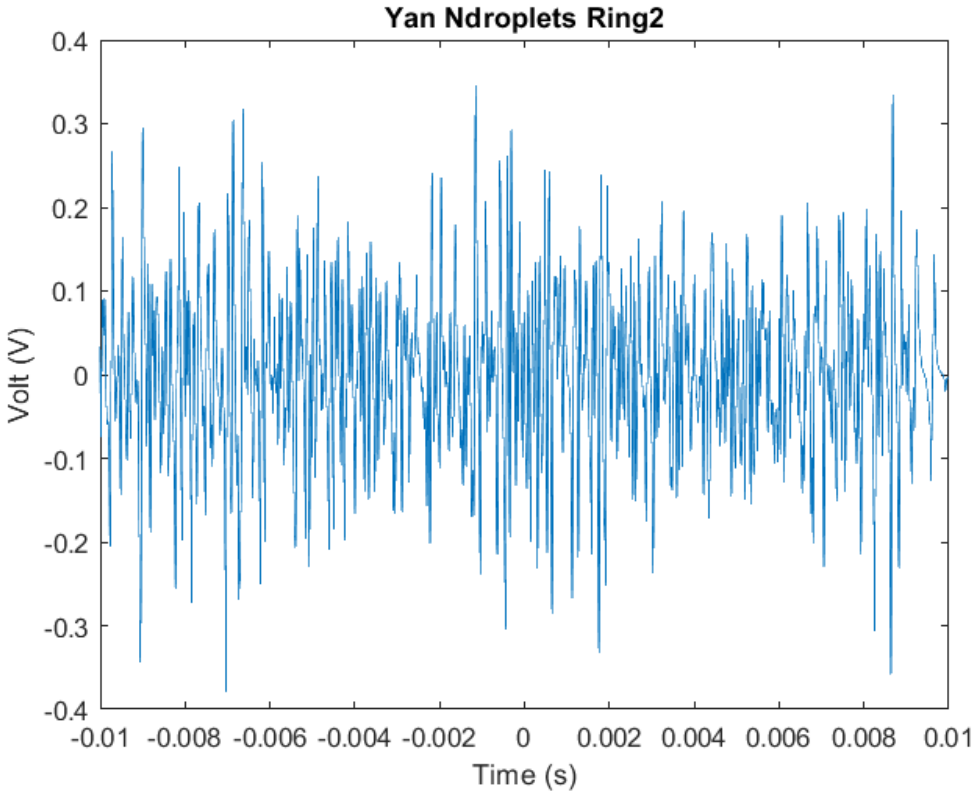

Figure 6-25: Volt-time for 1000 droplets for ring 2 generated by implementing the effect of droplets decay and droplets delay which is the time taken by the droplets to travel from ring 1 to ring 2.

6.7 Discussion

The main objective from this work is using a non-contact method to provide an estimate value of charge on individual droplets and if not possible, average charge for multiple droplets would be determined. Double ring electrodes outside the capillary tube has been used as it has potential advantages over other measuring techniques such as less droplets charge loss, less plasma interference as collector is far from the plasma and less gas and droplets flow disruptions. The signal generated on

ring 1 by the droplets has been recorded and analysed considering average pulses width (W_p), amplitude (A), and number of pulses per second (PPS). Where average W_p = 1 ms, A = 286 mV and average PPS was ~ 475 s^{-1} for the original signal and ~ 23 s^{-1} after applying a threshold of 0.4 to consider big droplets only. Although data from ring 1 would be sufficient for providing estimate charge value, ring 2 data was collected and analysed for the purpose of estimating charge decay with distance and the droplets velocity. The droplets velocity estimation from ring 1 and ring 2 are most likely to be successfully achieved when the signals are clean. From analysis of ring 2 signal, average W_p = 1.2 ms and A = 52 mV where average PPS were ~ 405 s^{-1} and ~ 18 s^{-1} for the original signal and after applying a threshold of 0.2, respectively. The number of pulses in ring 2 signal is slightly lower than ring 1 and that may be due to loss of smallest droplets in the gap between the two electrodes. Also, the voltage has been dropped by ~ 231 mV, but pulses width is almost similar.

Although droplets charge depends mainly on the voltage amplitude, average charge value cannot be estimated directly from the volt-time signal measurement because there are other factors involved according to the electrostatic theory e.g., droplets size and velocity. Therefore, the only practical solution is signal simulation to calibrate the ring collector so that measured voltage can be converted into droplet charge for the purpose of achieving our main objective of indicating the average charge on individual droplets or the average charge on multiple droplets would be estimated, if the first was not possible. Simulation done is based on Yan et al. [1] model depending on the particle distance from ring (Z), the radial distance from axis of ring (x), the ring diameter (D) and width (W). Simulation of single droplet carrying a unit charge (q = 1.0 e) at x = 0 was conducted and followed by estimation of droplet charge to match one pulse in the experimental signal. Charge estimation was evaluated by comparing the amplitude of the simulated signal with the amplitude of a single selected peak from the experimental signal and the droplet charge was estimated as $q = 5.0 \times 10^4$, approximately. This comparison is based on implanting the droplets size distribution of the experimental sample in the simulation. The effect of the droplet's radial location x on the width of the signal has also been demonstrated as well as the effect of increasing number of droplets on pulses width and amplitude.

Simulation parameters of random q, x, v_s was implemented for 1000 droplets based on few assumptions. The droplets sizes are expected to follow lognormal distribution and droplets rate was implemented as 5.0 x10^4. The model is sensitive to both of them because the charge on the droplets relies on the droplets size and the timeshift between droplets depends on the droplets rate. The lognormal distribution has a creditable value based on the experimental sample CMD and GSD however, an analysis can be performed in future work to judge the distribution sensitivity to these values. In a previous work of NIBEC team [6], the droplets rate has been estimated and droplets average velocity was evaluated to have similar value of gas velocity which is the base of our assumption in the simulation. This estimation was based on specific plasma operating conditions so the distribution might change when applying different conditions and different gas flow whereas more size measurements can be done as a future work if needed. In addition, a laminar gas flow is assumed so the laminar flow equation has been used to calculate the droplets velocity based on their radial distance. X – distribution is based on the observation of uniform droplet density in a 2D plane of a certain thickness (i.e. depth of field) where the droplets position data is also presented in [6]. The Q - R_{drop} relationship is assumed to follow the P-H model and it has been evaluated in [15] for the first time in APP. The external circuit, e.g., stray capacitance and the amplifier, has been assumed not to affect the measurements, however they may reduce the measured voltage if they have a long time constant. Also, the amplifier could function as an integrator which would change shape of peak from bipolar peaks to unipolar peak, reducing the peak height and making the peak wider. Nevertheless, the profile of the measured signal shows bipolar peaks which means that the amplifier in the system does not function as integrator. Also previously measured signals with and without amplifier showed no change in pulse width and confirming that integration is not occurring. The final result simulated signal has a close approximate profile to the experimental signal which can validate these assumptions as revealed below.

From simulation and after implementing q = 5.0 x 10^4, Figure 6-26, the average pulse width W_p= 0.13 ms compared to W_p = 1 ms for the experimental sample. This shows simulation to have much narrower pulses and that could be due to the electrical response of the circuit – with stray capacitance between the ring and oscilloscope. When a voltage pulse charges the capacitance, it has to discharge before the next pulse.

Discharging a capacitor is exponential ~ $e^{-t/RC}$ where RC is the time constant with values of R = 1 MΩ of oscilloscope resistance and capacitance of C ~10 pF. This leads to RC ~10 μs, which is much smaller than milliseconds observed, therefore it is unlikely that the wider peaks of the experimental are due to the circuit. The fact of amplifier may act as an integrator has been considered and experimental data were collected for amplified and unamplified signals whereas results showed similar peak width for both of them, consequently the amplifier in the circuit does not affect the signal as integrator. There are few options to make the simulation pulse width wider such as larger x which leads to an increase in the pulse width as shown from Figure 6-20. Also, smaller droplets velocity would lead to wider peaks, and this was evaluated from pulse signal analysis at x = 0 where the pulse width of a single droplet at v = 20 m/s was 0.06 ms and when v = 10 m/s, W_p was 0.11 ms. Furthermore, the addition of multiple droplets increases the width of pulse signal as been indicated from Figure 6-21 where W_p = 33 μs for a single droplet was compared to W_p = 37.5 μs for two droplets separated by 20 μs.

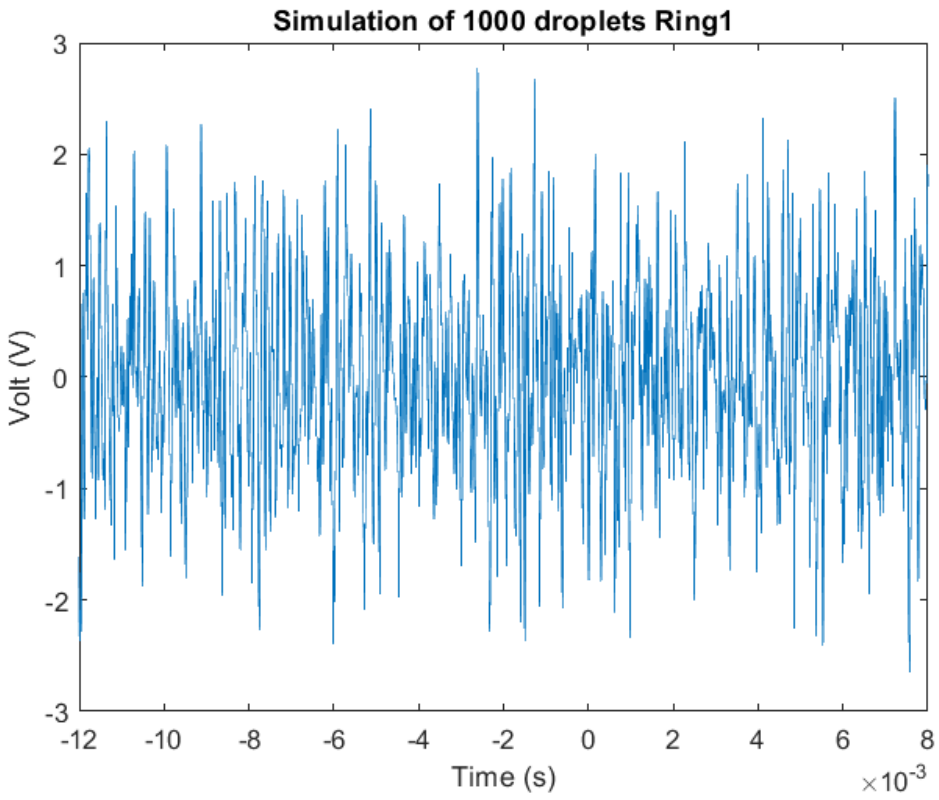

Figure 6-26: Volt-time signal of 1000 droplets for ring 1 where q = 5.0 x 10^4.

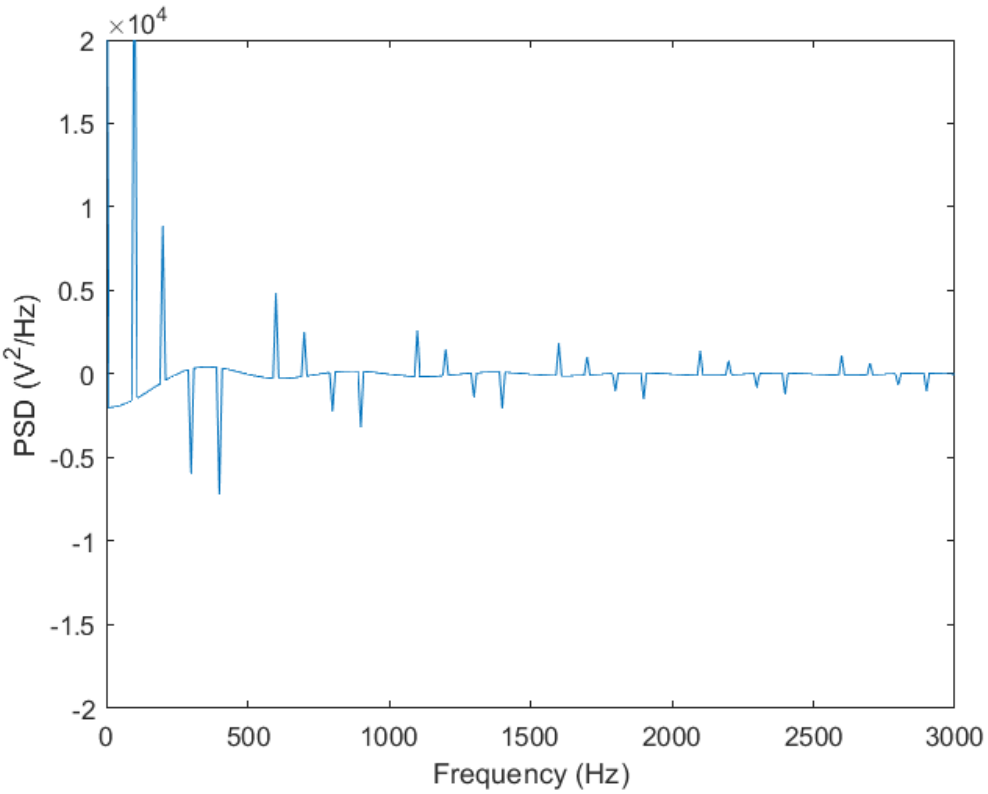

Figure 6-27: Theoretical power spectral density (PSD) of a pulsetrain with a 125 Hz pulse rate and each pulse of 4 ms pulsewidth. The PSD shows most of the power is at 125 Hz as indicated by the largest peak. Other frequency components exist at higher frequencies, as shown.

The power spectral density (PSD) is widely used in signal processing to analysis random signals by overlaying and comparing them. PSD measures relative signal power at each frequency. Since the measured PSD showed a wide range of frequencies, it is necessary to determine what is expected theoretically due to the charged pulses and therefore what is due to noise and artefacts. *Pulsetran()* is a MATLAB function which prototype continuous pulses by generating series of pulse trains to help understanding our signal [18]. For a train of single pulses, in the example of Figure 6-27, the maximum power, i.e. dominant signal, is in the frequency given by the pulse rate, 125 Hz in this case. However, there are other peaks generated at higher frequencies than 125 Hz but smaller in amplitude. So, in comparison with the experimental results which has a 50 kHz droplet i.e. pulse rate, a 50 kHz peak would be expected as the dominant peak along with higher frequency peaks. However since the droplets travels at different values of x from the centreline of the capillary tube,

this means the signal will consist of many pulsetrains, one for each x, with different velocities at each x and hence different pulse rates. Also since the cross section of the capillary tube is circular, the number of droplets at each x value is proportional to the cross section area of the shell. The number of droplets at each x and their velocity determine the frequency of pulsetrain x. Therefore, each x-value is supplying a pulsetrain collection of frequencies with a different main frequency (and associated harmonics) which then are summed together and overlapped. Therefore a very complex signal can be expected.

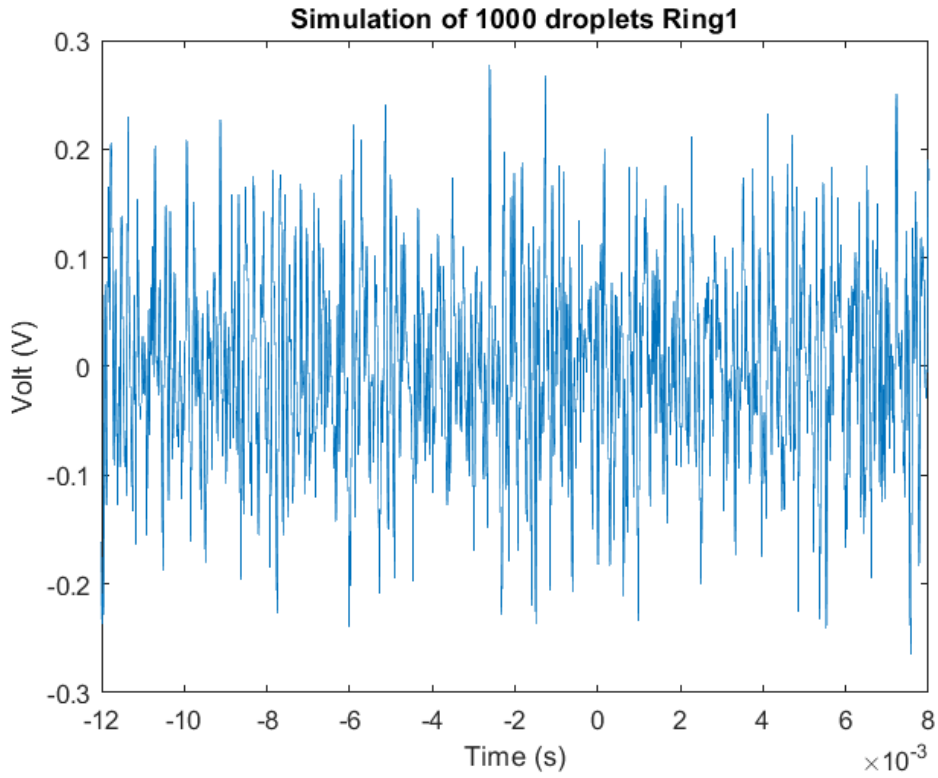

Figure 6-28: Volt-time signal of 1000 droplets for ring 1 where q = 5.0 x 10^3.

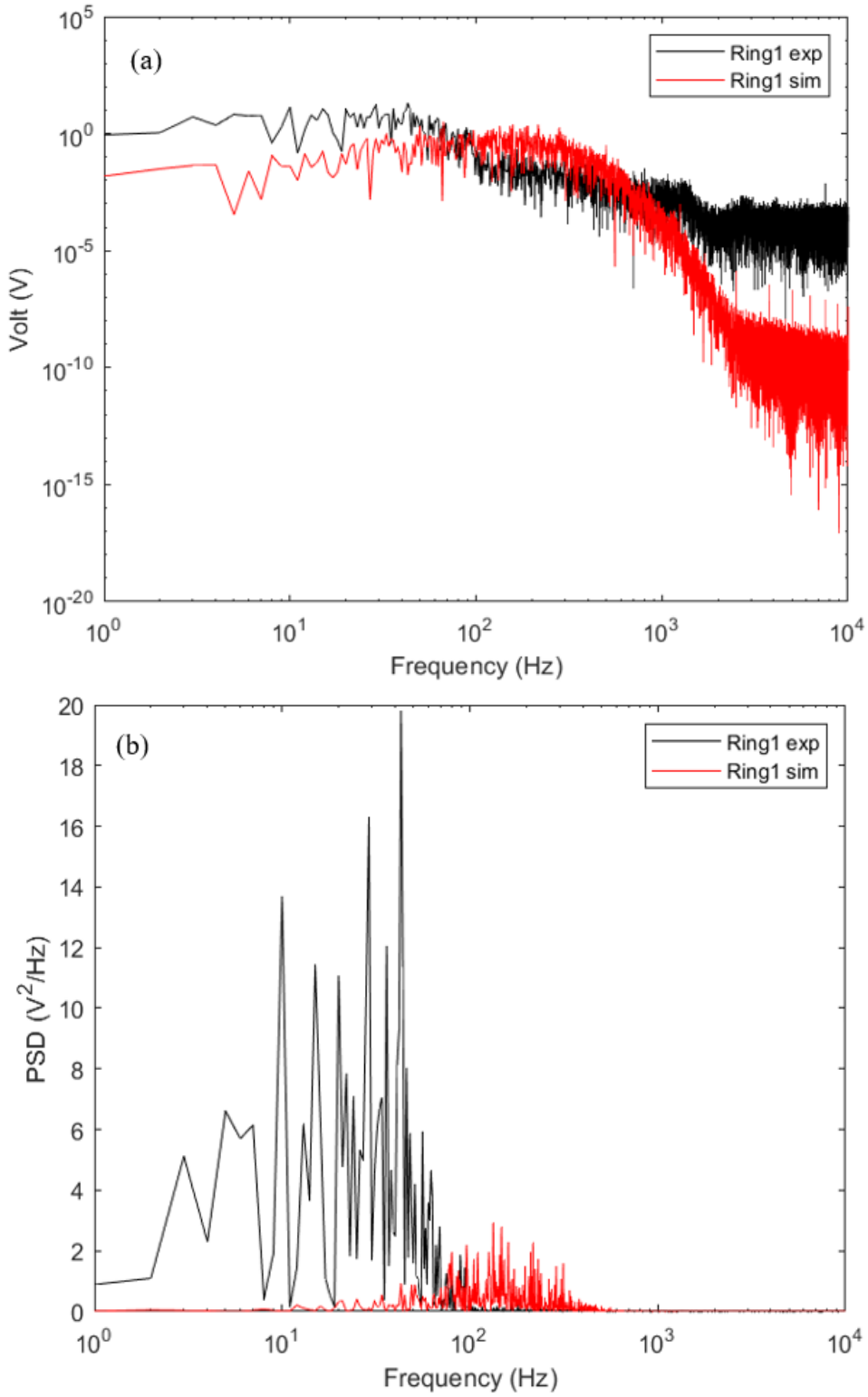

Figure 6-29: PSD comparison between experimental and simulated signal for ring 1 where q = 5.0 x 10^3 for a time shift between droplets of 20 µs in a) log scale, and b) linear scale.

To achieve our main objective of charge estimation on individual droplets or multiple droplets, charge value needs to be adjusted to make the amplitude of the simulation signal as close as possible to that of the experimental signal. Using a simulation charge value of 5.0×10^3, Figure 6-28, leads to an average pulses amplitude of 0.15 mV which is very close to the measured signal. Figure 6-29 (a) shows the PSD of the experimental and simulated signal from ring 1 and demonstrates that the simulation signal is nearly identical to the experimental signal over the mid-frequency range (100 – 1 kHz). The difference between the simulation and experimental signals low frequencies (< 100 Hz) is due to nebulizer noise. Figure 6-29 (a) shows that the simulation noise at higher frequencies, is almost zero i.e. it is < 1% of the measured at $>10^3$ Hz and $< 10^{-5}$ of the measured at 10^4 Hz. In the range between 100 Hz and 1kHz, Figure 6-29 (b) which is the linear version of Figure 6-29 (a), the simulation noise appears slightly greater than the measured but the difference is negligible. The PSD demonstrates an effective way of comparing to signals and revealed that the main frequencies in the simulation should be between 100 Hz and 1 kHz which is also found in experimental signal.

In comparison with results obtained from plate electrode collector in Chapter 5, the value of Q from ring measurements 5.0×10^3 is compared with collector plate values at the same distance from the plasma. Ring 1 is ~12 mm from plasma lower electrode. From the charge versus plate collector distance plot, Figure 5-18. the equivalent charge at distance 12 mm, at the equivalent lower power, has a value between 5.0×10^3 and 1.0×10^4 which illustrates a confirmation that the model selected, and the ring electrodes simulation provide similar charge value results to plate electrode results. This provides supporting evidence that the plate collector results in chapter 5 for distances much closer to plasma i.e., 3 mm are valid.

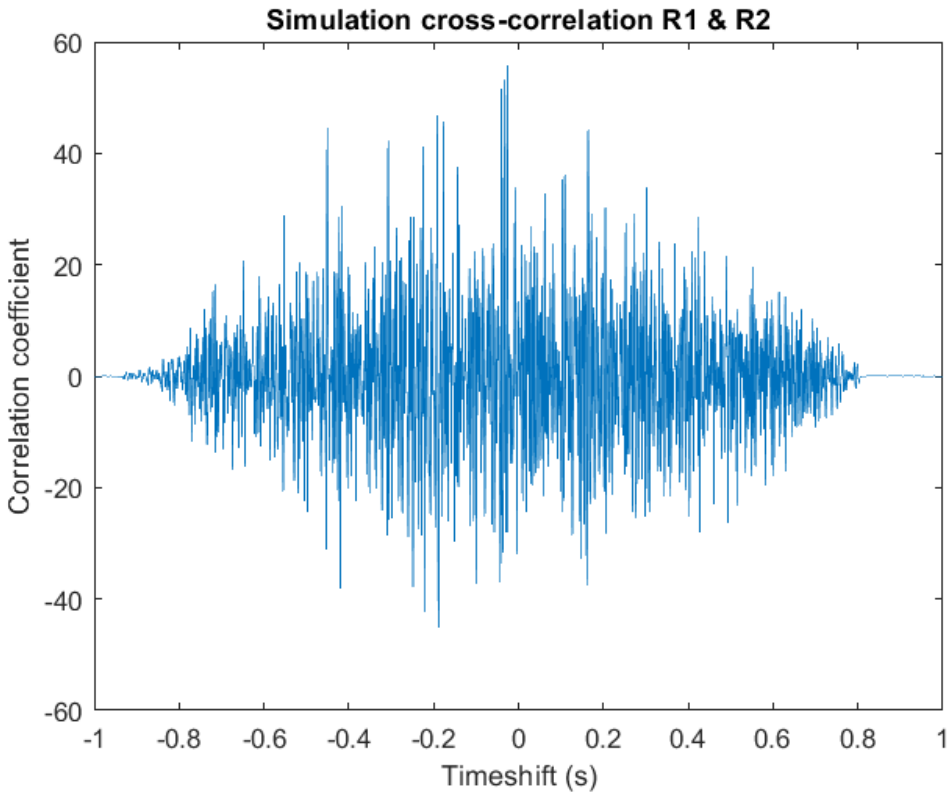

Figure 6-30: Cross-correlation from simulation between R1 and R2.

Droplets velocity could be estimated from simulation by cross-correlation between ring 1 and ring 2 using MATLAB which provides the timeshift between them and that can be converted to a velocity by dividing the distance between the two electrode (22 mm) over the timeshift. The droplets velocity range of the measured data is 19.0 – 24.6 m/s for different power values and a total gas flow rate of 4.5 slm as shown in Table 5 when the velocity of the gas flow has an average value of 17 m/s. Ring 2 was implemented in the simulation by inducing charge decay to ring 1 calculated from the difference in average peak amplitudes between ring 1 and ring 2. The decay is equal to 361 mV which is equivalent to 57.2 %, approximately, when average peak amplitudes of ring 1 = 631 mV, from Table 6, and average peak amplitudes of ring 2 = 270 mV, from Table 7. The velocity obtained from simulation cross-correlation, Figure 6-30, is 7.6 m/s where the droplets intervals are 20 µs. The ideal cross-correlation would be shown as a clear peak near t = 0 and the rest of the plot is small. Although the cross-correlation of the simulation does not show a clear peak nor the velocity has an exact value as that from the experiment, it is an indication

of similarity between ring 1 and ring 2 and it shows the simulation is mostly correct. The velocity range obtained from the measured data is dominant although wide range of droplets velocities is expected. However, the droplet velocity distribution and cumulative frequency distribution demonstrated in Chapter 5, Figure 5-2, shows 50% of droplets travel at ≤ 12 ms^{-1}, and 75% at ≤ 17 ms^{-1}. Also, early analysis was carried out previously in NIBEC by others [19] on this original data to compare ring 2 signals with ring 1 signals by hand. They state: "Data was filtered to remove low frequency (50 Hz) and high frequency (>50 kHz) noise and then Savitsky-Golay smoothing, and differentiation routines were used to manually select individual peaks in ring 1 data and their corresponding peaks in ring 2 data from which the timeshift is calculated". Some of the results are shown in Figure 6-31. Figure 6-32 shows droplets cumulative frequency versus velocity from where a polynomial fit is given. This equation could be used to randomly selecting the droplets velocity as an alternative technique to the one used in this simulation of randomly selecting x and then calculating the corresponding v. Although it would depend on picking a specific value of x as an approximation, it may improve the cross-correlation and it can be investigated as part of future work.

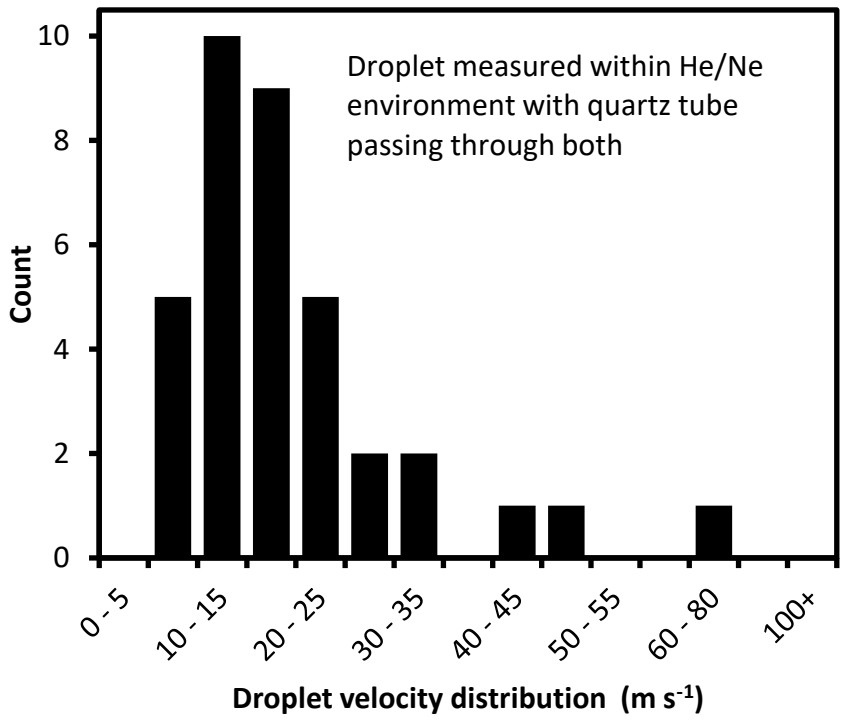

Figure 6-31: Droplets count vs. their velocity distributions.

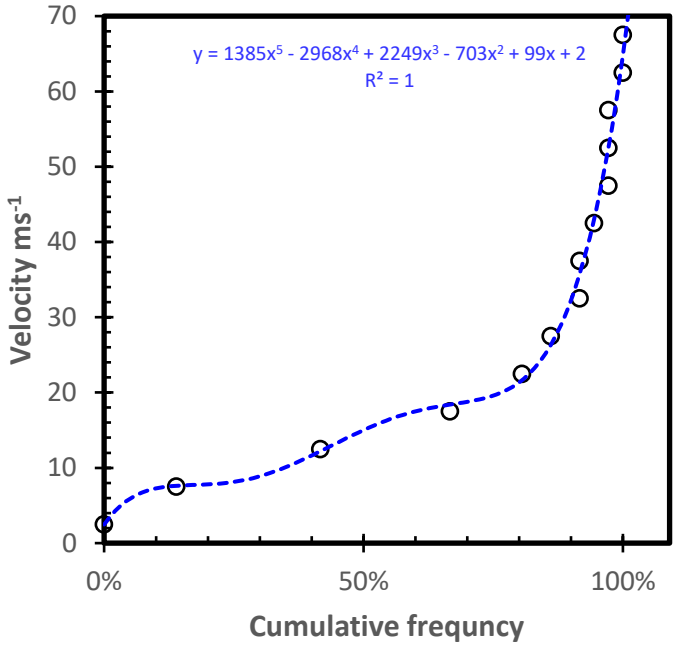

Figure 6-32: The relation between droplets velocity and cumulative frequency.

The droplet Q value from Equation 13 obtained by Gajewski analysis [3] is 500 approximately for, t = 0 and average volt of 631 µV. This value is less than the value estimated from Yan analysis and has a very large discrepancy from the value estimated from plate electrode analysis in chapter 5. Therefore, Yan analysis is more likely to be correct as it provides results that agree better than Gajewski with results of chapter 5.

6.8 Conclusion

The simulation using Yan analysis has provided promising results for estimation of average charge on droplet using experimental data collected from double ring electrodes for the comparisons. The estimated value is 5.0 x 10^3 at 12 mm distance from plasma and it very similar to the estimated value from plate electrode analysis in chapter 5 which provides indication that assumptions and calculations existing in the analysis are almost correct. The velocity has been also estimated as 7.6 m/s from cross-correlation between ring 1 and ring 2. This value is slightly lower than the velocity estimated from the experimental signal however, it is good indication for the similarity between the two rings and it can be improved in the future by considering different droplets velocity distribution. In addition, further checks can be done to evaluate the sensitivity of the droplets lognormal distribution on changes of the contributed factors.

6.9 References

[1] Y. Yan, B. Byrne, S. Woodhead, J. Coulthard, Velocity measurement of pneumatically conveyed solids using electrodynamic sensors, Meas. Sci. Technol. 6 (1995) 515–537. https://doi.org/10.1088/0957-0233/6/5/013.

[2] T. Hussain, W. Kaialy, T. Deng, M.S.A. Bradley, A. Nokhodchi, D. Armour-Chélu, A novel sensing technique for measurement of magnitude and polarity of electrostatic charge distribution across individual particles, Int. J. Pharm. 441 (2013) 781–789. https://doi.org/10.1016/j.ijpharm.2012.10.002.

[3] J.B. Gajewski, B. Glod, R.A. Grobelny, W. Kala, Continuous non-contact measurement of electric charges of solid particles in pipes of pneumatic transport - II: Measuring system and its application, Conf. Rec. - IAS Annu. Meet. (IEEE Ind. Appl. Soc. (1989) 1964–1969. https://doi.org/10.1109/ias.1989.96909.

[4] J.B. Gajewski, Electrostatic nonintrusive method for measuring the electric charge, mass flow rate, and velocity of particulates in the two-phase gas-solid pipe flows - Its only or as many as 50 years of historical evolution, IEEE Trans. Ind. Appl. 44 (2008) 1418–1430. https://doi.org/10.1109/TIA.2008.2002276.

[5] A250 Charge Sensitive Preamplifier – Amptek – X-Ray Detectors and Electronics, (n.d.). https://www.amptek.com/internal-products/a250-charge-sensitive-preamplifier (accessed October 31, 2022).

[6] P.D. Maguire, C.M.O. Mahony, C.P. Kelsey, A.J. Bingham, E.P. Montgomery, E.D. Bennet, H.E. Potts, D.C.E. Rutherford, D.A. McDowell, D.A. Diver, D. Mariotti, Controlled microdroplet transport in an atmospheric pressure microplasma, Appl. Phys. Lett. 106 (2015). https://doi.org/10.1063/1.4922034.

[7] P.H.Y. Review, Theory of collectors in, 28 (1926).

[8] J.E. Allen, Probe theory - the orbital motion approach, Phys. Scr. 45 (1992) 497–503. https://doi.org/10.1088/0031-8949/45/5/013.

[9] I. Pilch, L. Caillault, T. Minea, U. Helmersson, A.A. Tal, I.A. Abrikosov, E.P. Münger, N. Brenning, Nanoparticle growth by collection of ions: Orbital motion limited theory and collision-enhanced collection, J. Phys. D. Appl.

Phys. 49 (2016). https://doi.org/10.1088/0022-3727/49/39/395208.

[10] J.E. Allen, A. Turrin, The collection of positive ions by a probe immersed in a plasma, Proc. Phys. Soc. 83 (1964) 177–179. https://doi.org/10.1088/0370-1328/83/1/120.

[11] R. V. Kennedy, J.E. Allen, The floating potential of spherical probes and dust grains. Part 1. Radial motion theory, J. Plasma Phys. 67 (2002) 243–250. https://doi.org/10.1017/S0022377802001691.

[12] L. Patacchini, Collisionless Ion Collection by a Sphere in a Weakly Magnetized Plasma by Leonardo Patacchini, (2007). http://hdl.handle.net/1721.1/41298.

[13] L. Patacchini, I.H. Hutchinson, G. Lapenta, Electron collection by a negatively charged sphere in a collisionless magnetoplasma, Phys. Plasmas. 14 (2007). https://doi.org/10.1063/1.2741249.

[14] J.J. Walker, Fine-Particle Charging-Rate-Limit Modification to Grain Dynamics in Abrupt and Gradual Inhomogeneities, (2015).

[15] N. Hendawy et al., The creation of highly charged micron-sized water droplets, In Preperation. (n.d.).

[16] S. Hamaguchi, R.T. Farouki, Polarization force on a charged particulate in a nonuniform plasma, Phys. Rev. E. 49 (1994) 4430. https://doi.org/10.1103/PhysRevE.49.4430.

[17] J. Neufeld, R.H. Ritchie, Passage of Charged Particles through Plasma, Phys. Rev. 98 (1955) 1632. https://doi.org/10.1103/PhysRev.98.1632.

[18] The pulstran Function - MATLAB & Simulink - MathWorks United Kingdom, (n.d.). https://uk.mathworks.com/help/signal/gs/the-pulstran-function.html (accessed November 2, 2022).

[19] P. Maguire, No Title, Privite Commun. (n.d.).

7 Conclusion and future recommendations

7.1 Conclusion

Non-thermal atmospheric pressure plasmas has a wide range of applications such as nanomaterials, water treatment, and plasma medicine etc. The properties of the plasma affects all application so understanding and controlling its properties such as plasma gas temperature would have high importance particularly for heat sensitive applications. Furthermore, the interaction between plasma and liquids has led to more applications due to the noticeable increase in the plasma reactivity. However understanding this system is challenging because the reactive species have a short lifetime and interact quickly with each other and with the medium. Electrons are one of the most reactive species but they have an extremely short lifetime so harder to measure.

The factors affecting gas temperature are rarely characterised particularly for plasma with microdroplets. Along with the importance for high sensitive applications, It is vital to control plasma characteristics as plasma gas temperature affects chemical, surface and composition reactions. The traditional in-situ and lab techniques such as Raman and Rayleigh scattering, Schlieren, optical emission spectroscopy, thermocouples, fibre optic thermometers, IR and thermal cameras have many limitations such as analysis and measurements complexity, high cost and some of them causes plasma disruption. Plasma gas temperature has been measured in this work using a small focal-spot IR sensor which was able to provide high accurate and continuous measurements. The temperature was measured with various plasma gas flow, mixture between Ar and He gases, and plasma power from the inner and outer wall of the capillary tube where the maximum temperature achieved was below 50 ^{o}C. In addition, plasma gas temperature was measured while containing small microdroplets of 12 μm – 15 μm size and the gas temperature was decreased by 10 ^{o}C due to the water microdroplets.

There has been a high substantial interest in charged droplets as chemical microreactors due to the acceleration of chemical reactions in confined volumes. High charge and high interfacial electric fields could be generated using free electrons in long-lasting gas-phase microdroplet reactors which is able to deliver continuous

reaction products instantaneously downstream. Free electron fluxes to liquid also provide a rich source of solvated electrons capable of initiating rapid reduction reactions in the injected droplets. Supplying such electrons needs a high density but low temperature plasma operating at atmospheric pressure under non-equilibrium conditions and capable of tolerating droplet injection without additional evaporation or electron loss. Although, from theoretical considerations, microscale particles in such a plasma are expected to acquire a net charge, this has yet to be demonstrated.

Droplets non-contact charging was applied in the literature by UV and corona discharges. Although charge distribution was possible, aiming at increasing the charge level requires large droplets with size over 100 μm which significantly reduce the surface to volume ratio and the consequent advantages of higher number of reactive species. Also the corona assisted ES has many limitation such as gas instability and high ion bombardment due to the high concentration of positive charge droplets in these systems. In contrast, charged droplets generated using glow discharge plasma led to higher plasma density and reactive species compared to corona discharge. The measurements of the average charge on a particle has been investigated for the first time in atmospheric pressure plasma using a plate collector and microdroplets at 50 kHz rate. For absorbed powers of 1.5 W and 5 W, at a distance of 3 mm from the downstream plasma electrode, the maximum average charge per droplet was 8×10^5 electrons (128 fC) and 2.5×10^6 electrons (400 fC), respectively. This charge value is higher than that of corona system or electron charging in low pressure plasmas by a 2 – 3 orders of magnitude. Where the charge was noted to decay within short distance from the plasma (30 mm) to a value of $10^3 – 10^4$ electrons per droplet.

Another collector, double ring electrodes outside the capillary tube, was utilised to measure droplets charge. The relation between the voltage generated by the droplets and the equivalent charge was investigated using a simulation model. The model is based on the droplets velocity (v_s), diameter (D) and radial location from the capillary tube centreline (x) where the droplets velocity was assumed to have same value as gas velocity which is following laminar flow. Also the charge is dependant on the droplets radius and can be estimated from the P-H model. Simulation of a single droplet when it passes by the tube centerline and at different radial locations was initiated to be compared with a selected pulse from the measured signal with respect

to pulse width and amplitude. Then multi droplets were simulated after implementing various parameters such as v_s, D and x. The estimated charge is 5.0×10^3 which makes the simulation average amplitude as close as possible to the equivalent one in the measured signal. This value was compared to estimated charge value from the plate collector and was found to fall in the charge range at the corresponding power and distance from the plasma. In addition, ring2 signal was simulated by inducing a charge decay to ring1 for the attempt of estimating droplets velocity. The droplets velocity was determined from cross-correlation between ring1 and ring 2 and had a value of 7.6 m/s which is lower than the average velocity from the experiment and that is may be due to the droplets velocity distribution.

The PAD is a specially designed chamber for the Plasma – Nanomaterials Group at Ulster University (NIBEC) attached to a standard XPS analysis. This system is designed to allow different plasma systems to be installed so various solids or liquids sample can be treated and then transferred directly to the XPS analysis chamber avoiding any environmental influence on the samples. The first main objective of this research was to plasma treat frozen water and then transfer the sample for XPS analysis. Where freezing the water sample very quickly after treatment would allow studying the reactions of the very short lifetime species and may offer a solution to understand this complex system of plasma-liquid interactions. The prospective results of this research may have high importance in many applications such as plasma medicine and in particular on cancer treatment. Unfortunately the supplied water freezing system did not work at atmospheric pressure and alternative methods were investigated. After overcoming many challenges such as water sample transfer, freezing the sample, vacuum leaks etc., a frozen water sample has been achieved. The sample also was proved to be exist without melting after transferring from the PAD to the preplock chamber.

7.2 Future work and recommendations

a) The plasma gas temperature measurements obtained using small focal spot IR sensor are promising particularly with the inclusion of microdroplets for their potential in increasing and delivering energetic reactive species. The research results can support many applications including plasma medicine. For example, wound healing and cancer treatment are heat sensitive applications and would highly benefit from plasma contained microdroplets so they would require a controlled heat and a continuous monitoring for the gas temperature to provide a rapid response to any undesired changes. Further measurements in a practical application would be required bearing in mind the location and size of the IR sensor focal spot with respect to the target area as they significantly affect the measurements.

b) The charge measurements using two different collectors, plate and double ring, are attractive. Further experimental trials can be performed to deliver a single droplet of known size, speed and charge down the tube to provide a calibration factor where the induced voltage is expected to be in the range of 0.1mV- 10mV. Then the result voltage signal can be measured and converted into a droplet charge though, our system cannot provide a single droplet. An electrospray setup which consists of a hypodermic needle attached to a known high voltage is an alternative option so the droplet charge and speed could be calculated by knowing the size of droplet. However, the droplet is always much bigger than the needle diameter in our system so achieving small enough droplets might be possible but challenging.

c) Successfulness in having a frozen sample in the PAD is a significant achievement that allows the move to next step which is installing the plasma system in the PAD. Further improvements to the current system are possible; first such as using smaller SST diameter pipe for the water delivery system to provide better control on the amount of water sample delivered and reduce any chance of water splatter outside the sample stage. To improve the sample cooling rate, a few suggestions can be considered such as connecting multiple double coils in series in individual dewars, operating LN2 coils at lower flow rate, and/ or using coils of microbore piping. However these ideas, would consume larger amounts of LN2 and may increase the process cost and time. Furthermore, to maintain the frozen sample,

an insulating jacket can be used as a cost effective solution that might help in reducing the temperature increase of the sample due to heat transfer by the wall. Another suggestion is to add shield enclosure around the sample with one side open to allow the transfer arm movement in and out. This might partially insulating the sample from the effects of heating of the N2 by the chamber wall. After installing the plasma system, it might be necessary to cool the plasma gas in order to help maintaining the frozen water sample which could be done by connecting a copper coil contained in a LN2 dewar to the line of the gas. In case of plasma contained microdroplets, the cooling rate should be reduced so as to allow time for plasma treatment and avoid frozen droplets clusters inside the tube. Nevertheless, the cold gas may affect the plasma properties and instability so further investigation would be required.